Next-generation technologies for gravitational wave detectors

Thesis by
Anchal Gupta

In Partial Fulfillment of the Requirements for the
Degree of
Doctor of Philosophy

Caltech

CALIFORNIA INSTITUTE OF TECHNOLOGY
Pasadena, California

2023
Defended 15 May, 2023

ACKNOWLEDGEMENTS

To my insanely understanding plants, thanks for being with me through all kinds of times and filling my life with love and hope.

To Twix and Munch, thanks for coming into my life and giving me your unconditional support and love, especially during these last few months. I wish you could read and understand this, you are the best kittens in the world.

To Anamika, the love of my life, thanks for being there for me and taking care of me. Your love and support helped me achieve everything I have today, I am the most lucky person on Earth to have you in my life. Thanks for being my cornerstone.

To my parents, and my brother, thanks for answering my endless questions and making me into a scientist. My dreams would not have come true if you all had not supported me. Thank you, mummy, for passing me your experimental skills, thank you, papa, for passing me your problem-solving skills, and thank you bhaiya for showing me the future and introducing me to science as a kid. Thank you bhabhi for your love and support.

ABSTRACT

Since the first detection of gravitational waves (GW) in 2015, gravitational wave detectors have continually been improved. Now, a compact binary coalescence (CBC) is detected once a week in a full sensitivity observation run of the Advanced Laser Interferometric Gravitational-wave Observatory (LIGO) detectors. This thesis describes research on a collection of projects aimed at developing next-generation of technologies for future gravitational wave detectors. In the first part, I describe my research on directly measuring the coatings Brownian noise of high-reflectivity coatings made out of crystalline AlGaAs. It is a part of the larger effort to reduce the classical noise limit in the 30 Hz to 300 Hz band in the current generation of detectors. The second part describes the Balanced Homodyne Readout (BHR) upgrade that was performed at the 40m prototype at Caltech. This new readout method would be instrumental in reducing excess noise at the lower frequencies in GW detectors. With several future detectors planned with an order of magnitude improvement in sensitivity, the parameter estimation about the merging bodies would be limited by the calibration uncertainty if the calibration method is not updated. In the third part of the thesis, I describe our work on developing a systematic-free absolute calibration of the detector. In this scheme, we refer the calibration to the ultra-stable optical common length mode of the arm cavities in the detectors. In the final part, I describe four new arm length stabilization schemes for the proposed cryogenic upgrade of Advanced LIGO detectors into Voyager.

"Never measure anything but frequency!"

- Arthur Leonard Schawlow

TABLE OF CONTENTS

I Coatings Thermal Noise 4

II Balanced Homodyne Detection 48

LIST OF ILLUSTRATIONS

LIST OF TABLES

INTRODUCTION

Next-generation technologies for gravitational wave detectors

As far back as we see in history, humans have tried to look into outer space for the answers about origins of our universe. Astronomy is an old scientific field that has been improved to unimaginable degrees as time progressed. Two binary black holes, each about 30 times as massive as our Sun merged and sent out gravitational wave ripples. After traveling for about 1.3 billion years, they reached Earth on September 14th, 2015, where we had just started looking for them. The pair of detectors of Laser Interferometer Gravitational-Wave Observatory[1] had observed a new kind of signal, heralding a new era in astronomy and giving us a new window to probe the universe.

Since then, we have made our detectors better and have observed more than 90 confirmed compact binary coalescences[2]. Eight years ago, we did not even know if gravitational waves existed and if Einstein's general theory of relativity produced correct results. This advancement took place through decades of planning and teamwork among a large collaboration of scientists. As I entered Caltech to learn how to do research in experimental physics, I was passed the baton to take it further. Constant advancement is the key to achieving the unimaginable. With that in mind, my thesis work comprised of working on developing the next generation of technologies to make gravitational wave detection more accurate, more precise, and more robust. Gravitational wave astronomy, like any other sub-field of astronomy, must move into the next phase of collecting a large sample of accurate and precise data. This will help in building statistics to improve our understanding of the universe from a new perspective.

This thesis is divided into four parts, representing the four next-generation technologies I have researched. The first part focusses on finding solutions for the coatings Brownian noise that limits the current generation of gravitational waves detectors from 30 Hz to 300 Hz region (see Fig. 0.1). This is a classical source of noise, fundamentally present in the high reflectivity coatings used in the test masses of the detectors. In this part, I'll describe an experiment we performed to directly observe
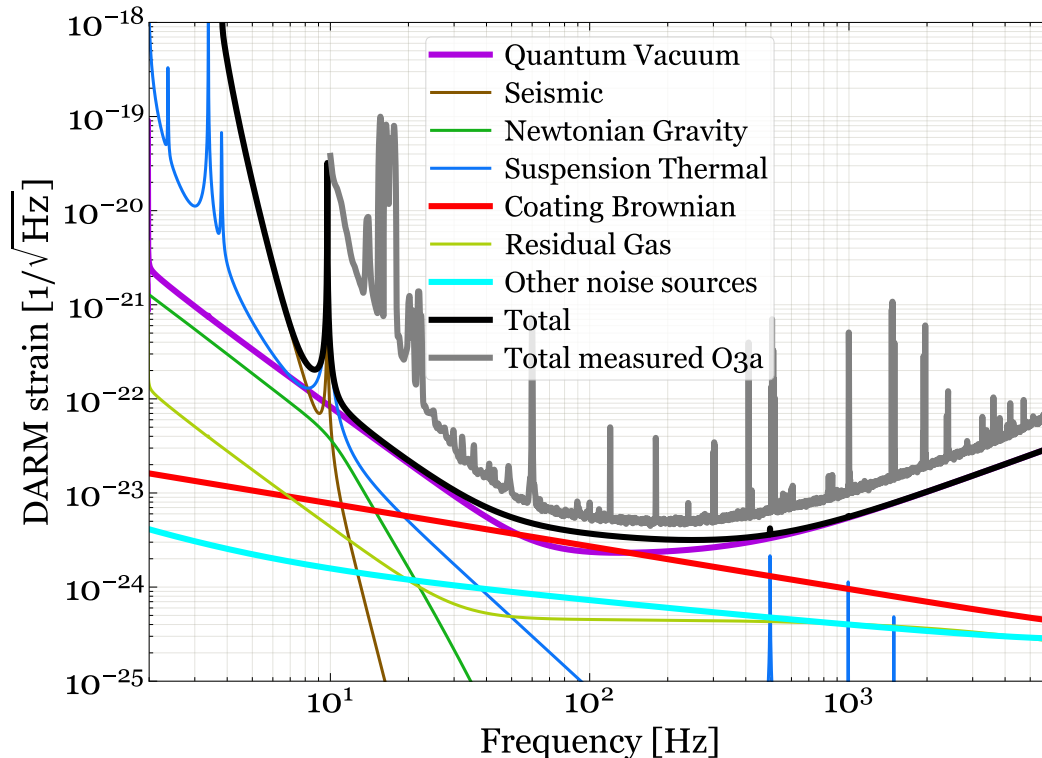
Figure 0.1: Advanced LIGO noise budget made using gwinc[3]. The grey curve is the measured noise in observation run "O3a" at LIGO Hanford Observatory.

the coatings Brownian noise due to a new class of crystalline coatings, measuring displacement noise at the level of 2×10^{-18} m/$\sqrt{\text{Hz}}$.

In the second part, I will describe our work at the 40m prototype of LIGO at Caltech, where we upgraded the interferometer layout to create a Balanced Homodyne Detection readout port. To the best of my knowledge, this is the first time this detection method has been implemented on a suspended interferometer. This method would be beneficial to remove the excess classical noise in the low-frequency band as seen in the measured noise trace in Fig. 0.1. We tested important bottlenecks in the implementation of this readout and measured preliminary noise improvement estimates for a successful follow-up by advanced LIGO to upgrade the site detectors later.

In the third part, we work on developing a new calibration method for future gravitational wave detectors. The gravitational waves detection community is planning to expand the network of detectors and build new detectors with plans to reduce the noise floor by more than an order of magnitude (see Fig. 0.2). While this is good for measuring more compact binary coalescences, the estimate of the event parameters
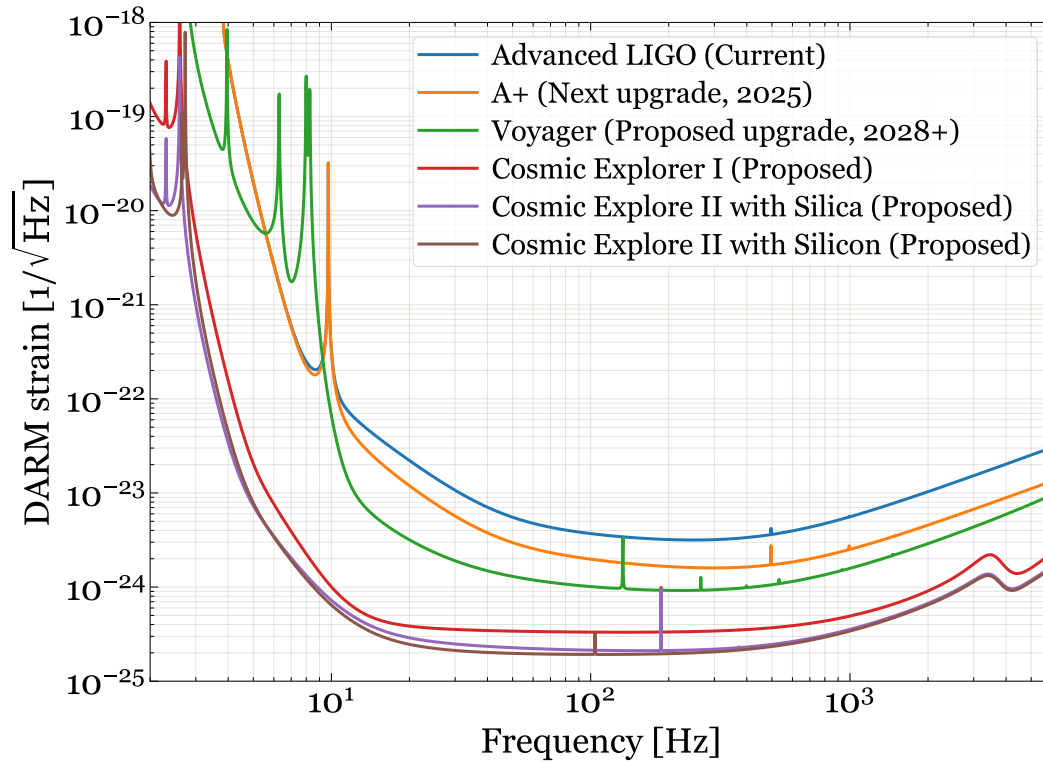
Figure 0.2: Sensitivty of future proposed detectors. Estimated using GWINC[3].

would become limited by the calibration uncertainty in the response function of the detectors, if the present calibration method is not updated. In this part, I will describe our work on developing an absolute calibration of the detector referred to the ultra-stable optical common length mode of the arm cavities in the detectors that would reduce systematic error contribution.

In the fourth part, I'll describe my small contribution to the ongoing work for the proposed cryogenic upgrade to LIGO sites, called Voyager. This upgrade would present new challenges to old solutions that worked in the current generation of detectors. I worked on designing the arm-length stabilization system for Voyager. This subsystem is currently used in locking several control loops in the detector to reach science observation mode. Thus it is crucial to find a solution for it along with planning of the detector upgrade.

Part I

Coatings Thermal Noise

for crystalline Al$_{0.92}$Ga$_{0.08}$As /GaAs coated mirrors

Chapter 1

INTRODUCTION TO COATINGS BROWNIAN NOISE

The astounding 10^{-19}m/$\sqrt{\text{Hz}}$ displacement sensitivity of advanced LIGO is achieved by using high circulating power in the 4-km arms. Higher circulating power means more photon averaging while reading the gravitational wave signal. This is achieved by utilizing special high reflectivity Bragg coatings on the test masses, with the End Test Mass mirror coating achieving 5 ppm transmission (that is 99.99975% reflectivity) for 1064 nm wavelength laser.

Presently these mirror coatings are made of alternate layers of amorphous silica and titania-doped tantala [4]. While this reduced the noise floor in AdvLIGO substantially, the 10-500 Hz region of the design sensitivity in AdvLIGO is limited by the coatings Brownian noise [5]. Coatings Brownian noise is the result of fluctuations in the material by virtue of it being at a finite temperature. Various methods are being pursued to reduce this noise [6]. These include new coating structures [7–10] and novel materials [11–14] for the coating. The fluctuation-dissipation theorem relates the energy dissipation in a mechanical system with its equilibrium noise fluctuations [15]. The disordered structure of amorphous materials leads to mechanical loss peaks at low temperatures [16]. The lack of strong cohesion and order between the molecules of the material result in internal friction that leads to Brownian noise. Hence, it is suggested that crystalline materials might be able to provide lower Brownian noise solutions.

Cole et al. [14] fabricated a coating with crystalline $Al_{0.92}Ga_{0.08}As$ and GaAs, and used substrate-transfer with optical bonding to apply the coating to a fused silica substrate. Preliminary results suggest that this material choice can improve Brownian noise performance. Penn et al. [17] performed indirect noise measurement for this coating structure by doing mechanical ring-down measurements of silica discs, with and without these coatings applied. This provides an estimate of the loss angles of the coating. Chalermsongsak et al. [18] optimized the coating structure made with these materials to achieve coherent cancellation of thermo-optic noise and demonstrated it as well.

In this part of my research, I delved into directly measuring the phase noise on light due to such crystalline coatings. We inherited the experiment Chalermsongsak et

al. [18] used to prove thermo-optic cancellation in these coatings, which I, with help from Andrew Wade, and Craig Cahillane, took to improved sensitivity limit, so that we can observe their coatings Brownian noise.

Our experiment complements the work in Penn et al. [17] as we can backtrack the same loss angle values using the theoretical model of Hong et al. [19]. This helps us not only in generating more information about these particular crystalline coatings but also understanding the nature of actual phase noise reflected by optically bonded coatings with small beam areas and verifying the theoretical understanding we have so far.

In this chapter, I will explain how fluctuation-dissipation theorem formalizes the relationship between internal friction in a material and the noise fields that emerge through interaction with environment. Then, we will take the case of a mirror with a Bragg coating on it, and see how brownian motion of the mirror surface and coating layers are related to their mechanical properties. Then, we'll look into how this affects the light that reflects off the mirrors and becomes a noise source for gravitational waves detectors.

1.1 Fluctuation-Dissipation Theorem

In our physics major education, we are taught how temperature is a measure of the average internal motion of a body, whether it is a collection of gas, liquid, or solid. The motion itself is supposed to be random and unpredictable, while we know the mean distribution of the particle kinetic energies or vibrational energies.

For fluids in particular, the seminal paper by Einstein puts a vivid picture of particle diffusion in fluids that is seen through microscopes. For a particle suspended in a liquid, the higher the temperature, the faster the diffusion of particle will happen through the fluid volume, and the more viscous the fluid is, the slower the diffusion would happen. This gives us important insight on the relationship of the degree of such brownian motion and the environment properties like temperature and frictional losses.

Fluctuation-dissipation theorem[15] generalizes this relationship by stating:

"Given that a system obeys detailed balance, thermodynamic fluctuations in a physical variable at equilibrium predict the dissipation of energy in the dynamics of the same physical variable, and vice versa."

This means that the channels or pathways through which a system dissipates energy to the environment are used in reverse when the system is at equilibrium but receives noise from the environment through the same channels.

In more technical terms, one can find out the frequency distribution of noise that an environment would cause to a system through the dissipation rate of energy in that system when oscillated at particular frequencies. For example, take a mechanical system of admittance $Z(f)$ for a parameter x, where the imaginary part of the impedance shows the reactance of the system and the real part shows the dissipation of the system.

$$\tilde{v}(f) = i\omega\tilde{x}(f) = Z(f)\tilde{F}(f) \tag{1.1}$$

Then, at equilibrium at temperature T, the single-sided power spectral density of the noise of the system is given by:

$$S_x(f) = \frac{k_B T}{\pi^2 f^2}\text{Re}[Z(f)] \tag{1.2}$$

This gives experimentalists access to predict and estimate the Brownian motion of this system, by measuring the mechanical impedance $Z(f)$. One can force the system at frequency f, and magnitude F_0 and observe the amount of energy dissipated by the system W_{diss} in one period of oscillation. Then the real part of admittance is:

$$\text{Re}[Z(f)] = \frac{4\pi f}{F_0^2}W_{diss} \tag{1.3}$$

The dissipation can be written as an angular fraction ϕ of the elastic energy stored in a single cycle of oscillation U as:

$$\text{Re}[Z(f)] = \frac{4\pi f}{F_0^2}U\phi \tag{1.4}$$

Such angular loss fraction is known as the loss angle of the admittance and will be a quantity of interest in future chapters. Note that another way to measure mechanical admittance is to measure the impulse response of the system. One can measure the quality factor of the decay of the system and the loss angle is inversely proportional to this quality factor:

$$\phi = \frac{2\pi}{Q} \tag{1.5}$$

1.2 Calculating Coatings Brownian Noise

The mirrors in LIGO test masses are coated with alternative layers of high and low refractive index materials. If the layers' thickness is such that the laser wavelength undergoes $\pi/4$ phase shift, then a special condition arises: the reflected electric field from each layer interface constructively interferes while the transmitted fields interfere destructively. As a stack, this allows the coating to provide very high reflection such as 99.9995% as the case for advanced LIGO coatings. High reflection is required to permit higher circulation of power in the arm cavities so that the sensitivity to the gravitational wave strain is more. Thus, the adoption of such highly reflective mirrors is required for detecting gravitational waves.

But this advantage also results in an extra noise source. The thin coatings on the mirror surfaces have vibrations originating purely because they are at a finite temperature. This noise is called Coatings Brownian Noise as it is similar to the Brownian motion of particles suspended in a liquid. Using the fluctuation-dissipation theorem mentioned in the last section, we can estimate the noise imparted on the phase of the reflected light from these coatings. In this section, I will mostly use the analysis presented by Hong et al. [19] to explain the origin of this noise and the relationship of the coatings' loss angle to it. This is an attempt to supplement their work by laying out a coatings thermal noise calculation roadmap for experimentalists. This work has been added to the Gravitational Waves Interferometer Noise Calculation tool[3].

Let's index the coating layers starting from the layer closest to the surface as the 0 layer and the last layer as the $N - 1$ layer. In our notations, we can consider the vacuum as -1 layer and the substrate of the mirror as layer N. Then one can calculate the reflectivity of the interface from $(j - 1)^{th}$ to j^{th} layer:

$$r_j = \frac{n_j - n_{j+1}}{n_j + n_{j+1}} \tag{1.6}$$

Next, we can calculate the one-way phase shift that occurs in light one passing from j^{th} layer is defined as:

$$\phi_j = 2\pi \frac{d_j n_j}{\lambda} \tag{1.7}$$

From these parameters, we define Transmission Matrix from j^{th} layer and Reflection Matrix at the interface from $(j-1)^{th}$ to j^{th} layer as [19, Eq. 98, 99]:

$$\mathbf{R_j} = \frac{1}{\sqrt{1-r_j^2}}\begin{pmatrix} 1 & -r_j \\ -r_j & 1 \end{pmatrix} \tag{1.8a}$$

$$\mathbf{T_j} = \begin{pmatrix} e^{i\phi_j} & 0 \\ 0 & e^{-i\phi_j} \end{pmatrix} \tag{1.8b}$$

These matrices transform onward and backward-going fields from the left side of an optical element to the right side of it. Multiplying these matrices in order of their appearance to light coming from the left, we get the total transformation matrix of the coating as [19, Eq. 101]:

$$\mathbf{M} = \mathbf{R_N T_{N-1} R_{N-1}...R_1 T_0 R_0} \tag{1.9}$$

Then the complex reflectivity of the entire coating stack can be written as [19, Eq. 102]:

$$\rho = -M_{21}/M_{22} \tag{1.10}$$

Note that we want to understand how changes in the individual layer parameters like its thickness and refractive index propagate into changes to the overall complex reflectivity of the entire coating stack. The layer thickness d_k is associated with the ϕ_k, and layer refractive index n_k is associated with the interface reflectivity r_{k-1} and r_k, so we will calculate the derivatives of ρ with respect to these variables. We define ρ_k as the complex reflectivity for k layered stack with layers from $(N-k+1)^{th}$ layer to Nth layer on top of the same substrate but the $(N-k)^{th}$ layer material on top instead of vacuum. Then the total transformation matrix for this k-layered stack would be:

$$\mathbf{M_k} = \mathbf{R_N T_{N-1} R_{N-1}...R_{N-k+1} T_{N-k} R_{N-k}}$$
$$\rho_k = -\mathbf{M_{k21}}/\mathbf{M_{k22}} \tag{1.11}$$

One can identify easily that:

$$\mathbf{M_{k+1}} = \mathbf{M_k T_{N-k-1} R_{N-k-1}} \tag{1.12}$$

This allows us to write a recursion relation for ρ_{k+1} as:

$$\rho_{k+1} = \frac{r_{N-k-1} + \rho_k e^{2i\phi_{N-k-1}}}{1 + r_{N-k-1}\rho_k e^{2i\phi_{N-k-1}}}, \quad \rho_0 = r_N \tag{1.13}$$

We can use this to calculate the following derivatives:

$$\frac{\partial \rho_{k+1}}{\partial \rho_k} = \frac{\left(1 - r^2_{-k+n-1} - 1\right) e^{2i\phi_{N-k-1}}}{\left(1 + \rho_k r_{-k+n-1} e^{2i\phi_{-k+n-1}}\right)^2}$$

$$\frac{\partial \rho_{k+1}}{\partial r_{N-k-1}} = \frac{1 - \rho_k^2 e^{4i\phi_{-k+n-1}}}{\left(1 + \rho_k r_{-k+n-1} e^{2i\phi_{-k+n-1}}\right)^2} \tag{1.14}$$

$$\frac{\partial \rho_{k+1}}{\partial \phi_{N-k-1}} = -2i \frac{\left(1 - r^2_{-k+n-1} - 1\right) e^{2i\phi_{N-k-1}}}{\left(1 + \rho_k r_{-k+n-1} e^{2i\phi_{-k+n-1}}\right)^2}$$

From here, it is straightforward to calculate derivates of $\rho = \rho_N$ by using (for $j \geq 1$):

$$\frac{\partial \rho}{\partial r_j} = \left(\prod_{k=N-j}^{N-1} \frac{\partial \rho_{k+1}}{\partial \rho_k}\right) \frac{\partial \rho_{N-j}}{\partial r_j}$$

$$\frac{\partial \rho}{\partial \phi_j} = \left(\prod_{k=N-j}^{N-1} \frac{\partial \rho_{k+1}}{\partial \rho_k}\right) \frac{\partial \rho_{N-j}}{\partial \phi_j} \tag{1.15}$$

And for $j = 0$:

$$\frac{\partial \rho}{\partial r_0} = 1, \quad \frac{\partial \rho}{\partial \phi_0} = 0 \tag{1.16}$$

Now, let's try to see the connection of these derivatives to the amplitude and the phase of the reflected light. Relative amplitude fluctuations of the reflected light can be given by:

$$\frac{\delta E_{refl}}{E_{refl}} = \frac{\delta |\rho|}{|\rho|} = \mathrm{Re}[\delta \log \rho] \tag{1.17}$$

While the phase fluctuations of the reflected light are given by:

$$\delta \phi_{refl} = \delta \angle \rho = \mathrm{Im}[\delta \log \rho] \tag{1.18}$$

Hong et al.[19] further define functions $\xi(\vec{x})$ and $\zeta \vec{x}$ to represent the phase fluctuations and amplitude fluctuations as:

$$\xi(\vec{x}) + i\zeta(\vec{x}) = -\frac{i}{2k_0} \delta \log \rho(\vec{x}) \tag{1.19}$$

where $\vec{x}$ is a transverse vector for the location on the mirror surface. These functions are expanded into individual contributions from ϕ_j and r_j using chain rule as:

$$\xi(\vec{x}) + i\zeta(\vec{x}) = -\delta z_s(\vec{x}) - \sum_{j=1}^{N} \int_{z_{j+1}}^{z_j} \left[1 + \frac{i\epsilon(z)}{2}\right] u_{zz}(\vec{x}, z) \tag{1.20}$$

Here z_j is in the position of the interface between j^{th} to $(j-1)^{th}$ layers, z_s is the position of the substrate surface, $u_{zz}(\vec{x}, z)$ is the longitudinal strain inside the coating layer, and $\epsilon(z)$ is defined as [19, Eq. 25]:

$$
\begin{aligned}
\epsilon_j(z) = (n_j + \beta_j) & \frac{\partial \log(\rho)}{\partial \phi_j} \\
& - \beta_j \left[\frac{1 - r_j^2}{2r_j} \frac{\partial \log(\rho)}{\partial \phi_j} - \frac{1 + r_j^2}{2r_j} \frac{\partial \log(\rho)}{\partial \phi_{j+1}} \right] \\
& \times \cos[2k_0 n_j (z - z_{j+1})] \\
& - t_j^2 \beta_j \frac{\partial \log(\rho)}{\partial r_j} \sin[2k_0 n_j (z - z_{j+1})]
\end{aligned}
\tag{1.21}
$$

where $t_j = \sqrt{1 - r_j^2}$, and $\beta_j = \frac{\partial n_j}{\partial \log l_j}$ is the elasto-optic coefficient for the jth layer.

The strain $u_{zz}(\vec{x}, z)$ is calculated by taking transfer functions from the bulk and shear strain fields to layer thickness and surface height [19, Table. I.]:

$$
C_j^B = \sqrt{\frac{1 + \sigma_j}{2}}
\tag{1.22a}
$$

$$
C_j^{S_A} = \sqrt{1 - 2\sigma_j}
\tag{1.22b}
$$

$$
D_j^B = \frac{1 - \sigma_s - 2\sigma_s^2}{\sqrt{2(1 + \sigma_j)}} \frac{Y_j}{Y_s}
\tag{1.22c}
$$

$$
D_j^{S_A} = -\frac{1 - \sigma_s - 2\sigma_s^2}{2\sqrt{1 - 2\sigma_j}} \frac{Y_j}{Y_s}
\tag{1.22d}
$$

$$
D_j^{S_B} = \frac{\sqrt{3}(1 - \sigma_j)(1 - \sigma_s - 2\sigma_s^2)}{2\sqrt{1 - 2\sigma_j}(1 + \sigma_j)} \frac{Y_j}{Y_s}
\tag{1.22e}
$$

The coatings material is assumed to have loss angles as the fractional imaginary parts in the bulk and shear modulus of the coatings materials as:

$$
\bar{K} = K(1 + i\Phi_B), \quad \bar{\mu} = \mu(1 + i\Phi_S)
\tag{1.23}
$$

Calculations for the strain noise fields in Bulk and Shear mode for each coating material is given by [19, Eq. 96]:

$$
S_j^X = \frac{4k_B T \lambda_j \Phi_j^X (1 - \sigma_j - 2\sigma_j^2)}{3\pi f n_j Y_j (1 - \sigma_j)^2 \mathcal{A}_{eff}}, \qquad X = B, S
\tag{1.24}
$$

Finally, we define transfer functions from each layer's bulk and shear stress noise fields to phase noise of reflected light [19, Eq. 94]:

$$q_j^B = \int\limits_{z_{j+1}}^{z_j} \frac{dz}{\lambda_j} \left[\left[1 - \mathrm{Im}\left(\frac{\epsilon_j(z)}{2} \right) \right] C_j^B + D_j^B \right]^2 \tag{1.25a}$$

$$q_j^S = \int\limits_{z_{j+1}}^{z_j} \frac{dz}{\lambda_j} \left[\left[1 - \mathrm{Im}\left(\frac{\epsilon_j(z)}{2} \right) \right] C_j^{S_A} + D_j^{S_A} \right]^2 + [D_j^{S_B}]^2 \tag{1.25b}$$

and to the amplitude noise of the reflected light as [19, Eq. 95]:

$$p_j^B = \int\limits_{z_{j+1}}^{z_j} \frac{dz}{\lambda_j} \left[C_j^B \mathrm{Re}\left(\frac{\epsilon_j(z)}{2} \right) \right]^2 \tag{1.26a}$$

$$p_j^S = \int\limits_{z_{j+1}}^{z_j} \frac{dz}{\lambda_j} \left[C_j^{S_A} \mathrm{Re}\left(\frac{\epsilon_j(z)}{2} \right) \right]^2 \tag{1.26b}$$

This allows us to write the single-sided power spectral density of the displacement noise of the coatings (due to phase noise in reflected light)[19, Eq. 94]

$$S_{\mathrm{coatBr}}^z = \sum_j \left(q_j^B S_j^B + q_j^S S_j^S \right) \tag{1.27}$$

And the single-sided power spectral density of the recoil of the mirror (due to amplitude noise imparted on the reflected light) [19, Eq. 95]:

$$S_{\mathrm{coatBr}}^z = \sum_j \left(p_j^B S_j^B + p_j^S S_j^S \right) \tag{1.28}$$

Note that both expressions above give noise in units of m^2/Hz. While it is trivial to understand how reflected phase noise generates an equivalent displacement noise, one would require using the mirror's overall mechanics to understand if the second contribution is meaningful or not. Hong et al.[19] provide an interesting discussion on this topic if anyone is interested, but for the coatings, we have considered so far, the coefficients p_j^B, p_j^B are 5 to 6 orders of magnitude smaller than q_j^B, q_j^B and thus the amplitude noise due to coatings thermal noise can be neglected. For further discussions and more details on calculations of the transfer functions and strain noise fields mentioned above, please refer to Hong et al.[19].

1.3 Search for better coatings

Advanced LIGO uses coatings made out of alternate layers of Silica (SiO_2) and Titanium doped Tantala ($Ti:Ta_2O_5$). These coatings have been instrumental in reaching to sensitivity goals required to start detecting gravitational wave signals. However, to look deeper into the universe for gravitational wave events, we need to reduce the classical noise floor which is dominated by the coatings Brownian noise. Thus a hunt for new materials for these coatings is ongoing.

As we noted in the last sections, the coatings Brownian noise is a result of the existence of dissipation channels in the coating structure. We can imagine this as a form of internal friction that dissipates energy when the coating is pushed sinusoidally. As also evident from Eq. 1.24, the loss angle parameter of these coatings is directly proportional to the power spectral density of produced strain noise fields in the coatings.

One interesting direction in the search for new materials for coatings is the study of crystalline materials. In contrast to amorphous coatings, crystalline coatings form more rigid covalent bond structures between the atoms of the materials, which barring the defects reduce the internal friction. In other words, there is less hysteresis when these structures undergo strain oscillations. This should result in lower loss angle values for these materials.

In recent years, $Al_{0.92}Ga_{0.08}As$ and GaAs have been studied for potential use as mirror coatings. There have been a few experiments that show promising results for low-loss angles for these coatings. But these measurements are done with non-optimized coatings[14] or the loss angles were measured using an indirect method of measuring the Q value of a resonator with or without these coatings applied to them[17]. Further, the mirrors are coated with such crystalline coatings unconventionally. Since a lattice-matched substrate is required to grow crystalline materials, the coatings are first grown on GaAs substrate, with alternate layers of $Al_{0.92}Ga_{0.08}As$ and GaAs, and then the substrate is etched away to get a thin film coating. This coating is then optically bonded to a fused silica substrate which is the current choice of mirror substrate material. There is yet a lot more to investigate on how such coatings behave when used as mirrors.

Chapter 2

EXPERIMENTAL SETUP

In this chapter, I'll describe the experiment I performed to directly measure the coatings Brownian noise due to coatings made with $Al_{0.92}Ga_{0.08}As$ and GaAs. The experiment involved building two identical test cavities out of four mirrors with the coatings under test. We locked two lasers to the cavities with a frequency stabilization servo such that the laser frequency noise was dominated by the cavity length noise in the frequency range of 100 Hz to 700 Hz. The transmitted light from the cavities carrying the cavity length fluctuations as frequency fluctuations are beaten together on a resonant RF photodiode. The beatnote frequency thus has frequency fluctuations that are twice as much as the displacement noise of a single mirror coating would cause. The beatnote frequency fluctuations are measured using a digital PLL which then are converted into an estimate for the coatings Brownian
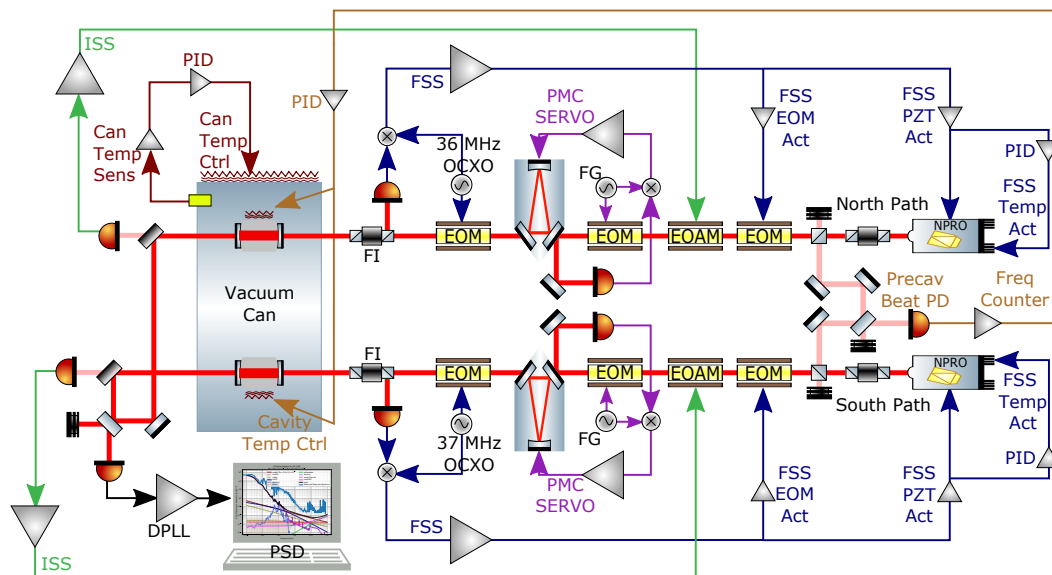
Figure 2.1: Complete Experiment Schematic. Thin solid arrowed lines are electrical signals which are part of control loops labeled in the same color. Red lines show the laser beam. Abbreviations: *Act*: Actuator, *Ctrl*: Control, *EOAM*: Electro-Optic Amplitude Modulator, *EOM*: Electro-Optic Modulator (Phase), *DPLL*: Digital Phase Locked Loop, *FI*: Faraday Isolator, *FG*: Frequency Generator, *FSS*: Frequency Stabilization Servo, *ISS*: Intensity Stabilization Servo, *NPRO*: Non-Planar Ring Oscillator (Laser), *OCXO*: Oven Controlled Crystal Oscillator, *PD*: Photo Detector, *PMC*: Pre-Mode Cleaner, *Precav*: Pre-cavity, *Sens*: Sensor, *Temp*: Temperature.
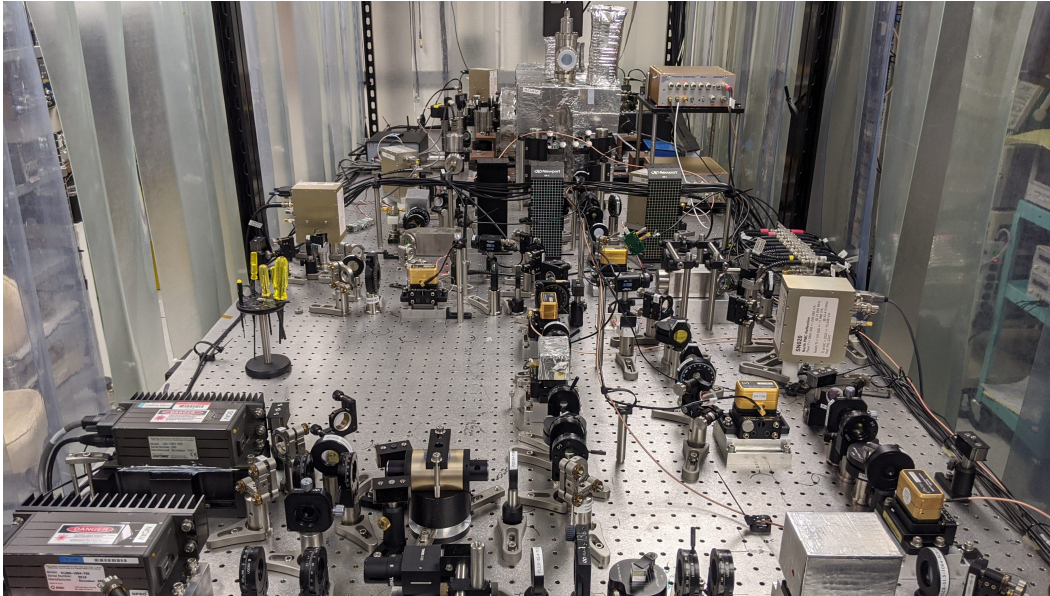
Figure 2.2: Photo of the optical table. The two lasers are one the right going through two triangular pre-mode cleaner cavities. Then the laer beams go into the vacuum can in the back covered in thermal shielding where the two cavities under test are housed. On the right of the can, you can see the table top frequency stabilization servos[20].

(a) Top-down view
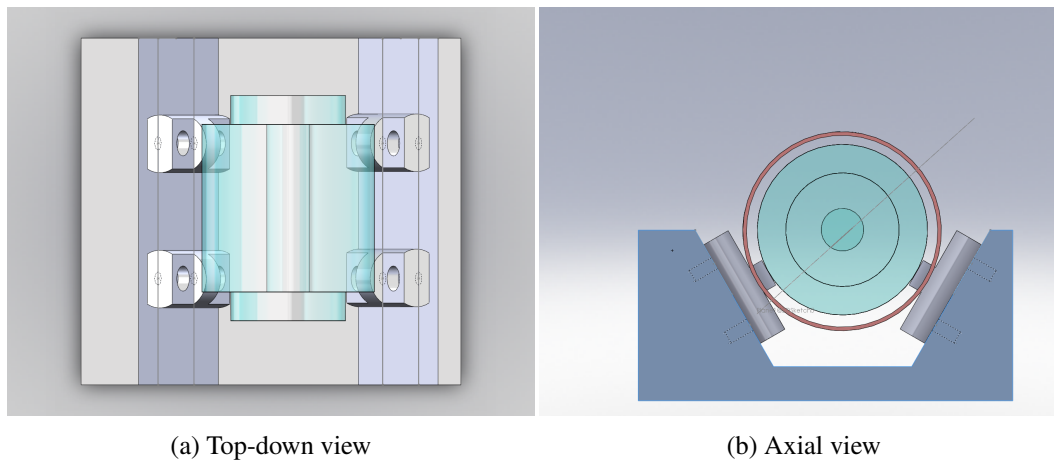
(b) Axial view

Figure 2.3: Cavity mounting and supports for 3.7 cm cavities. The locations of the four contacts were chosen for superior rejection of vertical seismic noise, as determined by FEA simulation. In the axial view, the red shell is the thermal shield used for temperature control. In the top-down view, this shield is not shown.

noise in displacement units.

2.1   Test cavities

The mirrors under test are used to make two identical cavities. The mirrors are optically bonded to fused silica spacers. The properties of these cavities are listed

Symbol	Description	North Cavity	South Cavity
L	Nominal spacer length	36.8 ± 0.3 mm [1]	
R_{sp}	Outer spacer radius	19.0 ± 0.3 mm	
r_{sp}	Inner spacer radius	4.8 ± 0.1 mm	
R_s	Mirror substrate radius	12.7 mm	
$\mathcal{R}$	Mirror ROC [2]	1.0 m	
$\mathcal{F}$	Finesse	16700(1400)	15100(340)
$\mathcal{T}$	Power transmission (per mirror)	297 ± 6 ppm	317 ± 3 ppm
P_{inc}	Incident power on cavity	2.7 mW	2.4 mW

Table 2.1: Parameters for test cavities.

in Table. 2.1. The coatings have been applied in an 8 mm diameter region at the center of the mirrors and an annulus of about 3 mm is left clean at the edges of the mirrors for proper optical contact.

The cavities are supported at their Airy points by four supports as shown in Fig. 2.3. Each support is cut from a cylindrical piece of Polyether ether ketone (PEEK) to have as close to a point contact as possible. The Airy points were found to minimize the coupling of seismic noise into the cavity longitudinal length changes[21]. The cavities are shielded from radiative heating or cooling by a copper cylinder around them.

Layer			d_j/λ_j		
1–5	0.1895	0.1121	0.4985	0.1	0.4597
6–10	0.1694	0.276	0.2146	0.251	0.2388
11–15	0.2404	0.2504	0.2368	0.2553	0.2375
16–20	0.2571	0.2392	0.2564	0.2414	0.255
21–25	0.2437	0.2532	0.246	0.2515	0.2481
26–30	0.2499	0.2497	0.2482	0.2514	0.2469
31–35	0.2528	0.2457	0.254	0.2447	0.2549
36–40	0.2438	0.2556	0.2433	0.2563	0.2427
41–45	0.2566	0.2423	0.2571	0.242	0.2574
46–50	0.2416	0.2577	0.2413	0.2579	0.2412
51–55	0.2581	0.2409	0.2585	0.2405	0.2587
56–57	0.2401	0.2556			

Table 2.2: Optical thickness of each coating layer, in fractions of wavelength ($\lambda_j = \lambda/n_j$) of laser in that material. Odd-numbered layers are GaAs ($n_o = 3.48$), and even-numbered layers are $Al_{0.92}Ga_{0.08}As$ ($n_e = 2.977$).
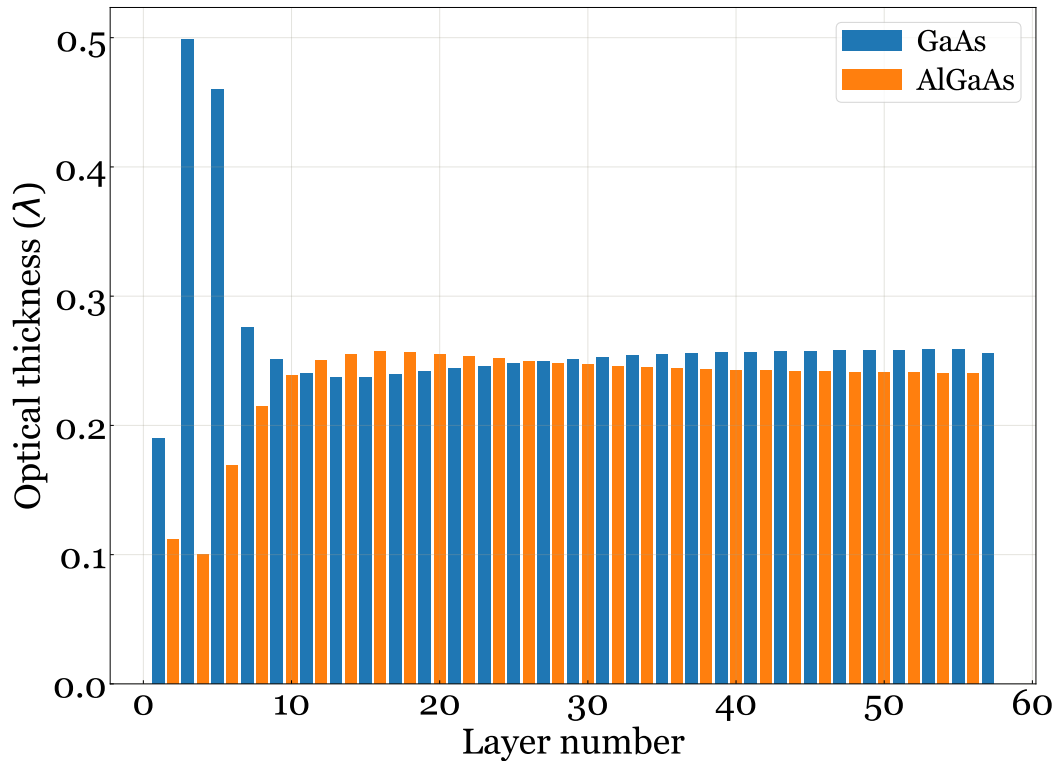
Figure 2.4: Optical Thickness of 57 layers of the optimized mirror coatings as fraction of wavelength of laser in vacuum (λ). See Table. 2.2 for the values.

2.1.1 Coating structure

The mirrors are made with 57 layers composed of alternating GaAs and Al$_{0.92}$Ga$_{0.08}$As . The layer thicknesses have been optimized and experimentally verified to show the cancellation of thermo-optic noise in the coatings [18]. See Fig. 2.4 for the optical thickness profile of the coating layers. In Table. 2.2 we give the thickness of each layer of our AlGaAs coatings, in terms of optical thickness d_j/λ_j. For each layer, the physical thickness d_j can only be controlled to the nearest 50 pm. Additionally, there is a systematic error in the thickness control for the GaAs and Al$_{0.92}$Ga$_{0.08}$As layers; the fractional uncertainties for this error are 0.5 % and 1.0 %, respectively.

2.1.2 Maximizing the effect of Coatings Brownian Noise

From Eq. 1.24, we can see that the coatings Brownian noise power spectral density is inversely proportional to the effective beam spot area on the coating. One simple way to understand this is that the strain noise fields have very short correlation lengths on the mirror surface, so if the beam is reflecting off of a larger surface area on the coating, the noise is averaged over a larger area and the effect of noise is less on the reflected light phase. Since we are interested in measuring the effect of coatings

Brownian noise directly on the reflected light phase, we designed the experiment to have a smaller beam spot size on the coating mirror. So for a given radius of curvature of the mirrors under test, we would like to shorten the cavity length as much as we can. However, we need to be able to control the beatnote frequency between the two cavities by heating them (see 2.3.2) and a very short cavity will require too high a temperature to give a required frequency shift. This places a lower limit on cavity length requirements. Besides this, further considerations were placed to ensure no higher order modes co-resonate with the TEM00 mode[21, E.1]. The cavity length was chosen to be 36.8 mm.

2.2 Frequency Stabilization Servo

Fig. 2.1 shows some parts of the frequency stabilization servo (FSS) used to lock the two NPRO lasers independently to the two cavities. This is a critical element of the experiment as this control loop ensures that our laser frequency tracks any minute changes in cavity length without getting saturated by intrinsic noise up to roughly 200 kHz.

Sidebands of 36 MHz and 37 MHz are created via broadband New Focus 4004
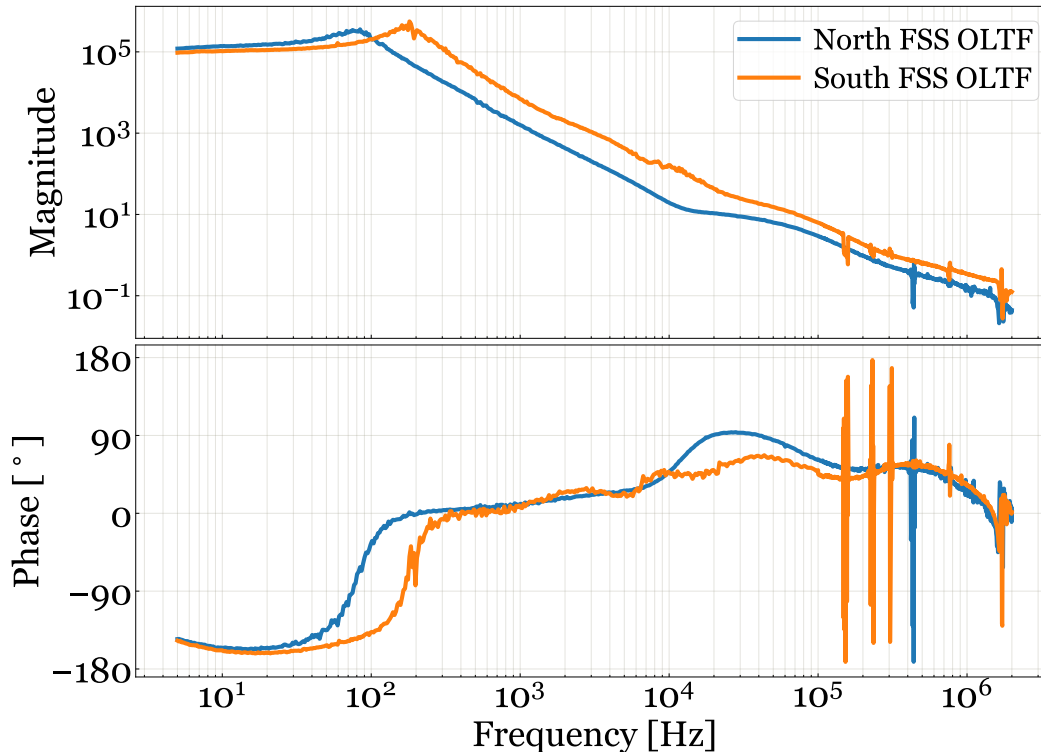
Figure 2.5: Open Loop Transfer Function for Frequency Stabilization Servo control loop.

Electro-Optics Modulators (EOM) with a modulation depth of 0.3 radians in the North and South paths respectively. These EOMs were driven by custom-built resonant EOM drivers[22], amplifying clean modulation signal by about 44 dB. The RF frequency source was provided by Oven Controlled Crystal Oscillators (Custom parts from Wenzel Associates Inc. with less than 165 dBc/$\sqrt{\text{Hz}}$ phase noise at 1 kHz).

A conventional PDH setup is used to read the error signal by separating reflection signals from cavities using Faraday isolators (FI in Fig. 2.1). Custom-built resonant photodiodes with both active and passive notches at 2-Omega frequencies are used to read the error signals (here Omega refers to phase modulation frequency). It was found that rejecting the 2-Omega frequency by a margin of about 46 dB with respect to the resonant 1-Omega peak is essential to ensure the linearity of mixers and avoid slew rate saturation in the electronics downstream. This ensures the smooth performance of FSS without saturation of any of the actuators.

The main servo for this control loop uses the LIGO 3$^{\text{rd}}$ generation Table Top Frequency Stabilization Servo [20]. There are two outputs from this servo, one for NPRO laser PZT which carries the noise suppression load up to about 10 kHz, and a second, for an EOM placed upstream in the path for fast actuation enabling unity gain frequencies up to 200 kHz and 300 kHz for the North and South paths respectively. The RMS value of the PZT actuation signal is also calculated in analog electronics and sent to an ADC. A Python PID script samples the low-frequency drift of the PZT actuation signal which is fed back to actuate on the temperature of NPRO crystal for slow and coarse correction. This ensures that the DC offset of NPRO PZT does not rail too far out and the NPRO PZT stays in a comfortable position (not too stretched, not too compressed). This maximizes the available dynamic range for the actuator and hence the bandwidth. Fig. 2.5 shows the full open-loop transfer function for this control loop including all the actuators resulting in suppression of frequency noise of free-running NPRO laser to the order of 10^5 in the frequency region of interest.

2.3 Beatnote Detection and Readout

The transmitted laser beams from the cavity carry displacement noise of the mirror surface as frequency noise because of the strong PDH locking explained above. The main purpose of having two equivalent paths is so that we can refer them against each other to measure their differential cavity length noise imprinted on their optical
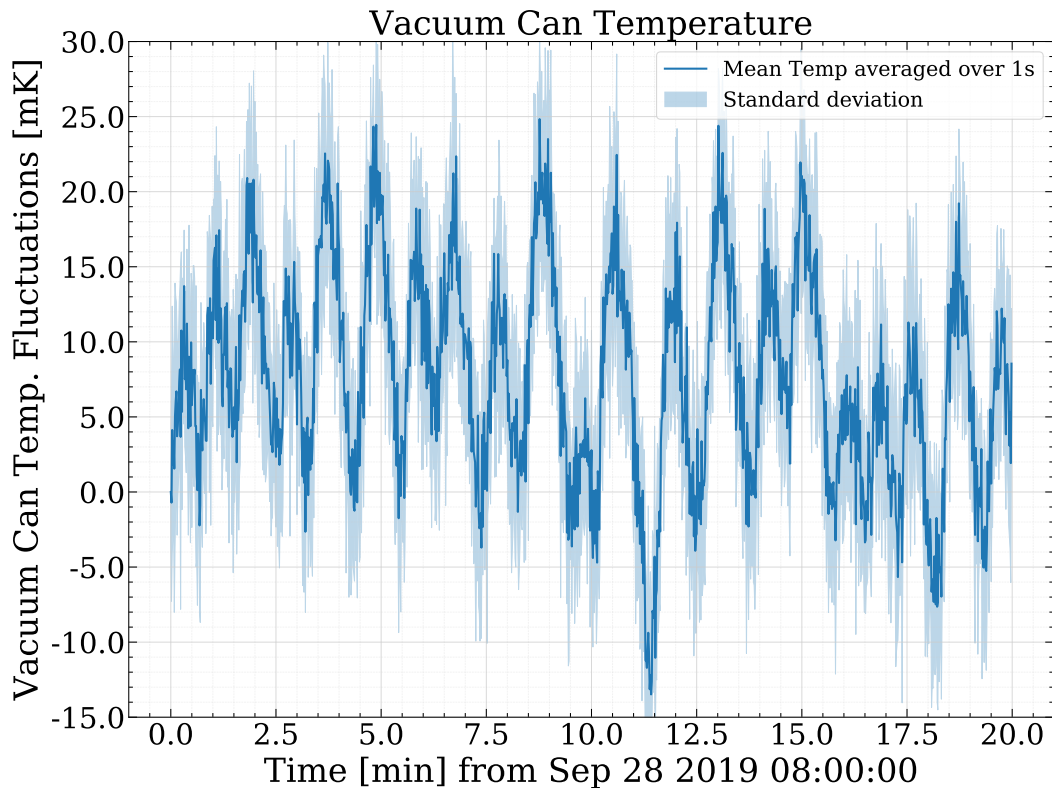
Figure 2.6: Fluctuations in vacuum can temperature after stabilization.

frequencies. The two beams are interfered with each other on a 50:50 beamsplitter and one of the outputs is read by a custom-built RF photodiode resonant at 27.34 MHz.

The resulting heterodyne beatnote is tracked by a digital phase-locked loop (DPLL) with 10 kHz bandwidth. This DPLL is implemented on an FPGA inside the Liquid Instruments' Moku:Lab which in turn records the beatnote frequency at 15.625 kSa/s. The digital implementation allowed for a larger dynamic range readout of the frequency with high precision. The clock of Moku was referenced to an SRS FS725 Rubidium atomic clock 10 MHz signal for reducing sensing frequency noise and increasing stability over long durations.

2.3.1 Vacuum can temperature control

To ensure the PLL tracked the heterodyne signal with good linearity, we made sure that the beatnote frequency did not drift more than the bandwidth capabilities during the measurement time, which was typically 960 s. For this, the cavity temperature needed to be controlled. The cavity temperature control required a uniform and constant temperature environment to cool off radiatively since we
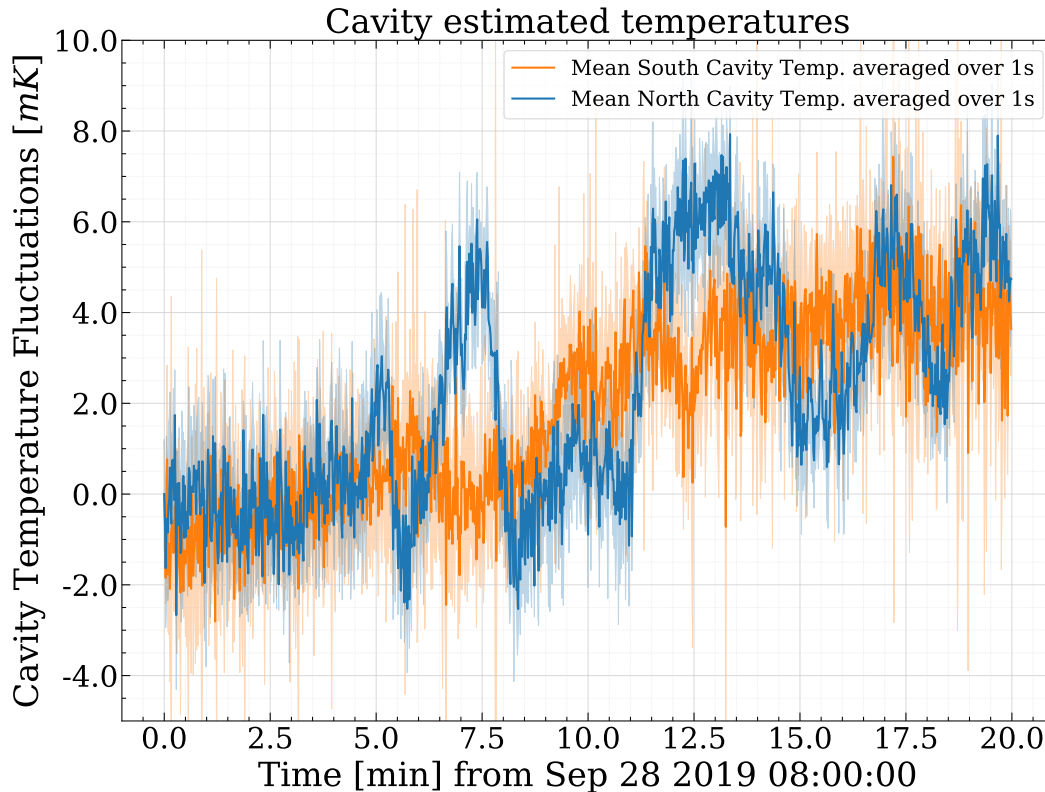
Figure 2.7: Fluctuations in cavity temperature after stabilization.

only employed heating actuation on cavities as explained in Sec.2.3.2. Thus the cavities were enclosed inside a vacuum can that was thermally insulated with 2-inch CERTIFOAM 25. This foam enclosure was further covered with aluminum tape to increase the reflectivity of the surface.

The temperature of the vacuum can is monitored with an Analog Devices AD590 sensor through custom-built low noise temperature sensing circuits [23]. This circuit was designed to have mK sensitivity to temperature changes. The temperature signal was sent to an ADC and controlled by a Python PID script. The control output was used to heat the vacuum can using OMEGALUX silicone rubber heaters wrapped around it. This provides temperature stability of ±30 mK in the cavity environment (see Fig. 2.6).

2.3.2   Cavity temperature control

With a stable environment for the cavities, we needed to control the beatnote frequency value to keep it parked at the center of the resonant photodiode frequency (27.34 MHz). This was achieved by differentially heating the cavities.
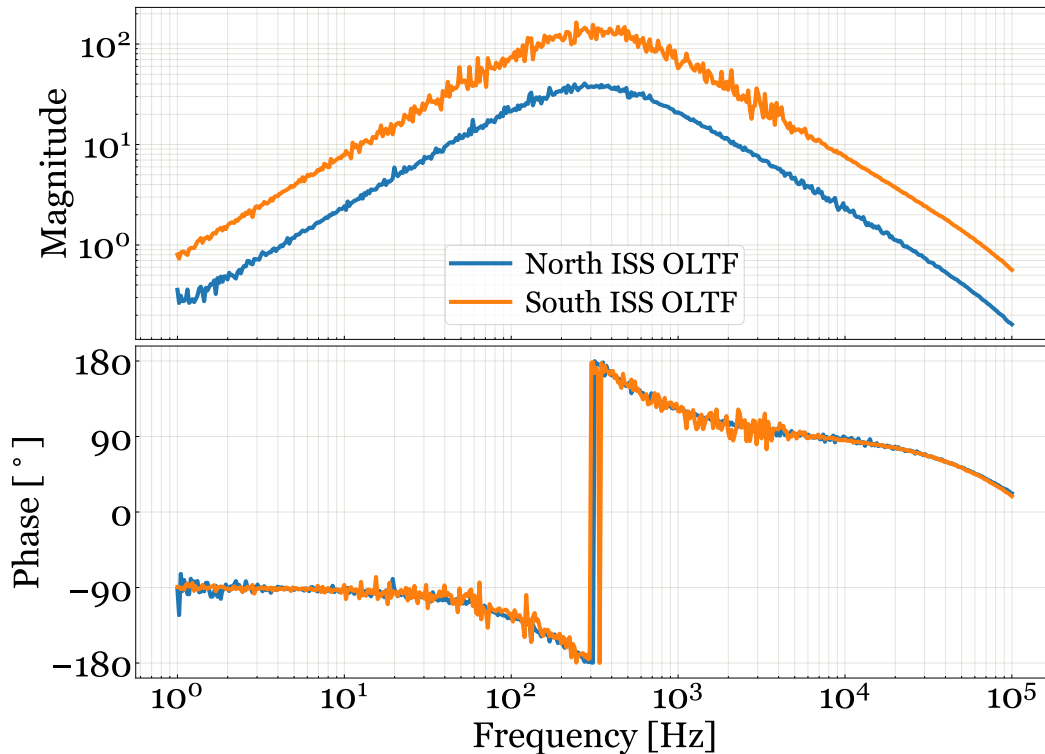
Figure 2.8: Open Loop Transfer Function for Intensity Stabilization Servo control loop.

The cavities were wrapped by nichrome wires which were used to actuate length changes to the cavity spacer by heating. The difference frequency is captured before cavities right after the laser heads on a wide bandwidth New Focus 1611 photodiode and read by a Mini-Circuits UFC-6000 frequency counter. This pre-cavity beatnote frequency is used by a Python PID script to control and limit the relative temperature of the cavities by controlling the currents in the nichrome wires via a custom-built MOSFET current driver circuit. Using the laser temperature control signal as a witness detector, we estimated the temperature fluctuations of the individual cavities and found it to be less than ±30 mK (see Fig. 2.7). All these efforts resulted in a stable beatnote frequency with a drift of less than 1 kHz in more than 20 minutes.

2.4 Other Control Loops

2.4.1 Laser Intensity Stabilization

Apart from stabilizing the frequency of the laser at the lock point, we controlled the relative intensity noise of the lasers as well. This is important because the noise in absorbed laser power in the coatings drives thermo-optic noise as well (see sec.3.5.5). A fraction of the transmitted laser beam is read with Thorlabs PDA10CS DC coupled
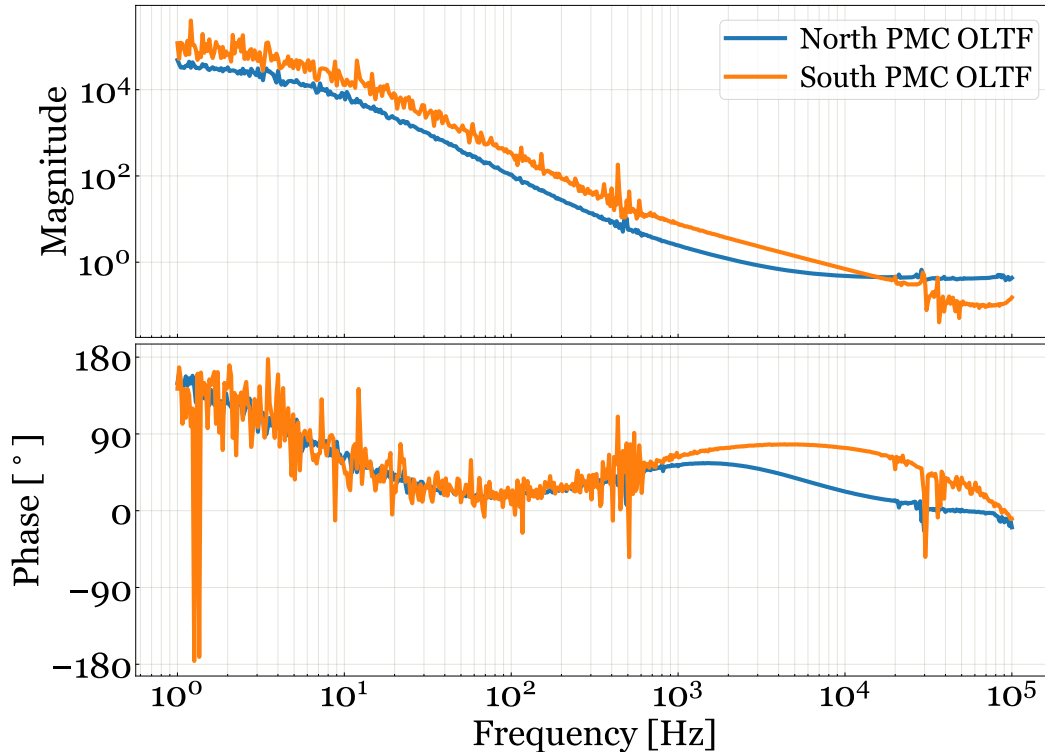
Figure 2.9: Open Loop Transfer Function for Pre-Mode Cleaner Servo control loop.

photodiodes and sent to the Intensity Stabilization Servo (ISS) implemented on SRS SR560. The ISS primarily consists of an AC-coupled pole-zero pair at 300 Hz and high gain to suppress the laser intensity noise in the measurement frequency band. A New Focus 4104NF Electro-Optic Amplitude Modulator (EOAM) is used in each path with a polarizing beam splitter (PBS) to create an effective intensity actuator. This brought down the relative intensity noise to 4×10^{-8} at 300 Hz.

2.4.2 Spatial-mode cleaning

Additionally, to ensure no higher-order modes are reflected from the cavity, and pollute the FSS PDH error signal, the laser beams are first spatially and spectrally cleaned by a Pre-Mode Cleaner (PMC). Our PMC is a fixed spacer triangular cavity with a PZT-actuated end mirror. The triangular cavity makes it easy to read reflected signals off of the cavity without using Faraday isolators. The reflection signal is read by a custom build RF photodiode whose output is fed to a custom-designed PMC servo card[24]. The output of the servo is used to drive the end mirror PZT and actuate the length of the PMC to lock it to the laser frequency. This ensures that only clean TEM_{00} are passed on to our test cavities and laser frequency noise above 2 MHz (PMC optical pole frequency) is rejected. As an added advantage, the

PMC also provides polarization filtering of the laser reducing residual amplitude modulation due to downstream EOMs used in FSS.

C h a p t e r 3

NOISE SOURCES IN THE EXPERIMENT

In this chapter, we describe the various sources of noise we have taken into account in inferring the coatings Brownian noise from our measurements. Fig. 3.1 illustrates most of the contributing noise sources that are indistinguishable from the coatings Brownian noise. All the symbols used in the equations in this chapter are explained in Table. 3.1. Noise power spectral densities (PSD) are denoted as S_{cause}. When a superscript of 'x' is present, it denotes cavity length noise PSD. A conversion factor of $(c/(L\lambda))^2$ is applied to convert cavity length variations to absolute laser frequency noise sampled by our beatnote readout.

3.1 Coatings Thermo-Optic Noise

Coatings thermo-optic noise is typically a dominant noise source in mirror coatings. When a Gaussian beam of laser falls on a mirror surface, stress inhomogeneity causes fluctuations in the temperature [25]. Due to thermo-elasticity, the thickness of each layer fluctuates with the temperature, proportional to their coefficient of thermoelasticity (CTE) α_j of the jth layer. The same thermal fluctuations also induce changes in the refractive indices of each layer that are proportional to their coefficients of thermo-refractivity (CTR) β_j.

Since these two pathways of noise are driven by the same noise source, they are coherently added such that total thermo-optic noise is given by [26, Eq. 4.]:

$$S^x_{coatTO} = \Gamma_{tc} S^{\Delta T} (\bar{\alpha}_c d - \bar{\beta}\lambda - \bar{\alpha}_s d \frac{C_c}{C_s}) \tag{3.1}$$

where $\bar{\alpha}_c$ and $\bar{\beta}$ are effective compound CTE and CTR for the coating respectively, $\bar{\alpha}_s$ is the effective CTE for the substrate, and Γ_{tc} is the thick coating correction factor (see Sec.3.1.1 below). $S^{\Delta T}$ is single-sided Gaussian beam profile weighted

Sym.	Description	Value used
n_s	Substrate Refractive Index	1.45 ± 0.1
Y_s	Substrate Young modulus	72(1) GPa
σ_s	Substrate Poisson ratio	0.170(5)
Φ_s	Substrate loss angle	1×10^{-7}
κ_s	Substrate thermal conductivity	1.38 W/(m K)
C_s	Substrate heat capacity (per vol.)	1.6×10^6 J/(K m^3)
α_s	Substrate CTE	$(5.1 \pm 0.3) \times 10^{-7}$ K^{-1}
n_e	Al$_{0.92}$Ga$_{0.08}$As Refractive Index	2.977 ± 0.03
Y_e	Al$_{0.92}$Ga$_{0.08}$As Young modulus	100 ± 20 GPa
σ_e	Al$_{0.92}$Ga$_{0.08}$As Poisson ratio	0.323 ± 0.065
Φ_e^B	Al$_{0.92}$Ga$_{0.08}$As bulk loss angle	$(5.33 \pm 0.03) \times 10^{-4}$ [17]
Φ_e^S	Al$_{0.92}$Ga$_{0.08}$As shear loss angle	5.2×10^{-7} [17]
κ_e	Al$_{0.92}$Ga$_{0.08}$As therm. conduct.	69.9 ± 5 W/(m K)
C_e	Al$_{0.92}$Ga$_{0.08}$As heat capacity	1.698 ± 0.001 MJ/(K m^3)
α_e	Al$_{0.92}$Ga$_{0.08}$As CTE	$(5.24 \pm 0.524) \times 10^{-6}$ K^{-1}
β_e	Al$_{0.92}$Ga$_{0.08}$As CTR	$(179.24 \pm 1.34) \times 10^{-6}$ K^{-1}
n_o	GaAs Refractive Index	3.48 ± 0.03
Y_o	GaAs Young modulus	100 ± 20 GPa
σ_o	GaAs Poisson ratio	0.311 ± 0.06
ϕ_o^B	GaAs bulk loss angle	$(5.33 \pm 0.03) \times 10^{-4}$ [17]
ϕ_o^S	GaAs shear loss angle	5.2×10^{-7} [17]
κ_o	GaAs therm. conduct.	55 ± 3 W/(m K)
C_o	GaAs heat capacity	1.75 ± 0.09 MJ/(K m^3)
α_o	GaAs CTE	$(5.97 \pm 0.597) \times 10^{-6}$ K^{-1}
β_o	GaAs CTR	$(366 \pm 7) \times 10^{-6}$ K^{-1}
λ	Laser wavelength	1064 nm
T	Cavity Temperature	310 ± 1 K
d	Total Coating thickness	4.68 μm
κ_c	Effective Coating therm. conduct.	61.5 ± 0.5 W/(m K)
C_c	Effective Coating heat capacity	1.724 ± 0.008 MJ/(K m^3)
$\bar{\alpha}_c$	Effective Coating CTE	$(1.96 \pm 0.05) \times 10{-5}$ K^{-1}
$\bar{\alpha}_s$	Effective Substrate CTE	$(1.19 \pm 0.07) \times 10{-6}$ K^{-1}
$\bar{\beta}$	Effective Coating CTR	8.3×10^{-5} K^{-1}
a_{coat}	Coating absorption coefficient	$(6 \pm 1) \times 10^{-6}$
P_{circ}	Circulating power in cavity	$P_{inc}\mathcal{F}/\pi$
f_T	Thermal relaxation frequency	5.9 ± 0.9 Hz
w	Beam spot radius on mirrors	215.4 ± 0.5 μm
$\mathcal{A}_{eff}$	Effective beam area on mirrors	πw^2

Table 3.1: Parameters used in the noise budget. Subscript 's' stands for substrate which is Fused Silica. Quantities for spacer material is in the expressions with subscript 'sp' use these value for Fused Silica. Subscript 'o' stands for odd-numbered layers and 'e' stands for even-numbered layers starting the count from 1 as the front layer. In the expressions below, the common subscript 'j' is used to denote this number. Thermal relaxation frequency is estimated as $f_T = \kappa_s/(\pi w^2 C_s)$ and the beam spot radius on the mirrors are calculated as $w = (\lambda \mathcal{R}/\pi)^{1/2}/(2\mathcal{R}/L - 1)^{1/4}$.
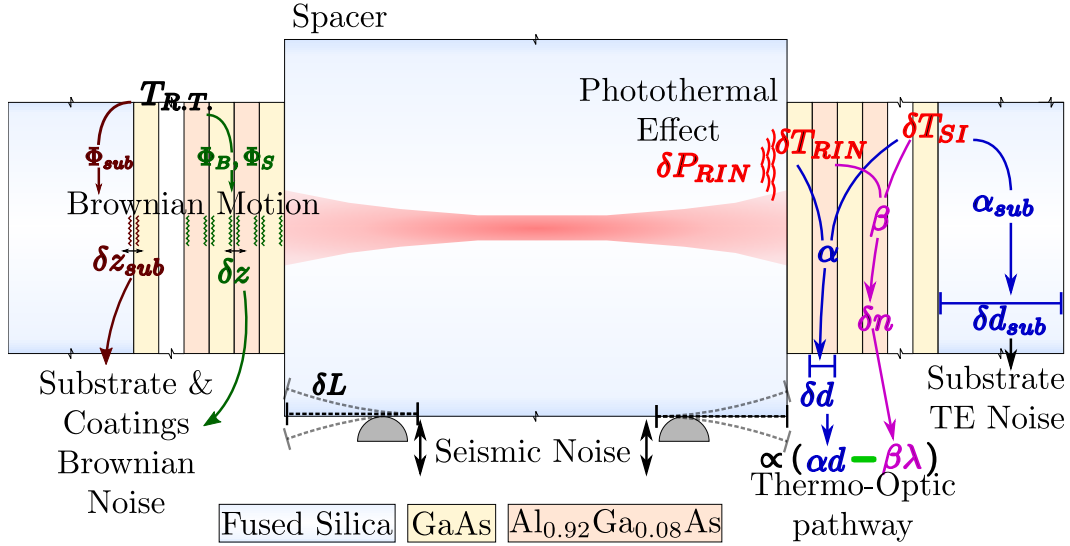
Figure 3.1: Schematic of how different noise sources affect the phase noise of light in the cavity. On the right side, the coupling of thermo-optic noise in the coatings and the thermo-elastic noise in the substrate (see Sec.3.4 and Sec.3.1) is shown. Both of these are driven by temperature fluctuations in the mirror δT_{SI} due to stress inhomogeneity when a gaussian beam of light hits the mirror. These temperature fluctuations cause refractive index and length fluctuations in the materials resulting in phase noise in reflected light. Another source of temperature fluctuations is the relative intensity noise (RIN) in the circulating laser power δP_{RIN} in the cavity a fraction of which gets absorbed by the mirror. This source follows the same pathway as the thermo-optic pathway of coupling to the phase noise of reflected light (see Sec.3.5.5). On the left side, it is shown that the room temperature $T_{R.T.}$ itself causes stress noise fields in the substrate and coating materials resulting in surface fluctuations ($\delta z_{sub}, \delta z$) of different interfaces. These fluctuations result in brownian noise in the reflected light field phase (see Sec.3.2 and Sec.3.3). Near the center, it is shown that the vertical motion of the cavity mounts cause bending in the cavity resulting in technical noise due to the seismic noise in the laboratory (see Sec.3.5.1). The symbols are defined in Table. 3.1.

temperature fluctuation PSD is given by (see Sec.3.1.2 below):

$$S^{\Delta T} = \frac{2^{3/2} k_{\mathrm{B}} T^2}{\pi \kappa_{\mathrm{s}} w} M(f/f_{\mathrm{T}}) \tag{3.2a}$$

$$M(\Omega) = Re\left[\int_0^\infty du \, \frac{u \, e^{-u^2/2}}{\left(u^2 - i\Omega\right)^{1/2}}\right] \tag{3.2b}$$

The negative sign in Eq. 3.1 means an optimization can be carried out to make these two coupling mechanisms cancel each other. The mirrors we are testing have a coating structure that is optimized to minimize this noise by adjusting the

layer thicknesses. This was experimentally demonstrated in previously published work[18].

In the following two subsections, I briefly describe the roadmap to calculating coatings thermo-optic noise by calculating the required effective parameters, correction factors, and temperature PSD.

3.1.1 Coatings effective parameter calculations

Effective thermal conductivity for the coating is defined as the harmonic weighted mean of individual layer conductivity:

$$\frac{1}{\kappa_c} = \sum_j \frac{1}{\kappa_j} \frac{d_j}{d} \tag{3.3}$$

Effective coefficients of thermoelasticity for the coating and substrate are [26, Eq. A2]:

$$\begin{aligned} \bar{\alpha}_j &= \alpha_j \frac{1+\sigma_s}{1-\sigma_j} \left[\frac{1+\sigma_j}{1+\sigma_s} + (1-2\sigma_s)\frac{Y_j}{Y_s} \right] \\ \bar{\alpha}_c &= \sum_j \bar{\alpha}_j \frac{d_j}{d} \\ \bar{\alpha}_s &= 2\alpha_s(1+\sigma_s) \end{aligned} \tag{3.4}$$

These can be used to define a condensed effective CTE given by [26, Eq.18]:

$$\bar{\Delta\alpha} = \bar{\alpha}_c - \bar{\alpha}_s d \frac{C_c}{C_s} \tag{3.5}$$

where C_c is the effective heat capacity per volume of coating calculated by taking a weighted average of all coating layers as:

$$C_c = \sum_j C_j \frac{d_j}{d} \tag{3.6}$$

The effective coefficient of thermorefractivity is given by [26, Eq.B8-B21]:

$$\bar{\beta} = -\frac{1}{4\pi} \sum_{k=1}^{N} \frac{\partial \phi_c}{\partial \phi_k} \frac{\partial \phi_k}{\partial T} \tag{3.7}$$

where

$$\frac{\partial \phi_c}{\partial \phi_k} = -\frac{1}{2}\frac{\partial \rho}{\partial \phi_j}$$

$$\frac{\partial \phi_k}{\partial T} = \frac{4\pi}{\lambda}(\beta_k + \bar{\alpha}_k n_k)d_k \tag{3.8}$$

Note that in Eq. 3.8 we utilize the calculation of derivatives of complex reflectivity of the coating done for coating Brownian noise (see Eq. 1.15) in this calculation as well. The factor of $-1/2$ comes because of different definitions of phase shift between [26] and [19].

We have also considered non-homogeneous dissipation of heat in the coatings due to finite thickness. This is incorporated by a thick coating correction factor Γ_{tc} given by [26, Eq.39]:

$$\Gamma_{tc} = \frac{p_E^2\Gamma_0 + p_E p_R \Xi \Gamma_1 + p_R^2 \Xi^2 \Gamma_2}{R\Xi^2\Gamma_D}$$

$$\Gamma_0 = 2(\sinh\Xi - \sin\Xi) + 2R(\cosh\Xi - \cos\Xi)$$

$$\Gamma_1 = 8\sin(\Xi/2)\left[r_T\cosh(\Xi/2) + \sinh(\Xi/2)\right] \tag{3.9}$$

$$\Gamma_2 = (1 + R^2)\sinh(\Xi) + (1 - R^2)\sin(\Xi) + 2R\cosh(\Xi)$$

$$\Gamma_D = (1 + R^2)\cosh(\Xi) + (1 - R^2)\cos(\Xi) + 2R\sinh(\Xi)$$

where p_E and p_R are power deposition fractions for thermoelasticity and thermorefractivity respectively, given by [26, Eq. 42]:

$$p_E = \frac{\bar{\Delta\alpha}\, d}{\bar{\Delta\alpha}\, d - \beta_c\lambda} \quad \text{and} \quad p_R = \frac{-\beta_c\lambda}{\bar{\Delta\alpha}\, d - \beta_c\lambda} \tag{3.10}$$

and R and Ξ are dimensionless scaling factors given by [26, Eq. 36, 41]:

$$R = \sqrt{\frac{\kappa_c C_c}{\kappa_s C_s}} \quad \text{and} \quad \Xi = d\sqrt{\frac{4\pi f C_c}{\kappa_c}} \tag{3.11}$$

3.1.2 Coatings temperature fluctuation power spectral density calculation

Here we calculate the PSD for temperature fluctuations of the mirror assuming that the coating is very thin and transfers all heat immediately to the substrate. This assumption is taken care of by incorporating thick coating correction as shown in Sec.3.1.1 during the calculation of thermo-optic noise.

Braginsky et al.[27, Eq. 9] calculated the general one-sided power spectral density of temperature fluctuations sensed by a Gaussian profile beam affecting thermo-refractive noise as:

$$
\begin{aligned}
S^{\Delta T} = {} & \frac{8K_B T^2 f_T^2 \pi^2 w^4}{\kappa_s} \int_0^\infty \mathrm{d}k_\perp \frac{2\pi k_\perp}{(2\pi)^2} \\
& \times \int_{-\infty}^\infty \frac{\mathrm{d}k_z}{2\pi} \frac{k_z^2 + k_\perp^2}{f_T^2 \pi^2 w^4 (k_z^2 + k_\perp^2)^2 + \omega^2} e^{-k_\perp^2 w^2/4} \\
& \times \left(\frac{1}{1 + k_z^2 l_{\text{pen}}^2} \right)
\end{aligned}
\tag{3.12}
$$

where f_T is thermal relaxation frequency (frequency at which thermal diffusion length becomes $\sqrt{\pi w^2}$), l_{pen} is the penetration depth of light into the coating and the assumption of a semi-infinite mirror has been taken. Note that all material properties are of the substrate as the coating is assumed to be negligible in this calculation.

With light penetrating only a few of the first few layers, l_{pen} is much smaller in comparison to beam spot radius w. Note that for k_z to be around $1/l_{pen}$ or more, where the rightmost term in parenthesis will become any significant, the denominator in the first term in the integrand will be around $f_T^2 \pi^2 w^4 / l_{pen}^4 + \omega^2$ and since $l_{pen} << w$, such values of k_z would not contribute to the integral. Therefore, we can safely ignore the last term in parenthesis as unity. With this assumption, the difference between the thermorefractive and thermoelastic effect of the temperature PSD vanishes and we can use the same PSD for both channels as done in Eq. 3.1.

Making substitutions $u = k_\perp w/\sqrt{2}$ and complex variable $z = k_z w/\sqrt{2}$, we get:

$$
\begin{aligned}
S^{\Delta T} = {} & \frac{2K_B T^2 f_T^2 w^4}{\kappa_s} \int_0^\infty \mathrm{d}u \frac{2}{w^2} u e^{-u^2/2} \\
& \times \int_{-\infty}^\infty \mathrm{d}z \frac{2\sqrt{2}}{w^3} \frac{z^2 + u^2}{4\pi^2 f_T^2 (z^2 + u^2)^2 + \omega^2} \\
= {} & \frac{2\sqrt{2} K_B T^2}{\pi^2 \kappa_s w} \int_0^\infty \mathrm{d}u u e^{-u^2/2} \int_{-\infty}^\infty \mathrm{d}z \frac{z^2 + u^2}{(z^2 + u^2)^2 + \Omega^2}
\end{aligned}
\tag{3.13}
$$

where $\Omega = \omega/(2\pi f_T) = f/f_T$.

Instead of assuming the thermal diffusion length to be much smaller than the beam spot radius, as generally done in large beam spot calculations, we calculate the z integral analytically as complex contour integral [21, G.2]:
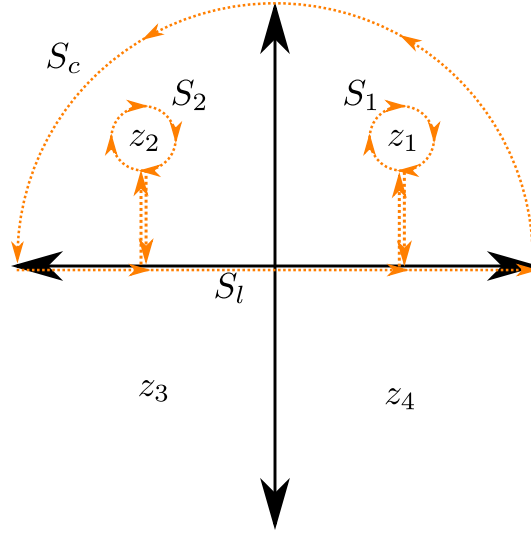
Figure 3.2: Contour integral to determine temperature fluctuations in coating

$$\int_{-\infty}^{\infty} dz \frac{z^2 + u^2}{(z^2 + u^2)^2 + \Omega^2} = \int_{-\infty}^{\infty} dz \frac{z^2 + u^2}{\left((z^2 + u^2) + i\Omega\right)\left((z^2 + u^2) - i\Omega\right)}$$
$$= \int_{-\infty}^{\infty} dz \frac{z^2 + u^2}{(z - z_1)(z - z_2)(z - z_3)(z - z_4)} \tag{3.14}$$

where

$$z_1 = i\sqrt{u^2 - i\Omega}$$
$$z_2 = i\sqrt{u^2 + i\Omega)}$$
$$z_3 = -i\sqrt{u^2 - i\Omega)} \tag{3.15}$$
$$z_4 = -i\sqrt{u^2 + i\Omega)}$$

are the poles of the integrand with subscripts denoting the quadrant of the complex plane they belong to.

Now, we imagine a closed integral of the integrand as shown by the dotted curve in Fig. 3.2 which does not enclose any poles and hence must be zero. The line integral along S_l is the part that we are trying to calculate. For a closed curve:

$$\oint dz\, g(z) = 0$$

$$0 = \int_{S_1} dz\, g(z) + \int_{S_2} dz\, g(z) + \int_{S_l} dz\, g(z) + \int_{S_c} dz\, g(z) \tag{3.16}$$

$$\int_{S_l} dz\, g(z) = -\int_{S_1} dz\, g(z) - \int_{S_2} dz\, g(z)$$

Integral around curved path S_c goes to zero as it happens at infinity where the integrand vanishes. The remaining integrals can be easily calculated using Cauchy's residue theorem (note the negative sign due to the clockwise direction of curves S_1 and S_2) as:

$$\int_{S_1} dz\, g(z) = -2\pi i \frac{u^2 + z_1^2}{(z_1 - z_2)(z_1 - z_3)(z_1 - z_4)}$$
$$= \frac{-\pi}{2\sqrt{u^2 - i\Omega}} \tag{3.17}$$

and

$$\int_{S_2} dz\, g(z) = -2\pi i \frac{u^2 + z_2^2}{(z_2 - z_1)(z_2 - z_3)(z_2 - z_4)}$$
$$= \frac{-\pi}{2\sqrt{u^2 + i\Omega}} \tag{3.18}$$

Therefore, we have:

$$\int_{-\infty}^{\infty} dz \frac{z^2 + u^2}{(z^2 + u^2)^2 + \Omega^2} = \frac{\pi}{2\sqrt{u^2 - i\Omega}} + \frac{\pi}{2\sqrt{u^2 + i\Omega}}$$
$$= Re\left[\frac{\pi}{\sqrt{u^2 - i\Omega}}\right] \tag{3.19}$$

From here, we reach the final expression as shown in Eq. 3.2.

3.2 Coatings Brownian Noise

Once coatings thermo-optic noise is reduced, the predominant remaining noise source in mid-range frequencies is coatings Brownian noise. I have described the calculation roadmap for this noise source in Sec.1.2. This is the quantity of interest for this experiment and in our noise budget, we use this calculation to estimate the loss angle of the coatings inferred from the measured noise in the experiment.

In Fig. 3.3, I have plotted q_j^B and q_j^S, which represent each layer's contribution transfer functions to the phase noise of light reflected from Bulk or Shear stress
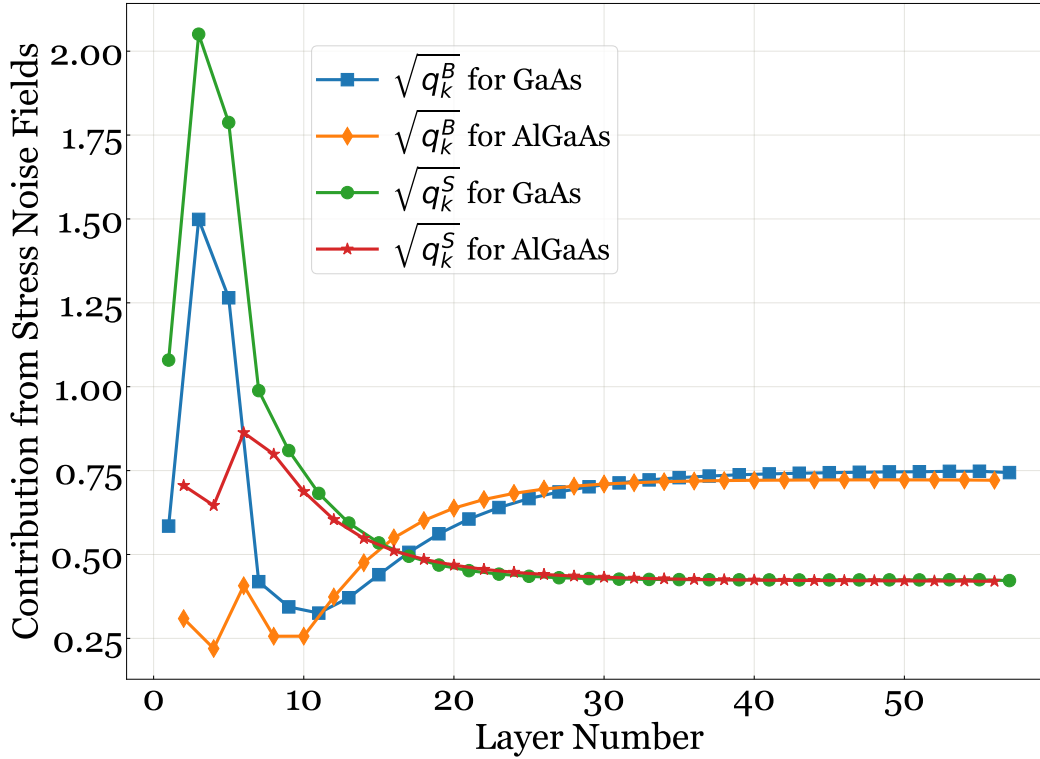
Figure 3.3: Contribution of Bulk and Shear stress noise fields from each layertowards phase noise ASD of reflected light.

noise fields respectively. This raises an interesting point about coatings Brownian noise optimization. The back layers that are closer to the substrate have the most contribution to the coatings Brownian noise and the contribution is evenly spread out. This means one can trade-off extra reflectivity for the reduction in the coatings Brownian noise, or if materials are chosen such that their refractive indices differ by a larger amount, less number of coating layers will be required, resulting in reduced coatings Brownian noise from the stack.

3.3 Substrate Brownian Noise

Through the same mechanism as coatings Brownian noise, the substrate also imparts phase noise on the light due to mechanical loss and finite temperature. However, fused silica has a very low mechanical loss (1×10^{-7}) and as seen in Eq. 1.24, the thickness of material does not matter in the contribution of Brownian noise, but multiple different materials would add up this contribution. Thus substrate Brownian noise is not as dominant in comparison with coatings Brownian noise.

Our noise model includes this source as:

$$S_{\text{subBr}}^x = \frac{2k_{\text{B}}T}{\pi^{3/2}f}\frac{1-\sigma_{\text{s}}^2}{wE_{\text{s}}}\Phi_{\text{s}} \tag{3.20}$$

3.4 Substrate Thermoelastic Noise

Temperature fluctuations cause fluctuations in the thickness of the substrate as well. Since most of the reflection happens at the coatings, the effect of this noise is reduced. We followed the analytical expression by Somiya et al. [28, Eq. 3, 8] to calculate this noise contribution:

$$S_{\text{subTE}}^x = \frac{4k_{\text{B}}T^2}{\pi^{1/2}}\frac{\alpha_{\text{s}}^2(1+\sigma_{\text{s}})^2w}{\kappa_{\text{s}}}J(f/f_{\text{T}}) \tag{3.21a}$$

$$\begin{aligned} J(\Omega) = &Re\left[\frac{e^{i\Omega/2}(1-i\Omega)}{\Omega^2}\left(\text{Erf}\left[\frac{\sqrt{\Omega}(1+i)}{2}\right]-1\right)\right] \\ &+\frac{1}{\Omega^2}-\sqrt{\frac{1}{\pi\Omega^3}} \end{aligned} \tag{3.21b}$$

3.5 Technical Noise Sources

In this section, I'll briefly describe all other noise sources in the experiment that are not fundamentally present for all mirrors with Bragg coatings but are present in this experiment due to our choice of setup, sensing, and control of the experiment.

3.5.1 Seismic Noise

Low-frequency acceleration of the experimental apparatus couples into the bending motion of the cavities as shown in Fig. 3.1. The bending of the cavity leads to changes in the longitudinal length of the cavity which directly affects the readout frequency from the cavity. This technical noise coupling is minimized by placing the cavity supports at the Airy points, and verifying the same with finite element analysis simulations [21]. If we assume mounting errors of ±0.5 mm and common-mode rejection due to mounting the two cavities on a common platform, the coupling from acceleration into cavity strain is estimated to be $6 \times 10^{-12}\ m^{-1}\ s^2$. The brown curve in Fig. 4.1 shows the estimated coupled seismic noise from measured seismic vertical acceleration in our laboratory.

3.5.2 Sensing Noise

The digital phase-locked loop (DPLL) used to readout the time series of beat note frequency injects its own frequency noise. Any frequency reading device can only read frequency noise as well as its own reference oscillator. With rubidium clock stabilization, the frequency noise of our DPLL was found to be less than 1 mHz/$\sqrt{\text{Hz}}$ up to 4 kHz. This was measured by generating a 27.344 MHz signal by Moku:Lab and feeding it back to itself through a long cable for frequency measurement. Along with this, the beatnote detector's dark and shot noise also contributes to the sensing noise. The green curve in Fig. 4.1 shows the contribution of this noise in the measurement.

3.5.3 Controls Shot Noise

Shot noise in the resonant RF Photodiodes used in the PDH loop for FSS (see Sec.2.2) adds noise to the frequency of the laser. We ensure that enough light is falling on these detectors to keep them shot noise limited rather than dark noise limited. For total power P_0 incident on the cavity, the PDH shot-noise is estimated by:

$$
\begin{aligned}
S_{PDHshot} = \left(\frac{f_p}{2P_0 m}\right)^2 \left(1 + \frac{f}{f_p}\right)^2 \\
\left(2h\nu P_0 \left[J_0(\Gamma)^2(1-\eta) + 3J_1(\Gamma)^2\right]\right)
\end{aligned}
\tag{3.22}
$$

Here, the first term in parenthesis is the PDH discriminant term with units of Hz/W, where m is the modulation index of sidebands used for PDH. The second term in parenthesis accounts for cavity pole f_p and the third term is simply the shot noise for the total power falling on the detectors including carrier and sidebands. Overall, this noise goes down as we increase the power of the laser. The grey curve in Fig. 4.1 shows the contribution of this noise in our experiment as negligible in all of the frequency ranges.

3.5.4 Laser Frequency Noise

NPRO lasers are inherently low linewidth as they are stabilized with a temperature-controlled crystal cavity in a monolithic non-planar geometry. The free-running frequency noise ASD of Nd:YAG NPRO is assumed to be 1 kHz/$\sqrt{\text{Hz}}$ at 10 Hz and assumed to fall as $1/f$ at higher frequencies [29]. We measured the frequency noise suppression of our FSS (see Sec.2.2) and applied that to get the estimated residual frequency noise of the laser in the transmission from the cavities. The magenta curve shows the suppressed laser frequency noise contribution in the beat

Sym.	Expression	Sym.	Expression
r_0	$\frac{w}{\sqrt{2}}$		
f_c	$\frac{\kappa_c}{\pi C_c w^2}$	f_s	$\frac{\kappa_s}{\pi C_s w^2}$
ξ_c	$\sqrt{\left(\frac{if}{f_c} + \xi^2\right)}$	ξ_s	$\sqrt{\left(\frac{if}{f_s} + \xi^2\right)}$
k_c	$\sqrt{\frac{2\pi i f C_c}{\kappa_c}}$	k_s	$\sqrt{\frac{2\pi i f C_s}{\kappa_s}}$
α_c	$\sum_j \alpha_j \frac{d_j}{d}$	κ_c	$\left(\sum_j \frac{1}{\kappa_j}\frac{d_j}{d}\right)^{-1}$

Table 3.2: Parameters used in photothermal transfer function calculations. Note the difference in definition of α_c from $\bar{\alpha}_c$ used in Eq. 3.1.

note frequency noise.

3.5.5 Laser Amplitude Noise

Some absorption of light always happens at the coatings. This means that the coating gets heated due to the incident power on it. In the case of a cavity, this is the circulating power inside the cavity. Therefore, any fluctuations in the intensity of light drive fluctuations in the temperature of the coating. Since the overall heat capacity of coatings is small, the delay in temperature rise/fall due to intensity rise/fall is negligible and a near-instant response is seen in the measurement frequency band. Since this is another source of temperature fluctuations, the phase noise follows the same thermo-optic pathway described in Sec.3.1 and can be written as:

$$S^x_{\text{photoThermal}} = |H(f)|^2 P^2_{abs} S_{RIN} \qquad (3.23)$$

where $H(f)$ is the complex photothermal transfer function (see below) for a mirror, $P_{abs} = a_{coat} P_{circ}$ is power absorbed by the mirror and S_{RIN} is the PSD of relative intensity noise (RIN) of the incident laser. The blue curve in Fig. 4.1 shows the contribution of this noise source in the beat note frequency noise.

Photothermal transfer function calculation

The photothermal transfer function consists of three contributions:

$$H(f) = H_c(f) + H_s(f) + H_{tr}(f) \qquad (3.24)$$

where subscripts c,s, and tr stand for coating, substrate, and thermorefractive contributions respectively. These contributions are calculated by [30, Eq. A44, A45,

A49]:

$$H_c(f) = \frac{\alpha_c}{\pi \kappa_c} \frac{f_c}{if} \int_0^\infty d\xi \, \xi e^{-\xi^2/2} F(\xi) \left[\gamma_1 G_1(\xi) - \gamma_2 \frac{\xi}{\xi_c} G_2(\xi) \right] \tag{3.25a}$$

$$H_s(f) = -\frac{\alpha_s(1+\sigma_s)}{\pi \kappa_s} \frac{f_s}{if} \int_0^\infty d\xi \, F(\xi)(1 - \xi/\xi_s)\xi e^{-\xi^2/2} \tag{3.25b}$$

$$H_{tr}(f) = \frac{\lambda_0 \beta_c}{2\pi \kappa_c r_0} \int_0^\infty d\xi \frac{\xi e^{-\xi^2/2}}{\xi_c} \frac{\sinh(\xi_c d/r_0) + \mathcal{R}\cosh(\xi_c d/r_0)}{\cosh(\xi_c d/r_0) + \mathcal{R}\sinh(\xi_c d/r_0)} \tag{3.25c}$$

where

$$F(\xi) = [\cosh(\xi_c d/r_0) + \mathcal{R}\sinh(\xi_c d/r_0)]^{-1} \tag{3.26a}$$

$$G_1(\xi) = \cosh(\xi d/r_0) + \mathcal{R}\frac{\xi}{\xi_c}\sinh(\xi d/r_0)$$
$$- \cosh(\xi_c d/r_0) - \mathcal{R}\sinh(\xi_c d/r_0) \tag{3.26b}$$

$$G_2(\xi) = \mathcal{R}\cosh(\xi d/r_0) + \frac{\xi_c}{\xi}\sinh(\xi d/r_0)$$
$$- \mathcal{R}\cosh(\xi_c d/r_0) - \sinh(\xi_c d/r_0) \tag{3.26c}$$

$$\mathcal{R} = \frac{\kappa_c \left(r_0^2 k_c^2 + \xi^2\right)^{1/2}}{\kappa_s \left(r_0^2 k_s^2 + \xi^2\right)^{1/2}} \tag{3.26d}$$

All extra parameters used in these equations which aren't already listed in Table. 3.1 are defined in Table. 3.2.

C h a p t e r   4

RESULTS

In this chapter, I describe the final results of the experiment we conducted. Our experiment has some environmental noise coupling which we tried to isolate and minimize as much as we could. But we get the added freedom of continuously monitoring the experiment and using the measurement made under optimal environmental conditions, with the lowest nearby activity and suppressed thermal fluctuations. I kept the two cavities locked and their beatnote frequency locked to 27.34 MHz for over 2 months. Several automated scripts made sure that the experiment stays in this science mode. The disturbance to the laboratory was kept at a minimum with very few visits and less foot traffic around the lab due to the ongoing pandemic. Therefore, our experiment establishes an upper limit on direct observation of coatings Brownian noise.

4.1   Measurement Results

4.1.1   Measured noise and estimation of noise budget

Fig. 4.1 shows the measured beatnote spectrum (orange curve) along with the estimated budget of different noise sources. For each curve, the shaded region is a 68% confidence interval estimated by measured noise or propagating errors of initial parameter uncertainties. The beatnote fluctuation ASD measurement as the output of the DPLL (see Sec.2.3) comes in units of $Hz/\sqrt{Hz}$ that is used on the left axis. An equivalent displacement noise of the cavity length is calculated by multiplying with $\frac{c}{L\lambda}$, to get the right axis in units of $m/\sqrt{Hz}$. Here we measured a noise level of $2 \times 10^{-18}\, m/\sqrt{Hz}$ at 200 Hz.

The black curve shows the estimated total noise of the experiment which includes coatings Brownian noise (red curve). The level of the coatings Brownian noise in this plot is adjusted to explain the observed total noise by fitting the bulk loss angle value of the coatings (see Sec.4.1.2 below).

The laser amplitude noise (blue) was measured by using the calculation mentioned in Sec.3.5.5. For S_{RIN} in Eq. 3.23, the relative intensity noise of the transmitted lasers were measured right before the beatnote measurement using two witness photodiodes (i.e. they were out of the intensity stabilization servo loop).
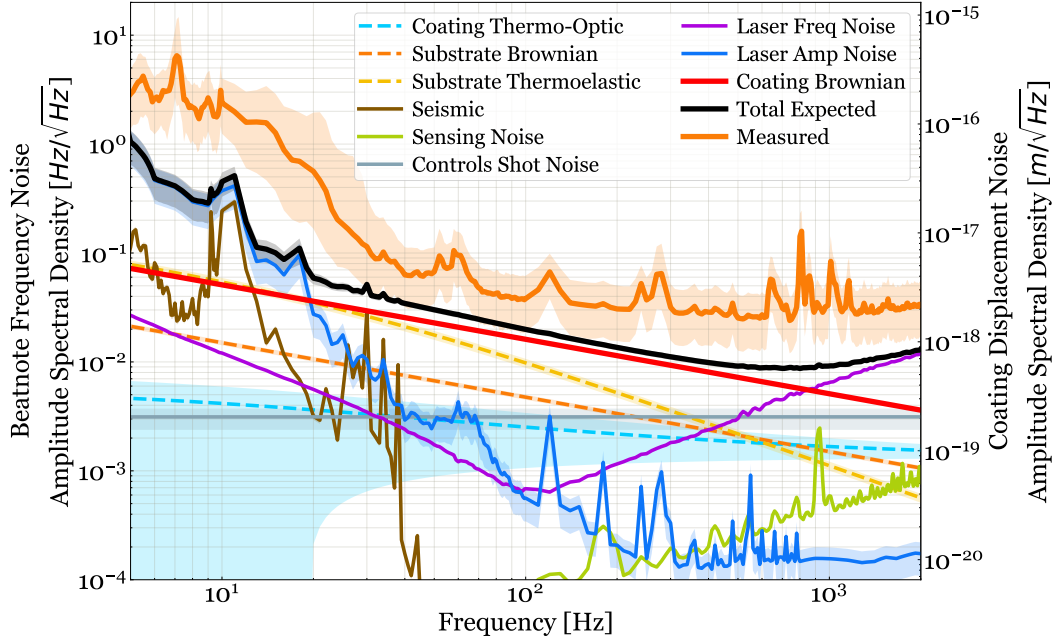
Figure 4.1: Noise Budget and measurement of the experiment. The parameters used for calculating estimates of noise contributions are listed in Table. 3.1. The orange curve is the median averaged amplitude spectral density of beatnote frequency calculated using Welch method. The shaded region corresponds to 68% confidence interval for the curves.

The laser frequency noise (magenta) was estimated as described in Sec.3.5.4. For this estimation, the open loop transfer function of the frequency stabilization servo measured earlier (see Fig. 2.5) was used. The DC power levels on the RF photodiodes were measured right before the beatnote spectrum measurement and were used to scale any changes in the frequency suppression due to different circulating laser power. However, this should be noted that the gain is high enough in the frequency band of interest that the minor changes in circulating laser power did not affect the performance of the loop much. Using the same DC power level, the controls shot noise (grey curve) of the experiment was also estimated in realtime (see Sec.3.5.3)

Coating thermo-optic (dashed blue, see Sec.3.1), substrate Brownian (dashed orange, see Sec.3.3), and substrate thermoelastic (dashed yellow, see Sec.3.4) noises were calculated using coatings material parameters listed in table 3.1.

The sensing noise (green, see Sec.3.5.2) of the measurement, and the seismic noise coupling (brown, see Sec.3.5.1) were measured before the setup of science mode and were assumed to remain the same during the entirety of the science mode observation run.

We believe the measured noise floor is the true noise floor of the experiment because

the measured noise level was not showing any reduction when the control loop gains were increased further or the incident power on the cavities was increased. This meant that the noise floor is due to a noise source that can not be suppressed by the different control loops. The excess noise below 70 Hz should be due to the scattered light inside the vacuum can reaching back to the PDH lock photodiode. Measured noise from 70 Hz to 600 Hz shows a near-flat dominant noise contribution which we believe is coming from the coatings thermal noise.

4.1.2 Bayesian analysis to infer loss angles

With the parameters listed in Table. 3.1, I derived an estimate of all noise curves except for the coatings Brownian noise. Then, for any assumed value of the bulk loss angle for coating layers (assumed to be the same for GaAs and $Al_{0.92}Ga_{0.08}As$), I can obtain an estimate of the total expected beatnote frequency noise (depicted as the solid black curve in Fig. 4.1).
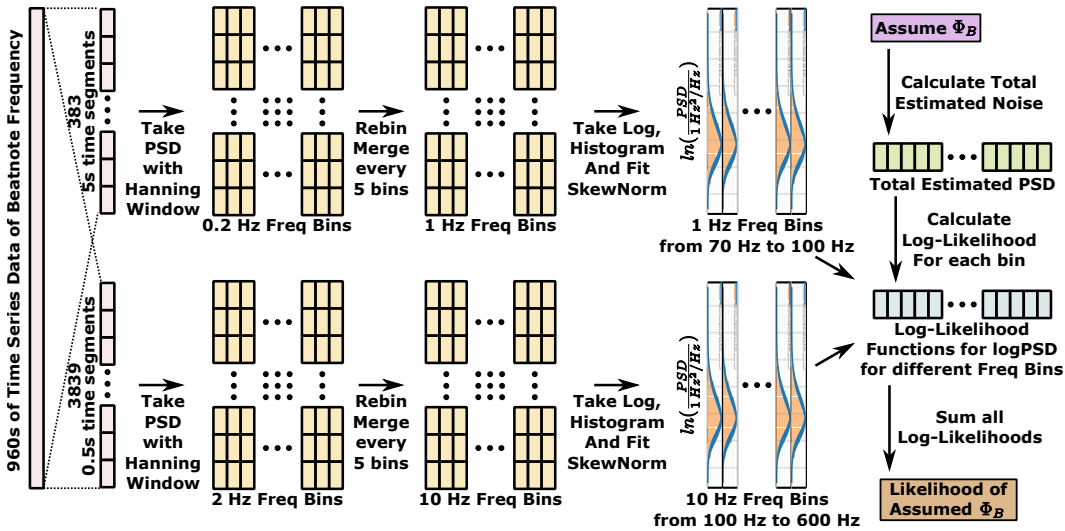
Figure 4.2: Schematic showing analysis of the measured data to get likelihood value for a given bulk loss angle.

The measured time-series data of the beatnote frequency was divided into segments of 5s with half overlap. Welch function of the Python library signal was used with the Hanning window to calculate a PSD estimate for each of these 5s long segments. This provided us with PSD with frequency bin widths of 0.2 Hz. Consecutive 5 bins were merged taking their median value to average out correlations in the neighboring bins due to the Hanning window used. This gave us 1 Hz frequency bins. Bins from 70 Hz to 100 Hz were chosen and the rest are discarded.

For each bin, we had as many PSD estimates as the number of time segments

we created. We took the logarithm of these PSD (logPSD) estimates and fit the histogram obtained to a skew-normal distribution to get an estimate of the probability distribution of logPSD of beatnote frequency noise in each of the frequency bins. An example of such a fit is shown in Fig. 4.3 for the frequency bin at 200 Hz.
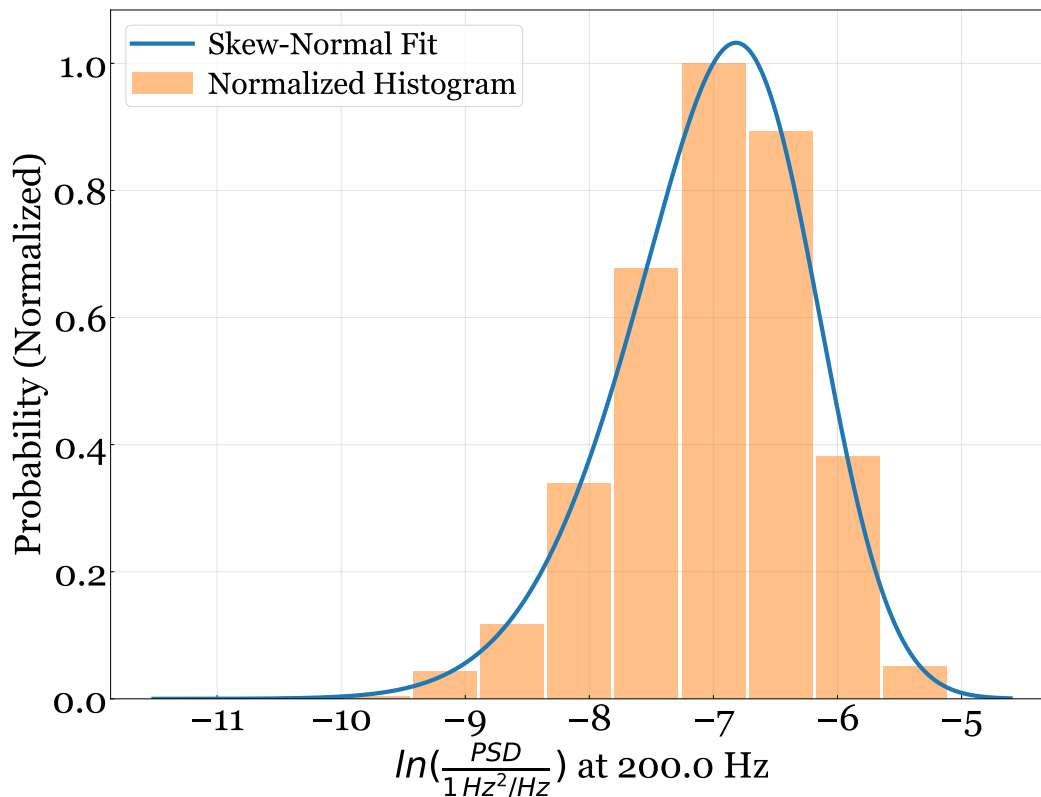
Figure 4.3: Example of fitting the histrogram of logPSD data at a particular frequency to a skew-normal distribution.

The same analysis as mentioned above is repeated with 0.5 s time-series segments, which gave logPSD probability distribution for frequency bins spaced at 10 Hz. We took bins from 100 Hz to 600 Hz from this set. This ensured that the weightage of different decades of frequency noise data is roughly equal in our noise analysis to get the correct coupling of power-law frequency dependence of the noise.

Further, from the data set, we removed frequency bins coinciding with harmonics of 60 Hz as this was a known source of noise due to leakage of AC power into our control loop electronics. The section between 260 Hz and 290 Hz is also removed as a known stationary noise peak which is always present.

With this, we have a distribution of logPSD of beatnote frequency for various frequency values. We calculated the log-likelihood function for each of these

frequency values using the distribution fitted above and summed them with each other to obtain the total log-likelihood value.
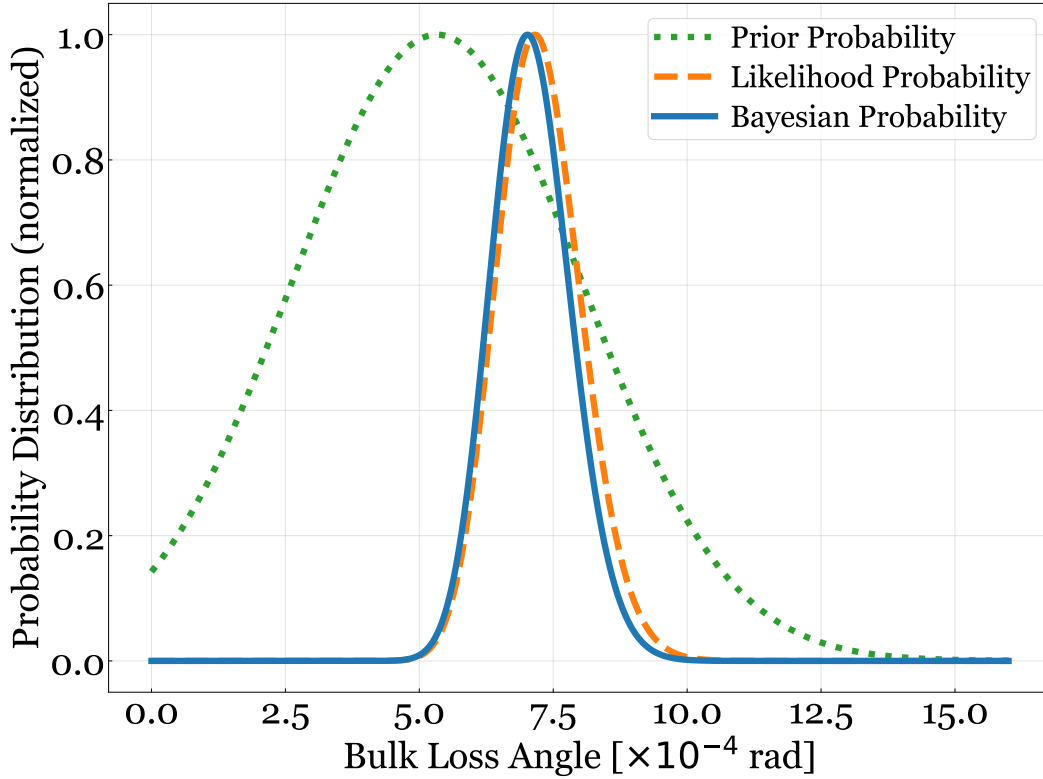
Figure 4.4: Bayesian probability distribution of the Bulk loss angle for the measured beatnote spectrum along with the assumed prior probability distribution and the likelihood distribution.

I did a grid search on possible values of the bulk loss angle between zero and 1.6×10^{-3} with a step size of 1×10^{-6} and calculated likelihood probability for each value as shown in Fig. 4.4 using the method described above. A prior distribution was assumed as shown in Fig. 4.4 in the shape of a Gaussian centered at 5.33×10^{-4} that was measured by Penn et al.[17]. The Bayesian probability distribution is calculated as the product of prior and likelihood distribution. The Bayesian inferred value came out to be:

$$\Phi_{\mathrm{B}} = (7.0 \pm 1.2) \times 10^{-4} \tag{4.1}$$

where the limits enclose a 90% confidence interval. This value was estimated with a shear loss angle value of 5.2×10^{-7} taken from Penn et al. [17] indirect measurements. Since the frequency dependence of total noise on the shear loss angle is similar to that of the bulk loss angle, we cannot fit two degrees of freedom into our result. Simulations done by Penn et al. [17] suggest that shear loss angle value should be

very low in these coatings, so its contribution to the coatings Brownian noise is assumed to be negligible as well. Hence, we decided to only fit for bulk loss angle value using shear loss angle value as determined by the indirect experiment.

4.2 Investigating frequency dependence of loss angle

Looking at Fig. 4.1 more closely, one can see that the measured noise floor in the experiment is less steep than 1/f dependence predicted by Eq. 1.24 for the coatings Brownian noise. We speculate that optical bonding might introduce zener damping-like noise[31] making the coatings Brownian noise curve less steep. To investigate this possibility, I ran another Bayesian inference analysis keeping the frequency dependence of the bulk loss angle as another variable along with the bulk loss angle itself.
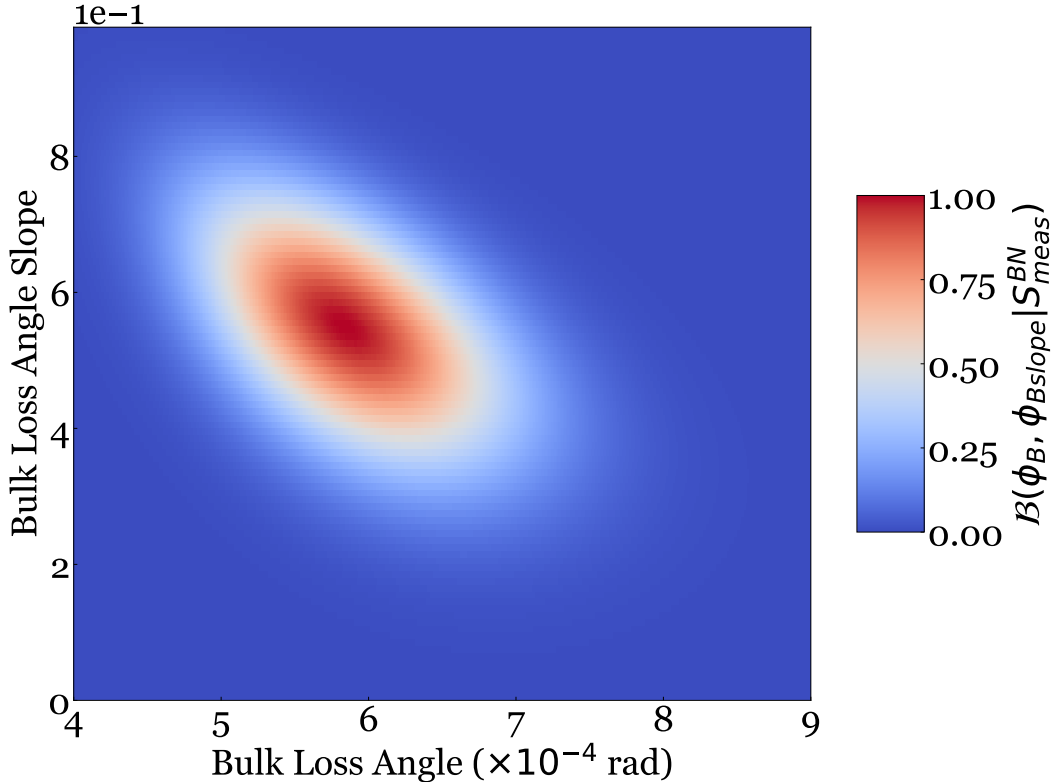
Figure 4.5: Bayesian probability distribution for the bulk loss angle and its frequency dependence power-law slope for the measured beatnote spectrum.

Fig. 4.5 shows the Bayesian probability distribution for this fit as a function of the parameter space of Bulk loss angle and its assumed frequency dependence. The inferred value for the bulk loss angle of $Al_{0.92}Ga_{0.08}As$, GaAs coatings from this method came out to be:

$$\Phi_{\mathrm{B}} = (5.8 \pm 1.0)\left(\frac{f}{100\,\mathrm{Hz}}\right)^{0.54\pm0.19} \times 10^{-4} \tag{4.2}$$

Fig. 4.6 shows the noise budget of the experiment when the bulk loss angle is given this frequency dependence. The measured noise floor agrees with the estimated total noise from 70 Hz to 700 Hz. But of course, this can be a result of overfitting the data so this extra analysis result should be interpreted with caution. I have presented this analysis for reference for any future endeavors towards such a frequency dependence in coatings Brownian noise of optical contact bonded crystalline coating.
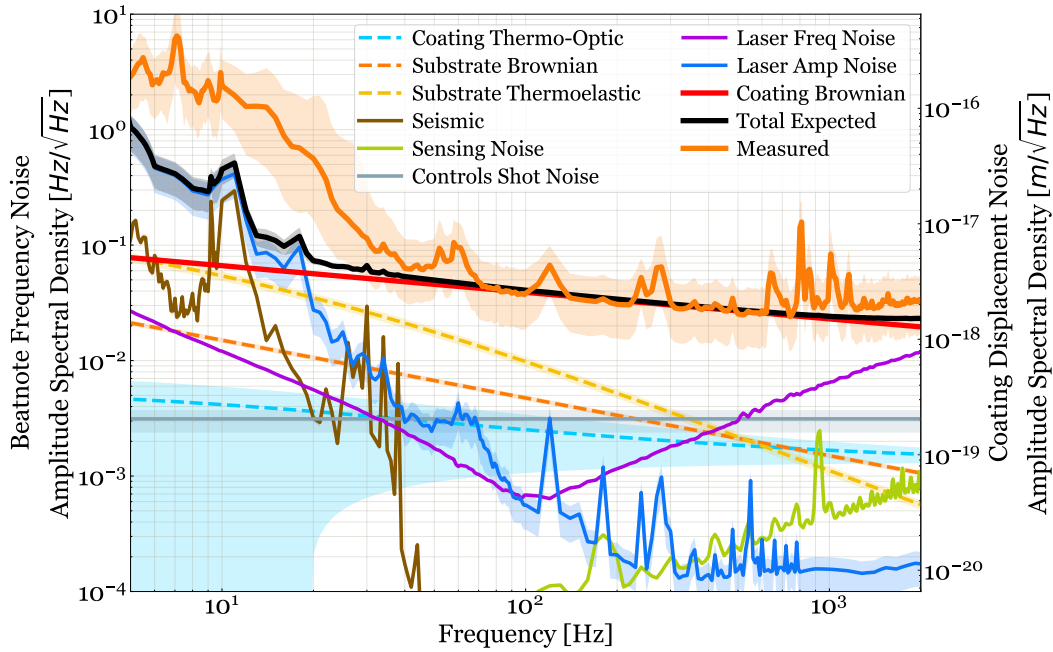
Figure 4.6: Noise Budget and measurement of the experiment with frequency dependent loss angle fitting. Here a mechanical loss angle of $\Phi_{\mathrm{B}} = (5.8 \pm 1.0)\left(\frac{f}{100\,\mathrm{Hz}}\right)^{0.54\pm0.19} \times 10^{-4}$ is determined by bayesian inference from the measured beatnote spectrum. The rest of the parameters are listed in Table. 3.1. The orange curve is the median averaged amplitude spectral density of beatnote frequency calculated using Welch method. The shaded region corresponds to 68% confidence interval for the curves. This figure is provided to demonstrate an alternative analysis of the results where we allow for a power-law dependence of the bulk loss angle. This model explains observed roll-off of beatnote frequency noise better.

4.3 Discussion with respect to other experiments

The particular sample of $Al_{0.92}Ga_{0.08}As$ and $GaAs$ coated mirrors that we had for this measurement were only available to us. These coatings were specially designed to cancel the thermo-optic effect that was experimentally observed in previous experiment[18]. So it is hard to compare the results of this measurement with other

experiments conducted in this field, but here I'll try to cover a pertinent discussion about using these materials for a crystalline coating candidate.

Penn et al.[17] measured the bulk and shear loss angles indirectly using Q measurements of disk resonators with or without a crystalline coating of $Al_{0.92}Ga_{0.08}As$ and GaAs. They measured the bulk loss angle to be 5.33×10^{-4} and 5.2×10^{-7} but report that overall coating loss angle is 4.78×10^{-5}. This indicates that their bulk and shear loss angle definitions might be different from ours. Cole et al.[14] also measured similar coatings using a direct measurement setup in which a cavity is made with the mirrors under test and compared with a ultra low expansion (ULE) reference cavity at 698 nm through a frequency comb. They reported the loss angle upper bound value to be 2.5×10^{-5}.

More recently, Yu et al.[32] performed a more advanced experiment with these coatings utilizing different polarizations of the laser resonating in the same cavity. They were able to perform a more careful study of spatial correlations of noise originating from the coatings which allowed them to separate global displacement noise from local displacement noise. Since the correlation length of coatings Brownian noise is very small, it appears as spatially local noise in these measurements. They reported coatings Brownian noise measurement at the same level as expected for a loss angle of 2.5×10^{-5} but they were able to see that after they removed global excess noise of unknown origin present in these coatings. This global excess noise seems to have the same frequency dependence as the coatings Brownian noise (1/f in ASD) but is about 30 times larger in PSD.

Yu et al.[32] also found intrinsic birefringence noise, attributed to fluctuations in refractive index along one polarization axis. This intrinsic birefringence noise added another factor of 10 to the observed PSD, measured by comparing it against a polarization-averaged locking scheme. Thus, overall the global excess noise and birefringence noise could cause about 300 times more observed noise in PSD. If wrongly attributed all to the loss angle of the coatings or if we call it an "effective loss angle", this would result in a loss angle value to be about 17 times higher than what indirect measurements measured.

In our direct measurement which can not distinguish between global excess noise, birefringence noise on single polarization, and the coatings Brownian noise, we get a loss angle value that is 15 times that measured by Penn et al.[17]. While we can not scientifically attribute our larger measured loss angle to these effects, with the new information the experimental setup can be improved to dig deeper into the noise

floor and confirm Yu et al.[32] measurements.

4.4 Possible future improvements to the experiment

Hindsight is always 20/20. Learning from our experience, I think we can improve this experiment in a variety of ways. The first obvious change to do is to utilize the polarization averaged locking scheme devised by Yu et al.[32]. By sending the laser first to an AOM and upshifting the first-order beam by cavity birefringence splitting (the difference between the resonance of the two polarization modes), we can cancel away the birefringence noise at the PDH error point.

Secondly, we can try to lock another laser to the same cavity in the same polarization-averaged way but to TEM01 mode while the first laser is locked to TEM10 mode. Just like Yu et al.[32], we would be able to get rid of any common mode global excess noise in this measurement. We do not need two cavities either for this setup, hugely reducing the complexity of the experiment and the need of controlling the beatnote frequency through thermal means.

Along with these major experimental design changes, many minor improvements can also be done. Our vacuum can window were glass with anti-reflection (AR) coatings but parallel surfaces. This made etalon effects feasible and the possibility of backscattered light reflecting back towards the cavity polluting the PDH signal. Whenever possible, such vacuum can windows should be wedged with an angle large enough to dump all scattered light to a designated beam dump.

Another interesting change would be to implement a frequency discriminator based on an optical delay line implemented on a thermally and mechanically stabilized pool of optical fiber cable (also see Sec.12.4). This would allow us to measure the frequency noise without using an identical cavity or additional laser. However, more work would be required to make sure that the fiber noise does not dominate in this case.

We can also put coils around the cavity and maybe ferrite material to produce magnetic fields to measure the effects of fluctuations in local magnetic fields on the electro-optic coefficients of such crystalline coatings. Similarly, some electrode plates can be placed as well to measure these effects for electric field couplings.

4.5 Future of crystalline coatings

Crystalline coatings are an active topic of research and are promising for achieving the target sensitivities for future gravitational wave detectors. More study is

required to understand the source of birefringence noise which is still unknown. If polarization averaging can be done at the PDH error point, maybe some clever material optimization and/or coating structure optimization can cancel this noise for crystalline materials within the coating itself.

The global excess noise though needs to be addressed, otherwise using these coatings would not be feasible for gravitational wave detection purposes. Since this noise is directly observed but is not present in loss angle measurements made with disk resonators, there is some indication that the optical contacting of these crystalline coatings on an amorphous substrate is not as harmless as thought earlier. This effect needs to be studied properly and mitigated if possible. Maybe new growth recipes are required to meaningfully use the low-loss crystalline coatings for ultra-precision measurements.

Finally, we need to improve our understanding of the coatings Brownian noise as well, particularly for crystalline coatings where the material is not necessarily isotropic and could be very anisotropic due to stress. We need to understand any frequency dependence of the loss angle as well, and if that can be utilized to further engineer better coatings for future gravitational wave detectors.

Part II

Balanced Homodyne Detection

testing and characterization at 40m prototype.

Chapter 5

INTRODUCTION

Advanced LIGO has achieved a high range of gravitational wave detection by successfully mitigating most of the classical noise sources that affect the frequency band of interest. This has resulted in Advanced LIGO being shot noise limited for frequencies above 200 Hz. For frequencies below 200 Hz, there are still some excess classical noise sources[33], but some of them can be subtracted through clever feedforward techniques[34, 35]. This situation is a carefully balanced one though. For improving the detector range in future generations, more circulating power is required in the interferometer. The same noise mitigation strategies would become sub-optimal for higher circulating power[36]. One proposed solution for solving this issue is to use a more sophisticated Balanced Homodyne Readout (BHR) method for the gravitational wave signal from the detector[37].

In this part, I'll describe the efforts of the Caltech BHR upgrade commissioning team that I was part of, for successfully prototyping and testing the BHR scheme at the Caltech 40m prototype. In this chapter, I'll introduce the current readout schemes used in gravitational wave detectors that have helped make gravitational wave detections but are limited in further lowering noise floors in the detectors. The idea is to understand the nuances of different readout schemes and understanding the benefits and potential drawbacks that the BHR scheme can bring.

5.1 Gravitational waves detector current readout methods

Gravitational wave detectors utilize a Michelson interferometer to detect differential arm length (DARM) changes produced by gravitational waves. Most of them are added with Fabry-Pérot arm cavities, power recycling cavity, and signal extraction cavity to improve the detection sensitivity, but the differential length sensing comes from the Michelson interferometer part. Fig. 5.1 shows a simplified schematic of how Michelson interferometer senses gravitational waves. Let's assume the input electric field amplitude of the laser to the interferometer be E_{in} in a frame of reference rotating at the optical frequency. We assume the following convention on phase rotations while reflecting from the beamsplitter: the transmitted light suffers no phase change and the reflection from the input port towards the X arm suffers a phase delay of $\pi/2$, and the reflection from the Y arm to the output port gets a phase
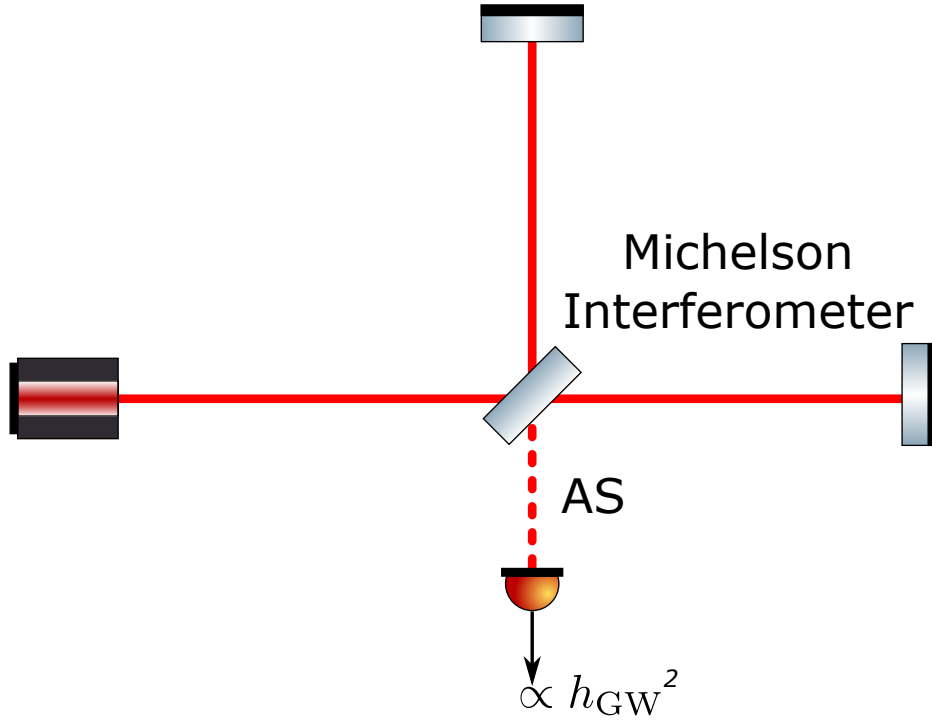
Figure 5.1: Simplified schematic of a Michelson Interferometer. For equal arm lengths, the AS port becomes dark. Gravitational waves passing through the interferometer increase phase delay in one arm length while decreasing it in the other. This generates a signal at the AS port which is quadratically proportional to the gravitational wave amplitude h_{GW}.

gain of $\pi/2$. This means that after the beam splitter, the field in the arms is given by:

$$
\begin{aligned}
E_{\mathrm{BS}\to\mathrm{X}} &= -\frac{i}{\sqrt{2}}E_{\mathrm{in}} \\
E_{\mathrm{BS}\to\mathrm{Y}} &= \frac{1}{\sqrt{2}}E_{\mathrm{in}}
\end{aligned}
\tag{5.1}
$$

The fields in the arms travel to the mirror and reflect, accumulating phase delay of kL_{X} and kL_{Y}, where $k = 2\pi/\lambda$ and L_{X} and L_{Y} are the arm lengths. The beams merge at the beam splitter to get the following fields at the AS and REFL ports:

$$
\begin{aligned}
E_{\mathrm{AS}} &= iE_{\mathrm{in}}\frac{e^{-i2kL_{\mathrm{Y}}} - e^{-i2kL_{\mathrm{X}}}}{2} = iE_{\mathrm{in}}e^{-i2kL_{\mathrm{C}}}\frac{e^{i2kL_{\mathrm{D}}} - e^{-i2kL_{\mathrm{D}}}}{2} \\
E_{\mathrm{REFL}} &= E_{\mathrm{in}}\frac{e^{-i2kL_{\mathrm{Y}}} + e^{-i2kL_{\mathrm{X}}}}{2} = E_{\mathrm{in}}e^{-i2kL_{\mathrm{C}}}\frac{e^{-i2kL_{\mathrm{D}}} + e^{-i2kL_{\mathrm{D}}}}{2}
\end{aligned}
\tag{5.2}
$$

Here, we define common arm length as $L_{\mathrm{C}} = \frac{L_{\mathrm{X}}+L_{\mathrm{Y}}}{2}$ and the differential arm length

as $L_D = \frac{L_X - L_Y}{2}$. Note that any field coming at the antisymmetric port is $\pi/2$ phase shifted with respect to the input beam. Readers can verify that this property of Michelson interferometers is independent of the BS phase convention. Now, the light power at the AS port is given by:

$$P_{AS} = E_{AS}^* E_{AS} = P_{in} sin^2(2kL_D) \tag{5.3}$$

If the Michelson interferometer is somehow maintained such that AS port is dark, then for small differential arm length changes such as those generated by gravitational waves, we can approximate the antisymmetric power output as the square of the gravitational wave signal.

$$P_{AS}(t) \approx P_{in} \left(\frac{4\pi L h_{GW}(t)}{\lambda} \right)^2 \tag{5.4}$$

where h_{GW} is the gravitational wave strain on an arm's length of L. From here onwards, we'll see how two different readout schemes are possible to read the gravitational wave signal.

5.1.1 DC readout (Offset readout)

There are two issues with relying on reading the Michelson interferometer at the absolute dark point. First, it is not possible to control the interferometer at this point since the light power (which is the only real quantity we can measure) is quadratically dependent on differential arm difference, so the output increases with DARM moving in either direction. For a successful lock point to exist, we need an error signal which crosses zero at the lock point, that is, it is positive after the lock point and negative before it, so that negative feedback can hold it at the zero point. Secondly, and more importantly, the output signal is a square of the gravitational wave signal reducing its sensitivity considerably.

To fix both these issues at once, a commonly used technique is to lock the Michelson at a small offset from the true dark point. This provides a non-zero slope at the lock point so that the interferometer can be locked reliably to the offset point, and it allows some of the interferometer circulating light to leak out of the AS port. This leakage electric field is strong and only depends on common length fluctuations of the interferometer. If the common length fluctuations are minimized by other loops (for example, by locking the main laser to the common length fluctuations of the
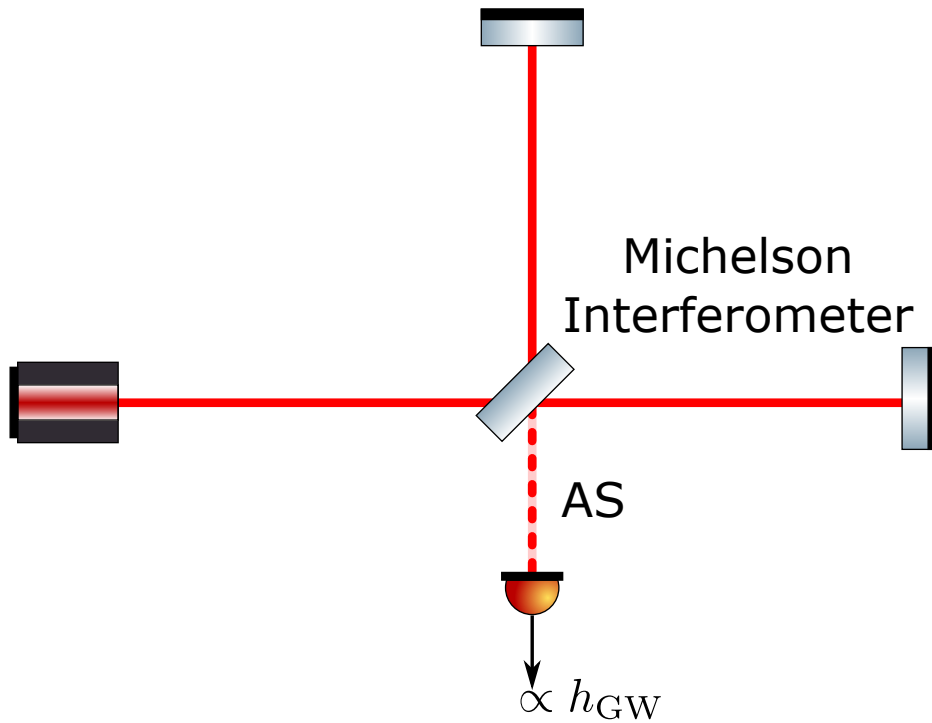
Figure 5.2: Simplified schematic of DC readout of Michelson Interferometer. By introducing a small offset in the the differential arm length, AS port is not completely dark and has small amount of light always present. In presence of gravitational waves, this light level modulates proportionally to the gravitational wave amplitude h_{GW}.

interferometer), then we get a strong local oscillator to beat the signal field with, thus giving a linear signal in the differential arm length. A simpler way to look at this is to simply Taylor series expand Eq. 5.3 around a DARM offset such that $L_{\text{D}} = \Delta L + L h_{\text{GW}}$:

$$P_{\text{AS},\Delta L} = P_{\text{in}} sin^2(2k\Delta L) + 2kLh_{\text{GW}}P_{\text{in}} sin(4k\Delta L) \qquad (5.5)$$

Thus we get a linear response in gravitational wave signal at this offset point on top of some light $P_{\text{in}} sin^2(2k\Delta L)$ that will always be present there. This scheme is currently employed in Advanced LIGO and is commonly referred to as the DC readout scheme. Note that in practice, the DARM signal is suppressed by the locking loop and we read out the signal by extracting the information from the error signal and control signal in the loop. See Sec.9.2.5 for how this is done.
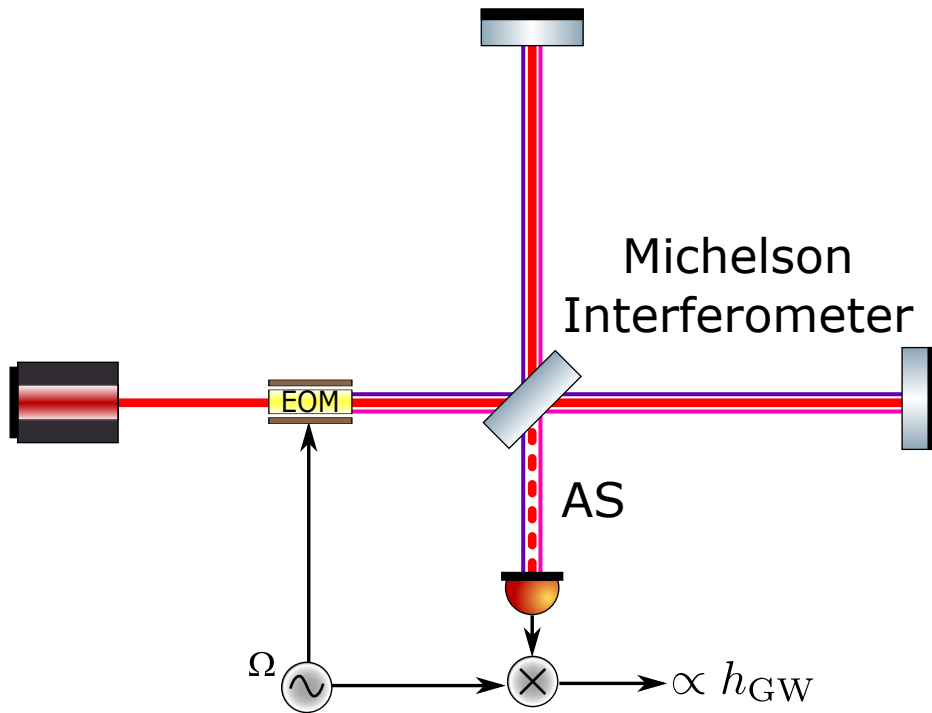
Figure 5.3: Simplified schematic of RF readout of Michelson Interferometer. Incident laser is phase modulated at an RF frequency Ω. While the carrier light destructively interferes at the AS port, the sidebands do not get cancelled completely due to macroscopic differential length difference, Schnupp Asymmetry. The sidebands thus sense the electric field generated in AS port due to gravitational wave. The signal comes at the RF frequency Ω and is linearly proportional to the gravitational wave amplitude h_{GW}.

5.1.2 RF readout

Just like there is PDH technique to utilize RF sidebands to lock a cavity at resonance instead of using offset locking, a similar technique is available to lock the DARM using RF sidebands to true dark point of the interferometer. Assume an RF angular frequency (Ω) phase modulation is applied to the input laser to the interferometer. For simplicity, we'll focus only on first-order sidebands. Thus input electric field to the interferometer is now:

$$E_{\text{in}} = E_{\text{c}} + E_{\text{s}}(ie^{i\Omega t} + ie^{-i\Omega t}) \tag{5.6}$$

Here, the 'c' subscript is for the carrier field, and 's' subscript is for the sideband field. Utilizing Eq. 5.2 the electric field at the anti-symmetric port is given by:
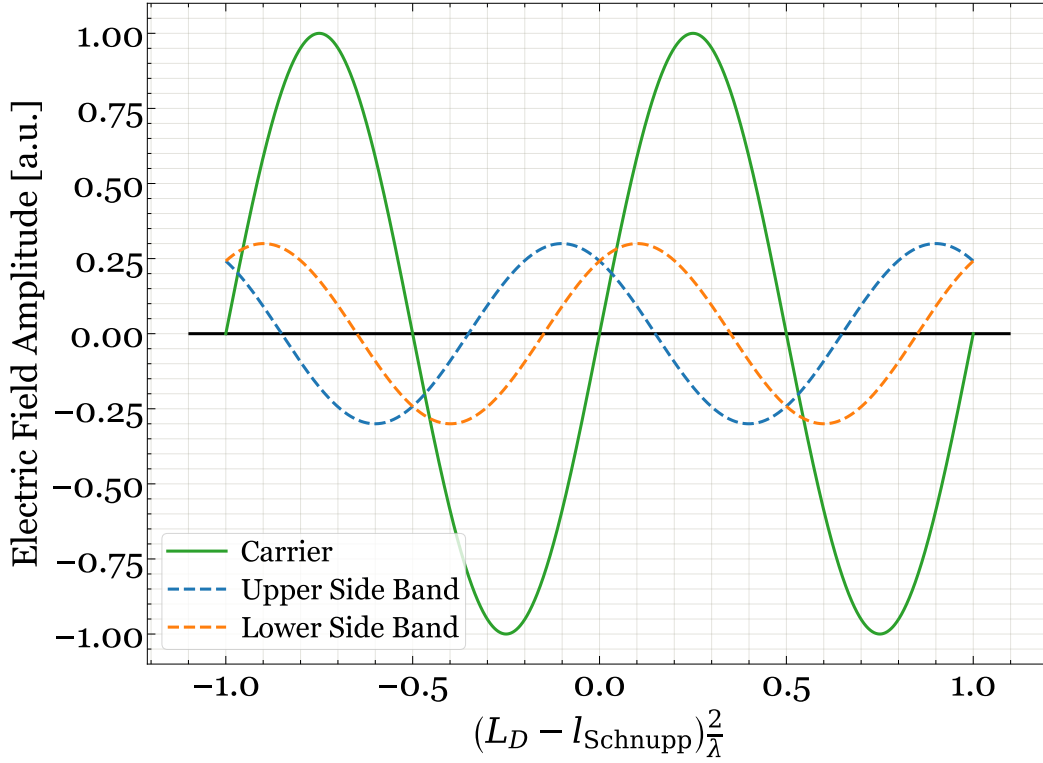
Figure 5.4: Electric field amplitudes at carrier and sideband frequencies at AS port of michelson interferometer. If the differential arm length has a macroscopic offset of $n\frac{\lambda}{4}$, then the sidebands do not become zero at the dark point of carrier. Any fluctuations in DARM length L_D around zero beat with strong sideband fields creating a signal at the sideband frequency at AS port. Note that the carrier field at AS port is $\pi/2$ phase shifted with respect to carrier at the input. Thus the beats with the two sidebands add up.

$$
\begin{aligned}
E_{AS} =& iE_c e^{-i2kL_C}\frac{e^{i2kL_D}-e^{-i2kL_D}}{2} \\
& - E_s e^{i\Omega t}e^{-i2k_+L_C}\frac{e^{i2k_+L_D}-e^{-i2k_+L_D}}{2} \\
& - E_s e^{-i\Omega t}e^{-i2k_-L_C}\frac{e^{i2k_-L_D}-e^{-i2k_-L_D}}{2}
\end{aligned}
\tag{5.7}
$$

where $k = 2\pi/\lambda_c = \omega_c/c$, $k_- = (\omega_c - \Omega)/c = k - \delta k$, and $k_+ = (\omega_c + \Omega)/c = k + \delta k$. ω_c is the carrier optical angular frequency. Further, let's assume that the interferometer is at the dark point so that $2kL_D = n\pi + \phi_{GW}$ where ϕ_{GW} is the small phase offset between the two arms due to gravitational wave signal, and $n \in \mathbb{Z}$. Fig. 5.4 shows the carrier and sideband electric fields at the AS port. If we place an RF photodiode at the AS port and we focus on the signals oscillating at the modulation frequency of Ω:

$$P_{\text{AS},\Omega} = 2\text{Re}\Big[\Big(iE_c e^{-i2kL_C}\frac{e^{i2kL_D}-e^{-i2kL_D}}{2}\Big)\Big(-E_s e^{i\Omega t}e^{-i2k_+ L_C}\frac{e^{i2k_+ L_D}-e^{-i2k_+ L_D}}{2}\Big)^*$$
$$+\Big(iE_c e^{-i2kL_C}\frac{e^{i2kL_D}-e^{-i2kL_D}}{2}\Big)^*\Big(-E_s e^{-i\Omega t}e^{-i2k_- L_C}\frac{e^{i2k_- L_D}-e^{-i2k_- L_D}}{2}\Big)\Big]$$
$$= -\frac{1}{2}E_c E_s \text{Re}\big[ie^{i2\delta k L_C - i\Omega t}\Big(e^{-i2\delta k L_D}+e^{+i2\delta k L_D}-e^{-i2(2k+\delta k)L_D}-e^{i2(2k+\delta k)L_D}\Big)$$
$$- ie^{i2\delta k L_C - i\Omega t}\Big(e^{-i2\delta k L_D}+e^{+i2\delta k L_D}-e^{-i2(2k-\delta k)L_D}-e^{i2(2k-\delta k)L_D}\Big)\big]$$
$$= -\frac{1}{2}E_c E_s \text{Re}\big[ie^{i2\delta k L_C - i\Omega t}$$
$$\Big(-e^{-in\pi\frac{\delta k}{k}-i2\phi_{\text{GW}}}-e^{+in\pi\frac{\delta k}{k}+i2\phi_{\text{GW}}}+e^{+in\pi\frac{\delta k}{k}-i2\phi_{\text{GW}}}+e^{-in\pi\frac{\delta k}{k}+i2\phi_{\text{GW}}}\Big)\big]$$

$$(5.8)$$

Note that we ignored products like $\frac{\delta k}{k}\phi_{\text{GW}}$ as it is the gravitational wave phase shift suppressed further by the ratio of RF frequency to the optical frequency. Demodulating this signal at Ω with a phase of $\pi/2 - 2\delta k L_C$ will give:
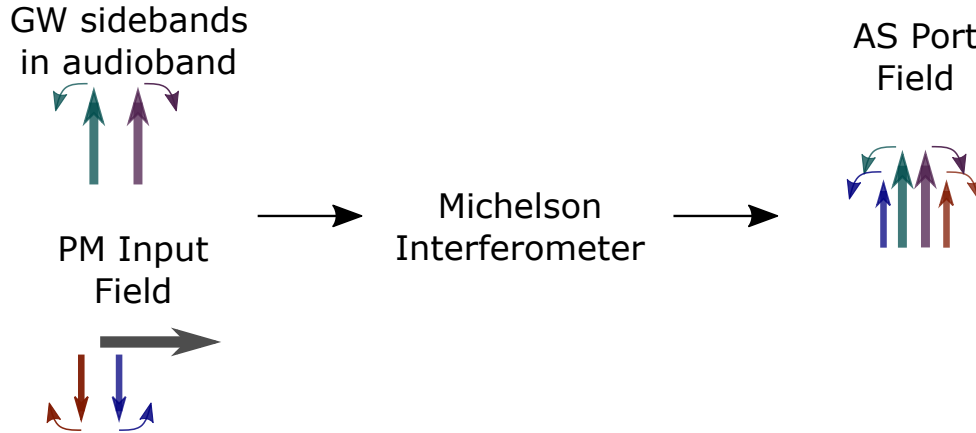
Figure 5.5: When phase modulated input beam interacts with the Michelson interferometer, the carrier beam is rotated by $\pi/2$ in both AS and REFL ports. The amplitude of the carrier field is proportional to sine of differential arm length difference L_D at the AS port and cosine of the same at REFL port. Near lock point, carrier field does not show up in the AS port but any phase modulations in carrier field inside the interferometer due to gravitational waves show as phase sidebands at audio frequency at the AS port. The RF sidebands still appear at the AS port due to Schnupp asymmetry and thus sample the gravitational wave signal.

$$P_{\text{AS},\Omega,Q} = -\frac{1}{2}E_\text{c}E_\text{s}\text{Re}[ie^{i\pi/2}$$

$$\left(-e^{-in\pi\frac{\delta k}{k}-i2\phi_{\text{GW}}} - e^{+in\pi\frac{\delta k}{k}+i2\phi_{\text{GW}}} + e^{+in\pi\frac{\delta k}{k}-i2\phi_{\text{GW}}} + e^{-in\pi\frac{\delta k}{k}+i2\phi_{\text{GW}}}\right)]$$

$$= -E_\text{c}E_\text{s}\left(cos(n\pi\frac{\delta k}{k} + 2\phi_{\text{GW}}) - cos(n\pi\frac{\delta k}{k} - 2\phi_{\text{GW}})\right)$$

$$= 2E_\text{c}E_\text{s}sin(n\pi\frac{\delta k}{k})sin(2\phi_{\text{GW}})$$

$$(5.9)$$

Since we have a choice on what value of n to use, we can choose it to our advantage. If we choose n such that $n\pi\frac{\delta k}{k} = (4m+1)\frac{\pi}{2}$ where $m \in \mathbb{Z}$, then we would maximize the sensitivity of the signal. Note that the minimum macroscopic arm length difference that suffices this for a $\sim$ 50 MHz RF sideband is roughly 1.5m. This asymmetry is known as Schnupp asymmetry. In practice, the Schnupp asymmetry is smaller than this number, which only reduces the sensitivity to ϕ_{GW} slightly. Thus the demodulated signal in one quadrature is directly proportional to the phase shift due to a gravitational wave:

$$P_{\text{AS},\Omega,Q} \propto \phi_{\text{GW}} \qquad (5.10)$$

This method allows one to truly remain at a dark point while being linearly sensitive to the gravitational wave signal. Fig. 5.5 shows the phasor diagram representation of gravitational waves audio sidebands entering the Michelson interferometer with the input phase modulated field and how the sidebands then sample the gravitational wave signal at the AS port.

5.2 Noise couplings and limitations of the current readout methods

While at first glance, the RF readout scheme seems to have achieved all objectives we originally had for reading out the DARM strain at the true dark point of the interferometer, in our simplification and idealization of the layout, we have missed some important limitations with this approach. Several detailed studies are present on the topic of using RF readout in [38–40], where more shot noise contributions were found to be present. Parallel studies presented in [41–43] proposed ways to possibly perform quantum non-demolition measurements beating the standard quantum limit (SQL). However, when Buonanno et al. [44] analyzed the benefits of the RF readout scheme in the case of modern interferometers that required power recycling, and the additional shot noise contributions, it was found that

the RF detection scheme would always be beaten by the DC readout scheme, and any measurement window beyond SQL would be short bandwidth and modest improvements at best. In the real implementation of the RF readout, more issues were found[45]. Since the RF sidebands do not resonate within any of the cavities, they reach the AS port with different spatial modes and excess power in higher-order modes. This makes the detection poor and difficult to handle without photodiodes getting saturated by the higher-order modes.

This directed the efforts in second-generation gravitational wave detectors to use DC readout with offset locking[46, 47]. The output of the interferometer was sent through an output mode cleaner (OMC) to get rid of the RF sidebands at the GW detection photodiode which operates at DC. Note that the RF sidebands are still used and important for controlling the other 4 degrees of freedom in a dual recycled Fabry-Pérot Michelson interferometer. Only the DARM readout is kept at DC. Further optimizations led to the discovery of gravitational waves[1] and further noise coupling studies were conducted to push the noise floor of the detectors further down.

In particular, it was found in [48] that length fluctuations of the signal recycling cavity (SRCL), induce phase modulations to the carrier field present on the antisymmetric port side of the beamsplitter. This carrier field is present because a DARM offset is created for the DC readout scheme. The phase modulations on the antisymmetric port side of the beamsplitter become amplitude modulations on the symmetric side of the beamsplitter, just like how the gravitational wave phase modulations in the interferometer become amplitude modulations on the other side of the beamsplitter. The amplitude modulations are on top of a very strong circulating field in the arm cavities, that induce motions in the suspended mirrors due to radiation pressure effects. And from there, this noise couples back to the DARM readout port as phase modulation since the motion of mirrors is indistinguishable from gravitational wave modulations in the cavities.

This means that in the DC readout scheme, due to the presence of the DARM offset, the SRCL length noise couples into the GW detection signal. Since the SRCL length noise can be measured by using the error and control signals of SRCL control loops, this noise is subtracted in online feedforward from the DC readout signal[34], reducing the noise coupling significantly. However, with plans to increase the circulating arm power in the future, we can not keep relying on this feedforward technique to come to our rescue while using the DC readout method[36].

The presence of DARM offset also negatively affects other auxiliary control loops, like the angular stabilization loops that use wavefront sensing of higher order modes in the antisymmetric port get corrupted by the presence of TEM00 mode carrier light. The carrier light also back-scatters from the OMC and the chamber walls also induce environmental noise couplings to the GW detector, which are harder to quantify and are not consistently present at the same level.

Chapter 6

BALANCED HOMODYNE READOUT FOR GRAVITATIONAL WAVE DETECTOR

Fritschel et al. [37] proposed using Balanced Homodyne Detection (BHD) as an alternative to the DC readout scheme in gravitational wave detectors, primarily to tackle noise couplings associated with DC readout scheme, and to open up possibilities of using potential QND schemes with squeezed states of lights such as variational readout[42] and speedmeter readout[49]. The idea of performing balanced homodyne detection is of course not new, but implementing it in a suspended optical layout poses new control challenges that need to be ironed out. To this end, the 40m prototype at Caltech was upgraded to have a BHD readout port, and we have been testing it in various detector layouts. In this chapter, we will go through how a balanced homodyne readout scheme works, what the advantages are over previously tried schemes, and what possible drawbacks there are on implementing it.

6.1 Mathematical formalism

The idea of BHD is simple: just like the DC readout scheme, we want to bring a strong local oscillator to beat with the gravitational wave signal field. Instead of using a DARM offset to get this field locally, we can pick off this local oscillator field before the laser enters the Michelson interferometer, and then overlap it with the antisymmetric (AS) port output field on a beamsplitter. Fig. 6.1 shows a simplified schematic for this scheme.

Let's begin the AS port electric field presented in Sec.5.1.

$$E_{\text{AS}} = iE_{\text{in}}e^{-i2kL_{\text{C}}}\frac{e^{i2kL_{\text{D}}} - e^{-i2kL_{\text{D}}}}{2} = -2E_{\text{in}}e^{-i2kL_{\text{C}}}sin(2kL_{\text{D}}) \qquad (6.1)$$

The local oscillator (LO) field is at the same optical frequency as the carrier field as it is picked off from the input of the Michelson interferometer. However, since the LO field is traveling a different optical path than the AS field, it can have a different phase than the carrier field. So the local oscillator field is given by:
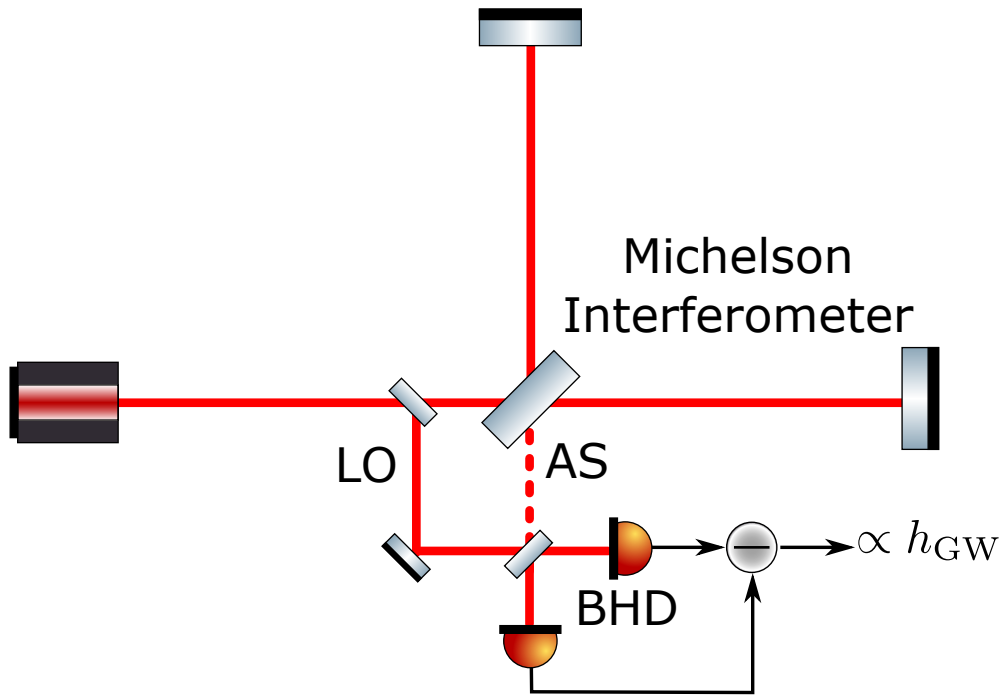
Figure 6.1: Simplified schematic of Balanced Homodyne Detection with Michelson Interferometer. A copy of the input field is picked off as local oscillator (LO) before it enters the interferometer. This beam is redirected and mixed with the antisymmetric (AS) port beam of the interferometer. The two outputs of the beamspltter are read on balanced photodiodes producing equal photocurrent for equal amount of light on them. The two photocurrents are subtracted to get the contribution from the product of LO and AS fields which is proportional to the gravitational wave strain sensed by the interferometer.

$$E_{\text{LO}} = E_{\text{in}}e^{-i\phi_{\text{LO}}} \tag{6.2}$$

When these two fields overlap with each other on a beamsplitter, the two output fields from the beam splitter are (assuming the beamsplitter is exactly 50:50):

$$
\begin{aligned}
E_1 &= \frac{1}{\sqrt{2}}E_{\text{LO}} + \frac{i}{\sqrt{2}}E_{\text{AS}} \\
E_2 &= \frac{i}{\sqrt{2}}E_{\text{LO}} + \frac{1}{\sqrt{2}}E_{\text{AS}}
\end{aligned}
\tag{6.3}
$$

Assuming equal transimpedance of the photocurrents on the two photodiodes are:

$$P_1 = \frac{T_I}{2}\left(|E_{\text{LO}}|^2 + |E_{\text{AS}}|^2 - iE_{\text{LO}}E_{\text{AS}}^* + iE_{\text{LO}}^*E_{\text{AS}}\right)$$
$$P_2 = \frac{T_I}{2}\left(|E_{\text{LO}}|^2 + |E_{\text{AS}}|^2 + iE_{\text{LO}}E_{\text{AS}}^* - iE_{\text{LO}}^*E_{\text{AS}}\right) \tag{6.4}$$

When the photocurrent from two photodiodes is subtracted, we get the following:

$$
\begin{aligned}
P_{\text{BHD}} &= iT_I\left(E_{\text{LO}}^*E_{\text{AS}} - E_{\text{LO}}E_{\text{AS}}^*\right)\\
&= -2T_I|E_{\text{in}}|^2\text{Im}[-2e^{i\phi_{\text{LO}}}e^{-i2kL_{\text{C}}}sin(2kL_{\text{D}})]\\
&= 4T_I|E_{\text{in}}|^2 sin(\phi_{\text{LO}} - 2kL_{\text{C}})sin(2kL_{\text{D}})
\end{aligned} \tag{6.5}
$$

During operation, when the laser is locked to the CARM mode, $2kL_{\text{C}} = 2n\pi$ where $n \in \mathbb{Z}$. For operating near the dark point in AS port, the gravitational wave signal h_{GW} will appear in DARM as $L_{\text{D}} = m\frac{\pi}{k} + L_{\text{C}}h_{\text{GW}}$, the the BHD output becomes:

$$P_{\text{BHD}} \approx 4T_I|E_{\text{in}}|^2 sin(\phi_{\text{LO}})2kL_{\text{C}}h_{\text{GW}} \tag{6.6}$$

Thus, in the ideal case, we get the maximum linear response of the BHD output to the gravitational wave signal for the choice of $\phi_{\text{LO}} = \pi/2$. Note that this expression is indeed equivalent to the DC readout expression when $\phi_{\text{LO}} = \pi/2$ but, there is no DC offset in the readout signal. The absence of DC light reduces the shot noise on the detector. Additionally, we have an extra free parameter in tuning the readout, the homodyne phase angle ϕ_{LO} which can be adjusted to read out different quadratures for quantum benefits if required.

6.2 Benefits of BHD

6.2.1 Zero DARM offset

As is the motivation for finding the new readout scheme, having no DARM offset is one of the biggest advantages of using this scheme. No intentional carrier light at the antisymmetric port results in negligible coupling of SRCL length noise to the gravitational wave signal as we saw in Sec.5.2. Further, this removes the requirement of using online feedforward noise cancellation which would have limited the improvement in circulating arm power in future generation detectors.

No carrier light at the dark port also means no back-scatter light noise from OMC or the chamber walls, significantly reducing the excess noise contributions that are hard to quantify and cancel in online subtraction. The angular stabilization loops for the arm cavities that rely on wavefront sensing of higher order modes at

the antisymmetric port also have less TEM00 light falling on them, which would improve the stability of these loops. This would also reduce the noise coupled through an angle-to-length coupling of arm cavity mirrors' angular fluctuations.

6.2.2 Tunability of homodyne phase angle

As we saw in Sec.5.1.1, the DC readout method is also a homodyne measurement but with a fixed local oscillator phase angle and no common mode rejection. This becomes an issue if the Michelson interferometer is not ideal which is always the case in real implementations. There is a contrast defect present in the interferometer due to unequal losses in the two arm cavities. This means that a small amount of carrier light leaks through the Michelson as the destructive interference at the beamsplitter is not completely destructive. This leakage light is different from the one that is generated by the DARM offset as it is not a result of different arm lengths of the interferometer is present even when DARM offset is zero (that means even in case of RF readout of BHD readout schemes.) The contrast defect carrier light is however in orthogonal quadrature from the GW signal and if we truly read the signal at $90°$ phase to the contrast defect light, we are unaffected by this light. However, in the case of the DC readout scheme, due to the presence of DARM offset, the phase of the carrier light (measured from GW signal quadrature) present at the antisymmetric port is given by $tan^{-1}\left(\sqrt{\frac{P_{CD}}{P_{DARM}}}\right)$ where P_{CD} is the contrast defect power level and P_{DARM} is the power released in antisymmetric port intentionally by creating a DARM offset.

This also means that the ideal readout quadrature of the GW signal shifts because of the presence of the contrast defect. For example, at LIGO Livingston Observatory, the contrast defect power was measured to be 1 mW while DARM offset produces 25 mW. This means the ideal readout homodyne phase angle is $\approx 11°$. This means that DC readout sensitivity is reduced by a factor of $cos^2(11°) \approx 0.96$, i.e. 4% loss in signal sensitivity. This is further aggravated by the fact that the contrast defect does not remain constant and changes with the thermal state of the interferometer resulting in fluctuating sensitivity and possible systematics in the calibration of the detector.

The BHD method does not suffer from the effects of contrast defect as any light measured due to contrast defect gets common mode rejected in taking the difference between the two BHD photocurrents. Further, the LO phase angle can be tuned to whatever quadrature the signal is present the most. Ideally, though, this angle

would be just zero, and one would need to keep the LO phase locked at this point. In the future, if a new technique requires signal readout in different quadratures, like variational readout[42] or speedmeter[49] techniques, this angle is a free parameter in the BHD scheme.

6.3 Possible drawbacks of BHD implementation

Despite the benefits of BHD, it is not a simple upgrade to the optical layout of the present gravitational wave detectors, and hence is worth exploring, if the drawbacks of implementing the path changes are worth the risk, time, and energy it would take.

Since a local oscillator path needs to be set up, this means installing new suspended optics in the interferometer, that pick off light from the power recycling cavity, and direct it towards the anti-symmetric port for mixing with the AS beam. At least two suspended optics are required in this path to be able to steer the beam so that good mode matching is achieved with the AS beam. The AS beam itself would require at least two suspended additional steering mirrors after the signal recycling cavity to get good mode matching. This means at least four more suspensions to control, damp pendulum and violin modes, and set up associated electronics.

Along with this, the LO and AS beams must remain mode matched always and the homodyne phase angle must be kept locked to a required value. This means additional length and angular sensing and control schemes. The current OMC at the antisymmetric port will need to be removed and replaced with two OMCs at the output of the BHD beamsplitter.

While these are challenging experimental projects, people at LIGO have been doing such projects long enough that the expertise of the collaboration is an advantage in rolling out such commissioning projects. But the risk lies in the amount of time and any irreversibility associated with the upgrade. If all these changes are made, the ability to use the existing DC readout scheme will get heavily curtailed due to two reasons. First, the local oscillator beam would be required to be blocked from coming to the DC readout port with a beam dump that does not backscatter any light. Secondly, due to the BHD beamsplitter, the light would get split into two photodiodes, increasing the dark noise for the DC readout scheme. In fact, due to different amounts of light that would fall on the readout photodiodes between the BHD scheme and the DC readout scheme, it might be the case that the photodiodes are not optimized for the power level that falls on them in the DC readout scheme. This almost certainly means that LIGO would take a large hit in detection sensitivity

if the BHD upgrade does not work. This lack of backward compatibility is certainly a big drawback in implementing an upgrade of this scale.

For this reason, LIGO Labs Caltech experimental group is prototyping the BHD upgrade at the 40m prototype, and performing the research required for all the length and angular sensing and controls of the new optical paths. I'm happy to report in the next chapter that the preliminary results are promising and optimistic.

Chapter 7

BHD IMPLEMENTATION AND TESTING AT CIT 40M

In this chapter, I'll give a brief description of the 40m prototype at Caltech and how we upgraded it to implement the first-ever suspended interferometer with Balanced Homodyne Detection (BHD). After going through the new optical layout and photodiodes, we'll discuss how the local oscillator phase angle is controlled. This control enables the use of the BHD port for locking the interferometer in different configurations. Finally, I'll report some preliminary results on MICH and FPMI locking and its comparison with the RF readout locking scheme that has been conventionally used at 40m.

7.1   The 40m prototype

The 40m prototype at Caltech (CIT 40m) was constructed to have a 1:100 scaled-down version of the LIGO observatory sites at Hanford and Livingston. Chapter 4 of Jennifer Driggers' thesis[50] gives a thorough description of this large-scale laboratory. I would redirect readers there for more details on any particular subpart not covered in this brief description. Fig. 7.1 shows the up-to-date 40m prototype optical layout schematic until 2021 when the upgrade work to install BHR started. At 40m, the main laser (2 W, 1064nm Nd:YAG NPRO) first goes through a monolithic triangular cavity known as Pre-Mode Cleaner (PMC). PMC is locked to the laser through a PZT attached to its end mirror. This cleans the raw laser output from the laser head and gets rid of any spatial higher-order modes at the carrier frequency. The laser is then locked to a suspended triangular cavity known as the Mode Cleaner cavity which serves the purpose of a reference cavity at 40m. The laser is actuated at its PZT and through an in-line EOM to get a locking bandwidth of about 200 kHz. The laser crystal temperature is controlled through a Python PID controller to keep the PZT actuation signal from saturating due to low-frequency drifts. The mode cleaner also serves as a point of low-frequency actuation for interferometer locking.

The transmitted laser from the mode cleaner goes through an in-vacuum Faraday isolator (IFI) and enters the interferometer through folded power recycling cavity made out of PRM, PR2, and PR3. For all the experiments mentioned in this thesis, we did not use power recycling by keeping the PRM misaligned due to which we suffered with 95% loss in transmission through PRM. The light splits at the
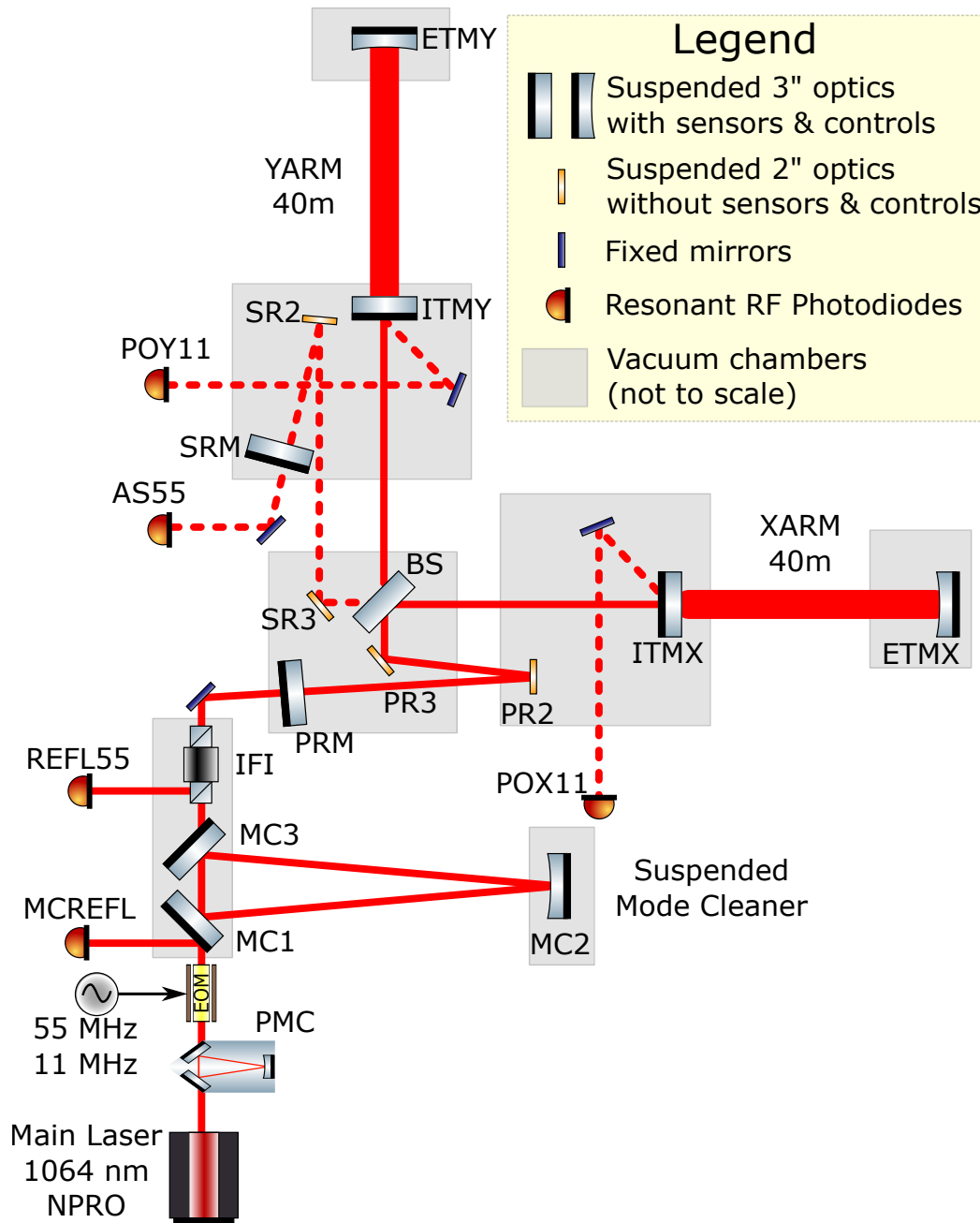
Figure 7.1: Simplified schematic of optical layout at CIT 40m before the BHD upgrade in 2021. The figure shows important optics the laser throughs at 40m. Auxiliary lasers, pick-off port (POP), DC photodiodes, quadrant photodiodes, and wavefront sensing photodiodes have been omitted for clarity. Actual positions of the photodiodes might be different from shown.

suspended beam splitter and goes towards the two arms. At 40m, we call the arm in the transmission of the BS, Y arm, and the one in reflection is called the X arm (note

the difference from site conventions). Each arm is a Fabry-Pérot cavity made with two suspended optics, Input Test Mass (ITM), and End Test Mass (ETM). Together, they form an over-coupled cavity with a finesse of about 400. After reflection from the cavities, the laser recombines at the beamsplitter where part of it goes back towards the exit port of the IFI where it is collected in REFL photodiodes (REFL11, REFL33, REFL55, REFL165). The other part, the AS beam enters the folded signal recycling cavity made with SR3, SR2, and SRM. Again, in all experiments mentioned in this thesis, signal recycling or extraction was not used by keeping SRM misaligned due to which 90light is rejected. After the signal recycling cavity, the AS beam is collected at AS photodiodes (AS55, AS110).

7.2 The BHD upgrade

In November 2021, the CIT 40m was vented for a large-scale upgrade to its optical layout to add a BHD readout port. Fig. 7.2 shows the final optical layout of CIT 40m after the upgrade was completed. This is only the first phase of the upgrade with in-vacuum Output Mode Cleaners due to be tested in phase II.

7.2.1 PR2 and PR3

The power recycling cavity at 40m used to have only the PRM equipped with OSEM sensors and coil actuators to control the position and alignment. PR2 and PR3 were suspended with small towers to passively isolate them from seismic noise. Further PR2 was a highly reflective mirror with a wrong radius of curvature which caused issues with power recycling cavity stability (See Appendix D.2 in Gautam Venugopalan's thesis[51]). Since BHD requires a local oscillator beam extracted before the laser enters the Michelson interferometer, it was decided to replace PR2 with a more transmissive mirror (~2%) mirror and place it in a small suspension tower (small with respect to the LIGO site's large suspension towers) with OSEM sensors and actuators. PR3 was upgraded into the sensed and controllable suspension stage as well giving us full steering control to the input of the interferometer. See appendix A for details on how each suspension was prepared.

7.2.2 SR2 and removing SR3

For the BHD upgrade, it was decided to convert the Resonant Sideband Extraction (RSE) configuration of the signal recycling cavity at 40m to a Signal Recycling (SR) configuration. This was done to enable possible experimentation and measurement of ponderomotive squeezing (see Chapter 4 of Gautam Venugopalan's thesis[51]).
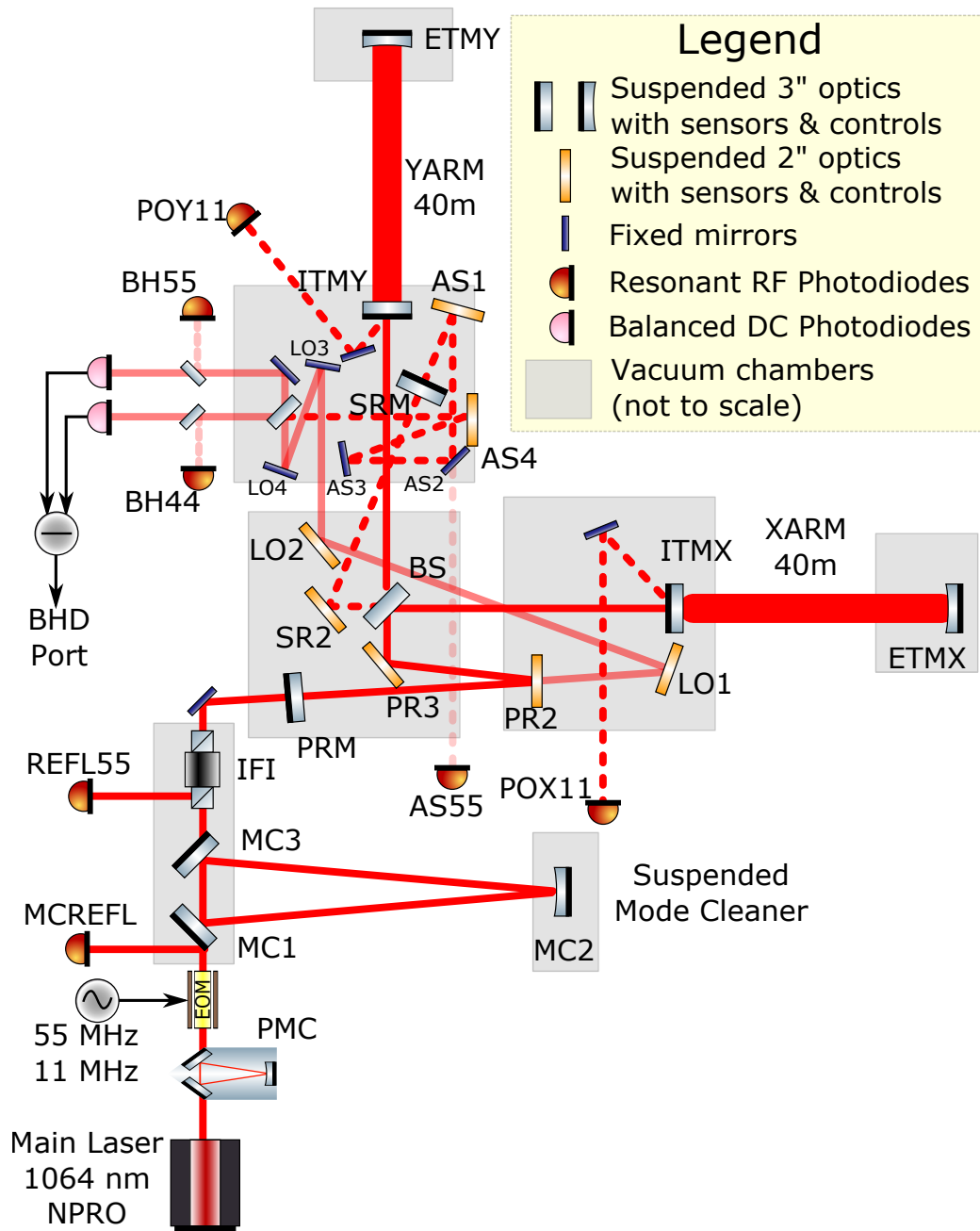
Figure 7.2: Simplified schematic of optical layout at CIT 40m after the BHD upgrade phase I in 2022. PR2, PR3, and SR2 were upgraded to SOS with OSEM sensors and coil actuators. New suspended optics, LO1, LO2, AS1, and AS4 were installed. The balanced homodyne detection port was setup in ITMY chamber. Actual positions of the photodiodes might differ.

This required removing SR3 and placing single folding mirror SR2 where SR3 used to be. SR2 steers the light from the antisymmetric port of the beamsplitter towards

the ITMY chamber.

7.2.3 LO1, LO2, AS1, and AS4

The transmitted power from PR2 is steered for the local oscillator beam by another suspended optic right next to ITMX, called LO1. This optic redirects the LO beam to another new suspension LO2 on the beam splitter chamber that steers the beam toward the BHD setup in the ITMY chamber. Here there are two fixed steering mirrors, LO3 and LO4, which direct the LO beam toward the BHD beam splitter (BHDBS). LO3 and LO4 are curved mirrors to perform mode matching with the AS beam at BHDBS. The AS beam is collected from SRM by the new suspended optic AS1. The AS beam goes through a fixed beam splitter AS2 where 10% of light is allowed to go through while the remaining goes towards another fixed optic AS3 on the ITMY chamber. AS3 redirects the beam toward the new suspended optic AS4. Both AS3 and AS4 are curved mirrors to allow for mode matching with the LO beam at the BHDBS. The 10% transmitted AS beam from AS2 is sent to the RF photodiode AS55 for keeping the option of using the RF readout method (see Sec.5.1.2) as well.

7.2.4 Suspension controls and diagnostics

While the suspensions greatly reduce the seismic noise at frequencies above the pendulum resonance of the suspension, the high Q of the pendulum resonances means that the suspensions can be easily excited at around 1 Hz through seismic or terrestrial noise. To avoid prolonged ringing of the suspensions at these resonances, the pendulum resonances are damped actively around the 1 Hz frequency region. The new suspensions required a new set of sensor and control electronics to be installed.

Fig. 7.3 shows the suspension control loop implemented for each suspension. The OSEM sensor signals are read in a satellite amplifier which converts the OSEM photodiode current to voltage. This signal is low passed by anti-aliasing filters at 8 kHz and then read by ADC at a 16 kHz sampling rate. In the digital domain, we take linear combinations of the 5 OSEM sensors to create 4 physical degrees of freedom of motion sensed by them, namely, Position, Pitch, Yaw, and Side motion. And we get a fifth orthogonal combination that represents unphysical motion for a rigid body, which we call the null stream or butterfly vector. To identify the correct linear combinations (the input matrix) required to take the information from OSEM basis to the physical DOF basis, we do a free swing test. During this test, the actuators to
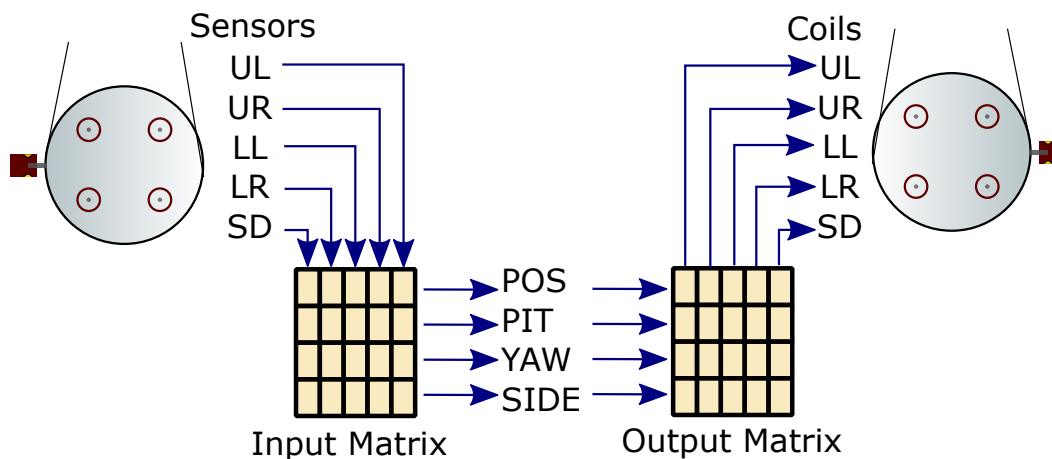
Figure 7.3: Sensing and control for suspension local damping.

the optics are shutoff (keeping any DC actuation still on to ensure the measurement is made near the nominal position of the optic), and then the optic is kicked by giving two 1 second long pulses on one of the face coils. Since the resonances of the optic are all near 1 Hz, these 1 sec-long pulses excite all resonances in the suspended optic. We take the OSEM data during this free swing and look at the power spectrum. We identify the resonance peaks associated with each degree of freedom based on the closeness to theoretical resonance values and create an input matrix that separates the resonances in individual outputs.

The separated signals for physical degrees of freedom are then amplified and low passed through the feedback filters. Coil actuation signals are created through these filtered signals using another output matrix which uses the coils to actuate on particular physical degrees of freedom. The coil outputs are sent through DAC to an anti-imaging filter (8 kHz low pass filter), and then to the coil driver circuits which drive current through the OSEM coils to actuate on the magnets.

7.2.5 Photodiodes

Four new photodiodes were installed for this upgrade. Two of the photodiodes are meant to read the BHD signal at DC. These are Laser Components IG17X3000G1i receiving most of the BHD output light. Pick-off light from the two outputs paths of the BHDBS is sent to two custom-built RF photodiodes, resonant at 44 MHz and 55 MHz. These were named BH44 and BH55 respectively. Each resonant RF photodiode output is demodulated in both quadratures and read through DAC for sensing and control purposes. Part of the pick-of light is also sent to a CCD camera (not shown in the figure) to help in aligning the LO and AS beams to overlap with

each other.

7.3 Local oscillator phase locking

As we saw in Eq. 6.6, the LO phase angle sets the sensitivity of BHD and it is a free parameter since the path length of LO beam can move independently of the carrier field in the interferometer. It is thus important to control this phase angle and keep it locked to the desired point, which is $\pi/2$ for conventional use of BHD. We looked into the following methods that can be used to lock the LO phase angle.

7.3.1 Single RF demodulation

As we saw in Sec.5.1.2, the phase modulation sidebands of the input field are present in the AS port. If we pick off a part of one of the output beams of the BHDBS, we get an overlapped field between the AS beam with sidebands and the LO beam. This overlapped beam of AS sidebands and the LO beam would be available even if the output of BHDBS is sent through output mode cleaners, in the reflected field from them. We picked off this beam in our experiment at CIT 40m and sent it to resonant RFPD, named BH55. This photodiode is resonant at 55 MHz. Let's look at the power on this photodiode that oscillates at the sideband frequency:

$$
\begin{aligned}
P_{BH55} &= \left(-iE_{\text{LO}}E_{\text{AS}}^* + iE_{\text{LO}}^*E_{\text{AS}}\right) \\
&= 2\text{Re}[iE_{\text{LO}}^*E_{\text{AS}}] \\
&= 2\text{Re}[iE_{\text{c}}e^{i\phi_{\text{LO}}}\left(-iE_{\text{s}}e^{i\Omega t - i2k_+L_{\text{C}}}sin(2k_+L_{\text{D}}) - iE_{\text{s}}e^{-i\Omega t - i2k_-L_{\text{C}}}sin(2k_-L_{\text{D}})\right)] \\
&= 2E_{\text{c}}E_{\text{s}}sin(2\delta kL_{\text{D}})\text{Re}[e^{i(\Omega t - 2\delta kL_{\text{C}} + \phi_{\text{LO}})} - e^{i(-\Omega t + 2\delta kL_{\text{C}} + \phi_{\text{LO}})}]
\end{aligned}
\tag{7.1}
$$

In the last step above, we use operation conditions where the laser is locked to the CARM mode, $2kL_{\text{C}} = 2n\pi$ where $n \in \mathbb{Z}$, thus $e^{-i2k_\pm L_{\text{C}}} = e^{\pm i2\delta kL_{\text{C}}}$. Similarly, at dark point operation $kL_{\text{D}} = m\pi$ where $m \in \mathbb{Z}$, thus $sin(2k_\pm L_{\text{D}}) = sin(\pm 2\delta kL_{\text{D}})$. On demodulation at Ω with demodulation phase angle of $-2\delta kL_{\text{C}}$, we get:

$$
\begin{aligned}
P_{BH55I} &= 2E_{\text{c}}E_{\text{s}}sin(2\delta kL_{\text{D}})\text{Re}[e^{i\phi_{\text{LO}}} - e^{i\phi_{\text{LO}}}] = 0 \\
P_{BH55Q} &= 2E_{\text{c}}E_{\text{s}}sin(2\delta kL_{\text{D}})\text{Re}[e^{i(\pi/2 + \phi_{\text{LO}})} - e^{i(-\pi/2 + \phi_{\text{LO}})}] \\
&= -4E_{\text{c}}E_{\text{s}}sin(2\delta kL_{\text{D}})sin(\phi_{\text{LO}})
\end{aligned}
\tag{7.2}
$$

So, we do have a signal proportional to ϕ_{LO} in one quadrature. But there is a catch here. If this signal is used for locking the LO phase angle, it will lock to $\phi_{\text{LO}} = 0$,

but as we saw in Sec.6.6, we want to lock it to $\pi/2$ otherwise the BHD signal would be zero. So this method cannot be used to lock the LO phase angle. We need the derivative of this signal, so that becomes a cosine function in ϕ_{LO} giving us a zero crossing at $\pi/2$.

	AS Field	LO Field	ϕ_{LO}	BH55 Error Signal	BHD Sensitivity
			$\frac{\pi}{2}$	$+$	$+$
PM Input Field	x		0	0	0
			$-\frac{\pi}{2}$	$-$	$-$
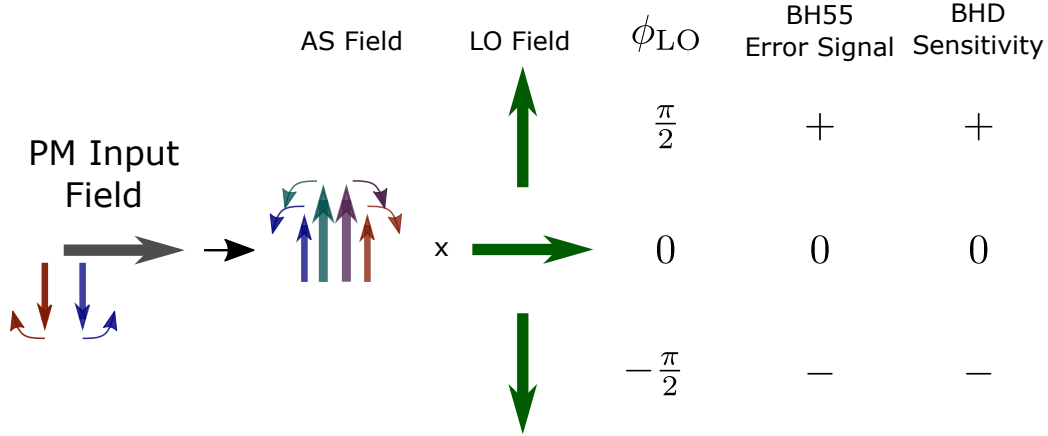
Figure 7.4: Single RF demodulation scheme generates signal from AS RF sideband mixing with LO carrier. For different values of ϕ_{LO}, the signal goes through a zero crossing at $\phi_{LO} = 0$, which means the loop locks at this phase angle. However, BHD sensitivity also goes to zero at this phase angle value because LO field is orthogonal to the GW audio sidebands at the AS port. See Fig. 5.5 to see the propagation of GW signal to AS port.

Fig. 7.4 shows how BH55 error signal has zero crossing at $\phi_{LO} = 0$ through phasor diagram. In practice though, we found that the BHD response of the 40m prototype was non-zero when we locked the LO phase angle with BH55. This probably happens because of a contrast defect in the interferometer. Leakage light at AS port due to contrast defect does not suffer through $\pi/2$ phase shift and since the LO beam also has 55 MHz phase sidebands on it, this leakage AS beam can beat with the LO sidebands at 55 MHz to give a zero-crossing at non-zero ϕ_{LO}.

7.3.2 RF + Audio dither dual demodulation

Since we need the derivative of the BH55 signal, we can dither the LO phase angle by either shaking one of the suspended mirrors in AS beam path, AS1 or AS4, or by shaking one of the suspended mirrors in LO beam path, LO1 or LO2. If the length of LO path (with respect to AS beam path) is modulated at angular frequency Ω_a, then the LO beam would get audio phase modulation sidebands on it:

$$E_{\text{LO},dithered} = E_c e^{-i\phi_{LO}} + iE_{s,a} \left(e^{-i\phi_{LO}+i\Omega_a t} + e^{-i\phi_{LO}-i\Omega_a t} \right) \qquad (7.3)$$

This would affect the Q quadrature of BH55 (using Eq. 7.2) as (only listing terms that are varying at Ω_a):

$$P_{BH55Q,dithered} = 2E_{s,a}E_s sin(2\delta k L_D)\text{Re}[ie^{i(\pi/2+\phi_{LO}+\Omega_a t)} - ie^{i(-\pi/2+\phi_{LO}-\Omega_a t)}] \tag{7.4}$$

We digitally demodulate the BH55Q signal at the audio angular frequency Ω_a, and get:

$$\begin{aligned} P_{BH55Q,I} &= -4E_{s,a}E_s sin(2\delta k L_D)cos(\phi_{LO}) \\ P_{BH55Q,Q} &= 0 \end{aligned} \tag{7.5}$$

Thus the BH55_Q_I signal can be used to lock the LO phase angle, and with this signal the locking point would be $\phi_{LO} = \pi/2$ just like we want.

We tried this method at CIT 40m with partial success. The lock was not very robust, because the noise at audio frequencies is still very high and the length modulation of the beams cause jitter in the angular alignment of LO beam with AS beam on BHDBS. Further, the UGF of the LO phase lock loop is limited by the audio dither frequency, so to get higher bandwidth, the audio dither frequency needs to be higher. But since the optics are suspended, actuation at higher frequencies is suppressed as f^{-2} limiting the loop gain that can be obtained.

7.3.3 Dual RF demodulation

Since we pick off LO beam from the transmission of PR2, the LO beam also has phase modulations on it as were applied to the carrier beam. At CIT 40m, two sets of phase modulations are applied on the input carrier beam, one at 11 MHz, and one at 55 MHz. Just like how the audio phase modulation sidebands get the derivative of the BH55 signal, the 11 MHz sidebands also get the derivative of the BH55 signal, at 44 MHz and 66 MHz. We chose to pick off another beam from another output of BHDBS and sent it to another resonant RFPD BH44 which is resonant at 44 MHz. This way, we do not need to demodulate twice, although we are losing half of the signal in the 66 MHz frequency. Fig. 7.5 shows the error signal zero crossing for this scheme. Note that any contrast defect or DARM offset generating carrier light at AS port does not affect the error signal in this scheme as it beats two RF sidebands with each other.

AS Field	LO Field	ϕ_{LO}	BH44 Error Signal	BHD Sensitivity
		π	$+$	0
		$\frac{\pi}{2}$	0	$+$
		0	$-$	0

PM Input Field

x
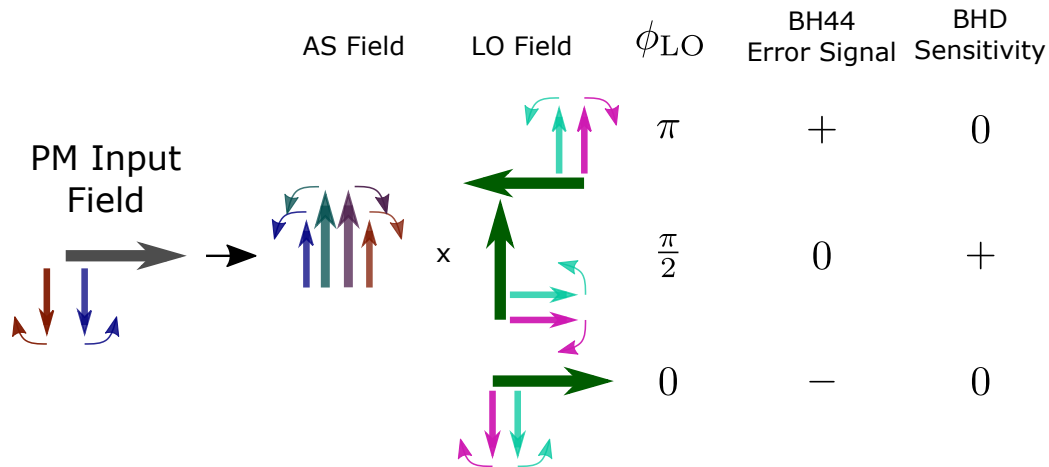
Figure 7.5: Dual RF demodulation scheme generates signal from AS RF sideband mixing with LO RF sideband at another frequency. At 40m, the two frequencies are 11 MHz and 55 MHz. For different values of ϕ_{LO}, the signal goes through a zero crossing at $\phi_{\text{LO}} = \pi/2$, which means the loop locks at this phase angle. This is also the desired phase angle for BHD scheme.

7.3.4 LO Phase control testing

We tested the LO phase control loop in three different configurations. In each configuration, the UGF was set to 50 Hz to have a fair comparison between two methods of locking: single RF demodulation with BH55 and dual RF demodulation with BH44.

Single bounce off ITMX, Mach-Zehnder:

First configuration was Mach-Zehnder between AS beam and LO beam. ITMY, ETMY, and ETMX are misalgined so that there is no michelson interferometer and AS beam is a simple single bounce off of ITMY. Fig. 7.6 shows the OLTF for the two locking methods. We see that with the same feedback filters, we get the same response while using the different sensors. The OLTFs are fitted with the model of the feedback loop. The fitted OLTF are used to compute unsuppressed noise in the loops and shown in the noise budget plot in Fig. 7.7 for this configuration. The unsuppressed noise curves in this configuration set the equality of the two sensors in terms of noise performance because, for a simple Mach-Zehnder configuration, the two sensors are optically equivalent and do not depend on fine-tuning of any other parameter for them to work. The suppressed noise performance is also almost the same: BH55 controlled LO phase has a residual RMS of 0.04 radians when averaged over 1 second in comparison to BH44 controlled LO phase residual noise
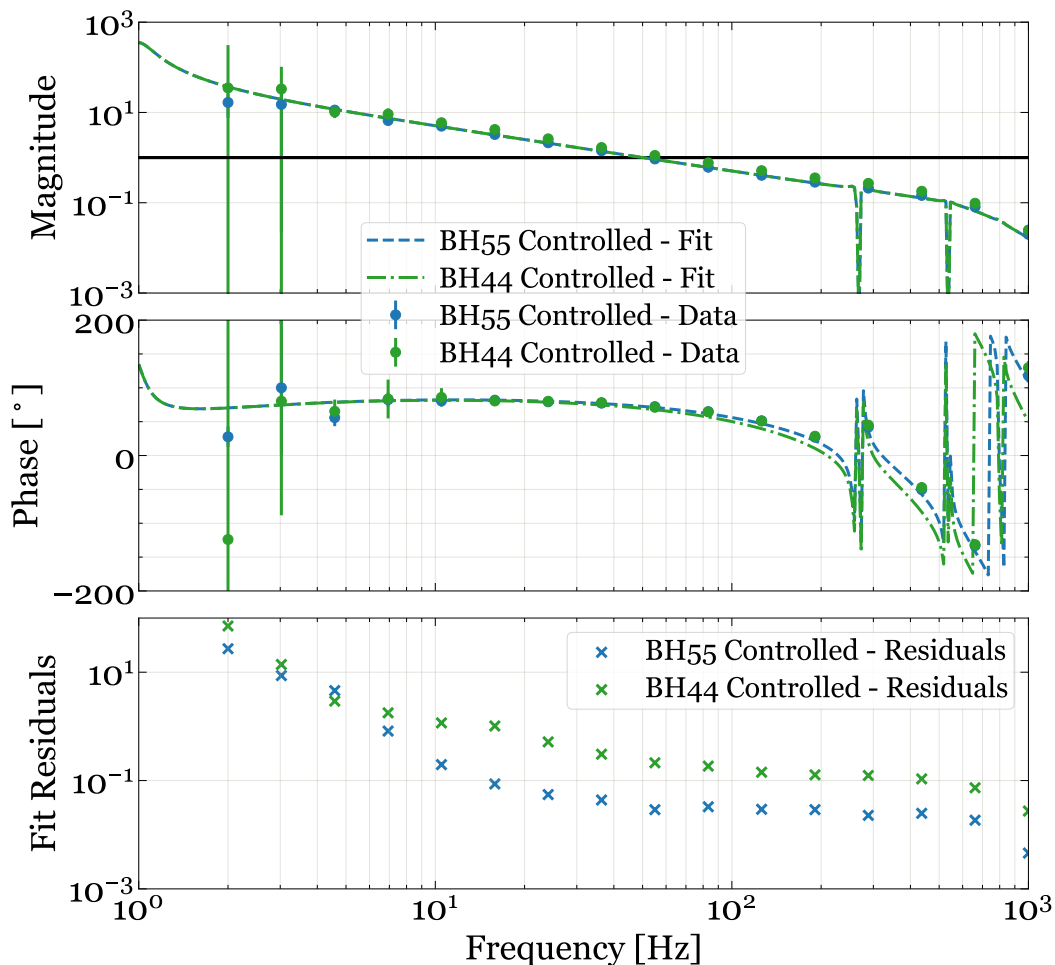
Figure 7.6: Open loop transfer function for LO phase control in Mach-Zehnder configuration with between AS beam and LO beam. The lock was tested with using single RF demodulation using BH55 and dual RF demodulation using BH44.

of 0.06 radians.

Michelson Interferometer:

Second configuration we tested was Michelson interferometer between BS, ITMX, and ITMY locked with the RF readout method (see Sec.5.1.2). Fig. 7.8 shows the OLTF for the two locking methods. Again, achieving almost the same OLTF in the two configurations was possible with UGF set to 50 Hz. Fig. 7.9 shows the noise budget for this locking configuration for the two methods. Note that the noise floor in this configuration increased by a factor of about 10 in comparison to the Mach-Zehnder case in the previous test (see Fig. 7.7). This is because the optical gain for both sensors has reduced due to the weaker 55 MHz sideband present at the
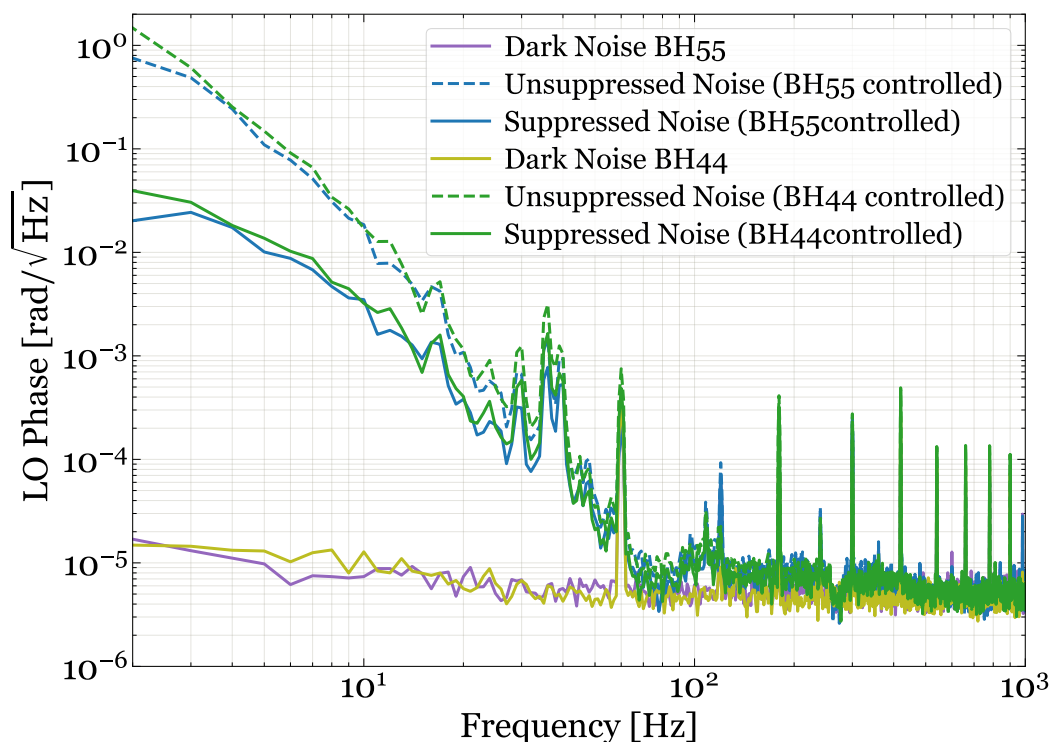
Figure 7.7: Noise budget of local oscillator phase control in Mach-Zehnder configuration between AS beam and LO beam. The suppressed noise is shown in solid blue and green lines for two different control loops, one using single RF demodulation with BH55 and other using dual RF demodulation with BH44.

AS port as Michelson is locked to the dark fringe. In this configuration, the BH55 loop suppressed noise twice as much as BH44, achieving LO phase residual RMS noise of 0.04 radians in comparison to BH44 controlled LO phase residual RMS noise of 0.08 radians when averaged over 1 second.

Fabry-Pérot Michelson Interferometer:

The third configuration we tested was Michelson interferometer with Fabry-Pérot arm cavities. We tested the two methods while keeping the similar OLTF with UGF set to 50 Hz. Fig. 7.9 shows the noise budget for the two locking configurations. We see that the BH44 LO phase lock is considerably more noisy above 20 Hz in comparison to the BH55 LO phase lock. Even though the two methods achieve the same residual RMS noise of 0.04 radians, the higher noise density above 20 Hz did not allow us to lock FPMI with BHD readout. While the two methods seemed comparable in the single bounce test, the fact that BH55 became better in MICH and FPMI configurations suggests that BH55 gains extra sensitivity with the presence
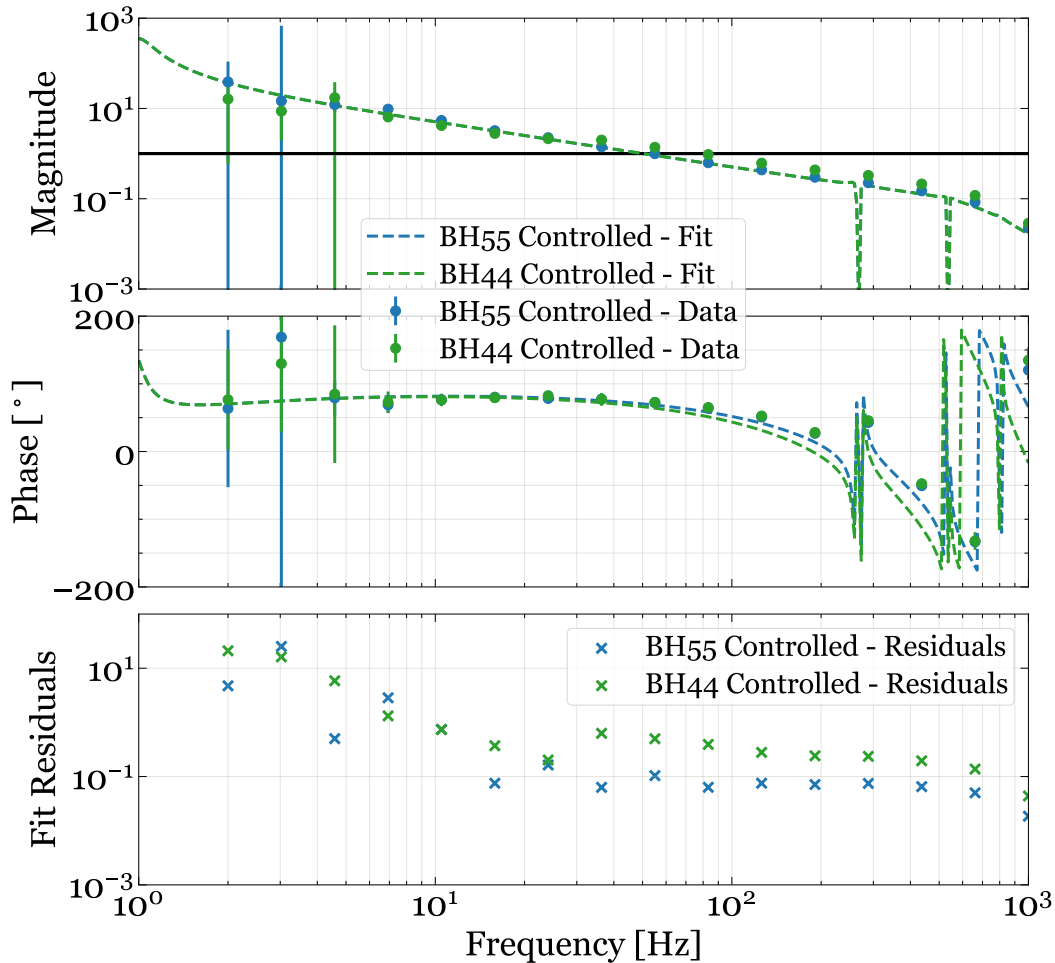
Figure 7.8: Open loop transfer function for LO phase control in Michelson interferometer configuration configuration with BS, ITMX, and ITMY. The lock was tested with using single RF demodulation using BH55 and dual RF demodulation using BH44.

of differential length offset in Michelson interferometer and contrast defect due to differences in reflectivities of the two Fabry-Pérot arm cavities. The team is further investigating these effects.

7.4 Preliminary results with BHD

We have been able to use the Balanced Homodyne Readout at CIT 40m using the LO phase locking mentioned in the last section. As a preliminary test, we locked the interferometer in two configurations, with RF readout, and with BHD readout, and compared the noise for the two cases.
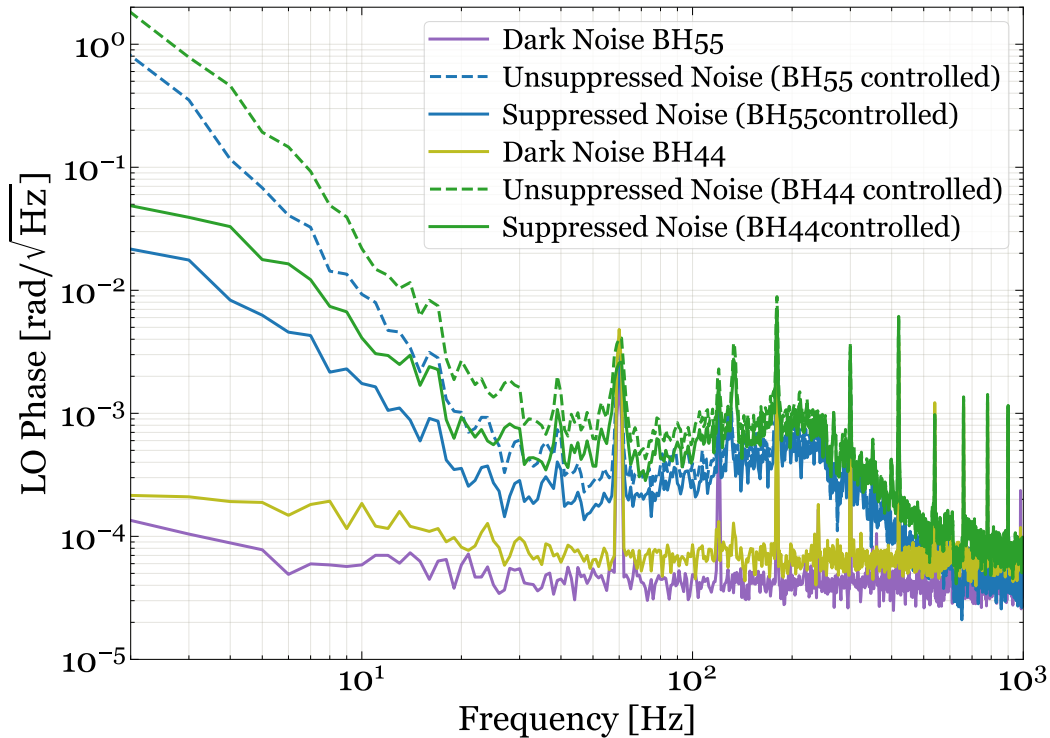
Figure 7.9: Noise budget of local oscillator phase control in Michelson interferometer configuration configuration with BS, ITMX, and ITMY. The suppressed noise is shown in solid blue and green lines for two different control loops, one using single RF demodulation with BH55 and other using dual RF demodulation with BH44.

7.4.1 Michelson Interferometer configuration

The interferometer was first locked in MICH configuration by using the usual RF readout method at the AS port. This uses the AS55Q channel to feedback to BS keeping the Michelson differential length changes locked to a point. The green traces in Fig. 7.11 show the total noise and the dark noise limit for this configuration. Then the LO phase angle was locked using the two methods: single RF demodulation using BH55 and dual RF demodulation using BH44. We can see in Fig. 7.11 that the dark noise floor for the BHD readout is considerably low in comparison to the RF readout method. However, this is because, in our current optical layout, only 10% of the AS beam reaches the AS55 RF photodiode. So the sensitivity of the RF readout scheme is reduced by 10 times than what would be when all of the AS beam goes to it. Even then, the sensitivity gain due to the bright LO beam is evident as the noise floor for the BHD scheme is less than more than an order of magnitude.

In this measurement, the noise of the BHD scheme is limited by the LO phase control noise from 20 Hz to 200 Hz. The noise bump at 50 Hz was an artifact in the
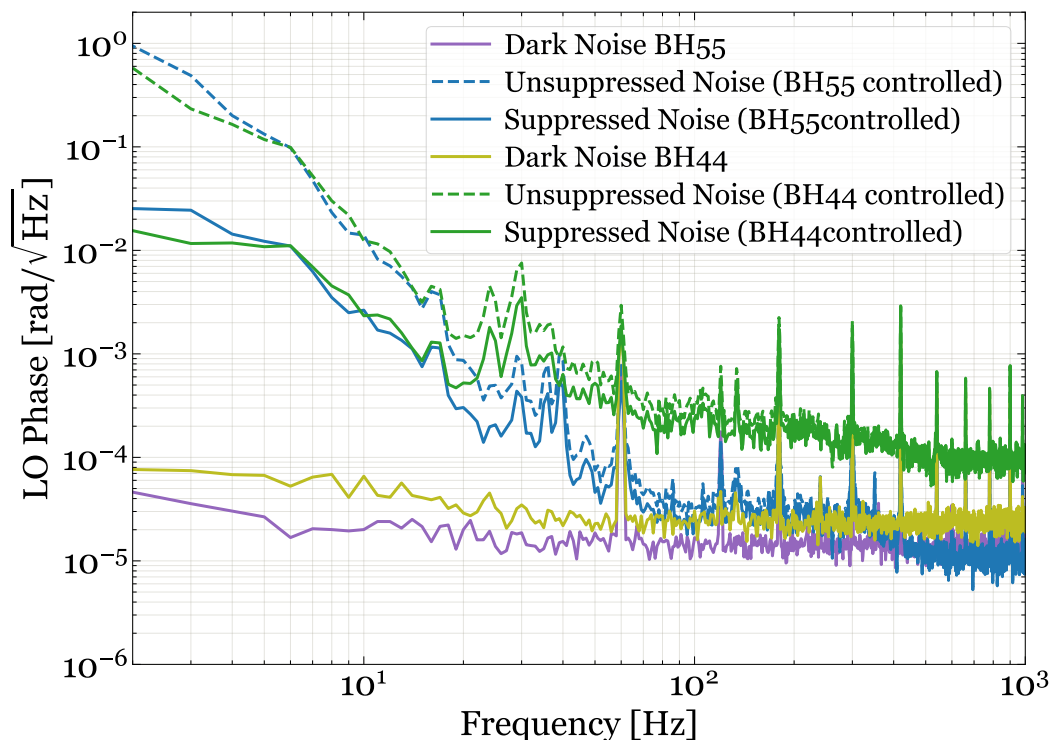
Figure 7.10: Noise budget of local oscillator phase control in Fabry-Pérot Michelson interferometer configuration. The suppressed noise is shown in solid blue and green lines for two different control loops, one using single RF demodulation with BH55 and other using dual RF demodulation with BH44.

LO phase control noise that we have successfully removed in the later attempts as can be seen in the noise curves presented in Sec.7.3 but we have not measured the MICH sensitivity with the better LO phase control yet.

We also see that the BHD scheme worked better with BH44 controlled LO phase. This is expected in the ideal case as BH44 locks the LO phase to the correct value. The fact that we get any sensitivity with the BH55 LO phase lock is already perplexing. We think that remnant differential arm offset or contrast defect light at AS port significantly changes the LO phase angle lock point with BH55 such that it gains MICH sensitivity. It needs to be investigated further how exactly we gained this sensitivity and if we can take advantage of this to sense and reduce differential length offset or contrast defect.

7.4.2 Fabry-Pérot Michelson Interferometer configuration

The interferometer was first locked in FPMI configuration using the usual RF readout method. This involves locking the CARM degree of freedom with REFL55I signal, the MICH with REFL55Q, and DARM with AS55Q. See Sec.10.3.2 for a more
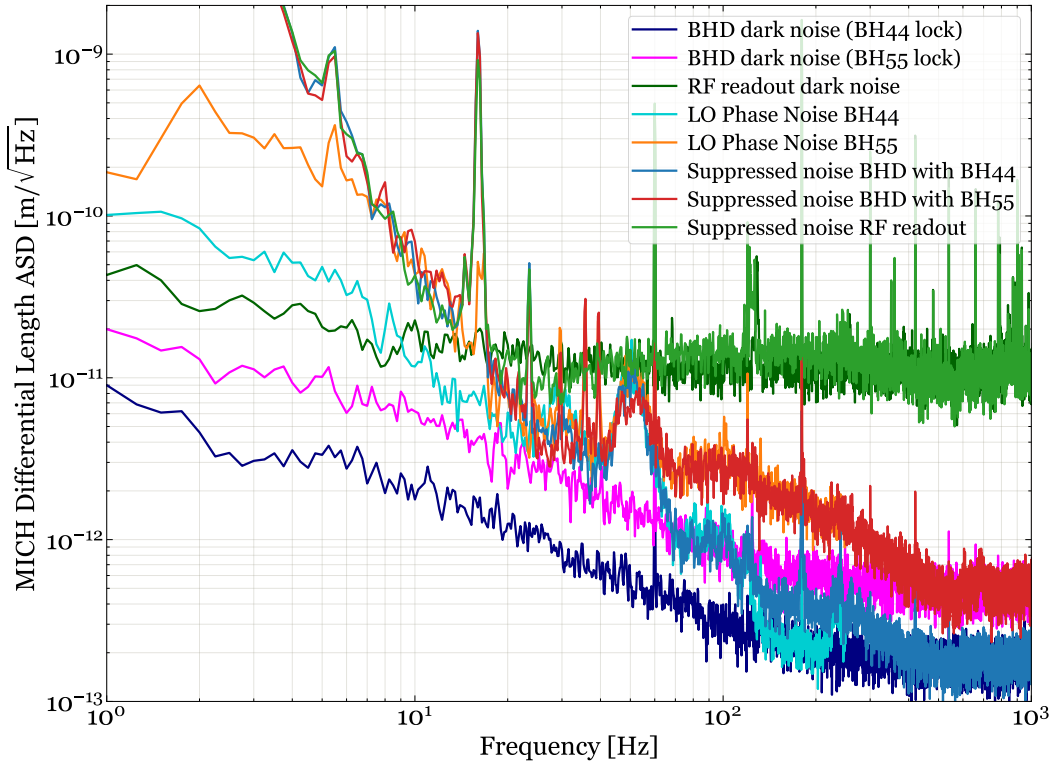
Figure 7.11: Noise comparison between RF readout and BHD readout in MICH configuration. For the BHD readout, we also compare the two different LO phase locking methods using single RF demodulation (BH55) or dual RF demodulation (BH44).

detailed description of achieving the lock in FPMI configuration using the RF readout. It is important to lock the interferometer before we can attempt using BHD readout because the LO phase angle fluctuates through multiple cycles of 2π radians in the absence of control of the DARM degree of freedom. None of our current DARM phase locking methods would work in locking the DARM phase angle with such a large dynamic range as all methods rely on a linear region of error signal production.

Once DARM is locked with AS55Q, we locked the DARM phase angle using BH55 with the single RF demodulation method (see Sec. 7.3.1) with a UGF of 50 Hz. Then we shift the error signal for the DARM loop from AS55Q to the BHD port which is the difference between the two DC photodiodes at the output of the BHDBS. Fig. 7.12 shows the noise of DARM degree of freedom when FPMI is locked with RF readout or with BHD.

Note that without many optimizations, we already see lower noise when BHD readout is used. We expect to see more noise reduction soon with the CIT 40m
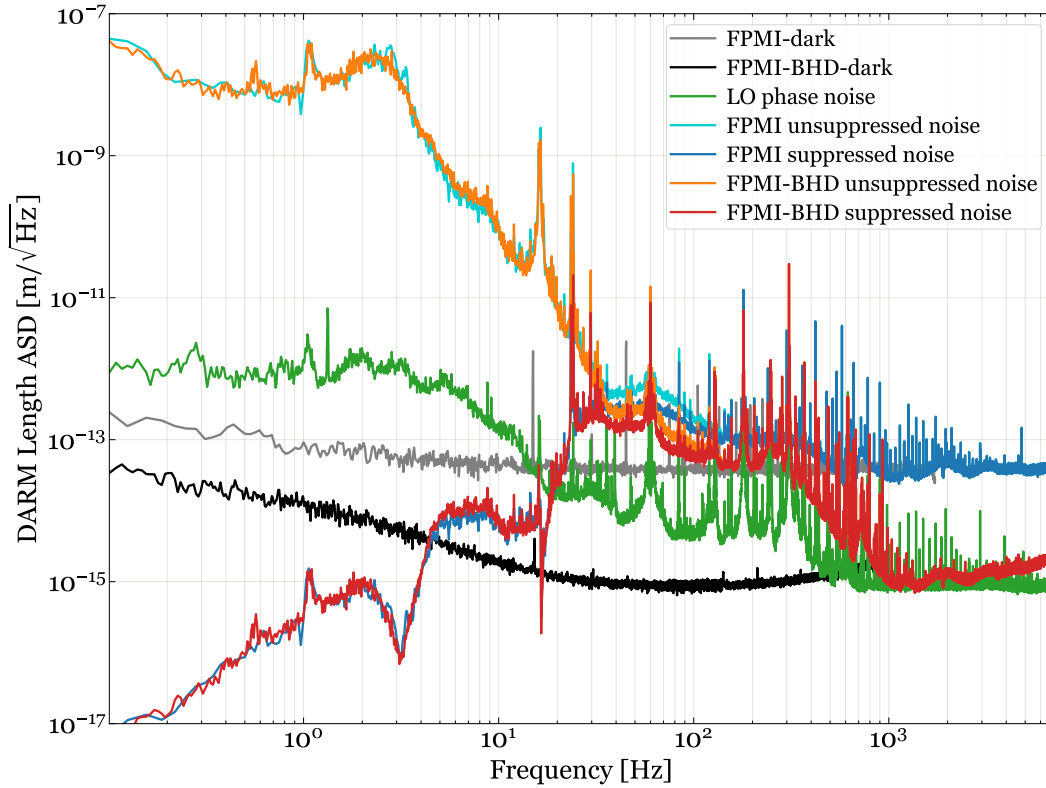
Figure 7.12: Noise comparison between RF readout and BHD readout in FPMI configuration.

BHD upgrade team working on achieving the LO phase lock at the true optimum DARM phase angle of ϕ_{LO}. Also, FPMI configuration is not the best one to see the benefit of BHD since the DARM beam is attenuated in transmission through the misaligned PRM. The current goal of the team is to achieve the BHD readout in PRMI configuration where the LO beam strength is amplified by the power recycling gain, significantly increasing the sensitivity of the BHD readout. The overall goal is to reach PRFPMI locking configuration to see improvement in DARM sensitivity for the full length of the interferometer.

Part III

Multicolor Calibration

Improving detector calibration to 0.1% uncertainty

C h a p t e r   8

INTRODUCTION

Advanced LIGO has detected more than 90 compact binary mergers of Black holes and neutron stars in distant galaxies so far[2]. This incredible feat is achieved by keeping the noise floor of the detector down to 10^{-20}m/$\sqrt{\text{Hz}}$. While we have started observing these events and measuring some properties of the merging bodies, science does not stop at merely proving that such bodies merge. We need to collect more data on the rates of mergers, and more importantly, precise information on the merging objects and the merging dynamics. That is, we need our detector output to be accurate and precise about the astrophysical and cosmological parameters that we estimate from the merging events.

Suppose gravitational wave h_{GW} from a merging event is arriving at the detector. The detector measures the strain and converts it into a digital count in its computer. This conversion in the Laplace domain can be written as the detector response function $\mathcal{R}(s)$ such that:

$$\tilde{Y}_{out}(s) = \mathcal{R}(s)\tilde{h}_{\text{GW}}(s) \tag{8.1}$$

We need to know the response function of our detector accurately and with high precision so that we can multiply the detected counts with the inverse of our response function model to get back the gravitational wave strain that must have come to the detector.

$$\tilde{h}_{\text{meas}}(s) = \mathcal{R}_{\text{model}}^{-1}(s)\tilde{Y}_{out}(s) \tag{8.2}$$

This measured strain h_{meas} is matched with different model waveforms of compact binary mergers to determine if an event has been detected and to estimate the parameters of the merging bodies.

Thus it is important to accurately and precisely estimate $\mathcal{R}(s)$ for the detector. If the signal is strong enough, we will be able to distinguish it as an event, but the uncertainty in the measured signal grows with the signal strength if the uncertainty in $\mathcal{R}_{\text{model}}$ remains the same. Thus, it is possible that for a strong signal the uncertainty in

the measured parameters of the events is dominated by uncertainty in $\mathcal{R}_{\mathrm{model}}$, rather than the statistical noise of the detector. This is the worst place for a metrological experiment to be in: being limited by the knowledge of the response function of your detector rather than the noise floor of the detector.

On the other hand, there are some continuous gravitational wave sources like pulsars which require long time averaging (over years) of the detector output. Such sources might be missed if the uncertainty in the calibration of $\mathcal{R}_{\mathrm{model}}$ is high.

Advanced LIGO currently reports the uncertainty in the response function phase and amplitude ranging from 2% to 5% in the detection frequency band[52]. This can be interpreted as the measurement uncertainties are limited by the detector noise for events with SNR up to about 50. If the next generation of gravitational waves detectors improve their sensitivity, they would need to measure the response function with better uncertainty to remain unaffected by calibration uncertainties. In this part of my research, I focused on working on a calibration technique that less sensitive to systematics, and scalable in achieving a desired calibration uncertainty. We set our goal to perform calibration with less than 0.1% uncertainty to show the proof of principle.

In this chapter, we'll go through a quick look at how calibration uncertainty affects astrophysical and cosmological parameters estimation and how the calibration is currently done in Advanced LIGO.

8.1 Astrophysical and cosmological parameter estimation

To get a bird's eye view of what is at stake due to calibration uncertainty, it is important to know possible astrophysical and cosmological measurements that can be made using gravitational waves. We list a few such parameter estimation problems that can benefit from improved sensitivity of future-generation gravitational wave detectors if the calibration uncertainty is reduced as well.

8.1.1 Binary black hole mass and spin distribution

With more than 90 detections of binary black hole mergers, we now have a measured distribution of mass and the effective spin of the black holes[53]. This data helps us determine the formation channels for such black holes and the origins of the blackhole population in general. Calibration uncertainty in amplitude and phase directly affects the uncertainty in measured estimates of black hole masses and effective spins. Further, since these parameters affect the gravitational waveform in

the first-order dynamics, the post-Newtonian correction terms rely on the powers of the blackhole masses and effective spins. Thus, it is important to measure these parameters with good certainty to avoid increasing uncertainty in derived quantities or parameters that affect higher-order post-Newtonian correction terms.

8.1.2 Neutron star equation of state

The neutron star equation of state has various candidate models based on nuclear model physics or phenomenological models. One of the determining parameters among the various proposed equation of state is the dimensionless tidal deformability (Λ) of neutron stars[54]. When binary neutron stars are about to merge, they tidally deform each other inducing quadrupole moments in each neutron star. The strength of this quadrupole moment and its evolution is determined by the tidal deformability factor Λ. The deformed neutron stars change the gravitational wave phase evolution in a characteristic way that can be measured with accurate GW phase information. Chatziioannou[54] has shown tidal deformability constraints on neutron star equation of state based on a study of the only confirmed binary neutron star merger detected by GW detectors GW170817[55], and for another likely binary neutron star merger GW190425[56]. This study also concludes that more detections with future gravitational waves would be helpful but the tidal deformability could be limited by detector calibration uncertainty and systematic waveform uncertainty[57, 58].

8.1.3 Tests of general relativity

Gravitational wave measurements allow a unique way to test predictions of general relativity. Many studies have tested general relativity on all the gravitational wave signals measured so far[59–62], but none have been able to find any significant deviations. The simpler form of these tests looks for correlations in the residual data when waveform has been subtracted from a measured gravitational wave. Other more involved tests look for departure in the gravitational waveform or the estimated parameters in higher order post-Newtonian terms in different frequency bands. These tests look for the same information from different parts of the event such as the inspiral time, merger, and ringdown after merger. With higher sensitivity detectors in the future and better calibration on them, we hope to find new physics through such tests on a larger set of observations.

8.1.4 Hubble constant estimation

The Hubble constant has been famously in tension due to conflicting measurements that are now at least 4.4 standard deviations apart[63]. On one side are the measurements based on X-ray observations of galaxy clusters and the spectral distortion of the cosmic microwave background with the Planck observatory, which utilizes the ΛCDM model to estimate the value of the sky. This method estimates the Hubble constant in the early universe to be 67.4 ± 0.5 km s^{-1} Mpc^{-1}[64]. It is in agreement with other high redshift measurements based on "inverse distance ladder" [65] or with baryonic acoustic oscillation measurements[66]. On the other hand, Hubble constant measurement made in the local universe by measuring Cepheid variable stars in the Large Magellanic Cloud gives a value of 74.03 ± 1.42 km s^{-1} Mpc^{-1}[63]. This is again corroborated by several other measurements in the local universe such as gravitational lensing in H0LiCOW[67], and supernovae in NIR[68, 69]. There has been a lot of research on this topic which I cannot fully list here, but we have found an interesting avenue for the possibility of finding new physics.

Gravitational waves can be used to calculate the Hubble constant value as well. When two compact binary objects coalesce together, the frequency evolution of the gravitational wave signal gives information about the "Chirp Mass" of the compact binary given by $\mathcal{M} = \frac{(m_1 m_2)^{3/5}}{(m_1 + m_2)^{1/5}}$. The amplitude of the gravitational waveform also depends on the same chirp mass, and thus one can infer how much the gravitational wave reduced in amplitude when it was detected on Earth. Since gravitational waves also reduce in amplitude as D_L^{-2} where D_L is the luminosity distance traveled by the gravitational wave, we can estimate the luminosity distance of the source. Thus gravitational waves serve as a standard siren for luminosity distance which can be used along with other methods of estimating the redshift of the source to measure the Hubble constant.

In particular, the binary neutron star detection GW170817[70] was also detected in multiple electromagnetic transient signals in different frequency bands. The redshift value of the source inferred from these electromagnetic detections was used to determine the Hubble constant[71] without using conventional cosmic 'distance ladder'[72] for the luminosity distance. However, since it is a single event, the uncertainty in the measurement is not enough to settle the Hubble tension.

Other ways to determine the redshift of the gravitational wave source have been used to utilize a larger set (47) of binary blackhole mergers[73]. In this study, 47 gravitational wave sources were used. The redshift of the sources was determined

by either using sky localization to determine the host galaxy of the event or by using a population model of the mass distribution of black holes. The Hubble constant from this analysis came out to be 68^{+8}_{-6} km s^{-1} Mpc^{-1}. The poor constraints are due to the fact that sky localization is not very good with present detectors and that galaxy catalogs are not complete. This study included the binary neutron star detection GW170817[70] which alone provides almost the same confidence in the Hubble constant values as estimated by the 46 other sources.

The uncertainty in the sky localization of the events is not entirely dependent on a single detector calibration but would be improved if all detectors improve in sensitivity and calibration precision. It is important to not miss follow-up electromagnetic confirmations of future binary neutron star mergers due to poor sky localization. On the other hand, the uncertainty in luminosity distance measured by gravitational waves directly contributes to the uncertainty of the estimated Hubble constant, and thus is an important parameter to estimate with more precision.

8.2 Calibration requirements for astrophysical parameter estimation

While determining the best strategy for calibration of the detector, it might seem that determining the detector parameters to a better certainty would be the goal. But as the end goal is to determine the astrophysical parameters better, the calibration method should be focused on achieving that. We performed the following Fisher information analysis adopted from Hall et al.[74] to estimate how the calibration uncertainty propagates to astrophysical parameter estimation.

8.2.1 Framework

Suppose a frequency-domain waveform h is described by a set of parameters $\mathbf{\Theta}$, $h = h(f; \mathbf{\Theta})$, and the detector's strain noise PSD is given by S_{det} which has units of [strain^2 Hz^{-1}]. The lower bound on the parameter estimation uncertainties on $\mathbf{\Theta}$ can be obtained by inverting a fisher matrix $\mathbf{I}^{\mathrm{ast}}(\mathbf{\Theta})$ as $\mathrm{Cov}(\mathbf{\Theta}) \geq \left[\mathbf{I}^{\mathrm{ast}}(\mathbf{\Theta})\right]^{-1}$. In particular, the (i, j)th element of this Fisher matrix is given by:

$$\mathbf{I}^{\mathrm{ast}}_{ij} = \left(\frac{\partial h}{\partial \Theta_i} \middle| \frac{\partial h}{\partial \Theta_j} \right) \tag{8.3}$$

where the derivatives are evaluated at $\mathbf{\Theta}_{\mathrm{t}}$, the true parameters describing the signal h, and we have defined the inner product as:

$$(a|b) = 4\text{Re}\left[\int df \frac{a^*(f)b(f)}{S_{det}(f)}\right] \tag{8.4}$$

As shown in Ref. [74], when the calibration of the interferometer is uncertain, we can define the "measured" waveform as:

$$g(f; \boldsymbol{\Theta}, \boldsymbol{\Gamma}) = \frac{R(f; \boldsymbol{\Gamma})}{R(f; \boldsymbol{\Gamma}_t)} h(f; \boldsymbol{\Theta}) \tag{8.5}$$

where R is the response function (with units of strain/W) that converts the detector output power fluctuations to the DARM strain, and $\boldsymbol{\Gamma}_t$ are the true parameters describing the interferometer's calibration.

Using $g(f; \boldsymbol{\Theta}, \boldsymbol{\Gamma})$ as the combined model of strain regeneration after detection, we can create a complete Fisher information matrix $\boldsymbol{I}^{tot}$ given by:

$$\boldsymbol{I}_{ij}^{tot} = \left(\frac{\partial g}{\partial \mu_i} \middle| \frac{\partial g}{\partial \mu_j}\right), \quad \mu \in \{\boldsymbol{\Theta}, \boldsymbol{\Gamma}\} \tag{8.6}$$

This matrix holds complete information on uncertainty propagation between calibration uncertainty and the astrophysical parameter estimation uncertainties, as well as, the lower bound on the astrophysical parameter estimation uncertainties due to statistical noise. If all astrophysical parameters appear first in the indices and then all calibration parameters appear in the indices, the total fisher matrix has the following shape.

$$\boldsymbol{I}_{ij}^{tot} = \begin{pmatrix} \begin{pmatrix} \boldsymbol{I}^{\text{ast}} \end{pmatrix} & \begin{pmatrix} \boldsymbol{I}^{\text{c2a}} \end{pmatrix} \\ \begin{pmatrix} \boldsymbol{I}^{\text{a2c}} \end{pmatrix} & \begin{pmatrix} \boldsymbol{I}^{\text{cal}} \end{pmatrix} \end{pmatrix}, \tag{8.7}$$

Symb.	Description	Nominal Value
BNS parameters		
M_1	Mass of heavier neutron star	1.35 $M_\odot$
M_2	Mass of ligter neutron star	1.3 $M_\odot$
D_L	Luminosity distance of merger	100 Mpc
$\tilde{\Lambda}$	Dimensionless tidal deformability	500
BBH parameters		
M_1	Mass of heavier blackhole	35 $M_\odot$
M_2	Mass of ligter blackhole	30 $M_\odot$
D_L	Luminosity distance of merger	100 Mpc
S_z	Spin along z direction of both blackholes	0.5
Assumed parameters		
ϕ_c	Coalescence phase	0.6 radians
t_c	Coalescence time	2.5 ms
Derived parameters		
M_c	Chirp Mass	$\frac{(M_1 M_2)^{3/5}}{(M_1+M_2)^{1/5}}$
q	Mass ratio	M_1/M_2

Table 8.1: Nominal compact binary coalescence parameters used for estimation of error propagation

The diagonal blocks are individual fisher matrices for astrophysical parameters and calibration parameters and the diagonal blocks serve as error propagation matrices. The error on the astrophysical parameters $\Delta\boldsymbol{\Theta}$ due to calibration uncertainties $\Delta\boldsymbol{\Gamma}$ can be computed as:

$$\Delta\boldsymbol{\Theta} = -\left(\boldsymbol{I}^{\text{ast}}\right)^{-1} \boldsymbol{I}^{\text{c2a}}\Delta\boldsymbol{\Gamma}, \tag{8.8}$$

Note that the number of rows of $\boldsymbol{I}^{\text{c2a}}$ is given by the size of $\boldsymbol{\Theta}$ and the number of columns given by the size of $\boldsymbol{\Gamma}$.

8.2.2 Effect of calibration errors on astrophysical parameter estimation

We calculated the effect of fractional calibration errors on the fractional errors of the estimated astrophysical parameters using the framework mentioned above. We ran the analysis for two kinds of compact binary mergers, binary neutron star (BNS) mergers, and binary black hole (BBH) mergers. Table 8.1 and Table 8.2 shows the nominal values of the coalescence event parameters and detector parameters used for calculating the error propagation. The detector responsivity is modeled as:

Detector Name	Length of detector arm L_{arm} [m]	Detector responsivity at DC g_0 [MW/m]	Detector pole frequency f_d [Hz]
Advanced LIGO	3995	428	1102
A+ LIGO	3995	428	1132
Voyager	3995	510	1378
Cosmic Explorer I	40000	830	49
Cosmic Explorer II Silica	40000	830	49
Cosmic Explorer II Silicon	40000	830	75

Table 8.2: Nominal detector parameters used for estimation of error propagation

$$R(f; g_0, f_d) = \frac{\left(1 + i\frac{f}{f_d}\right)}{L_{arm}g_0} e^{i2\pi \frac{f L_{arm}}{c}} \tag{8.9}$$

Fig. 8.1 shows the estimated total fractional errors for four parameters of the BNS event for different calibration errors in the detector pole frequencies. Moreover, we used GWINC[3] to project the calculations for the current upgrade on Advanced LIGO known as A+ LIGO, a proposed cryogenic upgrade on Advanced LIGO known as Voyager[75] (see Ch.11), and a few future detector proposals known as Cosmic Explorer[76] in various phases and configurations.

Note that for Advanced LIGO, a 1% calibration uncertainty is acceptable as parameter estimation for all four parameters are limited by statistical noise of the detector which is the desirable case. However, for upgraded LIGO and future detectors that improve the sensitivity, even though the statistical noise floor for each parameter is lower, we can only take advantage of the better sensitivity if the calibration error is less than 1%. For instance, the tidal deformability of the neutron stars can be estimated to much better than 8% uncertainty with the future Cosmic Explorer detectors, but the calibration error would dominate the results unless it is reduced to 0.1% level. Note that these calculations are very optimistic with simplified model of the event, for instance, the merger is assumed to happen face on with the detectors which is not always the case or known to a good certainty. Thus the noise floors obtained here are optimistic estimates and are worse in practice.

Fig. 8.2 shows similar analysis performed for a nominal BBH event. We see that that the fractional errors in the parameter estimates are right at the crossover with
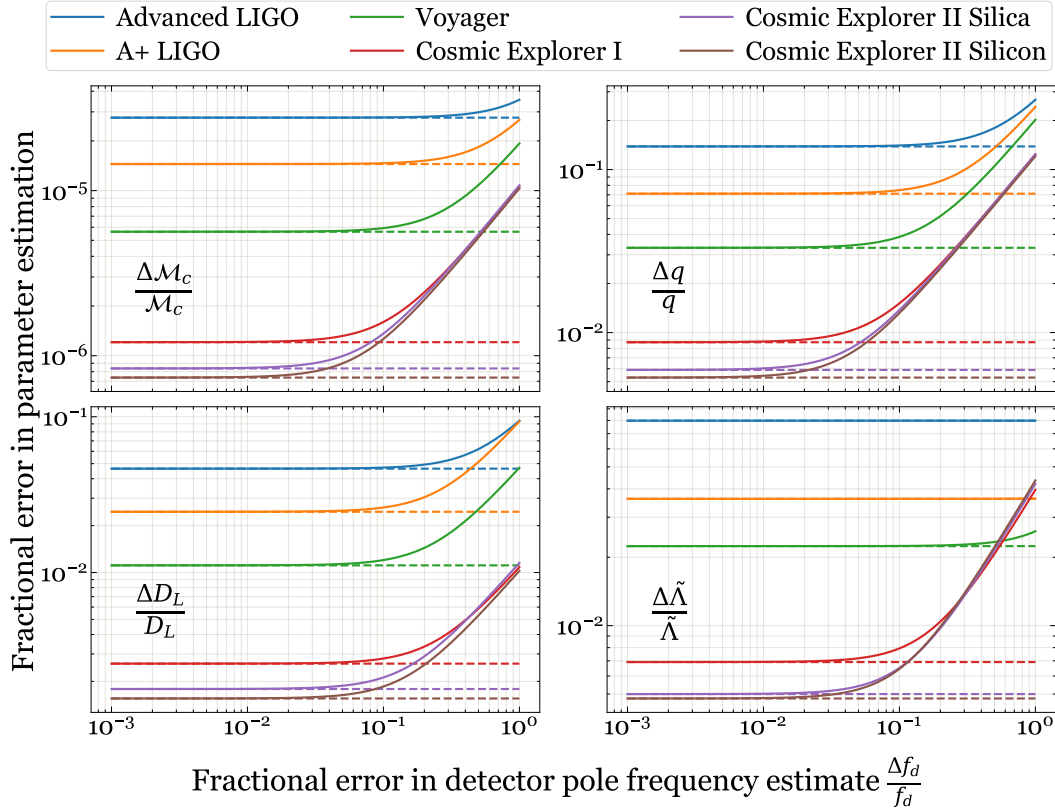
Figure 8.1: Fractional errors in parameter estimates of Binary Neutron Star (BNS) mergers with respect of calibration error in detector pole frequency for different gravitational wave detectors[75, 76]. The dashed curves represent the statistical noise floor for each parameter estimate, while the solid curve is the total fractional error along with the contribution from calibration error of the detector. The estimates are calculated for a nominal BNS merger event with parameters as listed in Table 8.1 using detector models based on parameters listed in Table 8.2.

the calibration uncertainty for Advanced LIGO. Any better detector is limited by calibration uncertainty for calibration errors above 0.1%. With better sensitivity, the restrictions on required calibration uncertainty wil be tighter. These two calculations set the basis for our target of developing a calibration method to reach 0.1% uncertainty. We might want to do even better in future if nearby events are too loud and the estimates for such events are limited by calibration error in uncertainty.

8.3 Current calibration methods and proposals

8.3.1 Photon calibrator

Advanced LIGO uses a technique known as Photon Calibrator (PCAL) [77]. The objective of calibration is to send a known input signal to the detector as a DARM strain and measure the detector output of the signal to get the response function of
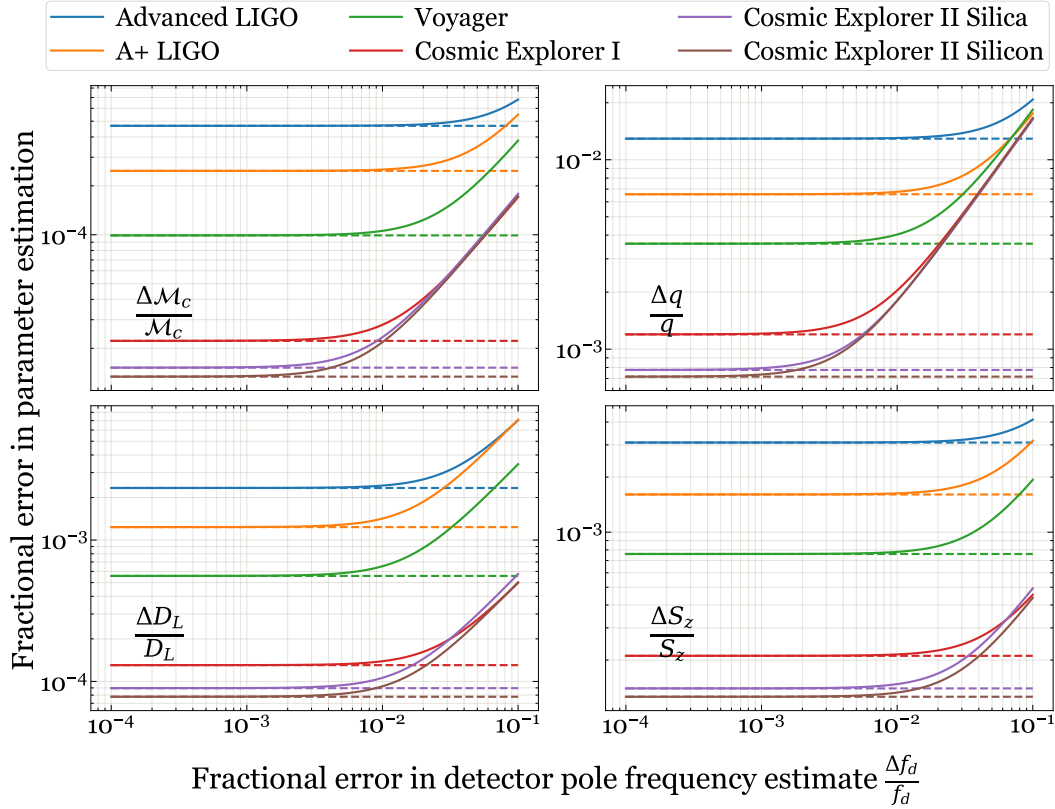
Figure 8.2: Fractional errors in parameter estimates of Binary Black Hole (BBH) mergers with respect of calibration error in detector pole frequency for different gravitational wave detectors[75, 76]. The dashed curves represent the statistical noise floor for each parameter estimate, while the solid curve is the total fractional error along with the contribution from calibration error of the detector. The estimates are calculated for a nominal BBH merger event with parameters as listed in Table 8.1 using detector models based on parameters listed in Table 8.2.

the detector. The input signal should be strong enough to give a good signal-to-noise ratio from the detector output. But it can not be too strong, otherwise the error readout for the DARM length control signal in the detector would become non-linear causing errors in the calibration.

To get around this, the PCAL method injects input signals only at specific calibration frequencies as sinusoidal waves and calibrates the response function at those frequencies. A detector model is used to interpolate the calibration at all other frequencies. Since the response function of the detector depends on a few parameters, only 4 or 5 calibration lines are enough to get these parameter values accurately and track their changes during the observation. Using discrete frequencies also allows for the calibration to be run while in observation mode, damaging sensitivity in only small frequency regions around the calibration line frequencies.
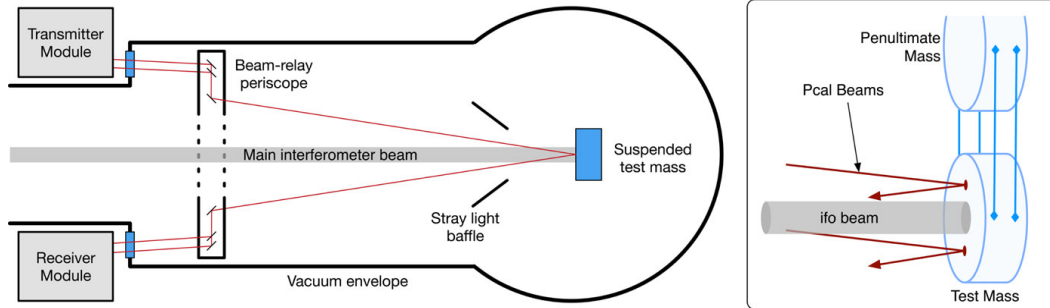
Figure 8.3: Photon calibrator schematic from Karki et al.[77]

PCAL method uses a 1047 nm laser beam that is reflected off of one of the suspended test masses. The radiation pressure of the laser beam moves the suspended test mass as a function of the laser power. The PCAL system modulates the power of the beam to inject motion at certain calibration line intensities. This creates motion in one of the mirrors in one of the arm cavities, modulating the length of that arm cavity, and thus creating a DARM and a CARM signal simultaneously. To ensure that the beam does not interfere with the thermal state of the coatings on the test mass, the beam incidence point is kept off-center. But then to ensure no angular motion of the optic is stimulated, another identical beam is sent at the diametrically opposite point on the other side of the center.

This takes care of how the actuation is done on the mirrors for simulating a signal. But to calibrate, we need to know how much the mirror moved from the power modulation on the beam. For this purpose, part of the laser power is measured in the transmitter module before being sent to the optic, and the reflected light is measured after it reflects off the optic. For measuring this light level, *Gold Standard* power sensors are used that are calibrated annually at the National Institute of Standards and Technology (NIST) in Boulder, CO. From the two measurements of light power level before and after it hits the mirror, photon radiation pressure on the mirror is estimated and then using an estimate of the mechanical transfer function from force to displacement, the actual motion of the optic is estimated. This is then used to calibrate the DARM output of the detector.

While this method works well for the desired uncertainty levels for the Advanced LIGO sensitivity, it can not be improved further as much for the next-generation detectors. In the best case scenario, the measured DARM strain uncertainty achieved by this method is in the range of 2% to 5% as reported for the first and second observation runs of Advanced LIGO detectors[52]. The main reason for this high

uncertainty despite very low characterized uncertainty ($\sim 0.75\%$) in the photon calibrator is due to the observed drift of the optomechanical response function in between each calibration run. This raises the issue of systematic calibration error and a more complicated topic of how to infer accurate calibration information across the detection frequency band with the few lines of calibration that are used during observation.

The major components in the uncertainty of the photon calibrator measurement come from laser intensity noise, photodiode calibration uncertainty, and rotation of the optic due to the imprecise location of the beam spot on the mirror. Besides these, there is a lot of room for systematic noise to creep in since an estimate of the mechanical transfer function is used. The large optics have vibration modes in a few kHz frequency range. These resonances could get rung up because of the localized forcing from the photon calibration beams. Because of these reasons, the estimates of laser power calibration and beam spot position on the mirrors vary over time and result in systematic errors. This method converts the DARM response function calibration problem to calibration of laser power measurement and precise estimation of beam location and mechanical transfer function, which are easier problems but have limits on how well one can estimate them. Thus there is a need for improving the calibration method for the next generation of gravitational wave detectors.

8.3.2 Newtonian calibrator

Another way to apply a known force on the test mass is to apply it using a modulating gravitational force. This method is used in the Virgo gravitational wave detector in Itay[79] for calibration, and used in conjunction with the photon calibrator method in KAGRA gravitational wave detector in Japan[80]. In this method, a rotating distribution of accurately known masses is used to apply a modulating gravitational wave force on the test mass from outside the vacuum chamber. Depending on the distance d from the rotor (see Fig. 8.4), different multipole moments of mass distribution apply the gravitational force with different amplitudes and at different harmonics of the rotation frequency. This method has been successfully tested and characterized recently at Advanced LIGO[78].

Since the actuation method does not involve anything touching the test mass, not even photons, and is applied to the whole mass rather than at small regions on the surface, this method has several advantages over the photon actuators used in the
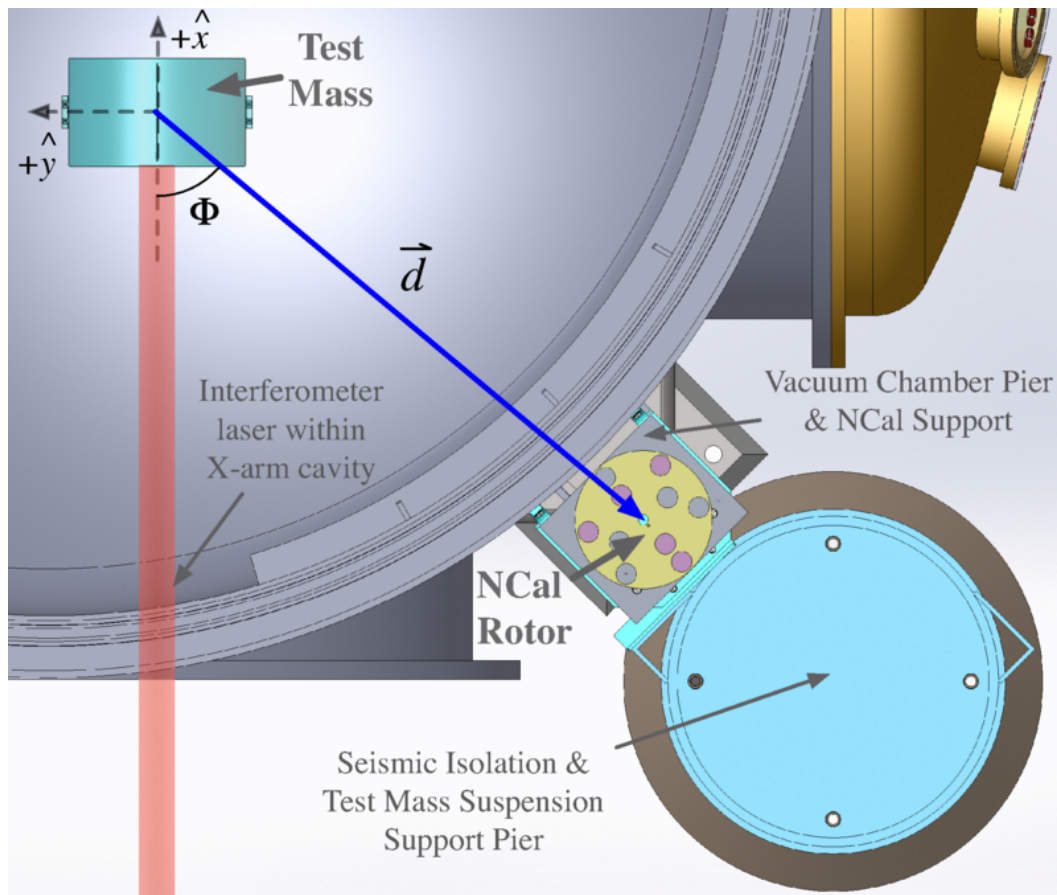
Figure 8.4: Newtonian calibrator schematic from Ross et al.[78]

photon calibrator method. There is no thermal distortion due to the absorption of the actuation laser, no known excitation of higher order modes, and no spurious rotation effects due to beam localization. The initial results of this method[78] suggest a less than 1% uncertainty in calibration which is statistical noise limited in measurement.

But the accurate estimation of applied force and displacement response to the applied force remains a possible systematic source of uncertainty in the future. Careful analysis of the effect of the modulating gravitational field on the penultimate mass in the suspension chain and interaction with the test mass through the suspension wires is required and modeled using finite element analysis simulations. The Newtonian calibrator also applies a modulating torque on the test mass causing it to move in angular degrees of freedom as well. The length changes in the interferometer arm due to these rotations are calculated by using beam position measurement on the test mass. This is then corrected in the measurement. The beam position on the optics is found to move around by about 0.5 mm over the course of hours[81]. This would result in a systematic error in calibration of the order of 3-4% assuming the same

beam offset positions as reported in O3[78]. Thus, it might be required to measure the beam position frequently to correct this systematic error.

The rotation of the rotator near the vacuum chamber inevitably transfers vibration through the ground to the optical table inside even through the seismic isolation system. Other bad effects like vibrations in the beam tube and chamber walls cause spurious scattering that can increase noise in the interferometer operation. This creates practical challenges in improving this technique further. Calibrating the detector using this method at high frequencies is hard to achieve as it would mean rotating the rotor at higher speeds quietly. Further, it can only simultaneously calibrate at two or three frequencies. Nevertheless, this is another exciting calibration method that with more development can help reduce the calibration uncertainty in future gravitational wave detectors.

Chapter 9

MULTICOLOR CALIBRATION SCHEME

In this chapter, I'll introduce a new calibration scheme that we have proved in principle to reduce the absolute calibration uncertainty of each detector to less than 0.1%. We will first go through a quick introduction to Arm Length Stabilization (ALS) in place in Advanced LIGO. Then, we would discuss how we can utilize the same system to calibrate the detector output without adding any new components. We will see the mathematical reasoning behind this method. Finally, we will look at the statistical and systematic uncertainty sources in this method.

9.1 Arm Length Stabilization (ALS)

$$L_C = \frac{L_X + L_Y}{2}$$

$$L_D = \frac{L_X - L_Y}{2}$$

$$L_M = \frac{l_x - l_y}{2}$$

$$L_P = l_p + \frac{l_x + l_y}{2}$$

$$L_S = l_s + \frac{l_x + l_y}{2}$$
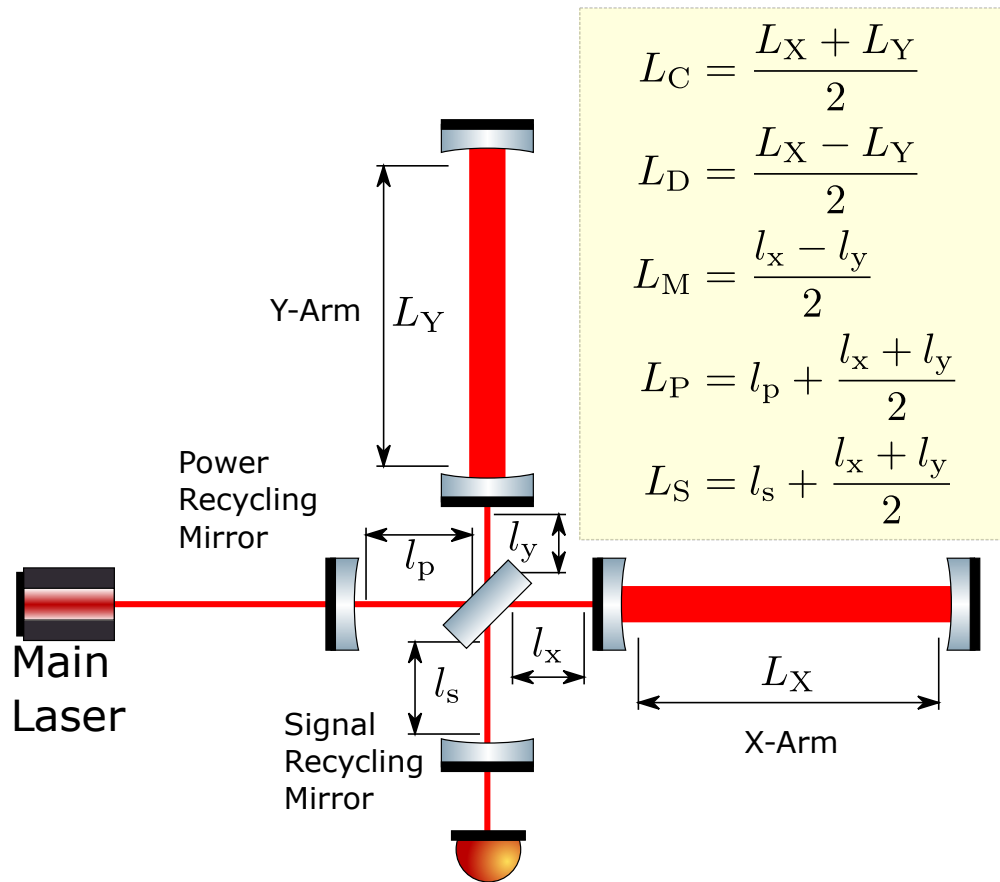
Figure 9.1: Dual recycled Febry-Perot Michelson interferometer layout.

Advanced LIGO and other current gravitational wave detectors achieve unprecedented sensitivity in part due to the dual recycled Fabry-Pérot Michelson interferometry. Fig. 9.1 shows the optical configuration required for this scheme to work. In short, the Michelson interferometer which senses the different arm length changes due to gravitational waves, is made more sensitive by making the photons go multiple roundtrips proportional to the finesse of each arm cavity. The amount of circulating power is further increased by recycling the reflected light out of the Michelson bright port through the power recycling cavity. Finally, another mirror is added at the dark port of the interferometer which is referred to as a signal recycling mirror, but in general is used for increasing or decreasing the bandwidth of the detector.

This optimized observation mode requires five degrees of freedom to be controlled simultaneously so that the common arm length L_C and power recycling cavity length L_P are resonant with the input laser beam, the differential arm length L_D is maintained at zero, the Michelson interferometer L_M remains such that the output port is dark, and the signal extraction cavity length L_S is maintained in resonance at the detection frequency range. This optimum point is one spot in a five-dimensional phase space and is hard to achieve starting from an arbitrary point.

The process of reaching the science observation stage is known as lock acquisition. Even if one tries to acquire lock sequentially for the five degrees of freedom, there is a fundamental issue present. To lock CARM to the main laser while keeping DARM at zero, one requires both arm cavities to reach resonance with the main laser simultaneously. Since the arm cavities are 4 km long and have high finesse, the cavity linewidth is very small, and the chances of both cavities coming within the PDH linear locking region simultaneously are minuscule.

To tackle this issue, Arm Length Stabilization (ALS) subsystem was employed. This topic has been described in detail in Izumi et al. [82] and Alexa Staley's thesis[83]. I present here a short simplified summary to bridge the gap to the calibration scheme described later. Two green lasers (auxiliary (AUX) lasers) are locked to the two arms individually by injecting them through the end stations through the end test masses. These green lasers are generated by frequency doubling 1064 nm Nd:YAG NPRO lasers by a single pass oven-controlled non-linear crystal optimized for second harmonic generation from 1064 nm to 532 nm. Since these are individual locks, this is fairly easier to acquire. Once locked, the transmitted green lasers carry information about the arm-length motion in their optical frequency. See Fig. 9.2 for

reference.

$$\Delta_C = \nu_0 - \nu_Y$$

$$\Delta_D = \nu_X - \nu_Y$$

$$\delta\Delta_C = \delta\nu_0 - \nu_0 \frac{\delta L_Y}{L_Y}$$

$$\delta\Delta_D \propto \delta L_X - \delta L_Y$$
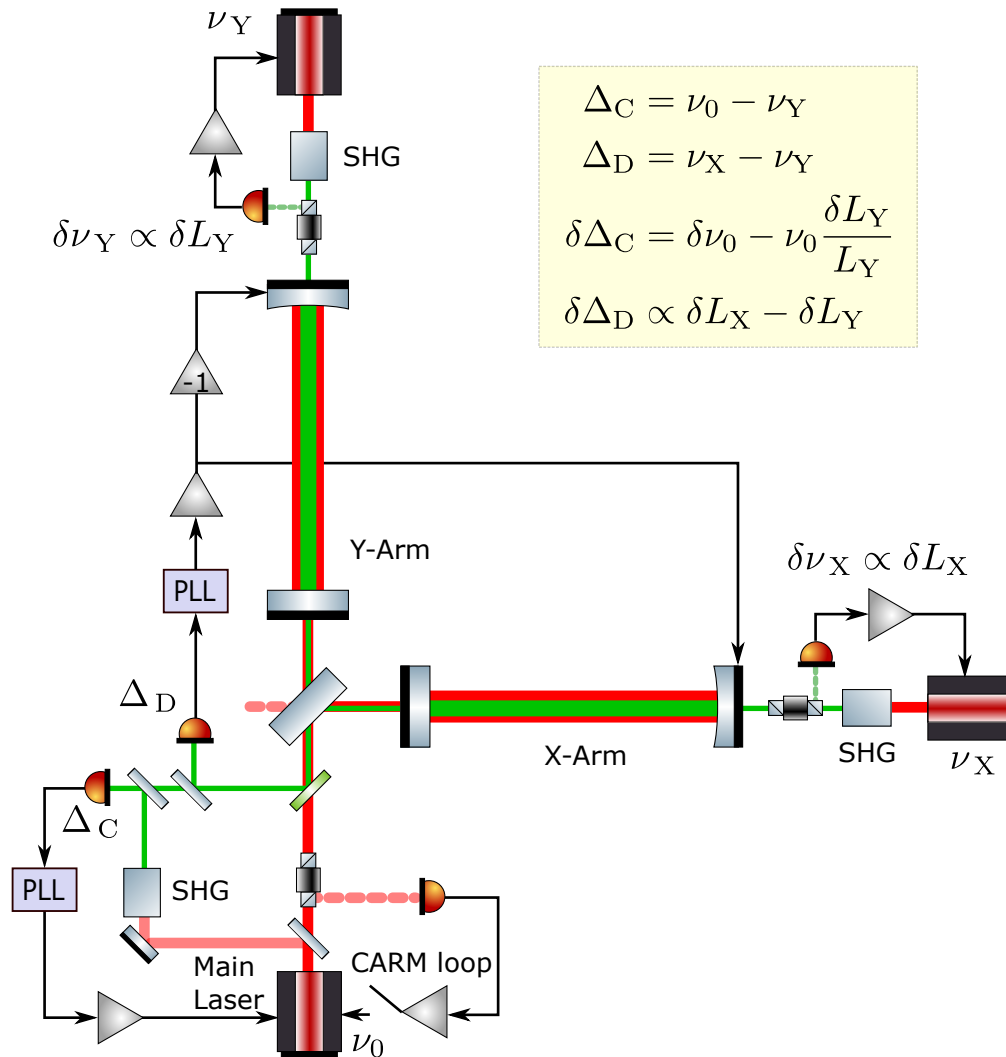
Figure 9.2: Simplified diagram of Arm Length Stabilization. 532 nm Green laser is generated using SHG crystal from 1064 nm seed laser. Each auxiliary laser is locked to a single arm. The beat note between the two transmitted green lasers gives DARM signal. When used to stabilize the arm lengths to each other, the beatntoe between second harmonic of main laser and one of the auxiliary lasers provide CARM signal used to feedback to laser instead of using short range PDH loop during lock acquisition.

By taking a beatnote with a frequency-doubled pick-off of the main laser and the transmitted AUX laser, we get a wide-range readout (in comparison to the PDH readout) of frequency difference of the main laser from arm cavity resonance. Since the readout is present regardless of the main laser resonating with the arm cavity, we can lock the main laser to arm cavity motion while still maintaining it at off-resonance by an appropriate offset. The beatnote between the two transmitted AUX

lasers on the other hand gives a readout of the DARM signal which can be used to lock DARM to zero without using the main laser. This way, CARM and DARM degrees of freedom are at their set point without using any error signal which requires a main laser and interferometer optics interaction.

From this point, the MICH, PRCL, and SRCL degrees of freedom can be locked to their respective lock points. Finally, the offset in CARM is reduced to zero, making the main laser resonant in both cavities while still locked through the ALS subsystem. A final switch in error point readout is made from the ALS beatnote to the interferometer photodiodes (where the system is within the PDH linear regime now), which results in lock acquisition. This is a good example of how frequency space measurement of arm lengths helps solve a complex control systems problem. Our proposed calibration scheme aims to utilize this advantage further.

9.2 Calibration Scheme

Once the lock is acquired in Advanced LIGO, they typically turn off the auxiliary lasers. But if the lasers are kept on, the individual arm length tracking by the auxiliary lasers can be used to calibrate the DARM the response function of the detector. Fig. 9.3 shows this multicolor calibration scheme in broad strokes. In this section, I'll introduce this scheme with mathematical details. Please note that the Fig. 9.3 uses beat notes between the seed laser of the auxiliary frequency and the transmitted main laser in comparison to taking beatnote at the auxiliary WaveLength in transmission as shown in the ALS scheme (Fig. 9.2), but there is no difference between the two cases and the same set of reasoning works no matter how the lasers are compared with each other.

9.2.1 Arm length modulation

Consider a single arm cavity with nominal length L_x. An auxiliary laser field of frequency ν_{aux} is locked to the q-th resonant mode at $\nu_q = qc/2L_x$, with $q \in \mathbb{Z}$ such that ν_{aux} measures fluctuations in L_x. To calibrate the linear strain response of the interferometer, we may inject one or more single frequency calibration lines of strength Γ_i and frequencies f_i, by modulating a single arm length such that:

$$\frac{\delta L_x(t)}{L_x} = \sum_i \Gamma_i \cos(2\pi f_i t) \tag{9.1}$$

While we set f_i, we typically only have an estimate of Γ_i through test mass actuation transfer function estimate, and method used to apply the actuation. If we can accu-

rately measure the actual Γ_i, we can calibrate the DARM strain in the interferometer since the DARM strain is given by:

$$\Gamma_{\text{DARM}} = \frac{\delta(L_x - L_y)(t)}{L_x + L_y} = \frac{\delta L_x(t)}{2L_x} = \frac{1}{2}\sum_i \Gamma_i \cos(2\pi f_i t) \tag{9.2}$$

Since we care about DARM strain and not the actual transfer function of our actuation, this method simply aims to measure Γ_i regardless of how it was generated in the system. This agnosticism of actuation is important to get rid of many possible systematic uncertainties that come with transfer function estimations.

The above equations are simplified in the sense that we are only talking about our excitation signal at those particular frequencies. In practice, there is noise present in all frequencies but we will demodulate our measurements at the particular calibration line frequencies so that we reject noise in other frequency bands. So only the noise present within demodulation bandwidth near the calibration line frequencies will enter the measurement which can be made negligible by using appropriate strength in driving the calibration lines. For now, we continue with this simplified model to get a basic understanding of this scheme.

9.2.2 Auxiliary laser control loop

The auxiliary lasers at the ends are locked to individual arm cavities using the conventional PDH technique. If we call the open loop transfer function of the frequency stabilization control loop for auxiliary laser $G_{\text{OL}}(s)$, then the fluctuations in arm cavity length are transferred to laser frequency such that:

$$\begin{aligned}
\delta\tilde{\nu}_{\text{aux}}(s) &= G_{\text{OL}}(s)\left(\delta\tilde{\nu}_{\text{aux}}(s) - \delta\tilde{\nu}_q(s)\right) \\
\delta\tilde{\nu}_{\text{aux}}(s) &= G_{\text{OL}}(s)\left(\delta\tilde{\nu}_{\text{aux}}(s) + \delta\tilde{L}_x(s)\frac{qc}{2L_x^2}\right) \\
\delta\tilde{\nu}_{\text{aux}}(s) &= G_{\text{OL}}(s)\left(\delta\tilde{\nu}_{\text{aux}}(s) + \delta\tilde{L}_x(s)\frac{\nu_{\text{aux}}}{L_x}\right) \\
\delta\tilde{\nu}_{\text{aux}}(s) &= \frac{G_{\text{OL}}(s)}{1 - G_{\text{OL}}(s)}\frac{\nu_{\text{aux}}}{L_x}\delta\tilde{L}_x(s) \\
\delta\tilde{\nu}_{\text{aux}}(s) &= G_{L\to\nu}(s)\frac{\nu_{\text{aux}}}{L_x}\delta\tilde{L}_x(s)
\end{aligned} \tag{9.3}$$

Here we defined the transfer function from length fluctuations to frequency fluctuations for this loop as:

$$G_{L\to\nu}(s) = \frac{G_{\text{OL}}(s)}{1 - G_{\text{OL}}(s)} \tag{9.4}$$

$$\delta L_{\mathrm{X}} = L_{\mathrm{X}}\Gamma cos(2\pi f_{\mathrm{exc}}t)$$

$$\frac{\delta L_{\mathrm{C}}(f_{\mathrm{exc}})}{L_{\mathrm{C}}} = \frac{\Gamma}{2}, \quad \frac{\delta L_{\mathrm{D}}(f_{\mathrm{exc}})}{L_{\mathrm{C}}} = \frac{\Gamma}{2}$$

$$\Delta_{\mathrm{X}} = \nu_0 - \nu_{\mathrm{X}}$$

$$\delta\Delta_{\mathrm{X}}(f_{\mathrm{exc}}) = -\nu_0\frac{\delta L_{\mathrm{C}}(f_{\mathrm{exc}})}{L_{\mathrm{C}}}$$

$$+ \nu_0\frac{\delta L_{\mathrm{X}}(f_{\mathrm{exc}})}{L_{\mathrm{X}}}$$

$$= \frac{\Gamma}{2} = \frac{\delta L_{\mathrm{D}}(f_{\mathrm{exc}})}{L_{\mathrm{C}}}$$

Figure 9.3: Multicolor calibration of the differential arm length (DARM). The main laser with nominal frequency ν_0 is locked to the common arm length (CARM) while second harmonic generated (SHG) auxiliary lasers are individually locked to the single arm lengths $L_{\mathrm{X}}, L_{\mathrm{Y}}$. The two beatnotes Δ_X, Δ_Y between the main laser and the auxiliary lasers are tracked by phase locked loops (PLLs). In the presence of an excitation at f_{exc}, the demodulated beatnote frequency signal is proportional to the differential arm length fluctuations at f_{exc}.

Thus the laser frequency encodes the strain $\delta L_x/L_x$ in it. In practice, we generate auxiliary laser fields through a second harmonic generation (SHG) stage seeded by a laser field operating near the main interferometer frequency $\nu_{\mathrm{seed}} = \nu_{\mathrm{aux}}/2$. Because

SHG is a highly coherent process [84], the relative frequency noise $\delta v_{\text{seed}}/v_{\text{seed}}$ in the main seed laser encodes the single-arm strain signal as well.

$$\delta\tilde{v}_{\text{seed}}(s) = \frac{v_{\text{seed}}}{v_{\text{aux}}}\delta\tilde{v}_{\text{aux}}(s) = G_{L\to v}(s)v_{\text{seed}}\frac{\delta\tilde{L}_x(s)}{L_x} \tag{9.5}$$

9.2.3 Main laser CARM control loop

Let the closest resonance frequency for CARM (Common mode between the two arms) degree of freedom of the interferometer be $v_p = pc/(L_x + L_y)$, where $p \in \mathbb{Z}$. If we call the open loop transfer function of the frequency stabilization control loop that locks the main laser to this resonance of CARM mode be H_{OL}. Then following the same calculations as Sec.9.2.2, we get:

$$\delta\tilde{v}_{\text{main}}(s) = H_{L\to v}(s)v_{\text{main}}\frac{\delta(L_x \tilde{+} L_y)(s)}{L_x + L_y}$$

$$\delta\tilde{v}_{\text{main}}(s) = \frac{1}{2}H_{L\to v}(s)v_{\text{main}}\frac{\delta\tilde{L}_x(s)}{L_x} \tag{9.6}$$

Here we used the fact that $L_x \approx L_y$ and we define the transfer function from CARM length fluctuations to frequency fluctuations for this loop as:

$$H_{L\to v}(s) = \frac{H_{\text{OL}}(s)}{1 - H_{\text{OL}}(s)} \tag{9.7}$$

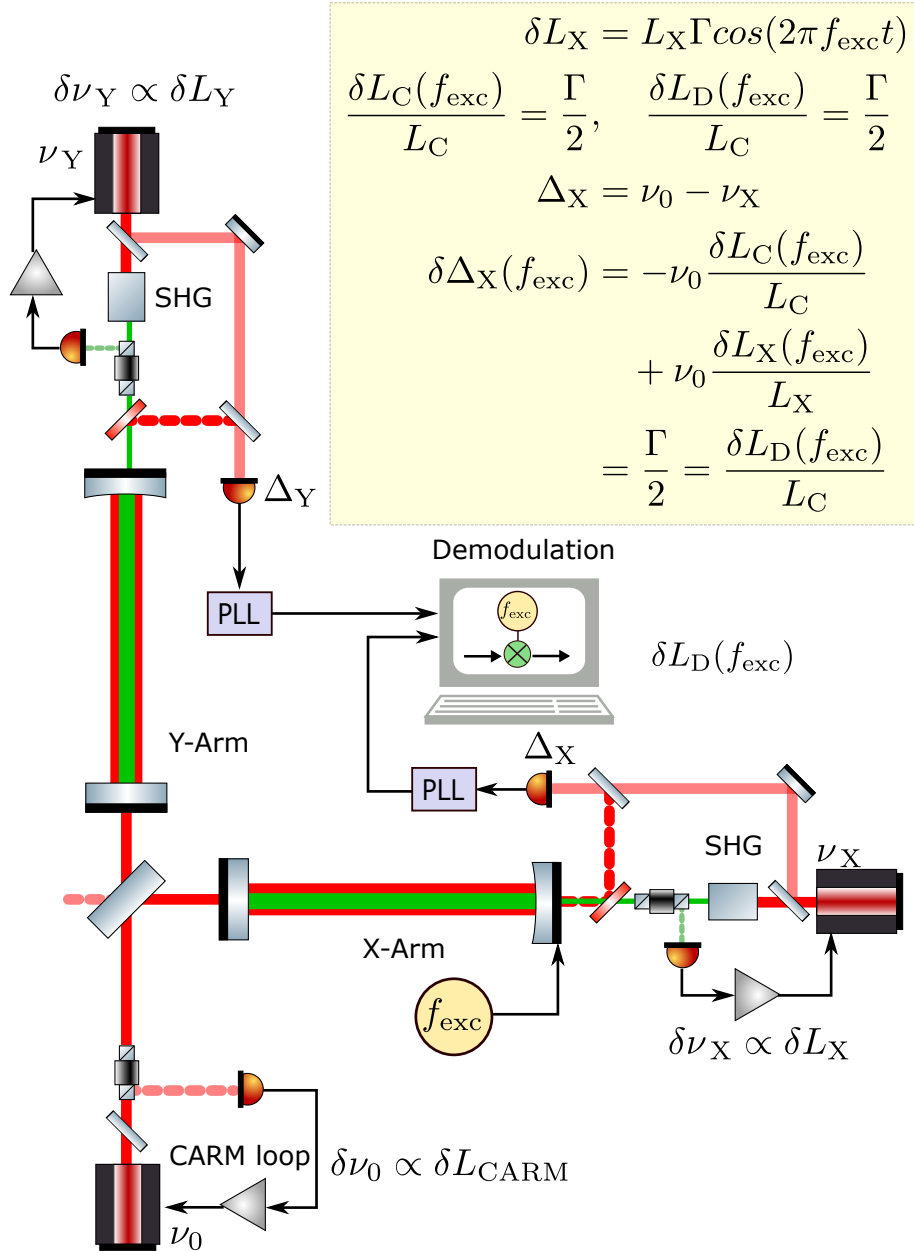Thus the main laser frequency carries half as much strain of a single arm within its loop bandwidth. This is interesting to look a bit deeper. The single-arm actuation is equivalent to applying half as much strain actuation in both DARM and CARM simultaneously. For calibration lines that are within the CARM loop bandwidth, half of the strain would transfer to relative main laser frequency fluctuations. For calibration lines outside the CARM loop bandwidth (which will not be the case in the full lock configuration of Advanced LIGO), the main laser frequency does not see these lines. The equal division of applied strain in DARM and CARM modes depends on the macroscopic arm lengths. If the arm lengths are equal to within 0.1%, we can take them to be equal in our calculations without worrying about the strain mismatch. Even if they are not equal, measuring 4 km arms to better than 40 cm accuracy is not that hard and can be easily done to get the correct division of strain. For now, we'll assume that the arm lengths are equal to each other within 0.1%.

9.2.4 Beatnote frequency measurement

If beatnote is measured between the locked main laser frequency and seed laser of the auxiliary laser, we get the following relations:

$$
\begin{aligned}
\delta\tilde{\nu}_{\text{beat}}(s) &= \delta\tilde{\nu}_{\text{main}}(s) - \delta\tilde{\nu}_{\text{seed}}(s) \\
&= \frac{1}{2}H_{L\to\nu}(s)\nu_{\text{main}}\frac{\delta\tilde{L}_x(s)}{L_x} - G_{L\to\nu}(s)\nu_{\text{seed}}\frac{\delta\tilde{L}_x(s)}{L_x} \\
&= \nu_{\text{main}}\left(\frac{1}{2}H_{L\to\nu}(s) - G_{L\to\nu}(s)\right)\frac{\delta\tilde{L}_x(s)}{L_x}
\end{aligned}
\tag{9.8}
$$

Here we used the fact that $\nu_{\text{main}} \approx \nu_{\text{seed}}$ within 0.1%. One can easily verify that the beatnote frequency fluctuations come out to be the same in the case when the beatnote is measured between the second harmonic of the main laser frequency and the auxiliary laser.

If the beatnote frequency is demodulated at the calibration line frequencies to get $\delta\nu_{\text{beat},i}$, then we get the following relationship:

$$
\begin{aligned}
\delta\nu_{\text{beat},i} &= \nu_{\text{main}}\left(\frac{1}{2}H_{L\to\nu} - G_{L\to\nu}\right)\Gamma_i \\
\Gamma_i &= \frac{\delta\nu_{\text{beat},i}\,\lambda_{\text{main}}}{c\left(\frac{1}{2}H_{L\to\nu} - G_{L\to\nu}\right)}
\end{aligned}
\tag{9.9}
$$

Thus, we have a physical calibration for Γ_i that can be used to calibrate the DARM strain. Let's verify this expression for a line at around 30 Hz which is within the bandwidth of both the CARM loop and the auxiliary loop. This line would very high open loop gains $H_{\text{OL}}(30\text{Hz}) \gg 1$, and $G_{\text{OL}}(30\text{Hz}) \gg 1$ so that $H_{L\to\nu}(30\text{Hz}) \approx -1$ and $G_{L\to\nu}(30Hz) \approx -1$ giving $\Gamma_{30\text{Hz}} = 2\delta\nu_{\text{beat},30\text{Hz}}\lambda_{\text{main}}/c$. While if the calibration line is at 500 Hz which could be outside the CARM loop bandwidth with still well within the auxiliary laser loop bandwidth, we get $H_{\text{OL}}(500\text{Hz}) \ll 1$, and $G_{\text{OL}}(500\text{Hz}) \gg 1$ so that $H_{L\to\nu}(500\text{Hz}) \approx 0$, and $G_{L\to\nu}(500\text{Hz}) \approx -1$ giving $\Gamma_{500\text{Hz}} = \delta\nu_{\text{beat},500\text{Hz}}\lambda_{\text{main}}/c$. Note that there is a factor of 2 difference between the two cases, but in either case, as long as the calibration lines are within the bandwidth of the auxiliary laser loop, we can utilize the demodulated beatnote to estimate the actual single arm strain Γ_i and thus the actual DARM strain that was applied $\Gamma_i/2$.
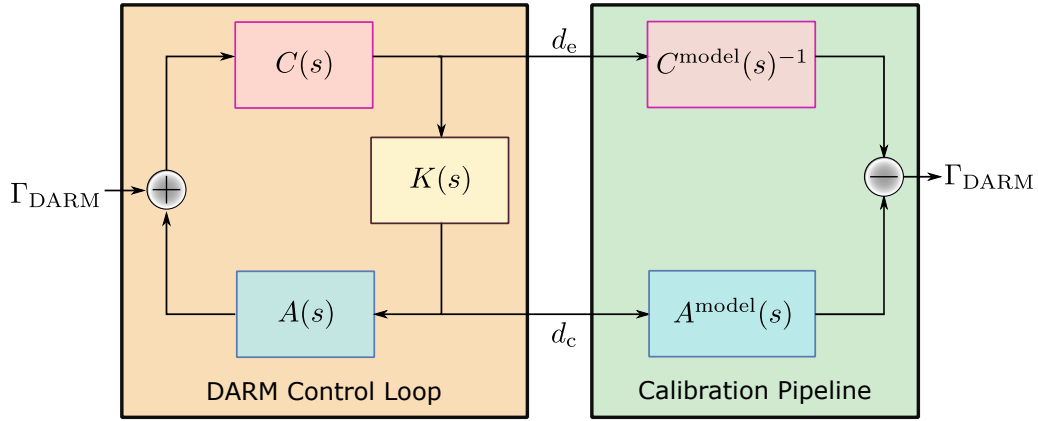
Figure 9.4: DARM loop controls the DARM strain to zero point. True injected DARM strain can be calculated by taking appropriate difference of DARM error point signal scaled by inverse of sensing transfer function $C^{\text{model}}(s)^{-1}$, and DARM control point signal scaled by the actuation transfer function $A^{\text{model}}(s)$. Since our calibration scheme gives direct access to injected DARM strain at the calibration line frequencies, one can fit the transfer function parameters to obtain true DARM strain output at the line frequencies.

9.2.5 Calibrating the DARM strain

For a DARM strain appearing in the arms, we can calculate the error point signal and control point signal using the control loop diagram shown in Fig. 9.4.

$$
\begin{aligned}
d_{\text{e}}(s) &= (\Gamma_{\text{DARM}} + d_{\text{c}}(s)A)C(s) \\
d_{\text{c}}(s) &= d_{\text{e}}(s)K(s) \\
d_{\text{e}}(s) &= \frac{C(s)}{1 - CKA(s)}\Gamma_{\text{DARM}} \\
d_{\text{c}}(s) &= \frac{C(s)K(s)}{1 - CKA(s)}\Gamma_{\text{DARM}}
\end{aligned}
\tag{9.10}
$$

Note, we have taken the convention of not assuming unaccounted negative signs in the loop. All signs are absorbed in the transfer function blocks in the loop shown. Then, the following combination of error and control points gives the injected DARM strain:

$$
\Gamma_{\text{DARM}} = \frac{d_{\text{e}}(s)}{C(s)} - d_{\text{c}}(s)A(s)
\tag{9.11}
$$

Thus to calibrate, we need to model transfer functions for $C(s)$ and $A(s)$. For Fabry-Pérot Michelson Interferometer (FPMI), we assume that $C^{\text{model}}(s)$ is a simple low pass filter due to the DARM cavity pole with some gain due to the optical gain. For

Symbol	Description	Units
g_d	DARM optical gain	DARM error point cts
f_d	DARM cavity pole freuqnecy	Hz
a_d	DARM strain actuation strength	Hz^2 / (DARM control point cts)

Table 9.1: Parameters for calibration model.

$A^{\mathrm{model}}(s)$, since we are interested in frequencies far above the suspension resonance frequencies ($\sim 1Hz$ for us), we can model it as a 2-pole at 0 Hz filter with some gain. This is because the suspension resonance frequency changes do not affect the shape of the transfer function above the resonance, it goes down as $1/f^2$ with changes in overall strength only. Thus we introduce the parameters listed in Table 9.1.

And we defined the model transfer functions as:

$$
\begin{aligned}
C^{\mathrm{model}}(f) &= \frac{g_d}{1 + if/f_d} \\
A^{\mathrm{model}}(f) &= -\frac{a_d}{f^2}
\end{aligned}
\tag{9.12}
$$

Thus while calibration lines are on, we demodulate the beat frequency signal at the calibration line frequencies to obtain $\Gamma_{\mathrm{DARM},i} = \Gamma_i/2$ and we demodulate DARM error and control points at the same line frequencies to get $d_{\mathrm{e},i}$ and $d_{\mathrm{c},i}$. Then we obtain the values for g_d, f_d, and a_d such that the following cost function is minimized (simple least squares estimate):

$$
\sum_i \left(d_{\mathrm{e},i} \frac{1 + if_i/f_d}{g_d} + d_{\mathrm{c},i} \frac{a_d}{f_i^2} - \Gamma_{\mathrm{DARM}} \right)^2
\tag{9.13}
$$

This completes one instance of calibration. Depending on how long we integrate that is how small the low pass filter cut-off frequency we use in the demodulation of the signals, we can repeat this calculation periodically to calibrate the DARM output in real time. For example, if we choose to integrate for 100s, we would implement a 0.01 Hz low pass filter in the demodulation, and would ideally wait for 500s after any changes to the calibration model to read back the demodulated signal. Thus we can correct the calibration model every 500s in this scenario.

9.3 Uncertainty sources

The calibration of the detector can be off of the true value due to two possible reasons. First, the measurement is noisy due to statistical noise in the different

terms appearing in Eq. 9.9. Second, the measurements of the different terms in Eq. 9.9 can be off the true value due to a systematic error, such as miscalibration of the measurement apparatus or 1/f noise in the measurement apparatus such as ADC, DAC, etc. It is important to understand why 1/f noise, also known as flicker noise, is not the same as statistical noise.

9.3.1 Systematic uncertainty due to flicker noise
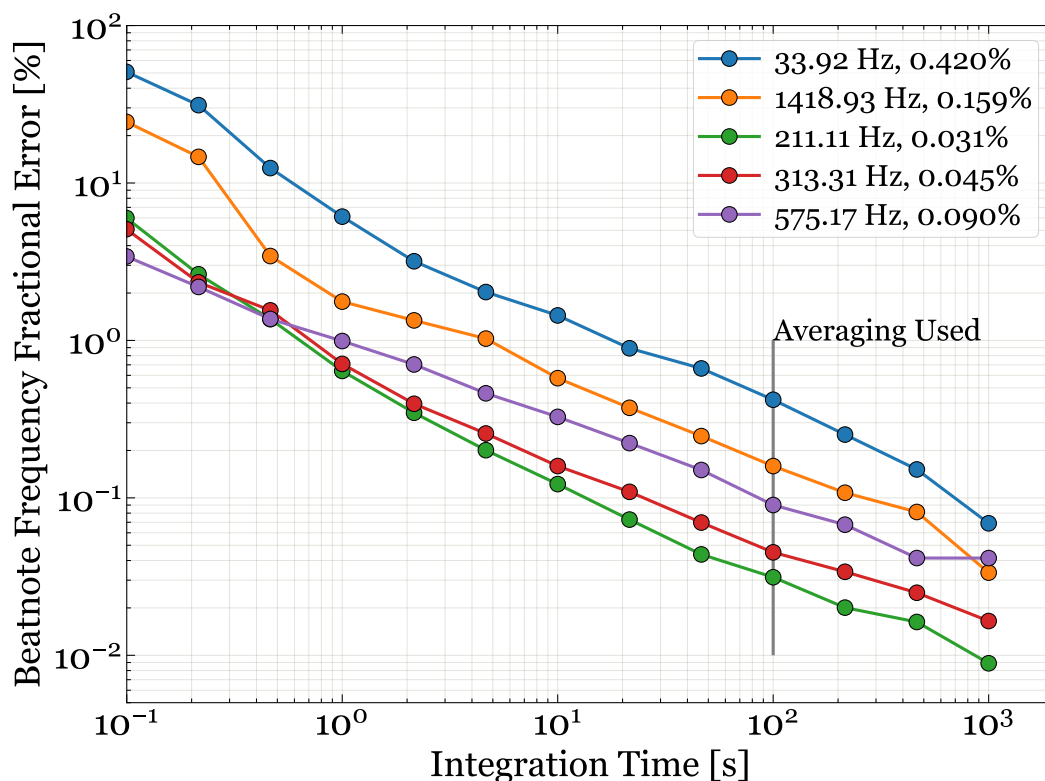
Figure 9.5: The beatnote frequency signal is demodulated at the calibration line frequencies to measure the content of strain signal coming at the calibration line frequency. To estimate how long we can average or how small filter cut off frequency can be used while demodulating, we need to see when the flicker noise limits the benefit of averaging longer. This is the ITMY actuation calibration signal used in Sec.10.2 averaged with different integration times. We chose 100 seconds of averaging in our proof of concept test but it can be seen that only 575.17 Hz line showed any sign of saturation above 500s of averaging while other lines could in principle be averaged longer than 1000s.

When averaging a measurement, common intuition is that if you average for longer, you sample more points, and thus the standard deviation of the measurement goes down as the square root of the number of sample points. But not all points are independent in time-varying signals. Taking an average for a time τ of a time-varying signal is equivalent to applying a low pass filter on the signal with a cut-off

frequency of $1/\tau$ and then summing up the output of the filter. The averaging reduces noise in the measurement by suppressing high-frequency noise above $1/\tau$ Hz. The noise is suppressed by the frequency domain response of the single pole low pass filter, that is, $1/f$. Thus averaging works for reducing the noise if the noise in the signal is dominated by a source, whose noise spectral density drops slower than $1/f$, like $1/f^{-0.5}$, or flat noise, etc. But if the noise spectral density is dominated by flicker noise which goes as $1/f$, then the averaging does not help and the standard deviation remains constant even after averaging for longer.

If the dominating noise source is worse, like $1/f^2$, one would see the standard deviation increasing with an increase in averaging time. Almost all processes and thus signals in the world are limited by flicker noise at low frequencies and even steeper noise sources below that. This means that there is an optimal averaging time for estimating the signal to the best possible estimate beyond which the estimate will become more uncertain because the system drifts over long periods. At this junction, this kind of error is systematic noise, since it is not possible to statistically remove it.

We analyzed the beatnote frequency signal to look for uncertainty due to systematic noise coming from low-frequency drifts like flicker noise. For this purpose, we looked at the beatnote frequency signal mixed with the calibration line frequency and averaged it with different averaging times. Fig. 9.5 shows the Allan deviation for one such dataset taken for calibration of ITMY actuation (discussed in Sec.10.2). We see that the fractional error is not saturating for any line up to 400 seconds of averaging, and except for 575.17 Hz, all other lines kept improving with averaging up to 1000s. Our goal for this calibration method is to have a calibrator running at a 0.01 Hz rate, so we do not plan to integrate longer than 100 seconds anyways. This measurement proves that the beatnote frequency measurement is not limited by systematic noise due to flicker noise, and provides the statistical uncertainty limit for each line. Alternatively, if the averaging is not limited by flicker noise, one can use this method with longer integration times to calibrated the photon calibrator and use the photon calibrator for the in-between time when it is not getting calibrated. To do this properly, the two methods should be run together to identify the drift time in photon calibrator calibration and this method can be used with long averaging times to calibrate photon calibrator once in a while to keep it corrected against systematic drifts.

9.3.2 Systematic offset uncertainty

If the measurement of any of the terms in Eq. 9.9 is at an offset from the true value, we would have a systematic uncertainty that is not possible to remove or avoid by careful averaging. The best we can do is make our measurement robust to such kind of systematics. The arguments become qualitative at this point as it is not possible to find such systematics until an even better calibration method can be used to compare against them. One simple first check would be to use whatever method is available with its worse uncertainty to compare if the two methods agree with each other within their confidence interval. In Fig. 10.5 we compared the actuation calibration of ITMY performed using the beatnote frequency and by using the Michelson interferometer fringes as that is the only other method available at CIT 40m to compare our calibration method against. Here, we do see a systematic offset between the two methods but we do not know which method the systematic is coming from. At the Advanced LIGO sites, Photon calibration should be used to perform this comparison test to rule out and/or debug any systematic offsets in this calibration method, if found.

Additionally, we can individually estimate how much each term in Eq. 9.9 could be off from the true value based on experience. Here we list some possible systematic uncertainty sources:

λ_{main}:

The main laser frequency is known accurately to 5 digits from the spec sheet of the laser. Since the tuning range of the NPRO laser we use is 30 GHz as per the datasheet, the systematic shift from tuning the laser crystal temperature can be a maximum of 0.01%. This is not a true limitation though since we can use the Iodine spectrum line P 83(33-0) [85] compared with the frequency-doubled main laser to measure the wavelength to better than 0.1 ppm. After this measurement, the temperature drift of the free-running laser is reported to be less than 50 MHz/hour which means even with no temperature stabilization efforts, the systematic error would be less than 0.2 ppm due to this drift. All these points support the fact that the high frequency of laser as a reference gives immense relative error advantage for making precision measurements.

Source	Estimated drift [%]	Estimated effect on calibration [ppm]				
		33.921 Hz	211.110 Hz	313.31 Hz	575.17 Hz	1418.93 Hz
Incident power fluctuations	10	0.05	95	0.03	0.04	0.02
RFPD response function	1	0.005	9.5	0.003	0.004	0.002
Laser Mode Matching	10	0.05	95	0.03	0.04	0.02
Laser phase modulation index	1	0.005	9.5	0.003	0.004	0.002
Actuator strength drift	1	0.005	9.5	0.003	0.004	0.002
Swept sine measurement bias	0.17	0.001	1.62	0.001	0.001	-
Total	-	0.071	135.5	0.044	0.051	0.022

Table 9.2: Worst case scenario estimation of systematic effects on calibration due to CARM loop fluctuations

$H_{L \to \nu}$:

The transfer function from CARM length fluctuations to the main laser frequency is used in the measurement. This transfer function is measured before the start of calibration (when calibration frequency lines are turned on). It can drift over time due to optical gain drift of the CARM PDH error signal. To increase the robustness of our calibration against such drifts, we implemented digital filters in the CARM servo loop. A resonant gain filter with 60 dB gain is applied at 33.921 Hz to ensure that the open loop gain for CARM loop is high and that the loop follows the length fluctuations faithfully at this calibration line. Using Eq. 9.7, we see that:

$$\frac{\Gamma_i}{\Gamma_i} = \left| \frac{H_{L \to \nu}}{H_{L \to \nu} - 2G_{L \to \nu}} \right| \frac{\Delta |H_{L \to \nu}|}{|H_{L \to \nu}|}$$
$$\frac{\Delta |H_{L \to \nu}|}{|H_{L \to \nu}|} = \left| \frac{1}{1 - H_{\text{OL}}} \right| \frac{\Delta |H_{\text{OL}}|}{|H_{\text{OL}}|} \tag{9.14}$$

To reduce the effect of fluctuations in OLTF, we implement resonant gain at 33.921 Hz in the CARM loop to have a very high gain at this frequency. While for calibration lines outside the loop bandwidth, we apply deep notches in the CARM loop to ensure the loop does not respond at those frequencies (see Fig. 10.6). Table. 9.2 lists different sources of drift in CARM loop gain and their effect on

Source	Estimated drift [%]	Estimated effect on calibration [ppm]				
		33.921 Hz	211.110 Hz	313.31 Hz	575.17 Hz	1418.93 Hz
Incident power fluctuations	10	61.3	74.4	324.2	1115	5194
RFPD response function	1	6.1	7.4	32.4	111.5	519.4
Laser Mode Matching	10	61.3	74.4	324.2	1115	5194
Laser phase modulation index	1	6.1	7.4	32.4	111.5	519.4
Actuator strength drift	1	6.1	7.4	32.4	111.5	519.4
Swept sine measurement bias	0.17	1	1.3	5.5	19	88.3
Total	-	87.4	106	462	1589	7401
Total with optical gain correction	-	12.3	14.9	65.1	224	1043

Table 9.3: Worst case scenario estimation of systematic effects on calibration due to AUX loop fluctuations. In the last row, it is assumed that by correcting with realtime measured transmitted laser power, the drift in optical gain is suppressed to 1%.

the calibration. We see that the uncertainty in the calibration of strain even with worst-case scenarios does not go beyond 0.1% (1000 ppm) for any of the lines. The uncertainty is maximum for the 211.11 Hz line because it is very close to the UGF of the loop (200 Hz) and the notch is not deep enough there.

$G_{L \to v}$:

The auxiliary loop transfer function is also used for the measurement and all lines are within the UGF of this loop. Ideally, we want the auxiliary loop to follow the lines with high fidelity, which means we should implement resonant gain filters in the feedback filter for this loop. Since this loop is high bandwidth though, it is implemented with analog filters at CIT 40m and the team is still working on trying to insert a digital resonant filter using FPGA in this loop. Without such resonant gains, the nominal gain of the loop at the calibration line frequencies will determine the uncertainty at different lines. Using Eq. 9.4, we see that:
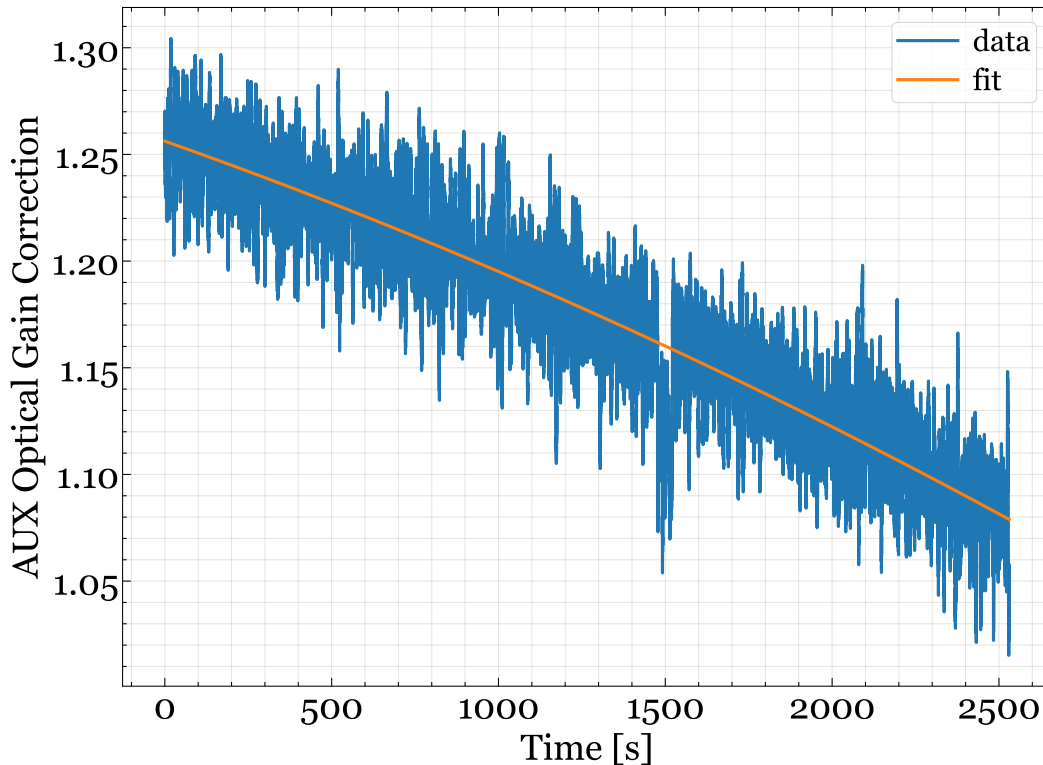
Figure 9.6: AUX loop optical gain correction applied while calibrating ITMY actuator response. The circulating power in the cavity drifts due to angular misalignment of the cavity with respect to the input beam. This can be avoided with good angular stabilization. We have found that hysteresis in coil actuators cause a slow DC drift when calibration lines are turned on the coil actuators.

$$
\frac{\Gamma_i}{\Gamma_i} = \left| \frac{G_{L \to v}}{\frac{1}{2} H_{L \to v} - G_{L \to v}} \right| \frac{\Delta |G_{L \to v}|}{|G_{L \to v}|}
$$
$$
\frac{\Delta |G_{L \to v}|}{|G_{L \to v}|} = \left| \frac{1}{1 - G_{\mathrm{OL}}} \right| \frac{\Delta |G_{\mathrm{OL}}|}{|G_{\mathrm{OL}}|}
$$
(9.15)

Fig. 10.7 shows the measured open loop gain during calibration measurement. We performed a fit to extract the value at 33.921 Hz where the loop gain is so high that the measurement setup runs out of dynamic range. Using the values from this curve, we estimate uncertainty contributions from different sources of drift in AUX loop gain in Table. 9.3. We again see that due to less gain at higher frequencies, the possible systematic uncertainty goes above 1000 pm, primarily due to laser power fluctuations or mode matching fluctuations that happen due to cavity misalignment. Both these effects reduce the circulating power inside the cavity which reduces the PDH error signal optical gain for the loop. To get around this problem, we

measure the transmitted power of the auxiliary laser from the arm cavity which is directly proportional to the circulating power inside the cavity. We calculate the ratio of this power from the power when the transfer function was measured and use this correction in real time for the value of $G_{L\to\nu}$ used in calculating Γ_i. Fig. 9.6 shows the optical gain correction applied in this measurement. This way, we reduce the contribution from circulating power fluctuations and the resulting possible systematic uncertainty. Note that these are still very pessimistic estimates but fluctuations in phase modulation index or RFPD response functions are not of the order of 0.1% in practice. This limitation is also not fundamental as laser locking bandwidths well above 100 kHz can be achieved easily if uncertainty from this source is to be reduced in the future.

Source	Estimated drift [%]	Estimated effect on calibration [ppm]				
		33.921 Hz	211.110 Hz	313.31 Hz	575.17 Hz	1418.93 Hz
L_X	0.13	653	17	18	18	18
L_Y	0.03	127	3	3	3	3
Total	-	665	18	18	18	18

Table 9.4: Systematic effects on calibration of DARM strain due to uncertainty in arm length

$\delta\nu_{\text{beat},i}$ measurement:

The beatnote measurement setup is specifically designed to accurately measure the beatnote fluctuations. The calibration of DFD is good to 0.03% certainty[51] which includes the effects of all electronics in the chain to digital counts. We measured the effect of amplitude modulation of beatnote frequency showing up as frequency modulation due to the phase tracker servo. This value is also very small, 0.09%. By normalizing the inputs before sending them to the phase tracker, we removed this source of error in our measurement (See Sec.10.1.1).

Arm length measurements:

In Eq. 9.9, the arm lengths do not show up explicitly because we made the assumptions about the arm length being equal to each other. The full form without any assumptions is:

$$\delta\Gamma_{\text{DARM}} = -2\frac{L_X L_Y}{(L_X + L_Y)^2}\frac{1}{\frac{L_Y}{L_X+L_Y}H_{L\to\nu} - G_{L\to\nu}}\frac{\lambda_{\text{main}}\delta\nu_{\text{beat,i}}}{c} \qquad (9.16)$$

Source	Symbol in Eq. 9.9	Estimated effect on calibration [ppm]				
		33.921 Hz	211.110 Hz	313.31 Hz	575.17 Hz	1418.93 Hz
Laser WaveLength	λ_{main}	100	100	100	100	100
CARM OLTF Drift	H_{OL}	0.071	135.5	0.044	0.051	0.022
AUX OLTF Drift	G_{OL}	12.3	14.9	65.1	224	1043
Beatnote Measurement	$\delta\nu_{\mathrm{beat},i}$	300	300	300	300	300
Arm Lengths	-	665	18	18	18	18
Statistical Uncertainty	-	4200	310	450	900	1590
Total	-	4264	464	554	980	1928

Table 9.5: Total uncertainty budget of multicolor calibration at 40m with worst case scenario systematic effects. As we would want, our uncertainty is limited by the statistical uncertainty for each line. We can improve this by increasing the strength of the signal or by increasing the averaging time, or by reducing the noise in beatnote frequency which is dominated by AUX loop residual frequency noise.

The derivative of this equation with respect to L_{X} and L_{Y} provide the uncertainty propagation. The arm length is measured by measuring the free spectral range of the arm cavity by locking the arm cavity to the auxiliary laser, locking the main laser to the beatnote frequency between itself and the auxiliary laser, and then scanning the laser by changing the offset in the lock point. Table. 9.4 lists the uncertainties in current arm length measurements at CIT 40m. The CIT 40m prototype suffers worse in this case than would be the case of Advanced LIGO as longer arms mean less uncertainty in individual arm length measurement. The above measurement can also be improved further.

Total uncertainty:

We estimate the total uncertainty in our results as the quadrature sum of statistical uncertainty and each worst-case scenario systematic uncertainty that we estimated in the previous sections. Table. 9.5 shows the summary of all the uncertainty sources and total uncertainty expected at each calibration line for measuring DARM strain. Note that we are limited by statistical uncertainty at each calibration line which is the ideal case. The statistical uncertainty can be reduced further by increasing the strength of modulation in each calibration line, increasing the averaging time, or reducing the statistical noise in the measurement by improving the AUX laser loop. The systematic effects can be studied further to narrow the uncertainty due to

them.

Chapter 10

SCHEME IMPLEMENTATION AND TESTING AT 40M PROTOTYPE

In this chapter, I'll describe how we implemented the Multicolor calibration technique at the 40m prototype at Caltech. We'll first go through how ALS is implemented at CIT 40m and how it is different but equivalent to the ALS implementation at the Advanced LIGO. Finally, we'll describe how we calibrated the DARM response of CIT 40m in the Fabry-Pérot Michelson interferometer configuration.

10.1 Arm Length Stabilization (ALS) at CIT 40m

Sec.9.1 introduced the functionality of Arm Length Stabilization (ALS) at the Advanced LIGO and 2nd generation gravitational wave detectors. At CIT 40m, since the arm length is much shorter than 4 km, there is an alternate way to implement the ALS. While Advanced LIGO takes the beatnote between frequency doubled (Green, 532 nm) pick off of the main laser and the transmitted AUX laser, since the AUX laser is generated itself by frequency doubling a seed 1064 nm laser, we can also take a beatnote between a pick off of the AUX seed laser and pick off of the main laser at IR (1064 nm). However, one will need to transmit the seed laser pick-off light from the end station to the vertex area where the main laser is present. For a 40m distance, this can be easily done with an optical fiber cable that does not introduce too much noise over this distance. But the same cannot be done so easily over 4 km at the Advanced LIGO.

However, there are many benefits of taking the beatnote at IR. First, the beatnote is always present whether the AUX laser is locked to the arm cavity or not. This helps in tuning the wavelength of the AUX laser with the laser crystal temperature to ensure the beatnote frequency is within the bandwidth of the beat note photodiode. Second, the beatnote amplitude does not suffer from angular misalignment or drifts of the arm cavity alignment over time. This is essential because as we'll see later, the beatnote amplitude can couple into the frequency motion tracking if it falls below a certain level. Since the AUX green and AUX seed IR are related to each other through a highly coherent[84] second harmonic generation process, the relative frequency noise of the two frequencies remains the same:

$$v_{\text{green}}(t) = 2v_{\text{IR}}(t)$$

$$\delta v_{\text{green}}(t) = 2\delta v_{\text{IR}}(t) \tag{10.1}$$

$$\frac{\delta v_{\text{green}}}{v_{\text{green}}}(t) = \frac{\delta v_{\text{IR}}}{v_{\text{IR}}}(t)$$

Thus, the beat note frequencies in the two cases carry the same information as the relative fluctuations are equal.

$$v_{\text{beat,green}}(t) = v_{\text{Main,green}}(t) - v_{\text{AUX,green}}(t) = 2v_{\text{Main,IR}}(t) - 2v_{\text{AUX,IR}}(t) = 2v_{\text{beat,IR}}(t)$$

$$\delta v_{\text{beat,green}}(t) = 2\delta v_{\text{beat,IR}}(t)$$

$$\frac{\delta v_{\text{beat,green}}}{v_{\text{beat,green}}}(t) = \frac{\delta v_{\text{beat,IR}}}{v_{\text{beat,IR}}}(t)$$

$$\tag{10.2}$$

Thus at CIT 40m, the IR beatnote is implemented. A pick-off from the AUX seed laser is carried over optical fiber to the main laser table in the vertex area. A pickoff from the main laser is coupled into another fiber optic, and the two cables meet in a fiber optic BS whose output is read by a New Focus 1811 fiber-coupled photodiode with a bandwidth of 125 MHz.

10.1.1 Beanote frequency tracking

The beatnote frequency from the photodiode is sent to a Delayline Frequency Discriminator (DFD). Fig. 10.1 shows the implementation of DFD. Due to damage thresholds associated with the fiber-coupled photodiode, the optical power needs to stay low. Thus the signal is amplified after the photodiode for the beatnote tracking. The amplified signal is then split into two paths. One going over 50m of LMR-195 low loss (8.4 dB/100m) coaxial cable. The delayed signal is mixed with the other path signal in LIGO LSC IQ Demodulator Board[86]. If the input beatnote signal is $V_{\text{beat}} cos(2\pi v_{\text{beat}} t)$, then the signal at the two paths is given by:

$$V_{\text{delayed}} = \frac{V_{\text{beat}}}{\sqrt{2}} cos(2\pi v_{\text{beat}}(t - \tau_d))$$

$$V_{\text{short}} = \frac{V_{\text{beat}}}{\sqrt{2}} cos(2\pi v_{\text{beat}} t) \tag{10.3}$$

Here, τ_d is the delay time in the 50m cable. The IQ demodulator creates two quadratures of the short leg signal by using a 90° splitter after amplifying it by 10 dB. Thus the two quadrature outputs of the demodulator look like this:
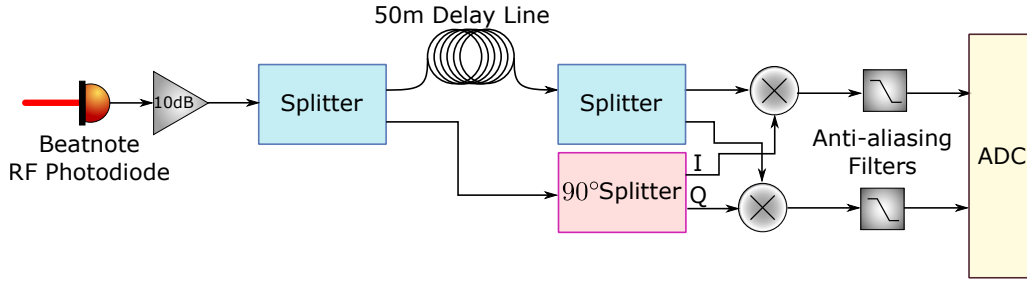
Figure 10.1: Delayline Frequency Discriminato. The beatnote signal is amplified and split into two paths, one 50m long coaxial cable and one connected to a 90° splitter. Mixing the two quadrature outputs with delayed signal measures the frequency of the signal as the arctangent of the two outputs.

$$
\begin{aligned}
V_{\text{beat,I}} &= V_{\text{beat}} M cos(2\pi \nu_{\text{beat}}(t - \tau_d)) cos(2\pi \nu_{\text{beat}} t) \\
&= \frac{1}{2} V_{\text{beat}} M \left(cos(2\pi \nu_{\text{beat}} \tau_d) + cos(2\pi \nu_{\text{beat}}(2t - \tau_d)) \right) \\
V_{\text{beat,Q}} &= V_{\text{beat}} M cos(2\pi \nu_{\text{beat}}(t - \tau_d)) cos(2\pi \nu_{\text{beat}} t - \frac{\pi}{2}) \\
&= \frac{1}{2} V_{\text{beat}} M \left(sin(2\pi \nu_{\text{beat}} \tau_d) + sin(2\pi \nu_{\text{beat}}(2t - \tau_d)) \right)
\end{aligned}
\tag{10.4}
$$

The demodulated signals are low passed at 8 kHz by anti-aliasing filters and read by ADC. This discards the twice-beat note frequency signal part above. The remaining signals are time-varying only because of any motion in the beatnote frequency itself:

$$
\begin{aligned}
V_{\text{beat,I}}(t) &= \frac{1}{2} V_{\text{beat}} M cos(2\pi \nu_{\text{beat}}(t) \tau_d) \\
V_{\text{beat,Q}}(t) &= \frac{1}{2} V_{\text{beat}} M sin(2\pi \nu_{\text{beat}}(t) \tau_d)
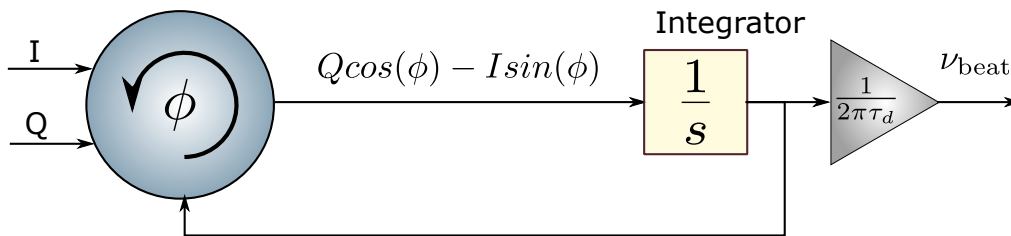\end{aligned}
\tag{10.5}
$$

Figure 10.2: Digital phase tracker schematic for measuring beatnote frequency. The demodulated beatnote I and Q signals from DFD are rotated by ϕ to create an error signal that is integrated. The resulting loop locks ϕ to the $tan^{-1}(Q/I)$ which can be converted into beatnote frequency by dividing by delay time of DFD.

Thus the information about the beatnote frequency and its motion is in the phase between the measured I and Q signals. To unwrap this information, a digital phase tracker is employed. Fig. 10.2 shows how the phase tracker works. The incoming I and Q signals are "rotated" in phase space by multiplying them with $-sin(\phi)$ and $cos(\phi)$ respectively and summing them, for some phase angle ϕ:

$$\epsilon(t) = -\frac{1}{2}V_{\text{beat}}M cos(2\pi v_{\text{beat}}(t)\tau_d)sin(\phi(t)) + \frac{1}{2}V_{\text{beat}}M sin(2\pi v_{\text{beat}}(t)\tau_d)cos(\phi(t))$$
$$= \frac{1}{2}V_{\text{beat}}M sin(2\pi v_{\text{beat}}(t)\tau_d - \phi(t))$$

(10.6)

This error signal is integrated with a 0 pole filter $K(s)$ and substituted for ϕ, thus creating a control loop. Near lock point, $\phi(t) \approx 2\pi v_{\text{beat}}(t)\tau_d$, and thus in Laplace domain:

$$\epsilon(s) = \frac{1}{2}V_{\text{beat}}M\,(2\pi v_{\text{beat}}(s)\tau_d - \phi(s))$$
$$\phi(s) = \frac{1}{2}V_{\text{beat}}MK(s)\,(2\pi v_{\text{beat}}(s)\tau_d - \phi(s))$$
$$\phi(s) = \frac{1}{\frac{2}{V_{\text{beat}}MK(s)} + 1}2\pi v_{\text{beat}}(s)\tau_d$$

(10.7)

Thus, if filter $K(s)$ is adjusted such that $\frac{1}{2}V_{\text{beat}}MK(s) \gg 1$ for the frequencies of interest, then $\phi(s) \approx 2\pi v_{\text{beat}}(s)\tau_d$. Thus one can read the beatnote frequency and its fluctuations by multiplying $\frac{1}{2\pi\tau_d}$ with the control signal of the above loop. This is how we measure the beatnote frequency.

Note that the gain required to have a certain UGF in the phase tracker the loop is dependent on the amplitude of RF power. This proved to be an issue for us since the beatnote amplitude fluctuations change the transfer function from $\phi(t)$ to $v_{\text{beat,meas}}$. We fixed this by normalizing the input to the digital phase tracker by quadrature sum of I and Q signals before applying the rotations. This removes the factor of $V_{\text{beat}}M$ in the above equation gives a clean stationary loop:

$$\phi(s) = \frac{1}{\frac{1}{K(s)} + 1}2\pi v_{\text{beat}}(s)\tau_d$$

(10.8)

With this change, the loop filter $K(s)$ is set to a constant value to get UGF of 2000 Hz, and it remains fixed. In the output of our signal, we can faithfully compensate by

the inverse of the transfer function shown above to get the true beatnote fluctuations as:

$$\nu_{\text{beat,meas}}(s) = \left(\frac{1}{K(s)} + 1 \right) \frac{1}{2\pi\tau_d} \phi(s) \tag{10.9}$$

Note that the above filter is not realistic to implement as it is as it has more zeros than poles. Two high-frequency poles will be required to implement this in real time but we can not put those poles much higher than 2 kHz as the CIT 40m CDS system runs at 16 kHz. So we'll have to correct for the complex gain factor in the demodulated signals offline.

10.2 Actuator calibration test

We tested the multicolor calibration scheme first for calibrating the actuation strength of ITMY. For this test, the scheme is slightly different. ITMY is sent modulation signal at calibration line frequencies to modulate the arm length:

$$L_Y = \sum_i \frac{A_{ITMY}}{f_i^2} \cos(2\pi f_i t) \tag{10.10}$$

Here, A_{ITMY} is the ITMY actuation transfer function strength. The factor of f^2 in the denominator comes from the pendulum suppression above 1 Hz (this expression is only true well above 1 Hz where our calibration line frequencies lie). We are interested in finding the value of A_{ITMY} in units of m Hz^2/cts. Here 'cts' refer to DAC counts that sends the signal to the ITMY actuator.

For the measurement, a single arm, the YARM in this case is locked to the main laser by actuating on cavity length through ETMY. Thus the main laser fluctuations are followed by the YARM length L_Y in this case:

$$\delta\tilde{L}_y(s) = \frac{J_{\text{OL}}(s)}{1 - J_{\text{OL}}(s)} \frac{L_y}{\nu_{\text{main}}} \delta\tilde{\nu}_{\text{main}}(s)$$
$$\delta\tilde{L}_y(s) = J_{\nu \to L_y}(s) \frac{L_y}{\nu_{\text{main}}} \delta\tilde{\nu}_{\text{main}}(s) \tag{10.11}$$

This is only to reduce the motion of the arm cavity with respect to the main laser. The OLTF J_{OL} has notches at the calibration line frequencies f_i to ensure that the arm length is free to move on these frequencies. So $|J_{\text{OL}}(f_i)| \ll 1$ resulting in $J_{\nu \to L_y}(f_i) \ll 1$. Thus at the calibration line frequencies, the arm length does not follow the main laser and is free to be modulated by the actuation provided on ITMY.
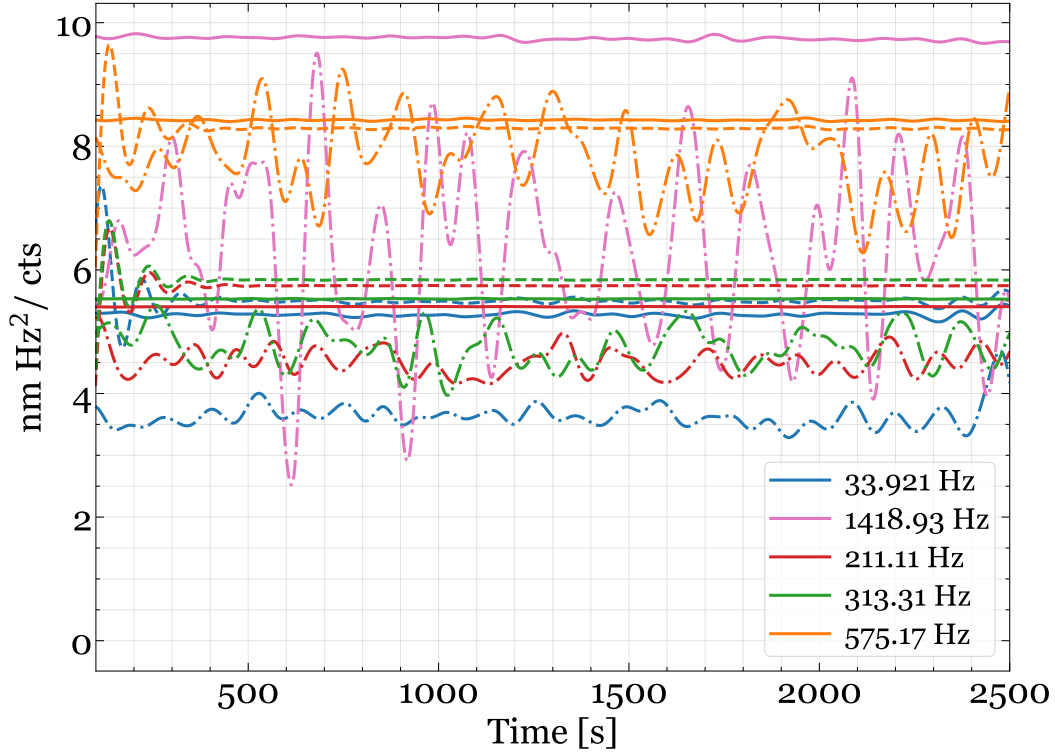
Figure 10.3: Time series of the calibration of ITMY position actuation using multi-color calibration for 3000 seconds duration. The beatnote frequency is demodulated and low passed at 10 mHz with 8th order butterworth filter. The counts (cts) here refer to DAC counts that sends signal to ITMY actuator.

The auxiliary laser is locked to YARM in the same way as shown Sec.9.2.2. The auxiliary laser seed frequency is given by:

$$\delta\tilde{\nu}_{\text{seed}}(s) = \frac{\nu_{\text{seed}}}{\nu_{\text{aux}}}\delta\tilde{\nu}_{\text{aux}}(s) = G_{L\to\nu}(s)\nu_{\text{seed}}\frac{\delta\tilde{L}_y(s)}{L_y} \qquad (10.12)$$

Since the main laser is quiet at the calibration line frequencies, while the auxiliary laser is following the modulations made through ITMY, the beat note frequency between the main laser frequency and seed laser of the auxiliary laser, on demodulation at the calibration line frequencies, gets signal contribution only from the auxiliary laser fluctuations.

$$\delta\tilde{\nu}_{\text{beat},i} = G_{L\to\nu}\nu_{\text{seed}}\frac{\delta\tilde{L}_y(s)}{L_y}$$

$$= G_{L\to\nu}\frac{c}{L_y\lambda_{\text{main}}f_i^2}A_{ITMY} \tag{10.13}$$

$$A_{ITMY} = = \frac{L_y\lambda_{\text{main}}f_i^2}{cG_{L\to\nu}}\delta\tilde{\nu}_{\text{beat},i}$$

This provides a calibration for ITMY actuation transfer function strength. For our test, the AUX loop OLTF had UGF of about 11 kHz, so for all calibration frequencies, $G_{L\to\nu}(f_i) \approx 1$, but we took drift in circulating optical power into account. Fig. 9.6 shows the applied optical gain correction while taking into account varying loop gain. Fig. 10.3 shows the time series of the calibration result where the beatnote frequencies are demodulated and low passed at 10 mHz which is equivalent to averaging for 100 seconds.
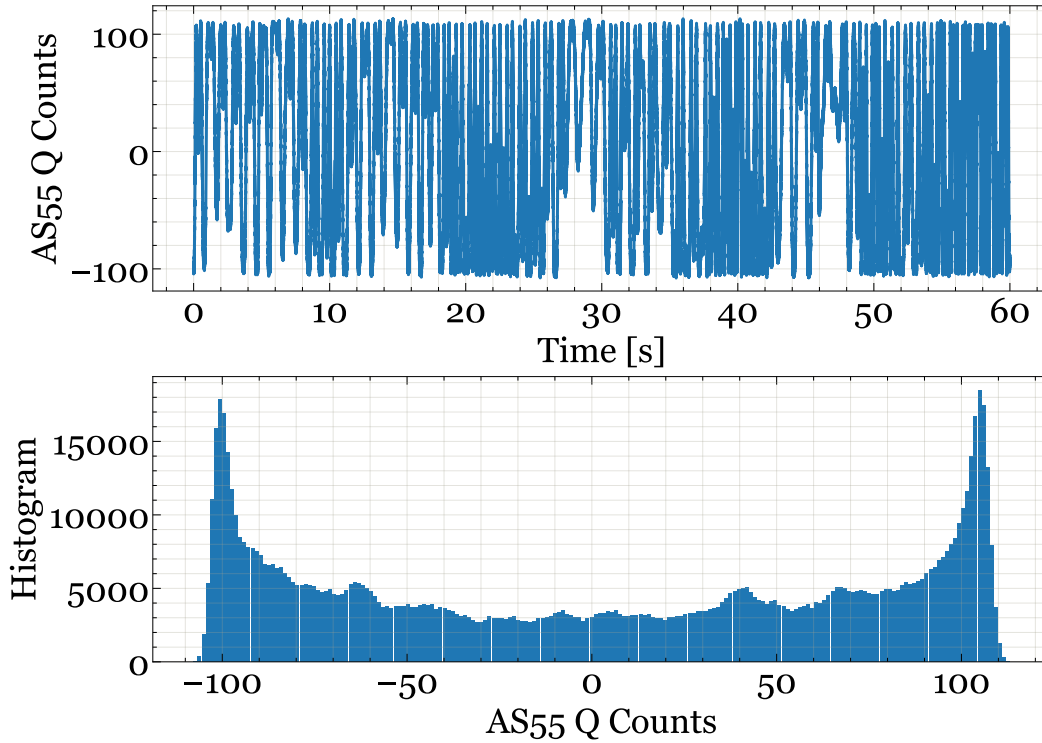
Figure 10.4: AS55 Q signal from the AS port is calibrated using Michelson interferometer when it is allowed to swing freely. The fringe peak-to-peak is proportional to wavenumber of the laser $2\pi/\lambda_{\text{main}}$.

For an ideal suspension, it is expected to get the calibration transfer function strength A_{ITMY} as a frequency-independent parameter. But we found that the actuation is higher for higher frequencies. To verify if this is due to our digital phase locked

loop not working correctly, we performed an offline analysis on the DFD output data. This involves taking the arctangent of the I and Q outputs of DFD directly (see Eq. 10.4). The computation of arctangent is not deployable in our real-time system to remain within the delay constraints, that is why we need the digital phase tracker to do this for us. But in offline analysis, we can verify if the phase tracker worked correctly. In Fig. 10.5 we present the output of the calibration with DFD and phase tracker, and with DFD and the offline analysis. The two measurements closely match, following the same frequency dependence. However, we are not sure what is the reason for the difference between the two. One possibility is that in offline demodulation, the local oscillator source is ideal and does not cancel out the dither and drift of the real-time oscillator which happens in real-time demodulation correctly.
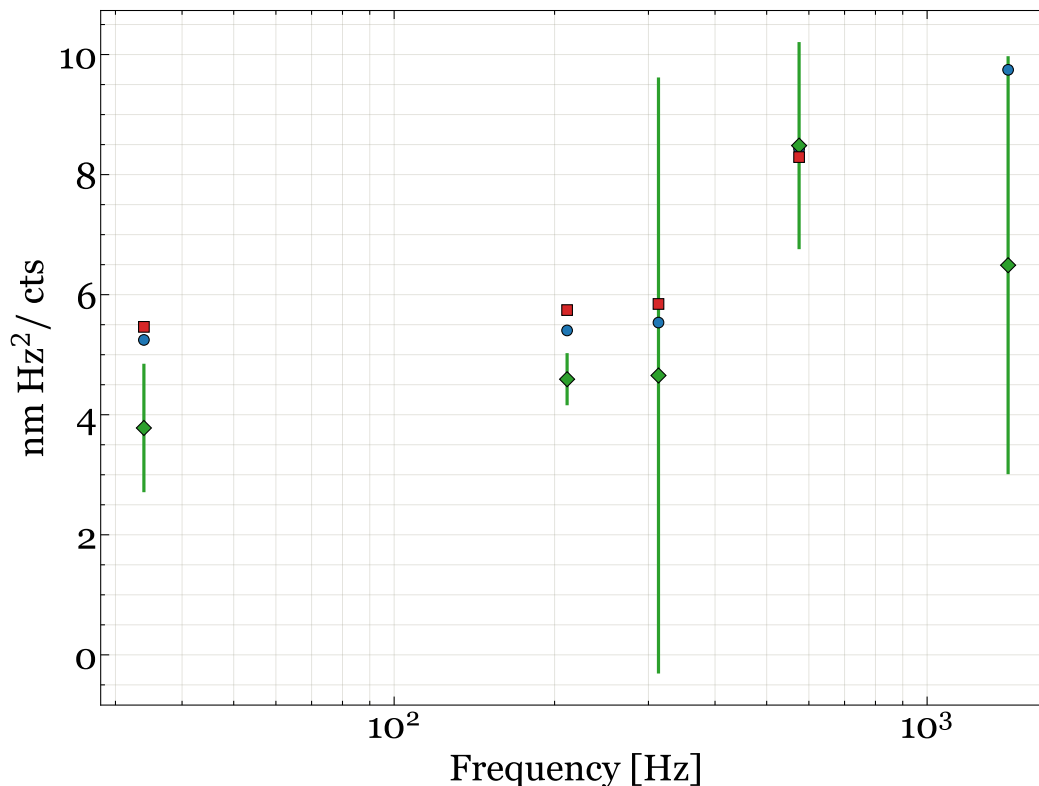
Figure 10.5: Calibration of ITMY position actuation using multi-color calibration and using MICH interferometer. 'circle': Multi-color calibration using the digital phase locked loop in realtime. 'square': multi-color calibration by doing offline analysis of only DFD data. 'diamond': Calibration using the error signal of MICH interferometer lock compared against the peak-to-peak swing in the error signal when MICH is freely swinging. The counts (cts) here refer to DAC counts that sends signal to ITMY actuator.

We used the only other calibration method, the Michelson interferometer, that is

available to us to verify the anomalous frequency dependence of the actuation strength. We first calibrate the error signal to differential displacement in m by measuring the peak-to-peak response of the error signal when the Michelson interferometer is freely swinging through the fringes. This is the most noisy part of this calibration method. To estimate some kind of error estimate, the free swing data is histogrammed and the difference in the 2 peak positions is taken as the full swing value, and the average full width at half maximum of each peak is taken as their standard deviation. Then, the interferometer was locked with UGF of 20 Hz to keep control bandwidth outside of calibration lines, and notches were introduced in the control loop filter at the calibration line frequencies. Thus the error signal in the presence of calibration line modulation at ITMY would measure the displacement of ITMY in meters. This method is prone to a lot of systematics, thus the error bars for Michelson calibration in Fig. 10.5 are still underestimates. However, this method also showed an increase in the actuation strength at high frequencies, but with poor confidence. So the anomalous frequency dependence is still to be solved.

10.3 Multicolor calibration measurement at the 40m prototype

We conducted several measurements for calibrating the DARM output of the 40m prototype in FPMI configuration. These measurements were made to identify the maximum averaging one can do with the multicolor calibration method, and to identify any systematics that can change between different measurements. The measurement sequence was run through a Python script to ensure standardized testing across multiple instances.

10.3.1 Arm locking and alignment

The sequence starts by attempting a lock on the YARM cavity with the main laser loop. Since the interferometer is routinely used to perform other measurements, the arm cavities are nominally aligned enough to acquire the lock at the very least, if not with maximum mode matching. Or the other way around, we ensured before the start of each measurement that the arm cavities are aligned enough that we see good TEM00 mode flashing in the arm cavities for incident main laser on the cameras that are pointed to the suspended test masses. Once the lock is acquired, the UGF of the YARM lock to the main laser is set to 200 Hz. For doing this quickly, a script injects band-limited Gaussian noise between 100 Hz to 400 Hz for 10 seconds and gets the open loop transfer function magnitude in this region. The UGF is identified by a simple linear fit to the transfer function in this region and the gain of the loop

is scaled to take it to 200 Hz. This process takes only 20 seconds and is automated, so every time we acquire a lock on any degree of freedom, we can quickly tune the gain of the feedback filter according to the current optical gain of the system.

Once the YARM is locked, Angular Dither Stabilization Servo (ASS) is run on YARM to match the pointing of the input beam angle to the cavity mode created by YARM (which is in the transmission of the beamsplitter), and to center the beam spots on ITMY and ETMY to reduce any angle-to-length coupling through these two optics. The ASS dithers ITMY , ETMY , PR2, and PR3 in PIT and YAW degrees of freedom at frequencies in the 30 Hz to 100 Hz range. Then we look for the error signal due to input pointing mismatch in the transmitted light intensity and the error signal for beam spot centering in the PDH error signal of the cavity lock. Once these error signals are sufficiently reduced (when the signal-to-noise ratio in measured demodulated signals go below 10 in an average over 2 seconds), the dithering is stopped.

Then we lock the XARM cavity with the main laser, set its UGF, and turn on ASS for this cavity. However, since there is only one steering optic for the XARM cavity (BS), we can not control all 8 degrees of freedom associated with input pointing mismatch and beam spot on the mirrors. We decide to not close the loop on ITMX beam spot centering as it is a flat mirror and thus the beam spot offset has less coupling from the angular motion to the length of the cavity. The beam spot is still centered on ETMX and the input alignment is made the same as the cavity mode alignment by aligning BS and ITMX appropriately. After this, the arm cavities are aligned well with the input main laser beam. Since the input test masses are flat mirrors, they get aligned so that the laser is at normal incidence to the cavities. This in turn aligns the Michelson interferometer as well, so no more alignment is required for the FPMI configuration.

10.3.2 FPMI Locking

The next step in the sequence is to lock FPMI . Three error signals are required to lock the DARM , CARM , and MICH degrees of freedom. For DARM , we used the RF readout technique (see Sec.5.1.2) AS55. For locking CARM and MICH , we use the symmetric port reflected light, demodulated at 55 MHz on REFL55 photodiode. The two quadratures of REFL55 give error signals for CARM and MICH.

The three error signals are dependent on each other to remain in a linear regime though, that is, the error signals are truly useable only when all of them are controlled

together or the interferometer is simultaneously near the lock point for all three error signals. This of course does not happen serendipitously. To get the lock started, we first lock the DARM and CARM using electronically generated CARM and DARM error signals through the individual cavity's PDH error signals. For this purpose, the ITMs have a small wedge angle, which picks off part of the reflected light from each arm cavity into the RF photodiodes named POX11 and POY11. The demodulated signal from these photodiodes is added and subtracted to create electronic CARM and DARM signals like:

$$
\begin{aligned}
\epsilon_{CARM} &= \frac{1}{2} \left(POX11_I + POY11_I \right) \\
\epsilon_{DARM} &= \frac{1}{2} \left(POX11_I - POY11_I \right)
\end{aligned}
\tag{10.14}
$$

The DARM error signal is fed back to the ETMs to create a differential length actuation and the CARM error signal is fed back to the mode cleaner end optic MC2 to lock the main laser (which is locked to the mode cleaner) to the common mode of the two arms:

$$
\begin{aligned}
\zeta_{CARM} &= \frac{1}{\sqrt{2}} MC2 \\
\zeta_{DARM} &= \frac{1}{2} \left(ETMX - ETMY \right)
\end{aligned}
\tag{10.15}
$$

This lock is not robust or clean as we are creating the common and differential arm modes electronically instead of optically using the beam splitter of Michelson, but it allows us to reduce the CARM error signal motion and keep CARM near the lock point. This makes locking MICH easier as it uses the orthogonal quadrature in REFL55 from the CARM quadrature. We adjust the demodulation phase such that the MICH signal appears only in REFL55_Q. We turn on the MICH loop to lock the interferometer output port at the dark point by feeding back to BS. This in turn allows us to swiftly change the error signal for CARM and DARM loops to true optical signals REFL55_I and AS55_Q. This completes the lock acquisition for FPMI . Using the same method mentioned above, the UGF for DARM and CARM are each set to 200 Hz.

Once the lock is acquired, we turn on a set of 5 filters in the CARM loop, each for a calibration line frequency, either increasing the gain at the calibration frequency by 60 dB using a resonant gain filter if it is within the CARM loop bandwidth or

introducing a notch at the calibration line frequency using a notch filter of depth 120 dB. See Sec.9.2.4 for the reasoning behind introducing these filters.
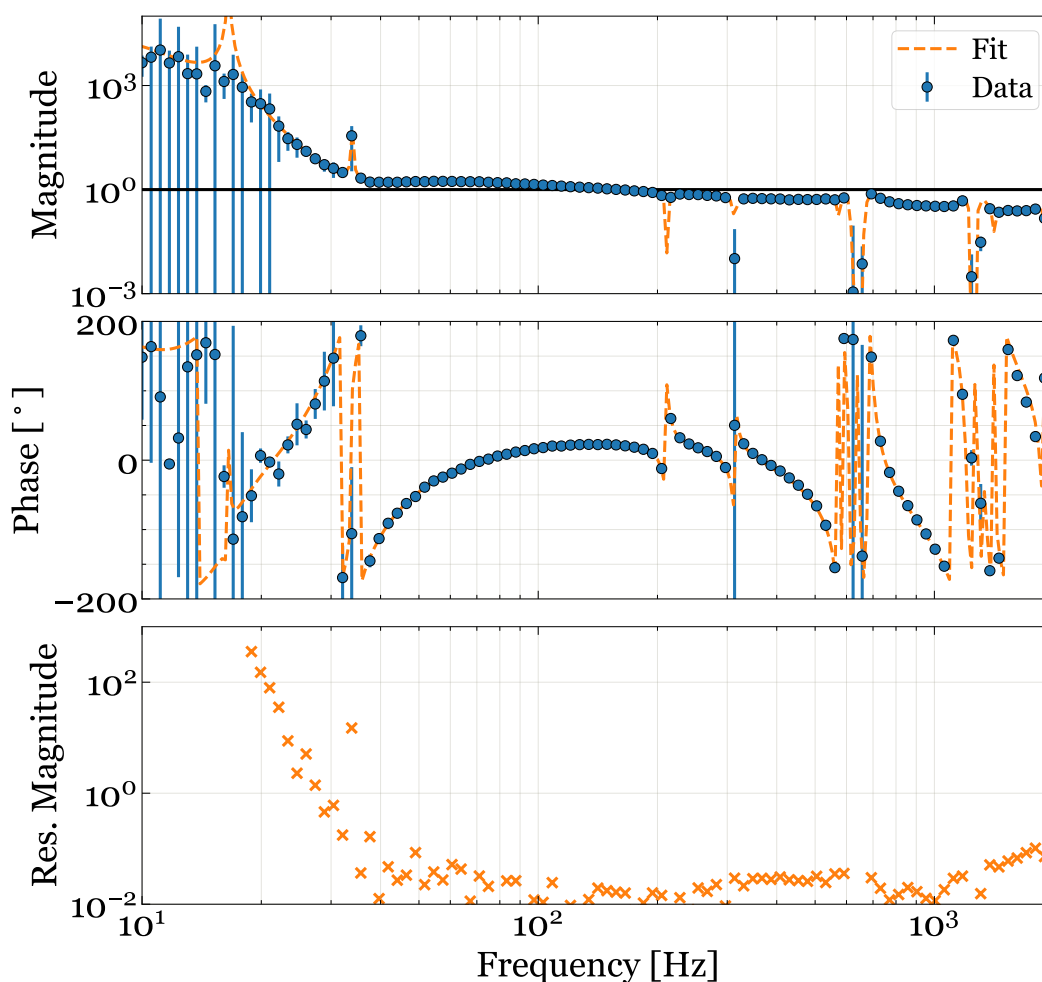

Figure 10.6: CARM OLTF during the measurement. A resonant gain is placed at 33.921 Hz and notch filters are placed at the other calibration line frequencies which are above the UGF of the CARM loop.

10.3.3 Auxiliary Laser Lock and beatnote frequency tuning

The auxiliary laser at the end station on YARM was used for the measurements. Before locking the laser to the YARM cavity, the laser crystal temperature is adjusted to obtain a beatnote of about 40 MHz between the auxiliary seed laser (sent over 40m optical fiber to the vertex area) and the main laser. The laser frequency is modulated at 230 kHz by exciting a PZT resonance on the NPRO crystal. This removes the need for any external phase modulator. The PDH error signal is read in the reflection from the cavity and sent through a PDH servo box to actuate on the laser PZT . We get about 20 kHz of unity gain frequency which is sufficient for this
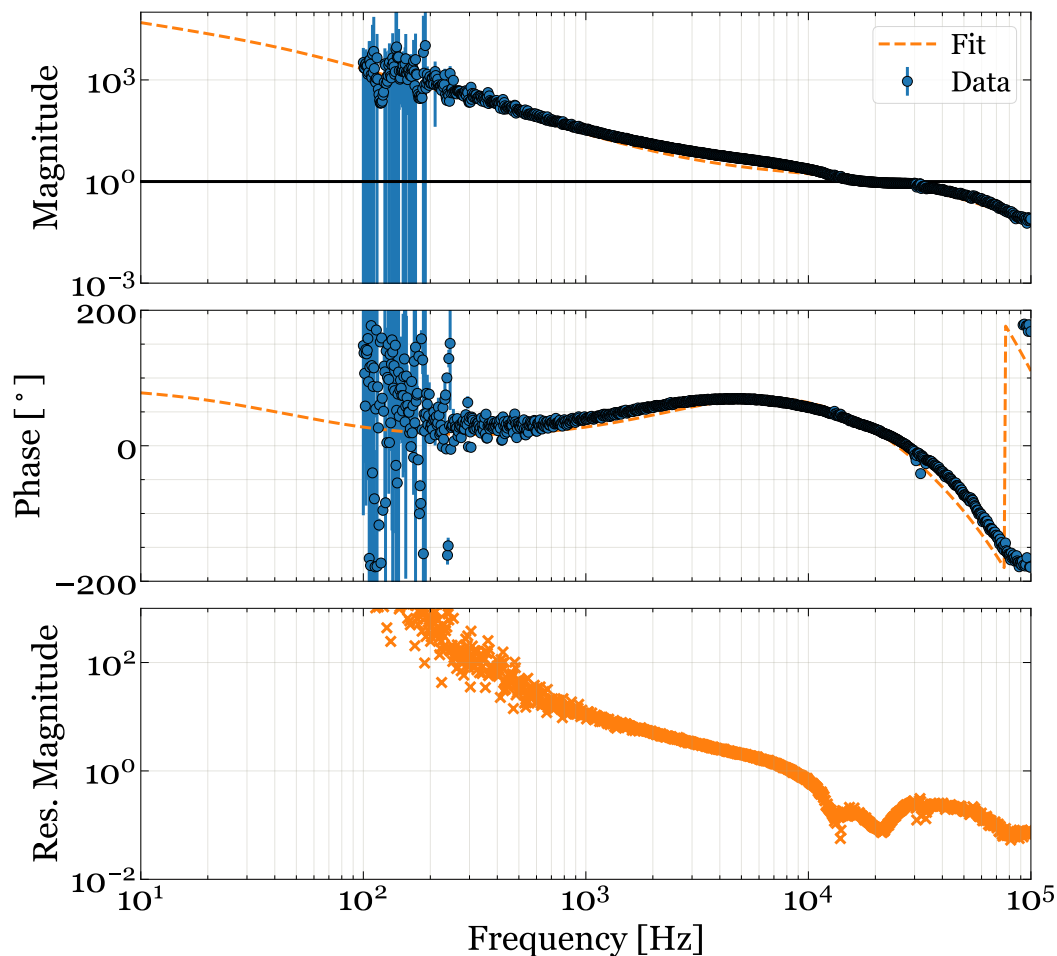
Figure 10.7: YEND Auxiliary laser to YARM lock OLTF near the calibration line frequencies.

proof of principle test, but ideally we need to either extend the UGF further to at least 100 kHz. Or we can use resonant gain filters at the calibration line frequencies used as the calibration uncertainty increases with the fluctuations in this loops gain if the gain is not high enough at the calibration line frequencies. To lock the laser to the YARM , we simply open and close the shutter a few times until the TEM00 mode is locked.

10.3.4 OLTF measurements

Before the calibration is measured, the open loop transfer function for DARM, CARM, and the auxiliary laser loop is measured. The CARM and auxiliary laser loops are important as their values are used in calibration (See Eq. 9.9). Fig. 10.6 shows the CARM OLTF taken at the calibration line frequencies. This measurement is taken to ensure that the loop gain is high at the line frequency within the bandwidth

Line Frequency	Digital DAC Counts	Physical Estimated Actuation [pm]
33.921	10	93.9
211.110	300	72.6
313.310	450	49.5
575.170	750	24.48
1418.930	2000	10.73

Table 10.1: Calibration line frequencies and the digital counts used for actuating at ETMY. The column of estimated physical actuation is obtained by calibrating the ETMY actuation using a beatnote between main laser and auxiliary laser when YARM was locked to the main laser with notches at the measurement lines and auxiliary laser was locked to the YARM.

and very low outside the bandwidth.

Fig. 10.7 shows the OLTF of the auxiliary laser lock with the YARM cavity. The measurement was taken near the calibration line frequencies. Ideally, we would like to have resonant gain filters placed in this loop at the calibration line frequencies to ensure the loop gain is very high at those frequencies. But due to lack of time and equipment availability, we had to make do with no gains and the usual loop filters with the UGF of about 20 kHz.

10.3.5 Reference data measurement

Before turning on the calibration lines, we let the lock stay with the applied settings for 500 seconds to measure the statistical noise in the measurement. This is essentially the integrated noise of the beatnote frequency at the calibration line frequencies when no actuation is applied at these frequencies. This gives us an estimate of the statistical noise in the measurement so that we can place statistical error bars around the calibration constants obtained later.

10.3.6 Calibration measurement and results

The measurement is started by injecting oscillations at the chosen calibration line frequencies. The chosen frequency values and the digital counts of amplitude used for actuating on the ETMY are shown in Table. 10.1. Note that less physical actuation is used at higher frequencies as the noise floor is also significantly less at higher frequencies. The frequencies are scattered around the frequency band of interest to mimic how Advanced LIGO uses the calibration line frequencies. For calibrating just FPMI though, not all these frequencies are required as the number of parameters associated with the model is very small. The filters used for demodulation are 10 mHz 8$^{\text{th}}$ order Butterworth low pass filters.
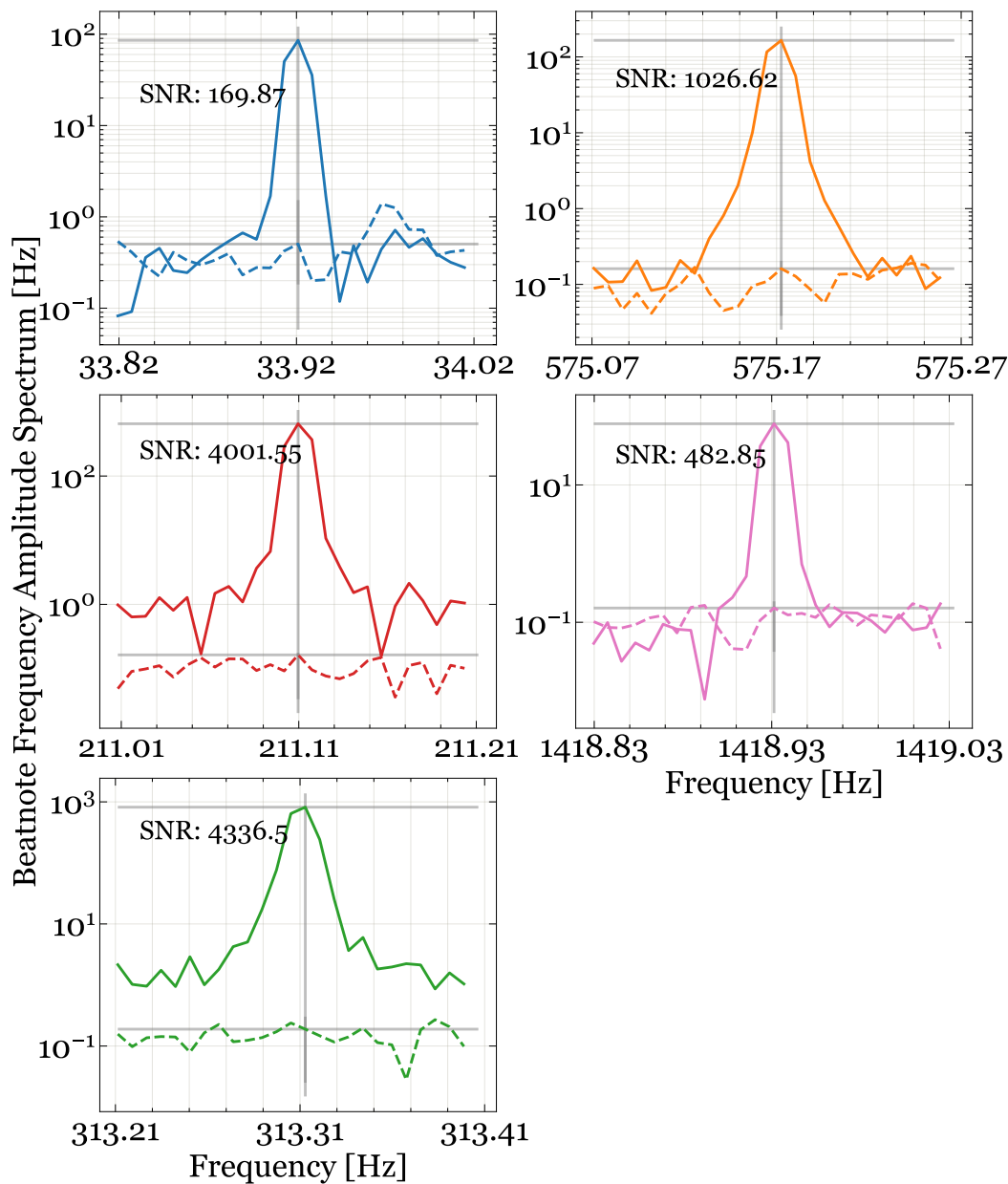
Figure 10.8: Signal-to-noise ratio of calibration lines in measured beatnote spectrum for integration time of 128s.

The first thing to identify is the signal-to-noise ratio (SNR) of each calibration line. We measure the spectrum of the beatnote frequency at 128s averaging which is close to the 100s averaging we applied on demodulated signal. Fig. 10.8 shows the calibration line height for each frequency. Note we achieved an SNR of more than 1000 on three central lines. The 33.921 Hz line could not be actuated any harder as the position-to-angle coupling in the imperfect coil actuation of ETMY resulted in the cavity getting misaligned too much and FPMI lock would fail. For

the 1418.93 Hz line, the actuation gets limited due to the high suppression of force by the suspension at this frequency.
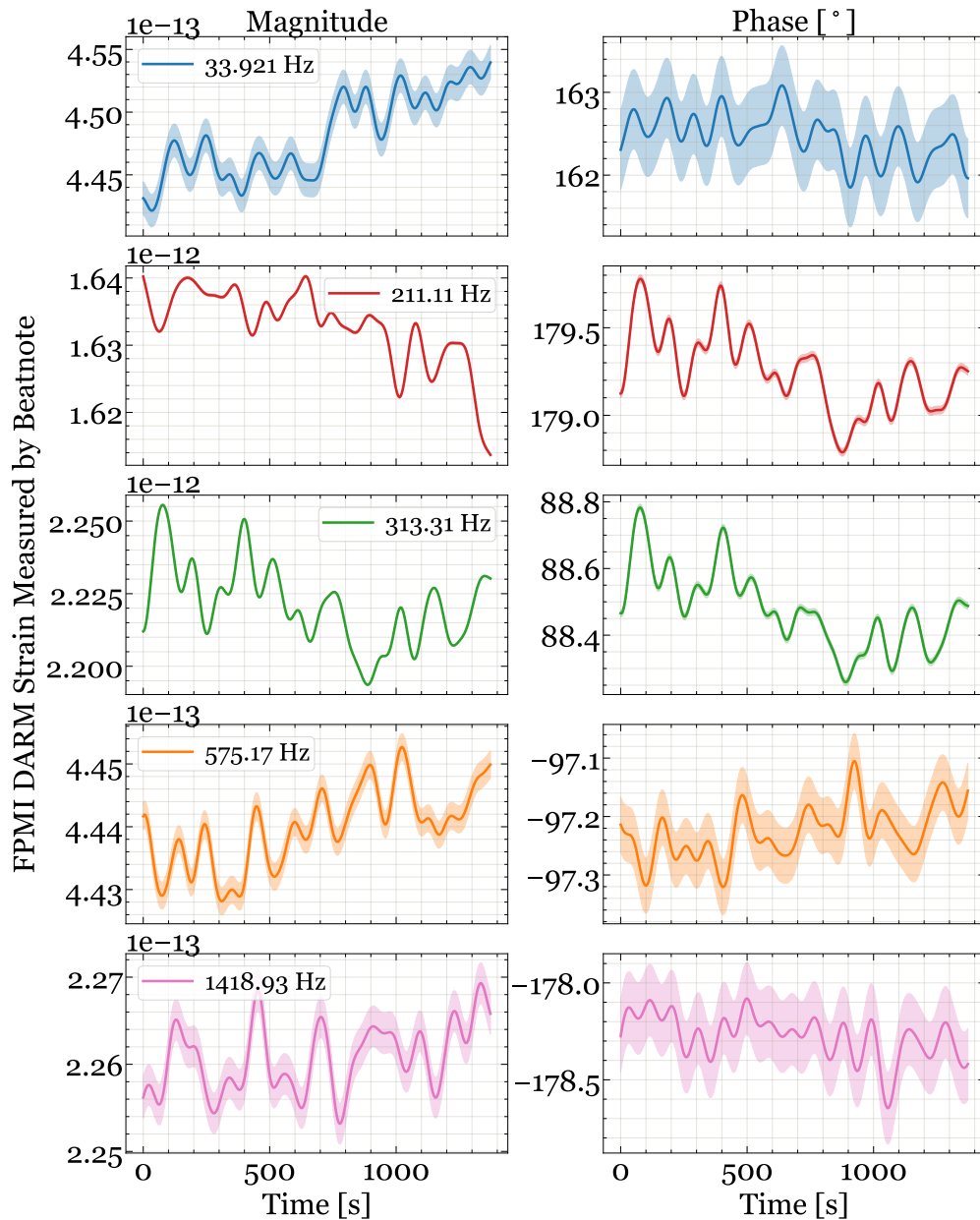
Figure 10.9: Time series of the calibration of DARM strain measured in FPMI configuration using the multi-color calibration scheme. The beatnote frequency is demodulated and low passed at 10 mHz with 8th order butterworth filter. The shaded region shows the statistical noise in the measurement.

Using Eq. 9.9, we calculated the DARM strain as defined in Eq. 9.2 from the measured demodulated beatnote frequency. Fig. 10.9 shows the time series of calibrated DARM strain. The measured value is of the correct order of magnitude. We per-

Figure 10.10: Ratio of the inferred DARM strain using optical gain estimation from Michelson interferometer to the DARM strain measured by beatnote signal. There is a frequency dependent discrepancy between the two measurements.

formed a verification by calibrating the DARM error signal with the Michelson interferometer (2.7×10^{-12} m/err-cts) and using the average actuation strength that was measure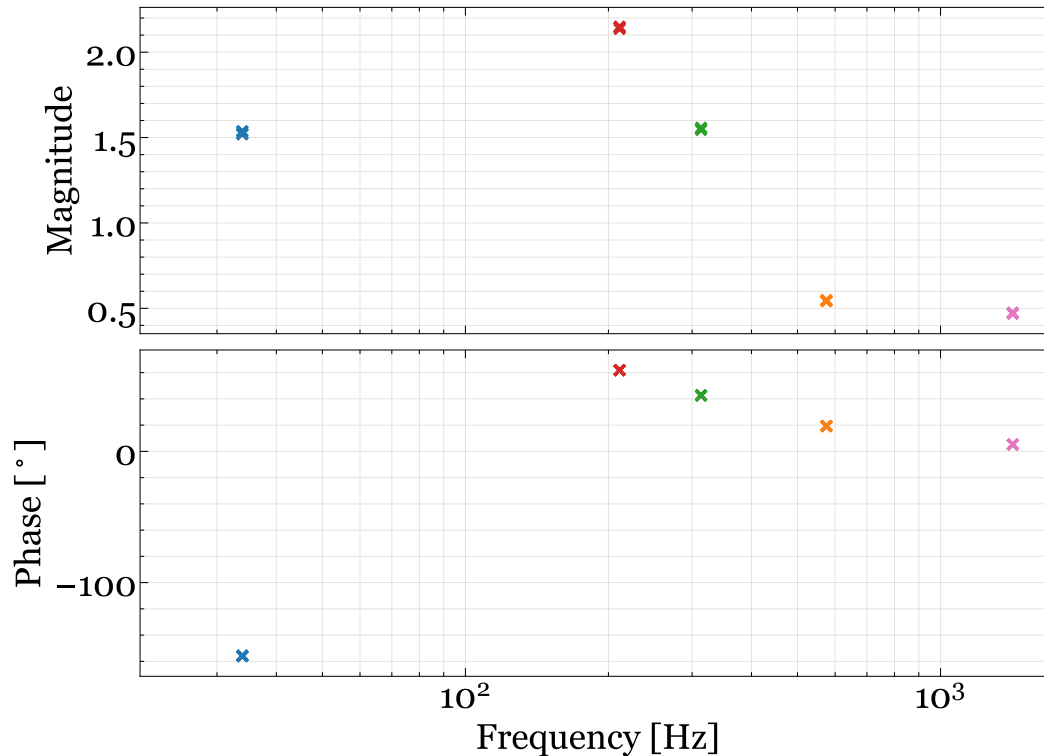d for ETMY and ETMX (10.9 nm Hz^2/ctrl-cts). The err-cts and ctrl-cts refer to the digital counts at the error and control points respectively. The DARM control and error points were also demodulated using the same low-pass filters and the same oscillators that were used for arm-length modulation. The demodulated values are multiplied with the above calibration factors and summed to get the inferred DARM strain by the Michelson calibration method.

Fig. 10.10 shows the ratio of the inferred DARM strain from Michelson calibration to the DARM strain measured by the multi-color calibration method. We see that there is a frequency-dependent discrepancy between the two methods. The discrepancy is large enough that we can not rule it out as uncertainty in either of the methods. To investigate this further, tried to establish the frequency independence of beatnote measurement and its correspondence to true arm length changes. The simplest test is to lock the YARM to the main laser and lock the AUX laser to YARM . Then we took a transfer function measurement between the beatnote frequency measurement

Figure 10.11: A swept sine transfer function measurement was made while exciting ETMY and taking the transfer function from the beatnote frequency measurement to the YARM loop error point or the PDH error signal between main laser and the YARM. Correction shape of DFD loop (from Eq. 10.9) has been applied.This verifies that the beatnote frequency indeed tracks the arm length modulation without frequency dependence in the bandwidth of DFD (2 kHz).

and the YARM error point while exciting at ETMY. Fig. 10.11 shows this transfer function. We see that the transfer function is flat as expected. So we verified that at least for the single arm case, the beatnote frequency does track the arm modulation as sensed by the PDH error signal.

Then we locked the interferometer in FPMI configuration and again ran the swept sine transfer function while exciting ETMY and taking the transfer function from the beatnote frequency measurement to the DARM loop error signal. Fig. 10.12 shows this transfer function. It is interesting to see a similar frequency dependence in this transfer function as seen in Fig. 10.10. We think that the DARM loop feedback actuation might not be perfect, any asymmetry between the actuation strengths of ETMY and ETMX, particularly a frequency-dependent asymmetry at higher frequencies can result in the DARM loop feeding back to the CARM loop.

Since the configuration we are testing is only FPMI and not the full interferometer
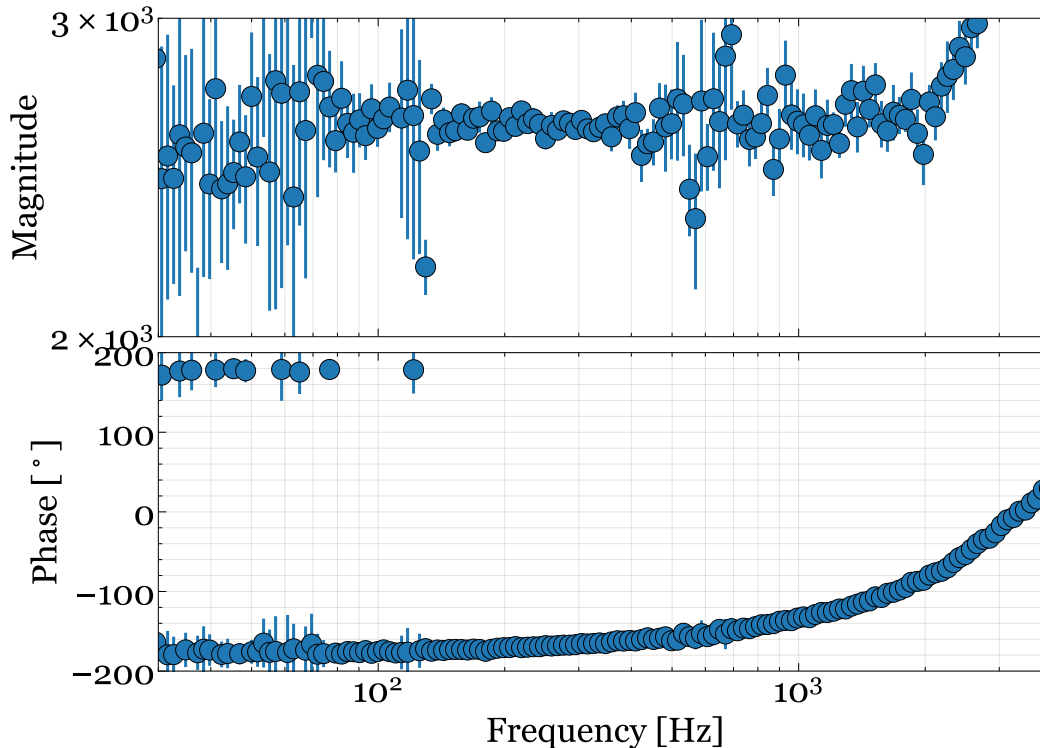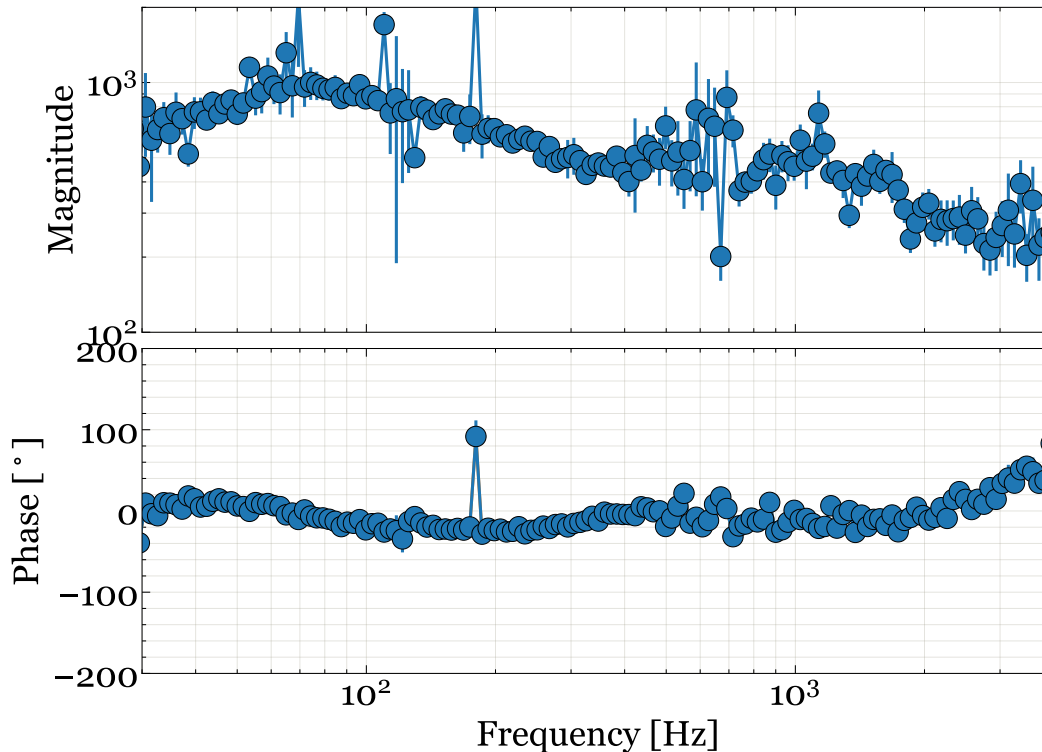
Figure 10.12: A swept sine transfer function measurement was made while exciting ETMY and taking the transfer function from the beatnote frequency measurement to the DARM loop error point in FPMI configuration. Correction shape of DFD loop (from Eq. 10.9) has been applied. This measurement also reveals an underlying frequency dependence between beatnote frequency and DARM strain as seen in Fig. 10.10.

lock, the CARM loop bandwidth is very small (only around 200 Hz) and is comparable with the DARM loop bandwidth. Thus the DARM loop might be interfering with the CARM loop during the calibration measurement since the calibration lines are high enough that even outside the bandwidth of the DARM loop, the loop actuates back at the line frequencies. Due to the asymmetry, the DARM loop feedback some of the actuation to the CARM loop which alters the beatnote measurement between the main laser (which is locked to the CARM degree of freedom) and the beatnote frequency. This effect warrants more investigation which is out of the scope of this thesis due to lack of time. But the silver lining is that in PRFPMI or DRFPMI lock of the interferometer, the CARM loop is locked with very high bandwidth so that even if there is an asymmetry in DARM feedback, the CARM loop can correct it faster than the DARM loop by adjusting the main laser frequency in feedback.

10.4 Implementation at LIGO observatories and future scalability

One of the biggest advantages of this method is that it is ready to be implemented at the Advanced LIGO observatories with very minimal extra hardware required. The observatories already utilize ALS system for acquiring the lock. This means the infrastructure for auxiliary laser injection and locking them to individual arms exist. However, the noise performance of the auxiliary laser lock would need to be improved significantly.

For lock acquisition, the noise requirement of the auxiliary laser loop is not very stringent as it is used to bring the common arm length motion to within the locking regime of CARM loop. The noise floor for CARM is about three orders of magnitude more than DARM loop which rejects the dominant residual main laser frequency noise. But for calibration, a beatnote between CARM and AUX loop needs to measure the same motion as measured by a much more sensitive DARM loop. The injected calibration line needs to be visible in the beatnote measurement without breaching the dynamic range of DARM loop or making it unstable due to non-linear effects. Craig Cahillane thesis[87, Fig. 4.12] shows how the current noise performance of the auxiliary laser loop is seven orders of magnitude worse than DARM loop noise. However, it also shows that the shot noise limit in the auxiliary laser loop is as good as the CARM noise performance. If the auxiliary laser loop is improved to achieve shot noise limited noise performance, then the beatnote measurement would be able to measure injected calibration lines with sufficient averaging time. Further quantitative analysis to calculate the required calibration line strength for a desired calibration update rate to achieve 0.1% uncertainty is required.

Since we need low noise around the particular calibration line frequencies, resonant gain filters can be used to further reduce noise floor in CARM and AUX loop at the calibration line frequencies. We demonstrated this for the 33.921 Hz line in the CARM loop in our experiment at the CIT 40m prototype. In the full Dual recycled Fabry-Pérot Michelson interferometer configuration, the CARM loop bandwidth covers the whole frequency band of calibration thus such resonant gain filters will be required at all calibration line frequencies. For this step, extra loop stability considerations might have to be taken into account as we do not want to affect the detector sensitivity for making a good calibration. So more work and experimentation are required on this part. The CIT 40m prototype would perform experiments on multicolor calibration with PRFPMI configuration to inform the observatories

better on this topic.

For the actuation of the calibration lines, the observatories can continue to use the photon calibration lasers to apply modulating force on the mirror since the multicolor calibration method is agnostic to the method used for actuation. The existing photon calibration would also serve as a good diagnostic tool for any systematic offset in the multicolor calibration scheme, up to the uncertainty of measurement in a photon calibration system.

The observatories can also utilize other actuators at their disposal if they can work better at higher frequencies. Photon calibration is particularly limited at higher frequencies because of a lack of faithful knowledge about mechanical transfer functions at high frequencies. This issue is not present for multicolor calibration as it does not matter if the actuation is perfect or even linear. In principle, even violin modes of the suspensions can be utilized to track the motion of DARM strain at kHz frequencies. However, additional knowledge of the detector response function at high frequencies would be necessary to make better estimates on phase delay effects in the DARM loop. This idea can be extended to the lower frequency band as well, where large noise peaks exist at 5-30 Hz region. In particular, bounce and roll modes of the suspended optics also naturally produce actuation in DARM degree of freedom that can be utilized for calibration if they are visible in the beatnote frequency with sufficient signal-to-noise ratio.

The observatories should implement multicolor calibration with beatnote measurements of both auxiliary lasers with the main laser. This will provide two simultaneous calibration systems that can shed more light on the possible systematics of the method.

While we chose 0.1% as a target for this calibration scheme, there is no reason to stop there. If in the future, new detector topologies or technologies make the noise floor of gravitational wave detectors better, this method is in principle scalable to even lower calibration uncertainties. For this purpose, the residual frequency noise in the auxiliary laser lock to the arm cavities would need to be suppressed further and the beatnote frequency fluctuations measurement would need to be improved. One can increase the calibration line actuation strengths as well if that is an option without disturbing the interferometer too much. Another option is to increase the integration time further to 1000 seconds and use multicolor calibration to calibrate photon calibration every 1000 seconds while faster real-time calibration is provided by the photon calibration in between its calibrations.

Part IV

Arm Length Stabilization for Voyager

Shortwave infrared multicolor metrology for cryogenic

gravitational wave detectors

Chapter 11

VOYAGER

The current generation of gravitational wave detectors is detecting about one compact binary merger event each week in a full sensitivity observation run. While this is an impressive achievement given less than a decade ago it was still unconfirmed if gravitational waves exist, to build more statistics and collect more details about these events, we need to improve the sensitivity of future detectors. The current range for Advanced LIGO is about 220 MPc for 1.4 $M.$ mass binary neutron star merger and about 1.3 GPc for 10 $M.$ binary black hole merger if the events are optimally oriented to the detector antenna pattern[88]. With the ongoing "A+" upgrade, the detector sensitivity might increase by 1.5 times.

At this time, no further upgrade of the Advanced LIGO sites is approved. A subset of the LIGO collaboration has proposed a cryogenic silicon interferometer to be placed at the Advanced LIGO sites[75]. This proposal aims to improve the range of the Advanced LIGO detectors by 4 to 5 times, increasing the detection rate of compact binary mergers by an estimated 100 times. This is exciting as this requires no site location search or new large-scale construction while serving as an intermediate research platform for larger and more complex proposed next-generation gravitational wave detectors such as Cosmic Explorer[76] and Einstein Telescope[89].

I contributed to the design study of Voyager as the final part of my thesis research. My contribution was limited to proposing the arm length stabilization schemes for Voyager. In this chapter, we'll go through a quick introduction to the main features of the proposed Voyager detector, and then we'll define the problem statement for the requirements from arm length stabilization system for this detector.

11.1 Proposed cryogenic silicon interferometer

The main feature of the Voyager proposal is to use cryogenic crystalline silicon as the substrate material for the test masses in the same dual recycled Fabry-Pérot Michelson interferometer configuration. Fig. 11.1 shows the proposed schematic of the detector[75]. The choice of crystalline silicon is motivated on multiple fronts. In current detectors, when the circulating power inside the arm cavities is attempted
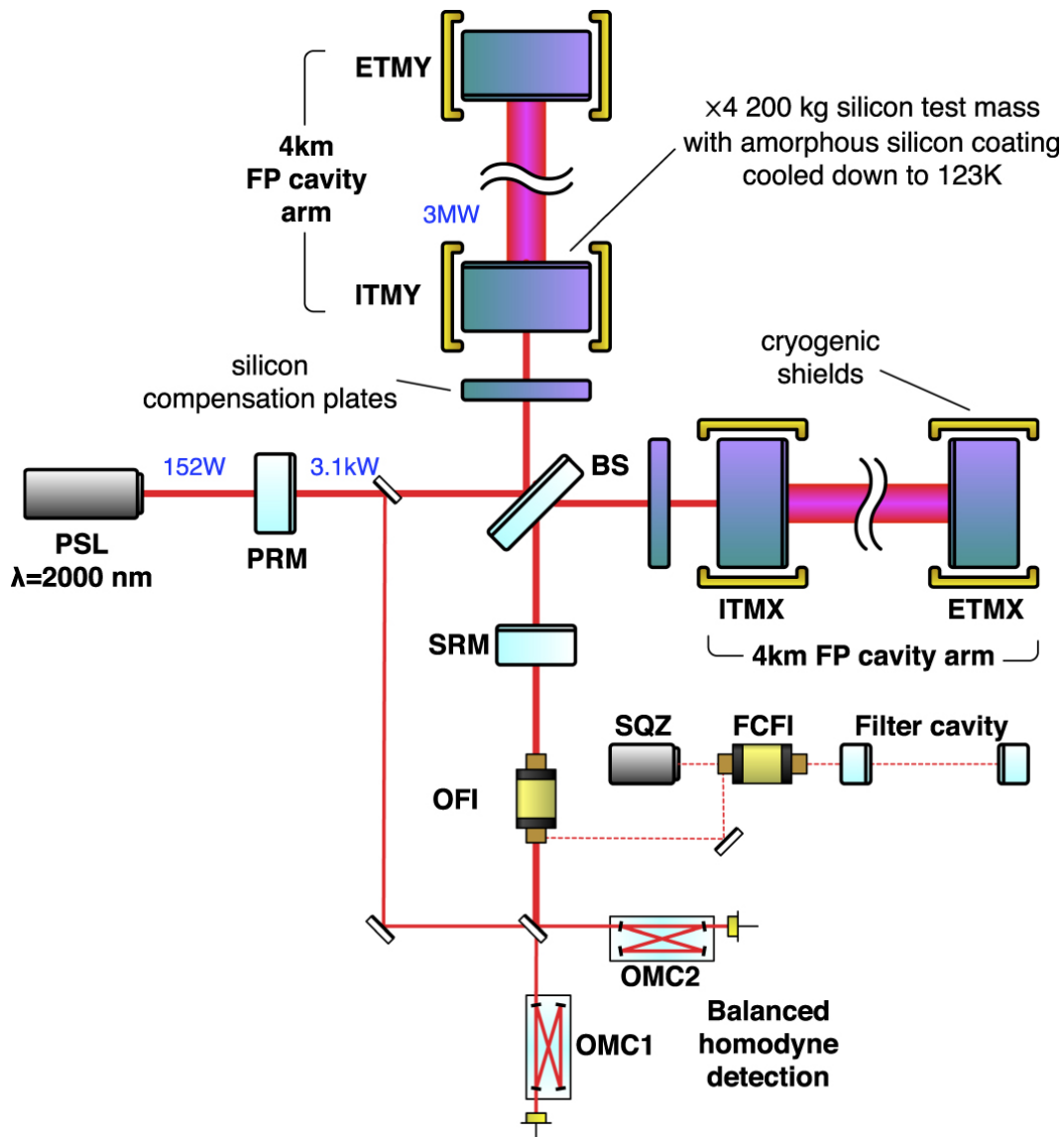
Figure 11.1: Schematic of proposed cryogenic gravitational wave detector - Voyager[75]. The four test masses would be replaced with crystalline Silicon substrate and would be radiatively cooled to 123 K. This requires change in main laser wavelength to near 2 μm.

to increase, it causes wavefront distortions at the mirror surface due to temperature gradients in the fused silica substrate for the test masses. This limits the circulating power and thus the achievable noise floor in high frequencies due to quantum shot noise. Since silicon is a good thermal conductor, the temperature gradient on the mirror body will be less severe, allowing for larger circulating power in the arm cavities without wavefront distortions.

Secondly, the thermo-elastic noise of the substrate limits the noise floor of the detector. Crystalline silicon has a zero crossing of the coefficient of thermal expansion

at 123 K. So if the test masses are cooled to this temperature, the test mass will be insensitive to thermal fluctuations to first order, greatly reducing the classical noise source in the detector at low frequencies. Third, the coating Brownian noise, which is currently the dominating classical noise source reduces due to low temperature and adoption of amorphous Silicon coatings. Fig. 11.2 shows the noise budget of the proposed Voyager detector and its comparison with Advanced LIGO and "A+" sensitivity.
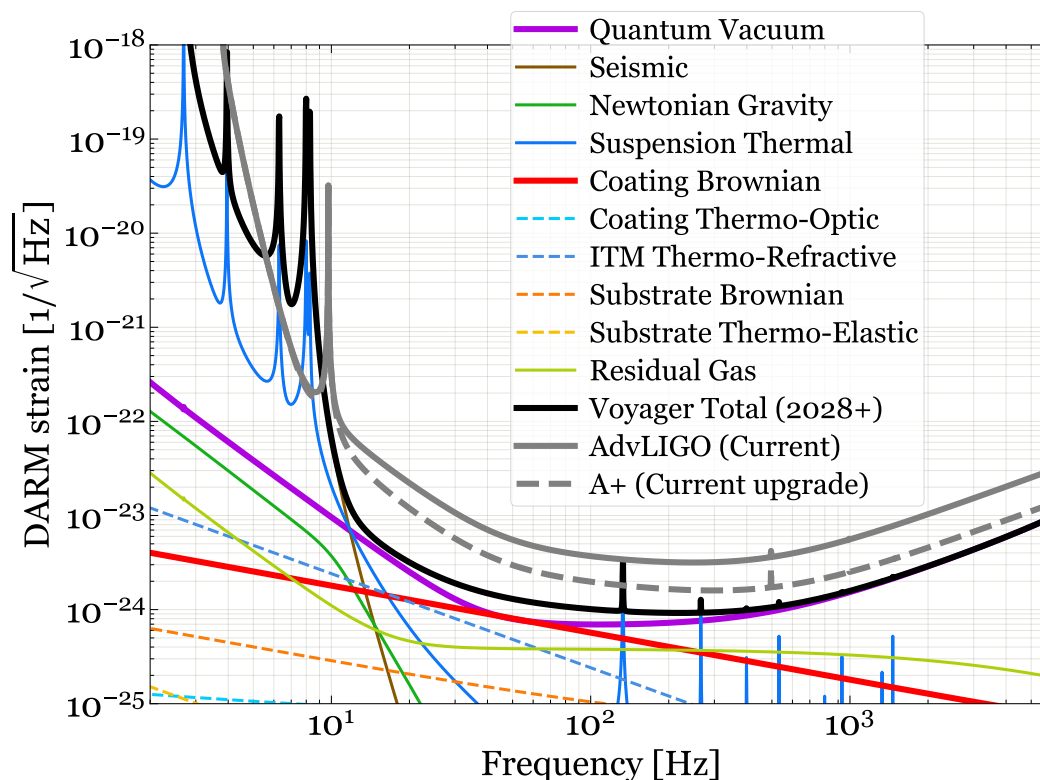
Figure 11.2: Voyager noise budget made using gwinc[3]

The switch in substrate material from fused silica to crystalline silicon can be very beneficial, but this requires major changes in the rest of the detector subsystems. For instance, Silicon is opaque to wavelengths smaller than 1200 nm. Thus the Voyager proposal adopted 2 um wavelength to be used for the main laser. More study is being done on developing a laser source at 2 um wavelength and amplifying it to high power for injecting it into the interferometer. To continue utilizing the benefits of squeezed vacuum injection and frequency-dependent squeezing through filter cavities, new squeezer designs and filter cavity designs are also required.

Further, achieving 123 K cooling without contacting the test masses is another big challenge. The proposal plans to achieve the cooling through radiative cooling with

cooled thermal shields around the test masses. Another important consideration due to the change of wavelength is to look into high quantum efficiency photodetectors for 2 um wavelength.

11.2 Laser frequencies and ALS requirements
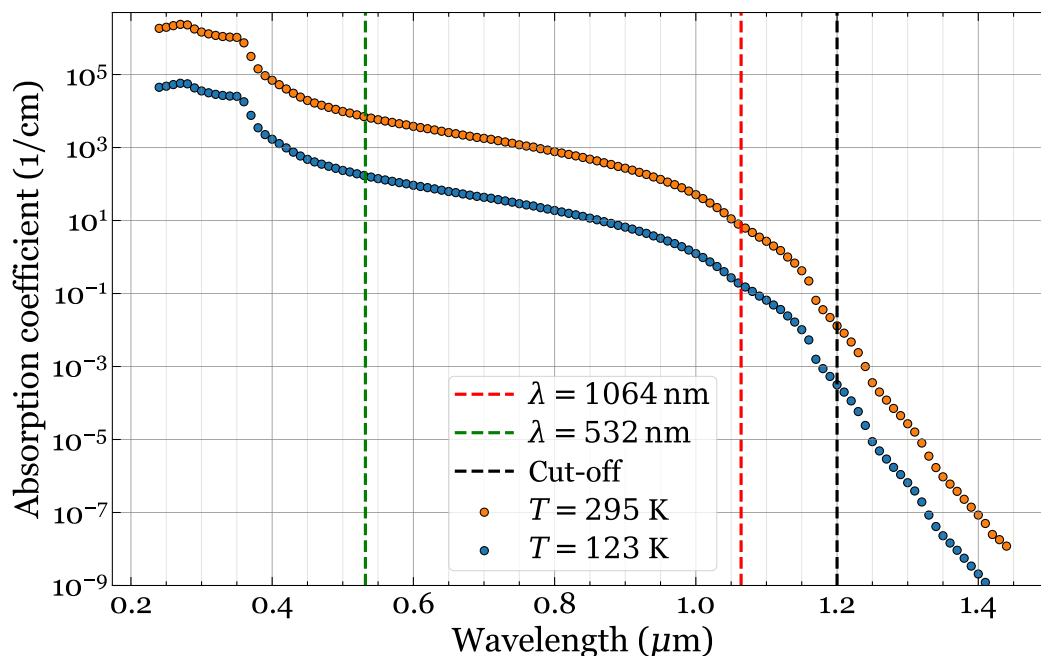

Figure 11.3: Absorption coefficient of Silicon at 295 K and 123 K. Room temperature data is obtained from M.A. Green[90] and estimate at 123 K is created using $\propto T^{4.25}$.

The choice of crystalline silicon substrates for the test masses of Voyager creates new requirements for the laser wavelengths to be used. Fig. 11.3 shows the absorption coefficient in silicon. Laser frequencies below 1.2 μm are severely absorbed in crystalline silicon. So the adopted choice of main laser frequency is around 2 μm.

A simple extension of the existing second harmonic generation method for ALS (see Sec.9.1) purposes would mean a 1 μm wavelength for the auxiliary laser, but that would get absorbed in the silicon test masses. So the auxiliary laser would have to be above 1.3 μm and we would need to find an alternate scheme for ALS in Voyager. In this section, I will first define our problem statement and the goal of ALS.

Figure Fig. 11.4 shows the general simplified scheme of ALS in voyager. The auxiliary laser is locked to one of the arms of the interferometer. Let's call this arm length, L_{arm}. This means that the auxiliary laser frequency ν_{ALS} obeys this relationship:
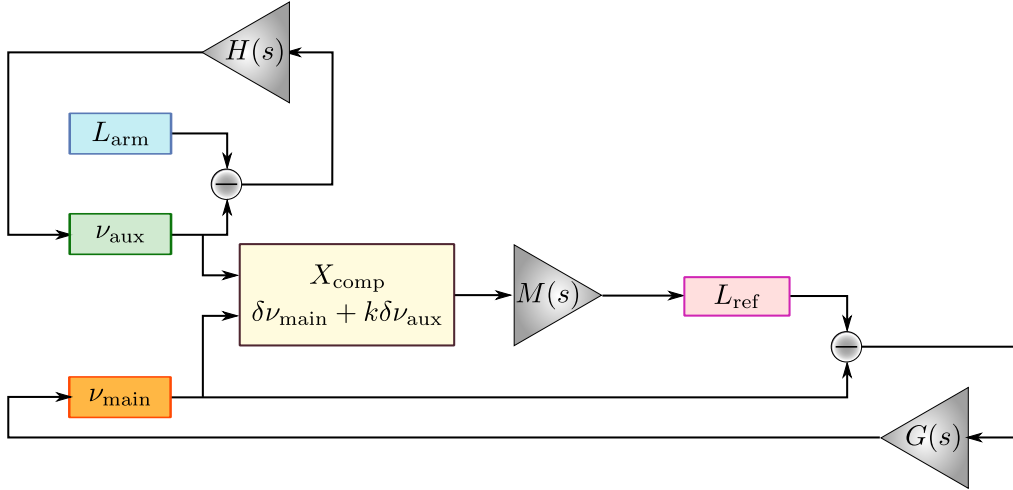
Figure 11.4: Generalised ALS scheme for Voyage.

$$\nu_{\text{aux}} = m_1 \frac{c}{2L_{\text{arm}}} \tag{11.1}$$

Here, m_1 is an integer to denote the cavity mode to which the auxiliary laser is resonant. The fluctuations of the arm cavity are transferred to auxiliary laser frequency through open loop gain H(s) (dropping s in equations for ease of notation) as:

$$\delta\nu_{\text{aux}} = \frac{H}{1 - H}\nu_{\text{aux}}\frac{\delta L_{\text{arm}}}{L_{\text{arm}}} \tag{11.2}$$

Our main objective in ALS is to bring the main laser to an offset lock with the arm cavity, that is, to transfer arm length fluctuations to the main laser frequency at an arbitrary offset, such that when the offset is reduced, the main laser is resonant with the arm cavity. Thus, our required lock point for the main laser frequency ν_{main} has the condition:

$$\delta\nu_{\text{main}} = -\nu_{\text{main}}\frac{\delta L_{\text{arm}}}{L_{\text{arm}}} \tag{11.3}$$

and

$$\nu_{\text{main}} = m_2\frac{c}{2L_{\text{arm}}} + \Delta\frac{c}{2L_{\text{arm}}} \tag{11.4}$$

Here m_2 is another integer corresponding to the closest resonant tooth in the resonance modes supported by the cavity and Δ is the fraction of free spectral range of the cavity by which the main laser frequency is away from resonance.

Now, let's assume a general optical frequency comparison scheme that provides the following output:

$$X_{\text{comp}}(\nu_{\text{main}}, \nu_{\text{aux}}) = \delta\nu_{\text{main}} + k\delta\nu_{\text{aux}} \tag{11.5}$$

where k is a constant defining the comparison function.

The main laser is typically locked to a reference cavity L_{ref} with an open loop gain of G as shown in the figure. If the output of the comparator is fed back to the reference cavity length with a feedback gain of M:

$$\delta L_{\text{ref}} = M(\delta\nu_{\text{main}} + k\delta\nu_{\text{aux}}) \tag{11.6}$$

Here δL_{ref} is written in units of frequency for ease of notation. Then at the control point of the ALS loop:

$$\begin{aligned}
\delta\nu_{\text{main}} &= G(\delta\nu_{\text{main}} - M(\delta\nu_{\text{main}} + k\delta\nu_{\text{aux}})) \\
\delta\nu_{\text{main}} &= -\frac{GMk}{1 - G + GM}\delta\nu_{\text{aux}}
\end{aligned} \tag{11.7}$$

Further, using the auxiliary laser lock condition from Eq. 11.2:

$$\begin{aligned}
\delta\nu_{\text{main}} &= -\frac{GMk}{1 - G + GM}\frac{H}{1 - H}\nu_{\text{aux}}\frac{\delta L_{\text{arm}}}{L_{\text{arm}}} \\
\delta\nu_{\text{main}} &= -\frac{k}{\left(\frac{1}{MG} - \frac{1}{M} + 1\right)\left(\frac{1}{H} - 1\right)}\delta\nu_{\text{aux}}\frac{\delta L_{\text{arm}}}{L_{\text{arm}}}
\end{aligned} \tag{11.8}$$

At high feedback gains (at low frequencies) for any general feedback loops where $|M| \gg 1$, $|G| \gg 1$, and $|H| \gg 1$ regardless of the sign of the feedback loop reduces down to:

$$\delta\nu_{\text{main}} = k\nu_{\text{aux}}\frac{\delta L_{\text{arm}}}{L_{\text{arm}}} \tag{11.9}$$

That is a comparator X_{comp} defined in Eq. 11.5 locks the main laser frequency fluctuations to k times the auxiliary laser frequency. To fulfill the condition laid down in Eq. 11.3, we will need:

$$-\nu_{\text{main}}\frac{\delta L_{\text{arm}}}{L_{\text{arm}}} = k\nu_{\text{aux}}\frac{\delta L_{\text{arm}}}{L_{\text{arm}}}$$

$$\nu_{\text{main}} = -k\nu_{\text{aux}}$$

$$m_2\frac{c}{2L_{\text{arm}}} + \Delta\frac{c}{2L_{\text{arm}}} = -km_1\frac{c}{2L_{\text{arm}}} \tag{11.10}$$

$$k = -\frac{m_2}{m_1} - \frac{\Delta}{m_1}$$

$$k \approx -\frac{m_2}{m1}$$

The offset of the main laser from the reference can be controlled as an offset in the ALS loop, so the second term above can be discarded. It is important though to have the first term to fulfill the condition in Eq. 11.3. Thus the comparator required for ALS in Voyager must have the following form:

$$k = -\frac{m_2}{m_1} \approx -\frac{\nu_{\text{main}}}{\nu_{\text{aux}}} \tag{11.11}$$

This means that to keep the main laser offset locked to the arm cavity, it must follow the fluctuations of auxiliary laser frequency in the same direction and must be scaled in proportion to the optical frequency ratio. Another way of looking at it is that the comparator function must take the difference between the relative frequency motion of the two optical frequencies, that is:

$$X_{\text{good}}(\nu_{\text{main}}, \nu_{\text{aux}}) = \frac{\delta\nu_{\text{main}}}{\nu_{\text{main}}} - \frac{\delta\nu_{\text{aux}}}{\nu_{\text{aux}}} \tag{11.12}$$

To test this, we should check the case of the current ALS scheme in advanced LIGO. The auxiliary laser is generated by frequency doubling the main laser frequency. Thus the ratio $-m_2/m_1$ becomes $-1/2$ for the required value of k. For comparing the frequencies, the current ALS scheme frequency doubles the main laser and takes a beatnote between it and the auxiliary laser, returning $\propto 2\nu_{\text{main}} - \nu_{\text{aux}}$ which is indeed equivalent to a comparator X_{comp} with $k = -1/2$.

C h a p t e r 1 2

ARM LENGTH STABILIZATION PROPOSED SCHEMES

In this chapter, I'll list a few schemes that we designed for ALS in Voyager. The work on these schemes has been done at a schematic level only to get a suite of "in-principle" working schemes. More detailed noise analysis and robustness in practical terms needs to be done in the near future. Then some selected schemes should be prototyped at CIT 40m for comparison.

12.1   Fractional harmonic generation scheme
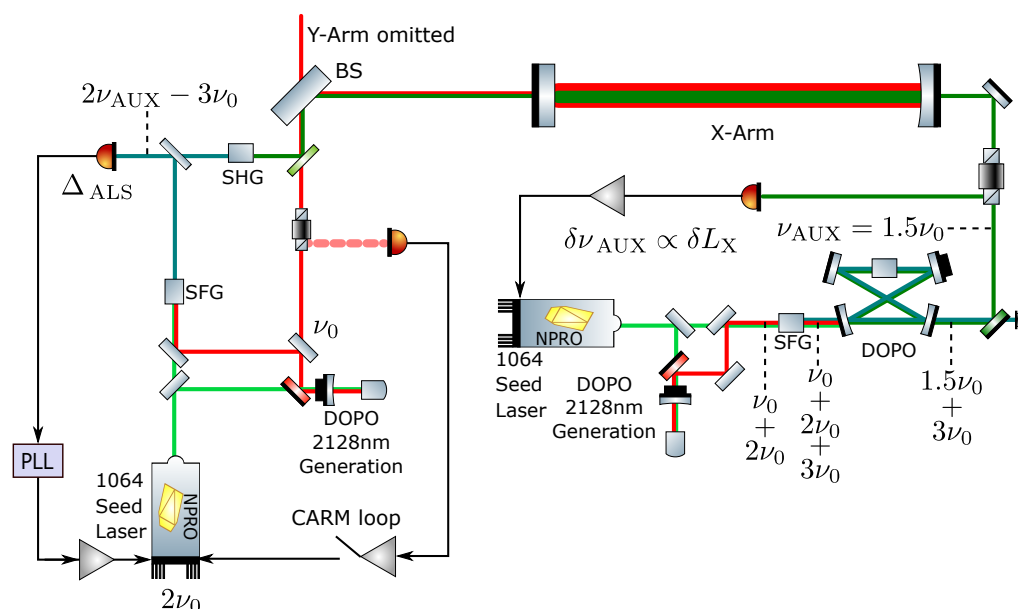
Figure 12.1: Proposed ALS scheme for Voyager using fractional harmonic generation. The main laser frequency is generated by using Degenerate Optical Parametric Oscillator (DOPO) that frequency halves a seed 1064 nm laser. The auxiliary laser is generated by doing a Sum Frequency Generation (SFG) of 1064 nm and 2128 nm to obtain 709.3 nm frequency which is sent through another DOPO to frequency half it to 1418.6 nm auxiliary wavelength. The beatnote for ALS is taken at 709.3 nm by doing a Second Harmonic Generation (SHG) on auxiliary laser and SFG of main laser with its seed laser.

Taking inspiration from current ALS, if simple second harmonic generation is not possible, we first looked into the possibility of using a fractional harmonic generation method. Fig. 12.1 shows a simplified schematic for this scheme. The auxiliary wavelength is chosen to be two-thirds of the main laser wavelength instead

of half in this scheme.

To generate the auxiliary laser, a 1064 nm seed laser is first passed through a degenerate optical parametric oscillator (DOPO). This is an optical cavity resonant at 1064 nm and 2128 nm with a periodically poled potassium titanyl phosphate crystal in the center or as one end of the cavity itself[91]. At an optimum temperature to create phase-matching conditions, such a crystal supports the splitting of a 1064 nm photon into two 2128 nm photons, enhanced by the cavity around the crystal. The output 2128 nm light is then passed through another periodically poled crystal together with a 1064 nm beam. This second crystal is poled for and kept at a temperature to support sum frequency generation (SFG) with 1064 nm photon and 2128 nm photon combining to output a 709.3 nm photon. This is further sent to another DOPO optimized to frequency half 709.3 nm photons to 1418.6 nm light which is used as the auxiliary wavelength in the scheme. Since the frequency conversion through a non-linear crystal is a highly coherent process[84], feedback to the 1064 nm seed laser is sufficient to lock this auxiliary wavelength to the arm cavity made with crystalline silicon test masses.

For the main laser, 2128 nm is generated using a similar DOPO at the vertex area. To measure the beatnote frequency, the 1064 nm seed laser of the main laser is sent through an SFG crystal together with the main laser to create 709.3 nm light. This is mixed with a frequency-doubled transmitted auxiliary laser to measure beatnote at 709.3 nm where high-efficiency photodiodes already exist.

This method is complex and involves the use of 6 non-linear crystals operating in different regimes. While the technology for converting laser frequencies using non-linear crystals is mature and routinely used in optical experiments, its use in precision measurements has been minimal. The conversion efficiency for these processes is often very low without the presence of a cavity. These factors make this scheme less desirable.

12.2 Frequency comb scheme

The invention of the frequency comb[92] at the start of this century springboarded the precision measurement community in optical physics to orders of magnitude improvements[93]. The ability to transfer stability from atomic clocks to other optical frequencies of choice improved the precision measurements one can do using frequency measured against these stable optical references[94]. An optical frequency comb is a source of light with multiple narrow linewidth frequencies
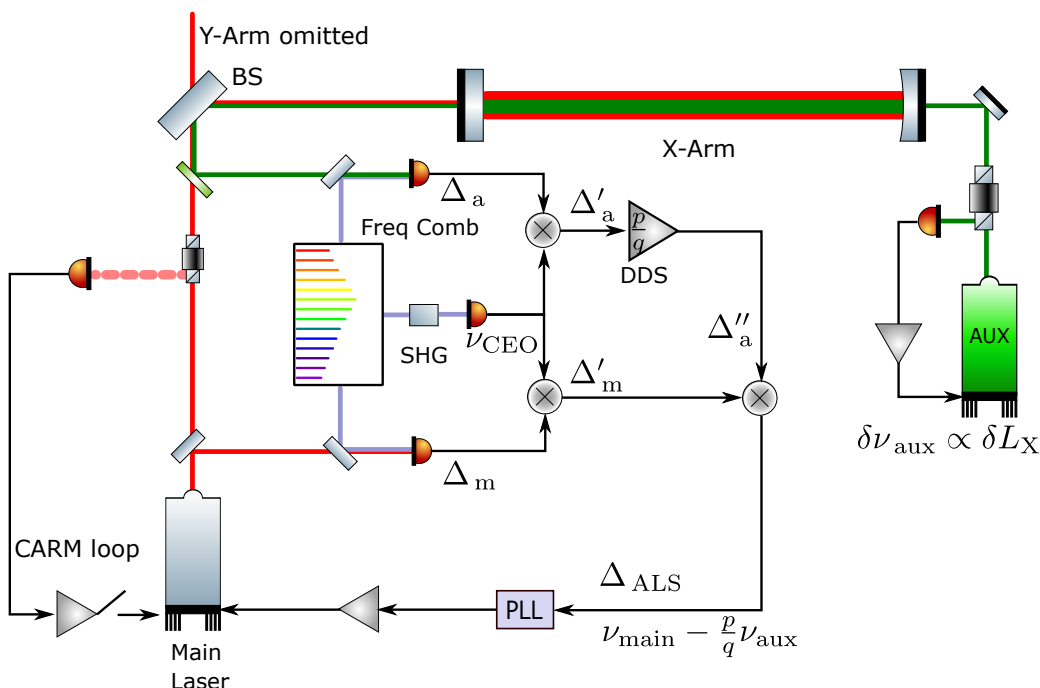
Figure 12.2: Proposed ALS scheme with Frequency Comb scheme for Voyager. The main laser frequency and auxiliary laser frequency can be chosen freely. An octave spanning frequency comb is used which covers the optical region from auxiliary wavelength to main laser wavelength. The carrier envelop offset is detected using Second Harmonic Generation with frequency comb and removed in feedforward. To take the difference of the two frequencies with correct scaling as per Eq. 11.12, a Direct Digital Synthesis (DDS) is used to scale the auxiliary laser beatnote with frequency comb before mixing it with the main laser beatnote. This also removed the repitition rate noise in feedforward.

present which are all separated from each other with a constant frequency, known as the repetition rate. A typical n^{th} tooth of a frequency comb can be described as:

$$\nu_n = \nu_{\text{CEO}} + n\nu_{\text{rep}} \tag{12.1}$$

where ν_{CEO} is known as the carrier offset envelope and ν_{rep} is called the repetition rate of the comb. A favorable condition arises if the frequency comb is so-called "octave spanning" that is its highest frequency tooth is at least twice in frequency as its lowest frequency tooth. In this particular case, one can measure the carrier envelope offset by frequency doubling the frequency comb light on a second harmonic generation stage optimized by frequency doubling the lower half of the comb[95]. The output of this stage naturally has the frequency doubled lower teeth beating with the original comb's upper teeth at the carrier-envelope offset frequency. This method is usually

used to feedback to the frequency comb and remove the carrier envelop offset, but we think for our purpose, we can use the measured carrier-envelope offset in feedforward.

Fig. 12.2 shows the scheme that will use such an octave-spanning frequency comb. The main laser frequency and auxiliary laser frequency can be any wavelength in the low absorption region of silicon and within the span of the frequency comb. This is a big benefit of this scheme as we do not need to generate specific wavelengths using non-linear crystals for being compatible with the ALS scheme. We can choose wavelengths that have low noise high power laser sources and amplifiers, and high quantum efficiency photodiodes already available.

The scheme beats the transmitted auxiliary laser and a pick-off of the main laser with the frequency comb. Each optical frequency beats with all the teeth of the comb, but the closest tooth in frequency generates an RF frequency tone that is picked up by the beat photodiodes. Let's assume that the main laser beats with the pth tooth and the auxiliary laser beats with the qth tooth. Then the beat frequencies will be:

$$
\begin{aligned}
\Delta_{\text{m}} &= \nu_{\text{CEO}} + p\nu_{\text{rep}} - \nu_{\text{main}} \\
\Delta_{\text{a}} &= \nu_{\text{CEO}} + q\nu_{\text{rep}} - \nu_{\text{aux}}
\end{aligned}
\tag{12.2}
$$

The frequency comb is also sent through a SHG stage and then onto a photodiode to get a signal corresponding to the ν_{CEO}. This signal is mixed with the two beats generated above and low passed to remove the carrier envelop offset and its fluctuations in feedforward. The two signals after this mixing become:

$$
\begin{aligned}
\Delta'_{\text{m}} &= p\nu_{\text{rep}} - \nu_{\text{main}} \\
\Delta'_{\text{a}} &= q\nu_{\text{rep}} - \nu_{\text{aux}}
\end{aligned}
\tag{12.3}
$$

Then the signal from the auxiliary beat is sent to a Direct Digital Synthesis (DDS) chip. This device takes an input sinusoidal signal and multiplies the frequency by a fixed number provided to it as a digital input. DDS chips with the frequency multiplier number in 64-bit precision are available these days. We provide this chip the number p/q to multiply with the auxiliary beat signal to get:

$$
\Delta''_{\text{a}} = p\nu_{\text{rep}} - \frac{p}{q}\nu_{\text{aux}}
\tag{12.4}
$$

After this step, the two beat frequencies are mixed on a mixer and low passed to take their difference. Upto the precision of the DDS chip, the repetition rate component and any fluctuations due to it get canceled in this step, giving an ALS error signal that is proportional to the correct difference between the two frequencies:

$$\Delta_{\text{ALS}} = \nu_{\text{main}} - \frac{p}{q}\nu_{\text{aux}} \tag{12.5}$$

Note that this difference follows the condition set in Eq. 11.12 for the ALS scheme to work. We also do not need a costlier low noise frequency comb for this method to work as all the noise in the frequency comb is canceled in feedforward. Nevertheless, creating an octave-spanning frequency comb is a challenging task, and would require significant time and money. So alternate methods would be desirable if possible.

12.3   Dichroic reference cavity scheme

Instead of using a frequency comb, one can also use a reference cavity with dichroic mirrors so that both the main laser and auxiliary laser can resonate with it at the same time. A reference cavity is also similar to a frequency comb as it supports resonances at equidistant positions separated by the cavity's free spectral range and if dichroic can support resonance with widely separate optical frequencies.

The objective of the ALS system is to compare the transmitted auxiliary laser and the main laser. To achieve this, a stable local copy of each laser upshifted by a common RF frequency (Ω) is generated by using two AOMs marked as AOM_{main} and AOM_{aux} in the schematic. An oven-controlled crystal oscillator should be used to seed the RF frequency. The upshifted copies are simultaneously locked to the dichroic reference cavity by feeding back to the AOMs. The transmitted lasers from the reference cavity are used to measure beatnote with the transmitted auxiliary laser and the main laser that need to be compared.

The beatnote from the auxiliary laser is multiplied in frequency by the ratio of the main laser frequency to the auxiliary laser using a direct digital synthesis chip (similar to the frequency comb scheme). The two beat notes are then mixed on a mixer and low passed. The remanent RF frequency ($\Omega(1 - \frac{p}{q})$) would carry the difference in main laser and auxiliary laser with the correct form as stated in Eq. 11.12. This beatnote would be tracked by a PLL and the resulting signal would be used for ALS.

Interestingly, there is one more place where the ALS signal can be measured in this
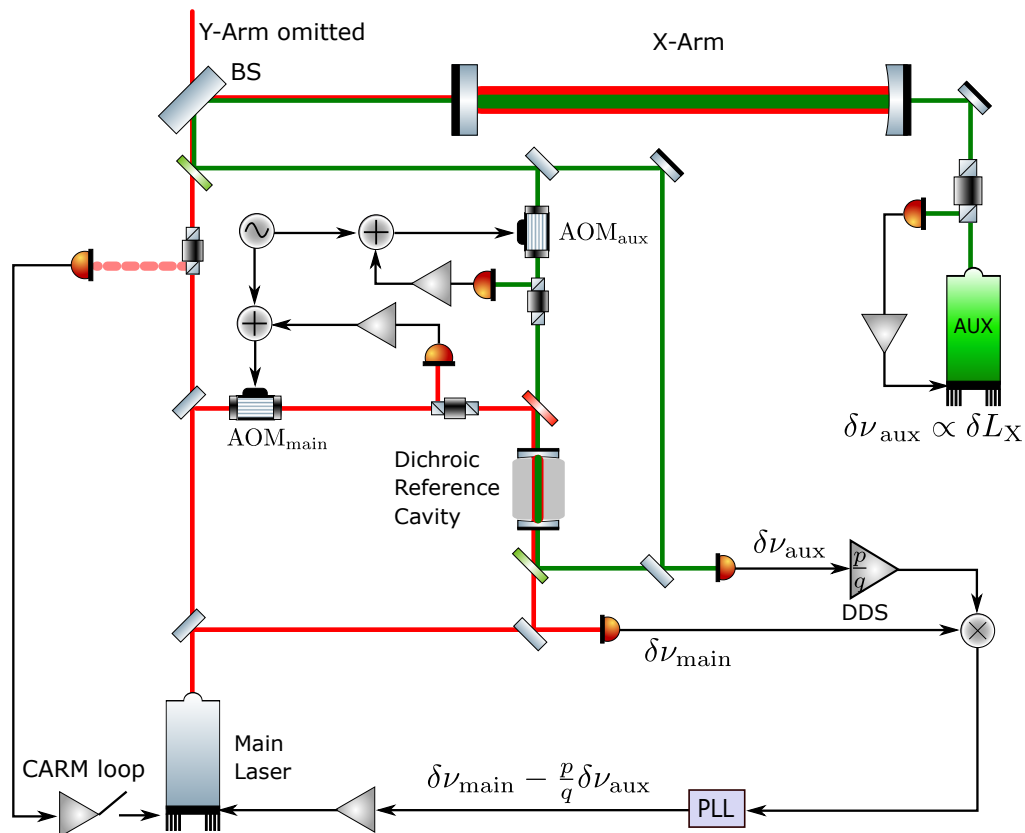
Figure 12.3: Proposed ALS scheme for Voyager using dichroic reference cavity. A local stable reference in same optical frequency is generated for transmitted auxiliary laser and the main laser using AOM to lock to a dichroic reference cavity. The transmitted stable references are then mixed with the transmitted auxiliary laser and the main laser to create beatnote signals that carry fluctuations of each laser. The beatnote for auxiliary laser is sent through a direct digital synthesis (DDS) chip to multiply with the ratio of main laser frequency to auxiliary laser frequency. The two beatnotes are mixed and sensed through a PLL to generate the ALS signal.

scheme, with some additional noise though. The difference between the control signals of the locking loops that lock the lasers to the reference cavity can also provide an ALS signal but will carry uncorrelated and unsuppressed AOM driver noise, and partially suppressed photodiode noise of each loop.

Note that one can get rid of the need for PLL in this method if the RF source for AOMs is used to generate two RF signals, one with frequency Ω for the main laser and one with frequency $\Omega\frac{q}{p}$. Then after the application of DDS, both beatnote frequencies would be the same in frequency and will generate a DC signal at the output of the mixer proportional to the ALS signal. However, reading signals at DC can be noisier than using a PLL, so a cost-benefit analysis of this would need to be

done.

Also, note that the noise of the reference cavity would be canceled in this measurement, which means the reference cavity does not need to be ultra-stable in length. I think using a cavity similar to the ones used in the coatings thermal noise experiment (see Sec.2.1) would suffice. Except for obtaining high-reflectivity dichroic coatings, everything else in this scheme would be low-cost and easy to procure.

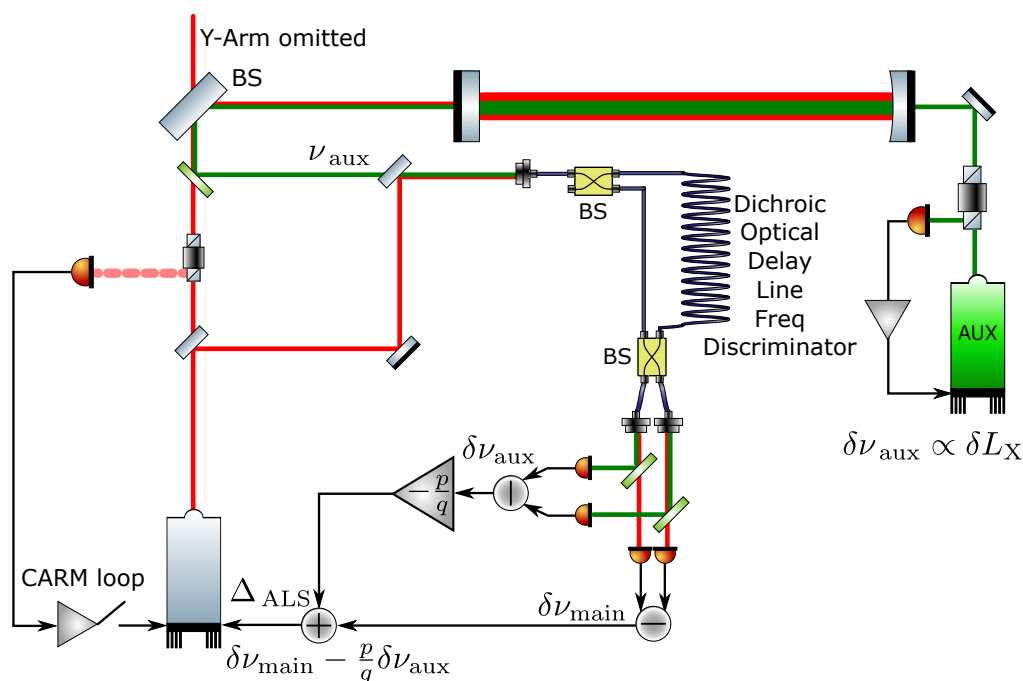## 12.4 Optical delay line frequency discrimination scheme

Figure 12.4: Proposed ALS scheme for Voyager using dichroic optical delay line frequency discrimination (ODFD) that supports both main and auxiliary laser wavelengths. The transmitted auxiliary laser is overlapped with a pick-off of the main laser and collimated into a dichroic optical fiber. This is sent through a beam splitter to create two paths, one going through long ODFD and another through a short path. The outputs are mixed on a beam splitted and the balanced homodyne detection is performed at each wavelength separately. This measured the fluctuations in both wavelengths in form of electronic signals that can be scaled and summed appropriately to create the ALS control signal.

Fig. 12.4 shows this scheme which uses long dichroic optical fiber cable in place of a reference cavity. The main feature of this scheme is the use of optical delay line frequency discrimination (ODFD) which works on the same principle as described in Sec.10.1.1 but at optical frequencies.

The transmitted auxiliary laser and a pick-off of the main laser are overlapped and

sent to a fiber collimator into a fiber optic cable that supports transmission of both the main laser wavelength and auxiliary laser wavelength. This fiber goes to a fiber beam splitter which launches the two outputs into two different paths, one path taking it through a long optical fiber spool which adds a time delay of τ_d, and the other path is short. The two paths are recombined on another beam splitter. The outputs of the second beamsplitter go to the free space through fiber collimators. Here, two dichroic mirrors separate the auxiliary wavelength from the main wavelength. This step can be done with waveguides also. The electric fields at the two output ports for each Frequency are then given by:

$$
\begin{aligned}
E_{out,1} &= \frac{1}{\sqrt{2}} E_{in} \left(e^{i2\pi\nu_\text{main/aux}t} + i e^{i2\pi\nu_\text{main/aux}(t-\tau_\text{d})} \right) \\
E_{out,2} &= \frac{1}{\sqrt{2}} E_{in} \left(i e^{i2\pi\nu_\text{main/aux}t} + e^{i2\pi\nu_\text{main/aux}(t-\tau_\text{d})} \right)
\end{aligned}
\tag{12.6}
$$

The two outputs are read on two balanced photodiodes and a difference is taken (similar to the balanced homodyne detection), the output is then:

$$
\begin{aligned}
P_\text{ODFD,main} &= E_{in}^2 \sin(2\pi\nu_\text{main}\tau_\text{d}) \\
P_\text{ODFD,aux} &= E_{in}^2 \sin(2\pi\nu_\text{aux}\tau_\text{d})
\end{aligned}
\tag{12.7}
$$

The short fiber can be stretched with a fiber stretcher to ensure that both $2\pi\nu_\text{main}\tau_\text{d}$ and $2\pi\nu_\text{aux}\tau_\text{d}$ both are integer multiples of 2π at DC. Then the fluctuations in both lasers will show as linear signals at the two outputs. The auxiliary laser signal can be multiplied in gain by $-p/q$ (ratio of the main laser frequency to auxiliary laser frequency) to generate the desired signal:

$$
\Delta_\text{ALS} = \delta\nu_\text{main} - \frac{\nu_\text{main}}{\nu_\text{aux}} \delta\nu_\text{aux}
\tag{12.8}
$$

This signal can be fed back to the main laser. This is an exciting way to solve the ALS problem for Voyager since it does not require high-cost equipment. The bottleneck in this scheme would be to keep τ_d from drifting, especially if the setup will be used for calibration of the interferometer as well. Further noise analysis is required to look into other possible noise sources and their effect on the performance of ALS.

GLOSSARY

ALS Arm Length Stabilization system. See Sec.9.1. 100, 116, 135, 141, 142, 143, 144, 145, 147, 148, 149, 150, 151, 152

AOM Accousto-optic Modulator. A quartz crystal with acoustic transducers around it. The electric signal creates sound waves in the crystal which diffracts and shifts the frequency of the passing light due to acousto-optic effect. 46, 149, 150

AS Antisymmetric output port in michelson interferometer. This is where field is zero if the michelson arm lengths are matched. 50, 51, 52, 53, 54, 55, 57, 59, 61, 63, 67, 69, 70, 71, 72, 73, 74, 75, 76, 78, 79, 122

AS55 Anti-symmetric port light demodulated at 55 MHz. See Fig. 7.1. 125

ASD Amplitude Spectral Density. 35, 38, 45

AUX Referring to auxiliary laser at the end station. The laser is frequency doubled in case of Advanced LIGO and 40m from 1064 nm to avoid interference with the main laser but have ease of comparison with the main laser. 99, 111, 112, 114, 116, 117, 122, 132, 135

BHDBS Balanced Homodyne Detection Beam Splitter. 69, 70, 71, 73, 80

BHR Balanced Homodyne Readout. Readout scheme name for Balanced Homodyne Detection. 65

BS Beam Splitter. 66, 75, 77, 78, 125, 126

CARM Common arm length between the two arm Febry-Perot cavities. Equal to $\frac{L_X - L_Y}{2}$. 61, 71, 79, 98, 99, 100, 103, 104, 110, 125, 126, 127, 128, 133, 134, 135

CDS Controls and Diagnostics System. In LIGO community, stands for everything to do with digital realtime control systems, data acquisition, and measurement systems. 120

DARM Differential arm length between the two arm Febry-Perot cavities. Equal to $\frac{L_X - L_Y}{2}$. 49, 51, 52, 53, 54, 56, 57, 58, 59, 61, 62, 73, 79, 80, 81, 91, 92, 93,

NPRO Non-Planar Ring Oscillator. A monolithic crystal which is cut in such a way that a non-planar optical mode is supported by reflections from the faces inside the crystal. The crystal itself acts as a gain medium for generating a narrow linewidth laser. 18, 65, 98, 109, 127

OLTF Open Loop Transfer Function. Total trasnfer function in a control system around the loop. 74, 75, 76, 110, 120, 122, 127, 128, 129

OMC Output Mode Cleaner. 61, 63

PDH Pound-Drevor Hall cavity locking technique. Phase modulated RF sidebands are created on the input laser to the cavity. The RF beatnote between the reflected sidebands and phase modulations in reflected carrier which are proportional to cavity length change with respect to the carrier frequency is used as error signal. This error signal is commonly referred to as PDH error signal. 19, 23, 35, 40, 46, 47, 53, 98, 99, 100, 101, 110, 112, 125, 126, 127, 133

PID Proportional-Integral-Derivative controller. 19, 21, 22, 65

PLL Phase Locked Loop. 20, 149, 150

PRCL Power Recycling Cavity Length. 100

PRFPMI "Power Recycled Fabry-Pérot (arm cavities) Michelson Interferometer". 81, 134, 135

PRM Power Recycling Mirror. 65, 67, 81

PRMI "Power Recycled Michelson Interferometer". 81

PSD Power Spectral Density. 27, 28, 29, 36, 40, 45

PZT Piezoelectric transducer. A type of electroacoustic transducer that contracts or expands when electric field is applied on it. 19, 23, 65, 127

REFL Symmetric output port in michelson interferometer. This is where all the field reflects back if the michelson arm lenghts are matched. 50, 55, 67

REFL55 Symmeteric port light demodulated at 55 MHz. See Fig. 7.1. 125, 126

RMS Root-mean-squared. 19, 74, 76

SHG Second Harmonic Generation. Frequency doubling using a non-linear crystal.. 99, 148

SRCL Signal Recycling Cavity Length. 61, 100

SRM Signal Recycling Mirror. 67, 69

UGF Unity Gain Frequency for a control loop. This is defined as the frequency where the open loop transfer function has magnitude 1. This is a special point of interest for determining the loop stability. This is also referred to as bandwidth sometimes as the control loop only functions for frequencies below this frequency and the system is free running above it. 73, 74, 75, 76, 80, 111, 119, 122, 124, 125, 126, 127, 128, 129

XARM X Arm of the interferometer. Also refers to the Febry-Perot cavity length formed in the X arm. Symbol: L_X. 125

YARM Y Arm of the interferometer. Also refers to the Febry-Perot cavity length formed in the Y arm. Symbol: L_Y. 120, 121, 124, 125, 127, 128, 129, 132, 133

BIBLIOGRAPHY

[1] B. P. Abbott et al. (LIGO Scientific Collaboration and Virgo Collaboration), "Observation of Gravitational Waves from a Binary Black Hole Merger", Phys. Rev. Lett. **116**, 061102 (2016).

[2] R. Abbott et al. (LIGO Scientific Collaboration and Virgo Collaboration and KAGRA Collaboration), "GWTC-3: Compact Binary Coalescences Observed by LIGO and Virgo During the Second Part of the Third Observing Run", 10.48550/arXiv.2111.03606 (2021).

[3] "Gravitational wave interferometer noise calculator", LIGO Scientific Collaboration.

[4] G. M. Harry, M. R. Abernathy, A. E. Becerra-Toledo, H. Armandula, E. Black, K. Dooley, M. Eichenfield, C. Nwabugwu, A. Villar, D. R. M. Crooks, G. Cagnoli, J. Hough, C. R. How, I. MacLaren, P. Murray, S. Reid, S. Rowan, P. H. Sneddon, M. M. Fejer, R. Route, S. D. Penn, P. Ganau, J.-M. Mackowski, C. Michel, L. Pinard, and A. Remillieux, "Titania-doped tantala/silica coatings for gravitational-wave detection", Classical and Quantum Gravity **24**, 405–415 (2006).

[5] D. V. Martynov et al., "Sensitivity of the Advanced LIGO detectors at the beginning of gravitational wave astronomy", Phys. Rev. D **93**, 112004 (2016).

[6] J. Steinlechner, "Development of mirror coatings for gravitational-wave detectors", Philosophical Transactions of the Royal Society A: Mathematical, Physical and Engineering Sciences **376**, 20170282 (2018).

[7] W. Yam, S. Gras, and M. Evans, "Multimaterial coatings with reduced thermal noise", Phys. Rev. D **91**, 042002 (2015).

[8] J. Steinlechner, I. W. Martin, J. Hough, C. Krüger, S. Rowan, and R. Schnabel, "Thermal noise reduction and absorption optimization via multimaterial coatings", Phys. Rev. D **91**, 042001 (2015).

[9] J. Steinlechner and I. W. Martin, "High index top layer for multimaterial coatings", Phys. Rev. D **93**, 102001 (2016).

[10] H.-W. Pan, S.-J. Wang, L.-C. Kuo, S. Chao, M. Principe, I. M. Pinto, and R. DeSalvo, "Thickness-dependent crystallization on thermal anneal for titania/silica nm-layer composites deposited by ion beam sputter method", Opt. Express **22**, 29847–29854 (2014).

[11] J. Steinlechner, I. W. Martin, A. S. Bell, J. Hough, M. Fletcher, P. G. Murray, R. Robie, S. Rowan, and R. Schnabel, "Silicon-Based Optical Mirror Coatings for Ultrahigh Precision Metrology and Sensing", Phys. Rev. Lett. **120**, 263602 (2018).

[12] H.-W. Pan, L.-C. Kuo, S.-Y. Huang, M.-Y. Wu, Y.-H. Juang, C.-W. Lee, H.-C. Chen, T. T. Wen, and S. Chao, "Silicon nitride films fabricated by a plasma-enhanced chemical vapor deposition method for coatings of the laser interferometer gravitational wave detector", Phys. Rev. D **97**, 022004 (2018).

[13] A. V. Cumming, K. Craig, I. W. Martin, R. Bassiri, L. Cunningham, M. M. Fejer, J. S. Harris, K. Haughian, D. Heinert, B. Lantz, A. C. Lin, A. S. Markosyan, R. Nawrodt, R. Route, and S. Rowan, "Measurement of the mechanical loss of prototype GaP/AlGaP crystalline coatings for future gravitational wave detectors", Classical and Quantum Gravity **32**, 035002 (2015).

[14] G. D. Cole, W. Zhang, M. J. Martin, J. Ye, and M. Aspelmeyer, "Tenfold reduction of Brownian noise in high-reflectivity optical coatings", Nature Photonics **7**, 644–650 (2013).

[15] H. B. Callen and R. F. Greene, "On a Theorem of Irreversible Thermodynamics", Phys. Rev. **86**, 702–710 (1952).

[16] R. O. Pohl, X. Liu, and E. Thompson, "Low-temperature thermal conductivity and acoustic attenuation in amorphous solids", Rev. Mod. Phys. **74**, 991–1013 (2002).

[17] S. D. Penn, M. M. Kinley-Hanlon, I. A. O. MacMillan, P. Heu, D. Follman, C. Deutsch, G. D. Cole, and G. M. Harry, "Mechanical ringdown studies of large-area substrate-transferred GaAs/AlGaAs crystalline coatings", J. Opt. Soc. Am. B **36**, C15–C21 (2019).

[18] T. Chalermsongsak, E. D. Hall, G. D. Cole, D. Follman, F. Seifert, K. Arai, E. K. Gustafson, J. R. Smith, M. Aspelmeyer, and R. X. Adhikari, "Coherent cancellation of photothermal noise in GaAs/Al0.92Ga0.08As Bragg mirrors", Metrologia **53**, 860–868 (2016).

[19] T. Hong, H. Yang, E. K. Gustafson, R. X. Adhikari, and Y. Chen, "Brownian thermal noise in multilayer coated mirrors", Phys. Rev. D **87**, 082001 (2013).

[20] D. Sigg and P. Schwinberg, "LIGO 3rd Generation Table Top Frequency Stabilization Servo", LIGO Scientific Collaboration **E1700065** (2017).

[21] T. Chalermsongsak, "High Fidelity Probe and Mitigation of Mirror Thermal Fluctuations", PhD Thesis, California Institute of Technology, `10.7907/7202-WT21` (2014).

[22] R. Abbott, "EOM Driver Circuit", LIGO Scientific Collaboration **D1200794** (2012).

[23] A. Gupta, "Transimpedance Amplifier for AD590 Temperature Sensor", LIGO Scientific Collaboration **D1800304** (2018).

[24] R. Abbott, "Pre Mode Cleaner Servo Card version A", LIGO Scientific Collaboration **D980352** (1998).

[25] C. Zener, "Internal Friction in Solids II. General Theory of Thermoelastic Internal Friction", Phys. Rev. **53**, 90–99 (1938).

[26]M. Evans, S. Ballmer, M. Fejer, P. Fritschel, G. Harry, and G. Ogin, "Thermo-optic noise in coated mirrors for high-precision optical measurements", Phys. Rev. D **78**, 102003 (2008).

[27]V. Braginsky, M. Gorodetsky, and S. Vyatchanin, "Thermo-refractive noise in gravitational wave antennae", Physics Letters A **271**, 303–307 (2000).

[28]K. Somiya, K. Kokeyama, and R. Nawrodt, "Remarks on thermoelastic effects at low temperatures and quantum limits in displacement measurements", Phys. Rev. D **82**, 127101 (2010).

[29]B. Willke, S. Brozek, K. Danzmann, V. Quetschke, and S. Gossler, "Frequency stabilization of a monolithic Nd:YAG ring laser by controlling the power of the laser-diode pump source", Opt. Lett. **25**, 1019–1021 (2000).

[30]A. Farsi, M. Siciliani de Cumis, F. Marino, and F. Marin, "Photothermal and thermo-refractive effects in high reflectivity mirrors at room and cryogenic temperature", Journal of Applied Physics **111**, 043101 (2012).

[31]C. Zener, "Internal Friction in Solids. I. Theory of Internal Friction in Reeds", Phys. Rev. **52**, 230–235 (1937).

[32]J. Yu, D. Kedar, S. Häfner, T. Legero, F. Riehle, S. Herbers, D. Nicolodi, C. Y. Ma, J. M. Robinson, E. Oelker, J. Ye, and U. Sterr, "Excess noise in highly reflective crystalline mirror coatings", `10.48550/ARXIV.2210.15671` (2022).

[33]B. Lantz, "Measurements and Mysteries of SRCL Noise", LIGO Scientific Collaboration **G2100193** (2021).

[34]A. Mullavey and V. Frolov, "Measurements and Mysteries of SRCL Noise", LIGO Scientific Collaboration **LLO alog 54677** (2021).

[35]G. Vajente, Y. Huang, M. Isi, J. C. Driggers, J. S. Kissel, M. J. Szczepa ńczyk, and S. Vitale, "Machine-learning nonstationary noise out of gravitational-wave detectors", Phys. Rev. D **101**, 042003 (2020).

[36]L. Barsotti, L. McCuller, G. Vajente, K. Kuns, A. Brooks, M. Evans, P. Fritschel, K. Kawabe, E. Oelker, and D. Sigg, "The Balanced Homodyne Detection Option for A+", LIGO Scientific Collaboration **T2100199** (2021).

[37]P. Fritschel, M. Evans, and V. Frolov, "Balanced homodyne readout for quantum limited gravitational wave detectors", Opt. Express **22**, 4224–4234 (2014).

[38]J. Gea-Benacloche and G. Leuchs, "Squeezed States for Interferometric Gravitational-wave Detectors", Journal of Modern Optics **34**, 793–811 (1987).

[39]T. M. Niebauer, R. Schilling, K. Danzmann, A. Rüdiger, and W. Winkler, "Non-stationary shot noise and its effect on the sensitivity of interferometers", Phys. Rev. A **43**, 5022–5029 (1991).

[40]B. J. Meers and K. A. Strain, "Modulation, signal, and quantum noise in interferometers", Phys. Rev. A **44**, 4693–4703 (1991).

[41]V. B. Braginsky and F. Y. Khalili, "Quantum nondemolition measurements: the route from toys to tools", Rev. Mod. Phys. **68**, 1–11 (1996).

[42]H. J. Kimble, Y. Levin, A. B. Matsko, K. S. Thorne, and S. P. Vyatchanin, "Conversion of conventional gravitational-wave interferometers into quantum nondemolition interferometers by modifying their input and/or output optics", Phys. Rev. D **65**, 022002 (2001).

[43]K. Somiya, "Photodetection method using unbalanced sidebands for squeezed quantum noise in a gravitational wave interferometer", Phys. Rev. D **67**, 122001 (2003).

[44]A. Buonanno, Y. Chen, and N. Mavalvala, "Quantum noise in laser-interferometer gravitational-wave detectors with a heterodyne readout scheme", Phys. Rev. D **67**, 122005 (2003).

[45]T. T. Fricke, N. D. Smith-Lefebvre, R. Abbott, R. Adhikari, K. L. Dooley, M. Evans, P. Fritschel, V. V. Frolov, K. Kawabe, J. S. Kissel, B. J. J. Slagmolen, and S. J. Waldman, "DC readout experiment in Enhanced LIGO", Classical and Quantum Gravity **29**, 065005 (2012).

[46]R. L. Ward, R. Adhikari, B. Abbott, R. Abbott, D. Barron, R. Bork, T. Fricke, V. Frolov, J. Heefner, A. Ivanov, O. Miyakawa, K. McKenzie, B. Slagmolen, M. Smith, R. Taylor, S. Vass, S. Waldman, and A. Weinstein, "dc readout experiment at the Caltech 40m prototype interferometer", Classical and Quantum Gravity **25**, 114030 (2008).

[47]R. L. Ward, "Length Sensing and Control of a Prototype Advanced Interferometric Gravitational Wave Detector", PhD Thesis, California Institute of Technology, `10.7907/20SX-2935` (2010).

[48]D. S. Kiwamu Izumi and K. Kawabe, "Frequency response of the aLIGO interferometer: part 3", LIGO Scientific Collaboration **T1500559** (2015).

[49]P. Purdue and Y. Chen, "Practical speed meter designs for quantum nondemolition gravitational-wave interferometers", Phys. Rev. D **66**, 122004 (2002).

[50]J. Driggers, "Noise Cancellation for Gravitational Wave Detectors", PhD Thesis, California Institute of Technology, `10.7907/Z94F1NNP` (2015).

[51]G. Venugopalan, "Prototype Interferometry in the Era of Gravitational Wave Astronomy", PhD Thesis, California Institute of Technology, `10.7907/ttwp-1h12` (2021).

[52]C. Cahillane, J. Betzwieser, D. A. Brown, E. Goetz, E. D. Hall, K. Izumi, S. Kandhasamy, S. Karki, J. S. Kissel, G. Mendell, R. L. Savage, D. Tuyenbayev, A. Urban, A. Viets, M. Wade, and A. J. Weinstein, "Calibration uncertainty for Advanced LIGO's first and second observing runs", Phys. Rev. D **96**, 102001 (2017).

[53] B. P. Abbott et al., "Binary Black Hole Population Properties Inferred from the First and Second Observing Runs of Advanced LIGO and Advanced Virgo", The Astrophysical Journal Letters **882**, L24 (2019).

[54] K. Chatziioannou, "Neutron-star tidal deformability and equation-of-state constraints", General Relativity and Gravitation **52**, 10.1007/s10714-020-02754-3 (2020).

[55] B. P. Abbott et al. (LIGO Scientific Collaboration and Virgo Collaboration), "GW170817: Observation of Gravitational Waves from a Binary Neutron Star Inspiral", Phys. Rev. Lett. **119**, 161101 (2017).

[56] B. P. Abbott et al., "GW190425: Observation of a Compact Binary Coalescence with Total Mass ~ 3.4 M_{cdot}", The Astrophysical Journal Letters **892**, L3 (2020).

[57] R. Dudi, F. Pannarale, T. Dietrich, M. Hannam, S. Bernuzzi, F. Ohme, and B. Brügmann, "Relevance of tidal effects and post-merger dynamics for binary neutron star parameter estimation", Phys. Rev. D **98**, 084061 (2018).

[58] A. Samajdar and T. Dietrich, "Waveform systematics for binary neutron star gravitational wave signals: Effects of the point-particle baseline and tidal descriptions", Phys. Rev. D **98**, 124030 (2018).

[59] B. P. Abbott, R. Abbott, T. D. Abbott, M. R. Abernathy, F. Acernese, K. Ackley, C. Adams, T. Adams, P. Addesso, R. X. Adhikari, V. B. Adya, C. Affeldt, M. Agathos, K. Agatsuma, N. Aggarwal, O. D. Aguiar, L. Aiello, A. Ain, P. Ajith, B. Allen, A. Allocca, P. A. Altin, S. B. Anderson, W. G. Anderson, K. Arai, M. C. Araya, C. C. Arceneaux, J. S. Areeda, N. Arnaud, K. G. Arun, S. Ascenzi, G. Ashton, M. Ast, S. M. Aston, P. Astone, P. Aufmuth, C. Aulbert, S. Babak, P. Bacon, M. K. M. Bader, P. T. Baker, F. Baldaccini, G. Ballardin, S. W. Ballmer, J. C. Barayoga, S. E. Barclay, B. C. Barish, D. Barker, F. Barone, B. Barr, L. Barsotti, M. Barsuglia, D. Barta, J. Bartlett, I. Bartos, R. Bassiri, A. Basti, J. C. Batch, C. Baune, V. Bavigadda, M. Bazzan, B. Behnke, M. Bejger, A. S. Bell, C. J. Bell, B. K. Berger, J. Bergman, G. Bergmann, C. P. L. Berry, D. Bersanetti, A. Bertolini, J. Betzwieser, S. Bhagwat, R. Bhandare, I. A. Bilenko, G. Billingsley, J. Birch, R. Birney, O. Birnholtz, S. Biscans, A. Bisht, M. Bitossi, C. Biwer, M. A. Bizouard, J. K. Blackburn, C. D. Blair, D. G. Blair, R. M. Blair, S. Bloemen, O. Bock, T. P. Bodiya, M. Boer, G. Bogaert, C. Bogan, A. Bohe, P. Bojtos, C. Bond, F. Bondu, R. Bonnand, B. A. Boom, R. Bork, V. Boschi, S. Bose, Y. Bouffanais, A. Bozzi, C. Bradaschia, P. R. Brady, V. B. Braginsky, M. Branchesi, J. E. Brau, T. Briant, A. Brillet, M. Brinkmann, V. Brisson, P. Brockill, A. F. Brooks, D. A. Brown, D. D. Brown, N. M. Brown, C. C. Buchanan, A. Buikema, T. Bulik, H. J. Bulten, A. Buonanno, D. Buskulic, C. Buy, R. L. Byer, L. Cadonati, G. Cagnoli, C. Cahillane, J. Calderón Bustillo, T. Callister, E. Calloni, J. B. Camp, K. C. Cannon, J. Cao, C. D. Capano, E. Capocasa, F. Carbognani, S. Caride, J. Casanueva Diaz, C. Casentini, S. Caudill, M. Cavaglià, F. Cavalier, R. Cavalieri, G. Cella, C. B. Cepeda, L. Cerboni Baiardi, G. Cerretani, E. Cesarini, R. Chakraborty, T. Chalermsongsak, S. J. Chamberlin, M. Chan, S. Chao, P. Charlton, E. Chassande-

Mottin, H. Y. Chen, Y. Chen, C. Cheng, A. Chincarini, A. Chiummo, H. S. Cho, M. Cho, J. H. Chow, N. Christensen, Q. Chu, S. Chua, S. Chung, G. Ciani, F. Clara, J. A. Clark, F. Cleva, E. Coccia, P.-F. Cohadon, A. Colla, C. G. Collette, L. Cominsky, M. Constancio, A. Conte, L. Conti, D. Cook, T. R. Corbitt, N. Cornish, A. Corsi, S. Cortese, C. A. Costa, M. W. Coughlin, S. B. Coughlin, J.-P. Coulon, S. T. Countryman, P. Couvares, E. E. Cowan, D. M. Coward, M. J. Cowart, D. C. Coyne, R. Coyne, K. Craig, J. D. E. Creighton, J. Cripe, S. G. Crowder, A. Cumming, L. Cunningham, E. Cuoco, T. Dal Canton, S. L. Danilishin, S. D'Antonio, K. Danzmann, N. S. Darman, V. Dattilo, I. Dave, H. P. Daveloza, M. Davier, G. S. Davies, E. J. Daw, R. Day, D. DeBra, G. Debreczeni, J. Degallaix, M. De Laurentis, S. Deléglise, W. Del Pozzo, T. Denker, T. Dent, H. Dereli, V. Dergachev, R. De Rosa, R. T. DeRosa, R. DeSalvo, S. Dhurandhar, M. C. Díaz, L. Di Fiore, M. Di Giovanni, A. Di Lieto, S. Di Pace, I. Di Palma, A. Di Virgilio, G. Dojcinoski, V. Dolique, F. Donovan, K. L. Dooley, S. Doravari, R. Douglas, T. P. Downes, M. Drago, R. W. P. Drever, J. C. Driggers, Z. Du, M. Ducrot, S. E. Dwyer, T. B. Edo, M. C. Edwards, A. Effler, H.-B. Eggenstein, P. Ehrens, J. Eichholz, S. S. Eikenberry, W. Engels, R. C. Essick, T. Etzel, M. Evans, T. M. Evans, R. Everett, M. Factourovich, V. Fafone, H. Fair, S. Fairhurst, X. Fan, Q. Fang, S. Farinon, B. Farr, W. M. Farr, M. Favata, M. Fays, H. Fehrmann, M. M. Fejer, I. Ferrante, E. C. Ferreira, F. Ferrini, F. Fidecaro, I. Fiori, D. Fiorucci, R. P. Fisher, R. Flaminio, M. Fletcher, J.-D. Fournier, S. Franco, S. Frasca, F. Frasconi, Z. Frei, A. Freise, R. Frey, V. Frey, T. T. Fricke, P. Fritschel, V. V. Frolov, P. Fulda, M. Fyffe, H. A. G. Gabbard, J. R. Gair, L. Gammaitoni, S. G. Gaonkar, F. Garufi, A. Gatto, G. Gaur, N. Gehrels, G. Gemme, B. Gendre, E. Genin, A. Gennai, J. George, L. Gergely, V. Germain, A. Ghosh, A. Ghosh, S. Ghosh, J. A. Giaime, K. D. Giardina, A. Giazotto, K. Gill, A. Glaefke, E. Goetz, R. Goetz, L. Gondan, G. González, J. M. Gonzalez Castro, A. Gopakumar, N. A. Gordon, M. L. Gorodetsky, S. E. Gossan, M. Gosselin, R. Gouaty, C. Graef, P. B. Graff, M. Granata, A. Grant, S. Gras, C. Gray, G. Greco, A. C. Green, P. Groot, H. Grote, S. Grunewald, G. M. Guidi, X. Guo, A. Gupta, M. K. Gupta, K. E. Gushwa, E. K. Gustafson, R. Gustafson, J. J. Hacker, B. R. Hall, E. D. Hall, G. Hammond, M. Haney, M. M. Hanke, J. Hanks, C. Hanna, M. D. Hannam, J. Hanson, T. Hardwick, J. Harms, G. M. Harry, I. W. Harry, M. J. Hart, M. T. Hartman, C.-J. Haster, K. Haughian, J. Healy, A. Heidmann, M. C. Heintze, H. Heitmann, P. Hello, G. Hemming, M. Hendry, I. S. Heng, J. Hennig, A. W. Heptonstall, M. Heurs, S. Hild, D. Hoak, K. A. Hodge, D. Hofman, S. E. Hollitt, K. Holt, D. E. Holz, P. Hopkins, D. J. Hosken, J. Hough, E. A. Houston, E. J. Howell, Y. M. Hu, S. Huang, E. A. Huerta, D. Huet, B. Hughey, S. Husa, S. H. Huttner, T. Huynh-Dinh, A. Idrisy, N. Indik, D. R. Ingram, R. Inta, H. N. Isa, J.-M. Isac, M. Isi, G. Islas, T. Isogai, B. R. Iyer, K. Izumi, T. Jacqmin, H. Jang, K. Jani, P. Jaranowski, S. Jawahar, F. Jiménez-Forteza, W. W. Johnson, N. K. Johnson-McDaniel, D. I. Jones, R. Jones, R. J. G. Jonker, L. Ju, M. K. Haris, C. V. Kalaghatgi, V. Kalogera, S. Kandhasamy, G. Kang, J. B. Kanner, S. Karki, M. Kasprzack, E. Katsavounidis, W. Katzman, S. Kaufer, T. Kaur, K. Kawabe, F. Kawazoe, F. Kéfélian, M. S. Kehl, D. Keitel, D. B. Kelley, W. Kells, R. Kennedy, J. S. Key, A. Khalaidovski, F. Y.

Khalili, I. Khan, S. Khan, Z. Khan, E. A. Khazanov, N. Kijbunchoo, C. Kim, J. Kim, K. Kim, N.-G. Kim, N. Kim, Y.-M. Kim, E. J. King, P. J. King, D. L. Kinzel, J. S. Kissel, L. Kleybolte, S. Klimenko, S. M. Koehlenbeck, K. Kokeyama, S. Koley, V. Kondrashov, A. Kontos, M. Korobko, W. Z. Korth, I. Kowalska, D. B. Kozak, V. Kringel, B. Krishnan, A. Królak, C. Krueger, G. Kuehn, P. Kumar, L. Kuo, A. Kutynia, B. D. Lackey, M. Landry, J. Lange, B. Lantz, P. D. Lasky, A. Lazzarini, C. Lazzaro, P. Leaci, S. Leavey, E. O. Lebigot, C. H. Lee, H. K. Lee, H. M. Lee, K. Lee, A. Lenon, M. Leonardi, J. R. Leong, N. Leroy, N. Letendre, Y. Levin, B. M. Levine, T. G. F. Li, A. Libson, T. B. Littenberg, N. A. Lockerbie, J. Logue, A. L. Lombardi, L. T. London, J. E. Lord, M. Lorenzini, V. Loriette, M. Lormand, G. Losurdo, J. D. Lough, C. O. Lousto, G. Lovelace, H. Lück, A. P. Lundgren, J. Luo, R. Lynch, Y. Ma, T. MacDonald, B. Machenschalk, M. MacInnis, D. M. Macleod, F. Magaña-Sandoval, R. M. Magee, M. Mageswaran, E. Majorana, I. Maksimovic, V. Malvezzi, N. Man, I. Mandel, V. Mandic, V. Mangano, G. L. Mansell, M. Manske, M. Mantovani, F. Marchesoni, F. Marion, S. Márka, Z. Márka, A. S. Markosyan, E. Maros, F. Martelli, L. Martellini, I. W. Martin, R. M. Martin, D. V. Martynov, J. N. Marx, K. Mason, A. Masserot, T. J. Massinger, M. Masso-Reid, F. Matichard, L. Matone, N. Mavalvala, N. Mazumder, G. Mazzolo, R. McCarthy, D. E. McClelland, S. McCormick, S. C. McGuire, G. McIntyre, J. McIver, D. J. McManus, S. T. McWilliams, D. Meacher, G. D. Meadors, J. Meidam, A. Melatos, G. Mendell, D. Mendoza-Gandara, R. A. Mercer, E. Merilh, M. Merzougui, S. Meshkov, C. Messenger, C. Messick, P. M. Meyers, F. Mezzani, H. Miao, C. Michel, H. Middleton, E. E. Mikhailov, L. Milano, J. Miller, M. Millhouse, Y. Minenkov, J. Ming, S. Mirshekari, C. Mishra, S. Mitra, V. P. Mitrofanov, G. Mitselmakher, R. Mittleman, A. Moggi, M. Mohan, S. R. P. Mohapatra, M. Montani, B. C. Moore, C. J. Moore, D. Moraru, G. Moreno, S. R. Morriss, K. Mossavi, B. Mours, C. M. Mow-Lowry, C. L. Mueller, G. Mueller, A. W. Muir, A. Mukherjee, D. Mukherjee, S. Mukherjee, N. Mukund, A. Mullavey, J. Munch, D. J. Murphy, P. G. Murray, A. Mytidis, I. Nardecchia, L. Naticchioni, R. K. Nayak, V. Necula, K. Nedkova, G. Nelemans, M. Neri, A. Neunzert, G. Newton, T. T. Nguyen, A. B. Nielsen, S. Nissanke, A. Nitz, F. Nocera, D. Nolting, M. E. Normandin, L. K. Nuttall, J. Oberling, E. Ochsner, J. O'Dell, E. Oelker, G. H. Ogin, J. J. Oh, S. H. Oh, F. Ohme, M. Oliver, P. Oppermann, R. J. Oram, B. O'Reilly, R. O'Shaughnessy, D. J. Ottaway, R. S. Ottens, H. Overmier, B. J. Owen, A. Pai, S. A. Pai, J. R. Palamos, O. Palashov, C. Palomba, A. Pal-Singh, H. Pan, Y. Pan, C. Pankow, F. Pannarale, B. C. Pant, F. Paoletti, A. Paoli, M. A. Papa, H. R. Paris, W. Parker, D. Pascucci, A. Pasqualetti, R. Passaquieti, D. Passuello, B. Patricelli, Z. Patrick, B. L. Pearlstone, M. Pedraza, R. Pedurand, L. Pekowsky, A. Pele, S. Penn, A. Perreca, H. P. Pfeiffer, M. Phelps, O. Piccinni, M. Pichot, F. Piergiovanni, V. Pierro, G. Pillant, L. Pinard, I. M. Pinto, M. Pitkin, R. Poggiani, P. Popolizio, A. Post, J. Powell, J. Prasad, V. Predoi, S. S. Premachandra, T. Prestegard, L. R. Price, M. Prijatelj, M. Principe, S. Privitera, R. Prix, G. A. Prodi, L. Prokhorov, O. Puncken, M. Punturo, P. Puppo, M. Pürrer, H. Qi, J. Qin, V. Quetschke, E. A. Quintero, R. Quitzow-James, F. J. Raab, D. S. Rabeling, H. Radkins, P. Raffai, S. Raja, M. Rakhmanov, P. Rapagnani, V. Raymond, M.

Razzano, V. Re, J. Read, C. M. Reed, T. Regimbau, L. Rei, S. Reid, D. H. Reitze, H. Rew, S. D. Reyes, F. Ricci, K. Riles, N. A. Robertson, R. Robie, F. Robinet, A. Rocchi, L. Rolland, J. G. Rollins, V. J. Roma, R. Romano, G. Romanov, J. H. Romie, D. Rosi ńska, S. Rowan, A. Rüdiger, P. Ruggi, K. Ryan, S. Sachdev, T. Sadecki, L. Sadeghian, L. Salconi, M. Saleem, F. Salemi, A. Samajdar, L. Sammut, E. J. Sanchez, V. Sandberg, B. Sandeen, J. R. Sanders, B. Sassolas, B. S. Sathyaprakash, P. R. Saulson, O. Sauter, R. L. Savage, A. Sawadsky, P. Schale, R. Schilling, J. Schmidt, P. Schmidt, R. Schnabel, R. M. S. Schofield, A. Schönbeck, E. Schreiber, D. Schuette, B. F. Schutz, J. Scott, S. M. Scott, D. Sellers, A. S. Sengupta, D. Sentenac, V. Sequino, A. Sergeev, G. Serna, Y. Setyawati, A. Sevigny, D. A. Shaddock, S. Shah, M. S. Shahriar, M. Shaltev, Z. Shao, B. Shapiro, P. Shawhan, A. Sheperd, D. H. Shoemaker, D. M. Shoemaker, K. Siellez, X. Siemens, D. Sigg, A. D. Silva, D. Simakov, A. Singer, L. P. Singer, A. Singh, R. Singh, A. Singhal, A. M. Sintes, B. J. J. Slagmolen, J. R. Smith, N. D. Smith, R. J. E. Smith, E. J. Son, B. Sorazu, F. Sorrentino, T. Souradeep, A. K. Srivastava, A. Staley, M. Steinke, J. Steinlechner, S. Steinlechner, D. Steinmeyer, B. C. Stephens, R. Stone, K. A. Strain, N. Straniero, G. Stratta, N. A. Strauss, S. Strigin, R. Sturani, A. L. Stuver, T. Z. Summerscales, L. Sun, P. J. Sutton, B. L. Swinkels, M. J. Szczepa ńczyk, M. Tacca, D. Talukder, D. B. Tanner, M. Tápai, S. P. Tarabrin, A. Taracchini, R. Taylor, T. Theeg, M. P. Thirugnanasambandam, E. G. Thomas, M. Thomas, P. Thomas, K. A. Thorne, K. S. Thorne, E. Thrane, S. Tiwari, V. Tiwari, K. V. Tokmakov, C. Tomlinson, M. Tonelli, C. V. Torres, C. I. Torrie, D. Töyrä, F. Travasso, G. Traylor, D. Trifirò, M. C. Tringali, L. Trozzo, M. Tse, M. Turconi, D. Tuyenbayev, D. Ugolini, C. S. Unnikrishnan, A. L. Urban, S. A. Usman, H. Vahlbruch, G. Vajente, G. Valdes, M. Vallisneri, N. van Bakel, M. van Beuzekom, J. F. J. van den Brand, C. Van Den Broeck, D. C. Vander-Hyde, L. van der Schaaf, J. V. van Heijningen, A. A. van Veggel, M. Vardaro, S. Vass, M. Vasúth, R. Vaulin, A. Vecchio, G. Vedovato, J. Veitch, P. J. Veitch, K. Venkateswara, D. Verkindt, F. Vetrano, A. Viceré, S. Vinciguerra, D. J. Vine, J.-Y. Vinet, S. Vitale, T. Vo, H. Vocca, C. Vorvick, D. Voss, W. D. Vousden, S. P. Vyatchanin, A. R. Wade, L. E. Wade, M. Wade, M. Walker, L. Wallace, S. Walsh, G. Wang, H. Wang, M. Wang, X. Wang, Y. Wang, R. L. Ward, J. Warner, M. Was, B. Weaver, L.-W. Wei, M. Weinert, A. J. Weinstein, R. Weiss, T. Welborn, L. Wen, P. Weßels, T. Westphal, K. Wette, J. T. Whelan, D. J. White, B. F. Whiting, D. Williams, R. D. Williams, A. R. Williamson, J. L. Willis, B. Willke, M. H. Wimmer, W. Winkler, C. C. Wipf, H. Wittel, G. Woan, J. Worden, J. L. Wright, G. Wu, J. Yablon, W. Yam, H. Yamamoto, C. C. Yancey, M. J. Yap, H. Yu, M. Yvert, A. Zadro żny, L. Zangrando, M. Zanolin, J.-P. Zendri, M. Zevin, F. Zhang, L. Zhang, M. Zhang, Y. Zhang, C. Zhao, M. Zhou, Z. Zhou, X. J. Zhu, M. E. Zucker, S. E. Zuraw, J. Zweizig, M. Boyle, M. Campanelli, D. A. Hemberger, L. E. Kidder, S. Ossokine, M. A. Scheel, B. Szilagyi, S. Teukolsky, and Y. Zlochower (LIGO Scientific Collaboration and Virgo Collaboration), "Tests of General Relativity with GW150914", Phys. Rev. Lett. **116**, 221101 (2016).

[60]B. P. Abbott et al. (LIGO Scientific Collaboration and Virgo Collaboration), "Tests of General Relativity with GW170817", Phys. Rev. Lett. **123**, 011102 (2019).

[61]B. P. Abbott et al. (The LIGO Scientific Collaboration and the Virgo Collaboration), "Tests of general relativity with the binary black hole signals from the LIGO-Virgo catalog GWTC-1", Phys. Rev. D **100**, 104036 (2019).

[62]R. Abbott et al. (LIGO Scientific Collaboration and Virgo Collaboration and KAGRA Collaboration), "Tests of General Relativity with GWTC-3", `10.48550/arXiv.2112.06861` (2021).

[63]A. G. Riess, S. Casertano, W. Yuan, L. M. Macri, and D. Scolnic, "Large Magellanic Cloud Cepheid Standards Provide a 1% Foundation for the Determination of the Hubble Constant and Stronger Evidence for Physics beyond ΛCDM", The Astrophysical Journal **876**, 85 (2019).

[64]Aghanim, N., Akrami, Y., Ashdown, M., Aumont, J., Baccigalupi, C., Ballardini, M., Banday, A. J., Barreiro, R. B., Bartolo, N., Basak, S., Battye, R., Benabed, K., Bernard, J.-P., Bersanelli, M., Bielewicz, P., Bock, J. J., Bond, J. R., Borrill, J., Bouchet, F. R., Boulanger, F., Bucher, M., Burigana, C., Butler, R. C., Calabrese, E., Cardoso, J.-F., Carron, J., Challinor, A., Chiang, H. C., Chluba, J., Colombo, L. P. L., Combet, C., Contreras, D., Crill, B. P., Cuttaia, F., de Bernardis, P., de Zotti, G., Delabrouille, J., Delouis, J.-M., Di Valentino, E., Diego, J. M., Doré, O., Douspis, M., Ducout, A., Dupac, X., Dusini, S., Efstathiou, G., Elsner, F., Enßlin, T. A., Eriksen, H. K., Fantaye, Y., Farhang, M., Fergusson, J., Fernandez-Cobos, R., Finelli, F., Forastieri, F., Frailis, M., Fraisse, A. A., Franceschi, E., Frolov, A., Galeotta, S., Galli, S., Ganga, K., Génova-Santos, R. T., Gerbino, M., Ghosh, T., González-Nuevo, J., Górski, K. M., Gratton, S., Gruppuso, A., Gudmundsson, J. E., Hamann, J., Handley, W., Hansen, F. K., Herranz, D., Hildebrandt, S. R., Hivon, E., Huang, Z., Jaffe, A. H., Jones, W. C., Karakci, A., Keihänen, E., Keskitalo, R., Kiiveri, K., Kim, J., Kisner, T. S., Knox, L., Krachmalnicoff, N., Kunz, M., Kurki-Suonio, H., Lagache, G., Lamarre, J.-M., Lasenby, A., Lattanzi, M., Lawrence, C. R., Le Jeune, M., Lemos, P., Lesgourgues, J., Levrier, F., Lewis, A., Liguori, M., Lilje, P. B., Lilley, M., Lindholm, V., López-Caniego, M., Lubin, P. M., Ma, Y.-Z., Macías-Pérez, J. F., Maggio, G., Maino, D., Mandolesi, N., Mangilli, A., Marcos-Caballero, A., Maris, M., Martin, P. G., Martinelli, M., Martínez-González, E., Matarrese, S., Mauri, N., McEwen, J. D., Meinhold, P. R., Melchiorri, A., Mennella, A., Migliaccio, M., Millea, M., Mitra, S., Miville-Deschênes, M.-A., Molinari, D., Montier, L., Morgante, G., Moss, A., Natoli, P., Nørgaard-Nielsen, H. U., Pagano, L., Paoletti, D., Partridge, B., Patanchon, G., Peiris, H. V., Perrotta, F., Pettorino, V., Piacentini, F., Polastri, L., Polenta, G., Puget, J.-L., Rachen, J. P., Reinecke, M., Remazeilles, M., Renzi, A., Rocha, G., Rosset, C., Roudier, G., Rubiño-Martín, J. A., Ruiz-Granados, B., Salvati, L., Sandri, M., Savelainen, M., Scott, D., Shellard, E. P. S., Sirignano, C., Sirri, G., Spencer, L. D., Sunyaev, R., Suur-Uski, A.-S., Tauber, J. A., Tavagnacco, D., Tenti, M., Toffolatti, L., Tomasi, M., Trombetti, T., Valenziano, L., Valiviita, J., Van Tent, B., Vibert, L., Vielva, P., Villa, F., Vittorio, N., Wandelt, B. D., Wehus, I.

K., White, M., White, S. D. M., Zacchei, A., and Zonca, A. (Planck Collaboration), "Planck 2018 results - VI. Cosmological parameters", A&A **641**, A6 (2020).

[65]E. Macaulay, R. C. Nichol, D. Bacon, D. Brout, T. M. Davis, B. Zhang, B. A. Bassett, D. Scolnic, A. Möller, C. B. D'Andrea, S. R. Hinton, R. Kessler, A. G. Kim, J. Lasker, C. Lidman, M. Sako, M. Smith, M. Sullivan, T. M. C. Abbott, S. Allam, J. Annis, J. Asorey, S. Avila, K. Bechtol, D. Brooks, P. Brown, D. L. Burke, J. Calcino, A. Carnero Rosell, D. Carollo, M. Carrasco Kind, J. Carretero, F. J. Castander, T. Collett, M. Crocce, C. E. Cunha, L. N. da Costa, C. Davis, J. De Vicente, H. T. Diehl, P. Doel, A. Drlica-Wagner, T. F. Eifler, J. Estrada, A. E. Evrard, A. V. Filippenko, D. A. Finley, B. Flaugher, R. J. Foley, P. Fosalba, J. Frieman, L. Galbany, J. García-Bellido, E. Gaztanaga, K. Glazebrook, S. González-Gaitán, D. Gruen, R. A. Gruendl, J. Gschwend, G. Gutierrez, W. G. Hartley, D. L. Hollowood, K. Honscheid, J. K. Hoormann, B. Hoyle, D. Huterer, B. Jain, D. J. James, T. Jeltema, E. Kasai, E. Krause, K. Kuehn, N. Kuropatkin, O. Lahav, G. F. Lewis, T. S. Li, M. Lima, H. Lin, M. A. G. Maia, J. L. Marshall, P. Martini, R. Miquel, P. Nugent, A. Palmese, Y.-C. Pan, A. A. Plazas, A. K. Romer, A. Roodman, E. Sanchez, V. Scarpine, R. Schindler, M. Schubnell, S. Serrano, I. Sevilla-Noarbe, R. Sharp, M. Soares-Santos, F. Sobreira, N. E. Sommer, E. Suchyta, E. Swann, M. E. C. Swanson, G. Tarle, D. Thomas, R. C. Thomas, B. E. Tucker, S. A. Uddin, V. Vikram, A. R. Walker, and P. Wiseman, "First cosmological results using Type Ia supernovae from the Dark Energy Survey: measurement of the Hubble constant", Monthly Notices of the Royal Astronomical Society **486**, 2184–2196 (2019).

[66]G. E. Addison, D. J. Watts, C. L. Bennett, M. Halpern, G. Hinshaw, and J. L. Weiland, "Elucidating ΛCDM: Impact of Baryon Acoustic Oscillation Measurements on the Hubble Constant Discrepancy", The Astrophysical Journal **853**, 119 (2018).

[67]S. Birrer, T. Treu, C. E. Rusu, V. Bonvin, C. D. Fassnacht, J. H. H. Chan, A. Agnello, A. J. Shajib, G. C.-F. Chen, M. Auger, F. Courbin, S. Hilbert, D. Sluse, S. H. Suyu, K. C. Wong, P. Marshall, B. C. Lemaux, and G. Meylan, "H0LiCOW - IX. Cosmographic analysis of the doubly imaged quasar SDSS 1206+4332 and a new measurement of the Hubble constant", Monthly Notices of the Royal Astronomical Society **484**, 4726–4753 (2019).

[68]Dhawan, Suhail, Jha, Saurabh W., and Leibundgut, Bruno, "Measuring the Hubble constant with Type Ia supernovae as near-infrared standard candles", A&A **609**, A72 (2018).

[69]C. R. Burns, E. Parent, M. M. Phillips, M. Stritzinger, K. Krisciunas, N. B. Suntzeff, E. Y. Hsiao, C. Contreras, J. Anais, L. Boldt, L. Busta, A. Campillay, S. Castellón, G. Folatelli, W. L. Freedman, C. González, M. Hamuy, P. Heoflich, W. Krzeminski, B. F. Madore, N. Morrell, S. E. Persson, M. Roth, F. Salgado, J. Serón, and S. Torres, "The Carnegie Supernova Project: Absolute Calibration and the Hubble Constant", The Astrophysical Journal **869**, 56 (2018).

[70] B. P. Abbott et al., "Multi-messenger Observations of a Binary Neutron Star Merger*", The Astrophysical Journal Letters **848**, L12 (2017).

[71] "A gravitational-wave standard siren measurement of the Hubble constant", Nature **551**, 85–55 (2017).

[72] W. L. Freedman, B. F. Madore, B. K. Gibson, L. Ferrarese, D. D. Kelson, S. Sakai, J. R. Mould, J. Robert C. Kennicutt, H. C. Ford, J. A. Graham, J. P. Huchra, S. M. G. Hughes, G. D. Illingworth, L. M. Macri, and P. B. Stetson, "Final Results from the Hubble Space Telescope Key Project to Measure the Hubble Constant", The Astrophysical Journal **553**, 47 (2001).

[73] R. Abbott et al. (LIGO Scientific Collaboration and Virgo Collaboration and KAGRA Collaboration), "Constraints on the cosmic expansion history from GWTC-3", `10.48550/arXiv.2111.03604` (2021).

[74] E. D. Hall, C. Cahillane, K. Izumi, R. J. E. Smith, and R. X. Adhikari, "Systematic calibration error requirements for gravitational-wave detectors via the Cramér-Rao bound", Classical and Quantum Gravity **36**, 205006 (2019).

[75] R. X. Adhikari, K. Arai, A. F. Brooks, C. Wipf, O. Aguiar, P. Altin, B. Barr, L. Barsotti, R. Bassiri, A. Bell, G. Billingsley, R. Birney, D. Blair, E. Bonilla, J. Briggs, D. D. Brown, R. Byer, H. Cao, M. Constancio, S. Cooper, T. Corbitt, D. Coyne, A. Cumming, E. Daw, R. deRosa, G. Eddolls, J. Eichholz, M. Evans, M. Fejer, E. C. Ferreira, A. Freise, V. V. Frolov, S. Gras, A. Green, H. Grote, E. Gustafson, E. D. Hall, G. Hammond, J. Harms, G. Harry, K. Haughian, D. Heinert, M. Heintze, F. Hellman, J. Hennig, M. Hennig, S. Hild, J. Hough, W. Johnson, B. Kamai, D. Kapasi, K. Komori, D. Koptsov, M. Korobko, W. Z. Korth, K. Kuns, B. Lantz, S. Leavey, F. Magana-Sandoval, G. Mansell, A. Markosyan, A. Markowitz, I. Martin, R. Martin, D. Martynov, D. E. McClelland, G. McGhee, T. McRae, J. Mills, V. Mitrofanov, M. Molina-Ruiz, C. Mow-Lowry, J. Munch, P. Murray, S. Ng, M. A. Okada, D. J. Ottaway, L. Prokhorov, V. Quetschke, S. Reid, D. Reitze, J. Richardson, R. Robie, I. Romero-Shaw, R. Route, S. Rowan, R. Schnabel, M. Schneewind, F. Seifert, D. Shaddock, B. Shapiro, D. Shoemaker, A. S. Silva, B. Slagmolen, J. Smith, N. Smith, J. Steinlechner, K. Strain, D. Taira, S. Tait, D. Tanner, Z. Tornasi, C. Torrie, M. V. Veggel, J. Vanheijningen, P. Veitch, A. Wade, G. Wallace, R. Ward, R. Weiss, P. Wessels, B. Willke, H. Yamamoto, M. J. Yap, and C. Zhao, "A cryogenic silicon interferometer for gravitational-wave detection", Classical and Quantum Gravity **37**, 165003 (2020).

[76] M. Evans, R. X. Adhikari, C. Afle, S. W. Ballmer, S. Biscoveanu, S. Borhanian, D. A. Brown, Y. Chen, R. Eisenstein, A. Gruson, A. Gupta, E. D. Hall, R. Huxford, B. Kamai, R. Kashyap, J. S. Kissel, K. Kuns, P. Landry, A. Lenon, G. Lovelace, L. McCuller, K. K. Y. Ng, A. H. Nitz, J. Read, B. S. Sathyaprakash, D. H. Shoemaker, B. J. J. Slagmolen, J. R. Smith, V. Srivastava, L. Sun, S. Vitale, and R. Weiss, "A horizon study for Cosmic Explorer", Cosmic Explorer Consortium **CEP2100003** (2021).

[77]S. Karki, D. Tuyenbayev, S. Kandhasamy, B. P. Abbott, T. D. Abbott, E. H. Anders, J. Berliner, J. Betzwieser, C. Cahillane, L. Canete, C. Conley, H. P. Daveloza, N. De Lillo, J. R. Gleason, E. Goetz, K. Izumi, J. S. Kissel, G. Mendell, V. Quetschke, M. Rodruck, S. Sachdev, T. Sadecki, P. B. Schwinberg, A. Sottile, M. Wade, A. J. Weinstein, M. West, and R. L. Savage, "The Advanced LIGO photon calibrators", Review of Scientific Instruments **87**, 114503 (2016).

[78]M. P. Ross, T. Mistry, L. Datrier, J. Kissel, K. Venkateswara, C. Weller, K. Kumar, C. Hagedorn, E. Adelberger, J. Lee, E. Shaw, P. Thomas, D. Barker, F. Clara, B. Gateley, T. M. Guidry, E. Daw, M. Hendry, and J. Gundlach, "Initial results from the LIGO Newtonian calibrator", Phys. Rev. D **104**, 082006 (2021).

[79]D. Estevez, B. Mours, and T. Pradier, "Newtonian calibrator tests during the Virgo O3 data taking", Classical and Quantum Gravity **38**, 075012 (2021).

[80]Y. Inoue, S. Haino, N. Kanda, Y. Ogawa, T. Suzuki, T. Tomaru, T. Yamanmoto, and T. Yokozawa, "Improving the absolute accuracy of the gravitational wave detectors by combining the photon pressure and gravity field calibrators", Phys. Rev. D **98**, 022005 (2018).

[81]"Private communication with Prof. Rana Adhikari.",

[82]K. Izumi, K. Arai, B. Barr, J. Betzwieser, A. Brooks, K. Dahl, S. Doravari, J. C. Driggers, W. Z. Korth, H. Miao, J. Rollins, S. Vass, D. Yeaton-Massey, and R. X. Adhikari, "Multicolor cavity metrology", J. Opt. Soc. Am. A **29**, 2092–2103 (2012).

[83]A. N. Staley, "Locking the Advanced LIGO Gravitational Wave Detector: with a focus on the Arm Length Stabilization Technique", PhD Thesis, Columbia University, `10.7916/D8X34WQ4` (2015).

[84]D. Yeaton-Massey and R. X. Adhikari, "A new bound on excess frequency noise in second harmonic generation in PPKTP at the 10^{-19} level", Opt. Express **20**, 21019–21024 (2012).

[85]J. Ye, L. Robertsson, S. Picard, L.-S. Ma, and J. Hall, "Absolute frequency atlas of molecular I/sub 2/ lines at 532 nm", IEEE Transactions on Instrumentation and Measurement **48**, 544–549 (1999).

[86]R. Abbott and C. Osthelder, "aLIGO LSC IQ Demodulator Board", LIGO Scientific Collaboration **D0902745** (2018).

[87]C. R. Cahillane, "Controlling and Calibrating Interferometric Gravitational Wave Detectors", PhD Thesis, California Institute of Technology, `10.7907/76jj-mr73` (2021).

[88]J. Miller, L. Barsotti, S. Vitale, P. Fritschel, M. Evans, and D. Sigg, "Prospects for doubling the range of Advanced LIGO", Phys. Rev. D **91**, 062005 (2015).

[89]E. steering committee et al, "Einstein Telescope: Science Case, Design Study and Feasibility Report", ET Docs **ET-0028A-20** (2020).

[90]M. A. Green, "Self-consistent optical parameters of intrinsic silicon at 300K including temperature coefficients", Solar Energy Materials and Solar Cells **92**, 1305–1310 (2008).

[91]C. Darsow-Fromm, M. Schröder, J. Gurs, R. Schnabel, and S. Steinlechner, "Highly efficient generation of coherent light at 2128 nm via degenerate optical-parametric oscillation", Opt. Lett. **45**, 6194–6197 (2020).

[92]T. W. Hänsch, "A passion for precision", Nobel Prize Lecture (2005).

[93]T. Fortier and E. Baumann, "20 years of developments in optical frequency comb technology and applications.", Communications Physics **2**, 153 (2019).

[94]L. Hollberg, S. Diddams, A. Bartels, T. Fortier, and K. Kim, "The measurement of optical frequencies", Metrologia **42**, S105 (2005).

[95]D. J. Jones, S. A. Diddams, J. K. Ranka, A. Stentz, R. S. Windeler, J. L. Hall, and S. T. Cundiff, "Carrier-Envelope Phase Control of Femtosecond Mode-Locked Lasers and Direct Optical Frequency Synthesis", Science **288**, 635–639 (2000).

[96]J. Romie and D. Coyne, "Small Optics Suspension (SOS) Assembly Specification, Rev. F", LIGO Scientific Collaboration **E970037** (1997).

A p p e n d i x   A

SUSPENDING OPTICS

In the BHD upgrade (see Sec.7.2), seven new Small Optic Suspensions were installed. These are suspensions to install 3-inch diameter optics that are suspended with wires from the top. We used steel adaptors to hold a 2-inch optic in the same suspensions, also allowing us to install the wires and the magnets on the adaptor. This differs the installation steps a little bit from what is mentioned in the assembly instructions[96]. This work was led by Yehonathan Drori in our team. Some of the photos in this section have been taken by him. Following are the steps we used for installing each optic in the adaptor, suspending the optic, installing OSEMs, balancing the suspended optic, and transporting it to the chamber.

Figure A.1: Gluing dumbells to magnets for suspensions. The North and South poles of the magnets are segregated and placed on the fixture. Dumbells with small amount of EP-30 glue is placed on the top and left to cure fo 24 hours.

1. Prepare the epoxy solution by mixing the two components of 'Vac Seal' together on a UHV aluminum foil boat and put a small dab on 5 dumbells.

2. Put magnets inside the gluing fixture. The magnets should be placed such that 3 of them have the same pole attached to the dumbell, and the other 2 have opposite poles attached to the dumbell (3 North, 2 South or 3 South, 2 North). Then put the dumbells with a small amount of epoxy in the fixture. Leave for 24 hours to cure. See Fig. A.1 for reference.

3. Clean the back surface of the adaptor. Place it on a clean aluminum foil.

Figure A.2: SOS towers prepared for suspending optics.

Figure A.3: Side plate for attaching wires and side magnet for 2" to 3" adapator.

4. Prepare more epoxy solution and add a small dab on the dumbell side of each magnet-dumbell assembly prepared earlier.

5. Place four magnets with epoxy side facing up on a piece of clean laminated paper with four marks separated by 2 inches forming a square. Arrange them such that two magnet-dumbell assemblies have a North pole facing down, and two have a North pole facing up, with the matching pair taking diagonal
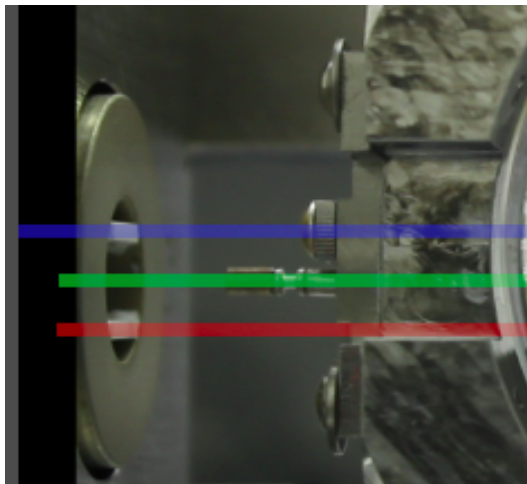
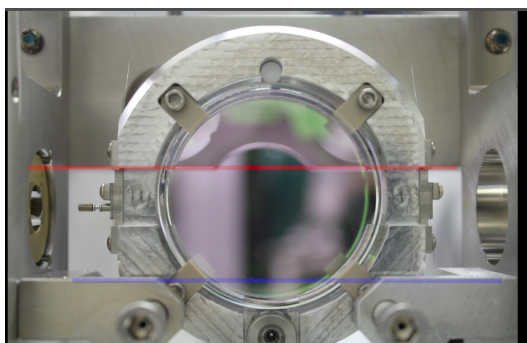Figure A.4: Height adjustment after suspending the optic on SOS tower.

Figure A.5: Roll balancing after suspending the optic on SOS tower.

positions.

6. Place the adaptor on the four magnets and press slightly. Leave for 24 hours to cure.

7. Put the fifth magnet with the epoxy side facing down on one side plate of the adaptor. Leave for 24 hours to cure.

8. Cut 2 pieces of about 50 cm of wire and gently place them on the grove of the side plates (one of whom has a magnet glued to it now). Be careful not to put any bends on the wire as it snaps very easily. See Fig. A.3 for reference.

9. Attach the side plates to the adaptor. using the two screws. To do so, place the adaptor on its face so that the glued magnets are facing up and come from the side to screw the side plates. Be careful to not knock off the magnets or damage the wires.

10. Now lift the adaptor and gently place it on the four magnet legs and the optic holding side is facing up. Gently place the optic in the adaptor and place the four nylon holding pads. Screw in the holders gently but do not tighten fully.

11. For tightening the screws completely, lift the adaptor using its side in your hand and then screw in the optic fully. This ensures no extra shear force is applied to the glued magnets while screwing in the optic.

12. Now the optic with the adaptor is ready for suspension. The next few steps require two people to work together.

13. Prepare the suspension tower (D960001) but keep the sensor/actuator plates (D960002) apart. Keep the bottom two earthquake stops on the tower as well.

14. Place the wire clamp (1205308-1) on the suspension block (D960003) but keep the screws loose to create space for wires to come through.

15. One person must hold the optic near the nominal position while the other one gently raises wires and send them through the space created above between the suspension block and the wire clamp. This part requires patience and care as the wires can easily develop kinks in which case the side plate assembly would need to be detached and prepared again.

16. Once the wires go through the groves, hold them taught and attach the wire to the winches (D970180) that are on top of the suspension block using the screws on the tapped holes.

17. The optic must be able to suspend on its own now.

18. Attach the two sensor/actuator plates (D960002) now. Attach the four face OSEMs and the side OSEM to the tower now, but do not push them into the adaptor all the way. Most probably, your suspension would be a little off such that the magnets of the adaptor assembly are not centered across the two plates inside the OSEMs.

19. Adjust the two winches now to get the magnets roughly centered between OSEM plates when looking through the OSEMs. One can use a camera to do this more accurately. See Fig. A.5 for reference.

20. Once the suspension is leveled correctly, screw in the wire clamp on the front side of the suspension block to press firmly on the wires. Now the winches can be removed and any extra overhanging wires on the top can be cut.

21. Once this adjustment is finished, pull back all OSEMs so that they are safely away from the optic and the earthquake stops would not let the magnets go inside the OSEMs. This is important for transportation later.

22. Setup a HeNe laser to create an optical lever with the suspended optic using a QPD. Ensure the input beam is leveled by placing two irises at the same height at two points in the input path.

23. Use the bottom set screw in the adaptor of the optic to adjust the center of mass of the optic and adaptor assembly to ensure that the optic is suspended flat by measuring the pitch of the reflected beam from the optic on the QPD.

24. Finally place all the earthquake stops and secure the optic in the suspension for transportation.

25. Open the chamber where the optic needs to be installed and prepare an area, ideally near the chamber entrance where the optic can be delivered.

26. Cover the suspension in aluminum foil from all sides while making sure that the aluminum foil only touches the tower and not the wires or the optic.

27. Have one person hold any doors for the person who will transport. The suspensions are most safely transported by carrying in hands, held tightly from beneath the base of the suspension and from the side plate.

28. Place the suspension in the chamber optical table and slowly tear away all the foil. For removing the foil underneath the base, slowly tilt the suspension on either side to get it out. Now the suspension is ready to be installed in the position.